THESIS FOR THE DEGREE OF DOCTOR OF PHILOSOPHY

Electrical Characterisations of Bearings

ABHISHEK JOSHI

Electrical Power Engineering
Department of Electrical Engineering
CHALMERS UNIVERSITY OF TECHNOLOGY
Göteborg, Sweden 2019

Electrical Characterisations of Bearings

ABHISHEK JOSHI
ISBN: 978-91-7597-839-0

Doctoral Dissertations at Chalmers University of Technology
Series Number: 4520
ISSN: 0346-718X

Division of Electrical Power Engineering
Department of Electrical Engineering
Chalmers University of Technology
SE-412 96 Göteborg
Sweden
Telephone +46 (0) 31 -772 1000

Cover – Plausible electro-physical mechanisms leading to electrical breakdown in bearings.

Printed by Chalmers Reposervice
Göteborg, Sweden, 2019

Electrical Characterisations of Bearings

ABHISHEK JOSHI
Department of Electrical Engineering
Chalmers University of Technology

Abstract

Mechanical bearings are an integral part of industry and are used in various places in order to reduce friction between two interacting surfaces and are used to transmit power and loads. Mechanical bearings are one of the most extensively used components within the wind industry, but on the other hand they are also one of the most dominantly failing components. In order to increase the feasibility of wind energy and to make the wind power more sustainable, a reduction in operation and maintenance cost of wind energy is important. The failures in bearings in the wind energy sector and other industries increased after the introduction of switched power electronic switches (Insulated Gate Bipolar Transistors, or IGBT) within the power converters. The reasons of early failures have been linked to the presence of a common mode voltage at the neutral of the converter and its coupling on the shaft, where the bearings are located. The system is also vulnerable to different types of bearing currents, which are discussed in this report.

A small voltage in range of 10's of volts could lead to large electric-field stress of 30 to 40 V/μm in a bearing depending on nominal film thickness at the operating point. The build-up of large electric field stresses in the bearing leads to ohmic electrical conduction through the bearing. Presently, the mitigation techniques mainly discharge the voltage across the bearing by providing a low resistance path for the flowing current using different methods, such as carbon brushes or shaft rings, but damages due to bearing current activity and early failures still exist. Another way to mitigate bearing currents is to use filters in the electrical connections, to obstruct or to reduce the amplitude of the bearing currents, but they fail to completely eliminate them. The use of insulating coating on surfaces of the bearing and ceramic rolling elements helps to provide a high resistive path for the current in case of DC voltage; but act capacitively and let the current pass through the bearing when high frequency circulating type bearing currents flow in the system. Nevertheless, to device a successful mitigation technique, it is important to fully understand the electrical breakdown and discharge activity within the bearing's insulation (i.e., the lubricating film) along with electrical properties of the bearing during running conditions.

In our research, we have focused on understanding the electrical properties of the mechanical bearing at different operating conditions and elaborating it through an electrical circuit model. The components of this electrical circuit model are found out experimentally through different laboratory tests. The mechanical bearing is sometimes found to behave as an insulator of electricity and is hence characterised by an impedance during the 'Insulating state' of the bearing in the model. The impedance in this insulating state is further categorized as a parallel combination of a resistor and a capacitor (parallel RC branch), which corresponds to the 'real' and 'imaginary' part of the measured bearing impedance. Furthermore, when the bearing enters into a partial breakdown state, the voltage across the bearing is 'discharged', resulting in flow of current through the bearing until the voltage across the bearing again recovers. The electrical characterisation of bearing lubricants has been performed in order to find out the relevant electrical properties, such as relative permittivity, electrical conductivity and electric breakdown strength at rather short gaps. The

electrical behaviour of the mechanical bearing at different operating conditions such as rotational speed, mechanical load along with magnitude, frequency and shape of applied voltage has been found out experimentally in order to understand and elucidate the electrical properties of a mechanical bearing in operation.

Index Terms: Bearing currents, Mechanical bearing, Ball bearing, Spherical bearing, Electrical characterisation, Electrical conduction, Bearing Capacitance, Lubricants, Equivalent circuit model.

ACKNOWLEDGEMENTS

This work has been carried out within the Swedish Wind Power Technology Centre (SWPTC) project “Current Induced Damages in Bearings - Mechanisms of Charging, Discharging and Damage Control” within theme group ‘TG5-2 Reliability and Maintenance’ for wind turbines and is made possible by a joint financial support by ABB Sverige, Chalmers University of Technology, Connected Wind Services A/S (formerly known as Triventus AB), Göteborg Energi AB, SKF Sverige AB and SWPTC. The SWPTC is a research centre at Chalmers, which is co-funded through the Swedish Energy Agency (SEA) and the industrial partners. I would like to thank all the project partners from the past and in the present, for quality discussions and research ideas during the theme group meetings.

I sincerely appreciate the financial support in form of scholarships from ‘Schneider Electric’s fund in memorial of Erik Feuk’ and ‘K. G. Hallbygg’s scholarship’ for attending conferences.

I am very grateful to my examiner Professor Stanislaw Gubanski for always providing a broader perspective to research, support for my studies and reviewing my thesis. My supervisor, Assoc. Professor Jörgen Blennow has shared his expertise and has taught me the philosophy of research and education in general. He has always been ready for discussing new ideas and sharing valuable knowledge. A big thanks to Professor Ola Carlson for valuable inputs and feedback for the finalisation of the thesis. My dear colleague Xiangdong Xu has helped very valuably by providing his close collaboration and support in dielectric characterisation measurements using AWIS technique. Dear Thomas, thanks for letting me pick your brain every now and then! Sara Fogelström has been very helpful while coordinating with the members of SWPTC, many thanks to you. I would like to thank Professor Lars Nyborg at the Department of Materials and Manufacturing Technology at Chalmers for providing surface morphology tools and specially thank Erik Tam for his work on surface analyses on bearings.

I would also like to thank Olle Bankeström of SKF, Göteborg, for providing test bearings of type 608 and type 22220 and lubricants Samples A and B along with access to their large-scale test rig located at their premises. Thank you for a great help in the project and providing your valuable point of view. I would also like to thank other employees and engineers at SKF, Göteborg, specially Peter Hagg, Jonas Peterson and Peter Boussard for assisting this project by conducting particle counting analysis for the test lubricant samples. I would also like to thank Connected Wind Services (formerly known as Triventus AB) for providing failed bearings for surface analysis.

All my colleagues from department of Electrical Engineering have all contributed to an enjoyable working atmosphere. Thank you all very much for your inputs, support and good memories.

My family members are sincerely thanked for their steady supply of care packages and encouragement. Most importantly, I would like to thank my wife Marika for her understanding, constant support and love during the extent of this work.

Abhishek Joshi
Göteborg, Sweden
April, 2019

PREFACE

The Swedish Wind Power Technology Centre (SWPTC) is a research centre for design of wind turbines. The purpose of the Centre is to support Swedish industry with knowledge of design techniques as well as maintenance in the field of wind power. The research in the Centre is carried out in six theme groups that represent design and operation of wind turbines; Power and Control Systems, Turbine and Wind loads, Mechanical Systems and Structures, Offshore, Maintenance and Reliability as well as Cold Climate.

This project is part of Theme group 5, Maintenance and Reliability.

SWPTC's work is funded by the Swedish Energy Agency as well as academic and industrial partners. The Region Västra Götaland also contributes to the Centre through collaborating projects.

LIST OF ABBREVIATIONS

SWPTC	Swedish Wind Power Technology Centre
SEA	Swedish Energy Agency
IEEE	Institute of Electrical and Electronics Engineers
IEC	International Electrotechnical Commission
ISO	International Organisation for Standardisation
VFD	Variable Frequency Drive
ASD	Adjustable Speed Drive
IGBT	Insulated Gate Bipolar Transistor
PWM	Pulse Width Modulation
HF	High Frequency
CM	Common Mode
CMS	Condition Monitoring System
EDM	Electrostatic Discharge Machining
EHL	Elasto-Hydrodynamic Lubrication
ATD	Arizona Test Dust
O&M	Operation and Maintenance
AWIS	Arbitrary Waveform Impedance Spectroscopy
SFIG	Stator-Fed Induction Generator
DFIG	Doubly-Fed Induction Generator
BVR	Bearing Voltage Ratio
THD	Total Harmonic Distortion
DC	Direct Current
ESIM	Electrostatically Shielded Induction Machine
TAN	Total Acid Number
RPM	Revolutions Per Minute
N.A.	Not Available
HD	Hydro-Dynamic
DF	Dielectric-loss Factor
OIP	Oil-In-Paper
RMS	Root Mean Square
FN	Fowler-Nordheim
ToC	Time of Conduction
DAC	Data Acquisition Card
VSI	Vertical Scanning Interferometry
IDA, IDAX	Insulation Diagnostics Analyser

TABLE OF CONTENTS

1 Introduction

Increased sustainability of wind turbines is important for manufacturers, owners and wind turbine maintenance companies; hence, emphasis is being made on reducing their life costs and optimising maintenance strategies. As mechanical bearing constitute one the key components for the reliability of wind turbines, it is important to reduce down-times due to premature bearing failures.

Mechanical bearings provide low friction in moving machine parts, transmit loads, supports and locate rotating equipment. Early failures of bearings in wind turbines and rotating machines in other industrial applications have gained attention in scientific world in the past three decades. Modes of bearing failures can differ, but of special interest remain premature failures in bearings due to electro-erosion of bearing steel, which are caused by flow of current during temporary electrical breakdowns of the bearing insulation. As a background, failure statistics in bearings of rotating machines in the industry is considered with focus on wind turbines.

Although studies of bearing currents in electrical drive systems in motor applications have already been performed, the discharge mechanism in the lubricant film still to a large extent remain unrevealed. In this thesis, electrical properties of bearings are studied at different operating conditions, involving variations of speed, bearing load, type of lubricant, voltage etc. This way the role of different plausible electro-physical mechanisms leading to breakdown of electrical insulation in the bearing is elucidated. The introductory chapter will outline the aim and research questions of the thesis. The scientific methods performed and their limitations are also discussed.

1.1 Background

Bearings have been the backbone of our industry, specifically in rotating machinery applications. Without correct functioning of bearings, the resultant friction will cause excessive heating, increased wear and increased noise, resulting in loss of power and efficiency. In wind turbines, bearings are used in the electrical generator. Bearings are also used in pumps, tachometers and different sub-assemblies within the wind turbine.

Early failures in bearings of electrical generators of modern wind turbines have increased after the introduction of Insulated Gate Bipolar Transistors (IGBT) based power electronic converters and have been linked to presence of shaft voltage and bearing currents within the system [1-5]. Switching times of these semiconductor switches have reduced since their introduction in 1980s, as faster switching times lead to lower losses. Commutation times of 40 ns to 50 ns can be reached with modern semiconductor switches. These power electronic converters are used to convert the voltage, frequency and active power acceptable by nationalised grid code requirements [6].

Early bearing failures were also found in induction machines when operated by Variable Frequency Drive (VFD), a type of Adjustable Speed Drive (ASD). In such a configuration, many VFDs induce a significant amount of potential on the main shaft of the motor that results in bearing currents [7-10] flowing within the system. The VFDs are operated by switching of IGBTs to produce the Pulse Width Modulation (PWM) waveform. The switching times of IGBTs in combination with the modulation scheme involved, produce system over voltages, which can be four times higher than the DC bus voltage [11] along with high slew rates, which could reach up to 10 kV/μs [12].

The origin of different kinds of bearing currents yielding premature failures has been described in various publications [13-19]. While damaged, bearings are also associated with being a primary cause of excessive vibrations, thus related to secondary failures caused to critical components along the main shaft [20]. These failures can be catastrophic in nature and typically, the Operation and Maintenance (O&M) costs constitute about 20 % to 30 % of Life Cycle Costs (LCC) of an on shore wind turbine [21] and can be up to 30 % of the considerably higher LCC in case of offshore wind parks [22]. It is therefore vital to reduce the O&M costs by continuously monitoring the health of critical components and devising mitigation techniques to avoid failures in bearings [5, 23-26].

In studies of bearing current activity the focus was primarily on identifying the source of shaft voltages and bearing currents [27-30] along with quantifying the influence of different system parameters such as presence of cables [31, 32], modulation scheme, carrier frequency, switching times [33] etc. Many researchers have adopted as the starting point the system level approach, providing threshold values of shaft voltages and bearing currents acceptable during normal operation of rotating machines of various sizes, types and configurations [7-9, 34-36]. There have also been circuit simulation studies based on measured system parameters and aiming to predict the level of bearing current activity and shaft voltages [1, 3, 7, 37, 38].

The effect of shaft voltages and bearing currents on the insulating properties of the rotating bearing under different operating conditions still remains to be studied extensively. Although there have been some steps in this direction [39], a systematic study on breakdown of the lubricant film as well as on current conduction characteristics are still to be investigated. As a step in this direction, a major part of this thesis investigates the electrical properties of the bearing and quantify them by via experiments and elaborate the behaviour them through an equivalent circuit model.

1.2 Aim and questions raised

The primary aims of the presented work are (i) to quantify electrical properties of bearing at different operating points, (ii) investigate role of different plausible mechanisms leading to breakdown of insulating properties of a running bearing and (iii) investigate the electrical properties of bearing lubricants. Answering the following questions will help understanding the electrical properties of the bearing.

- How can the properties of a running bearing be modelled using an equivalent electrical circuit?
- What are plausible mechanisms controlling a breakdown in bearing insulation?
- What are the typical operating conditions under which the said plausible mechanisms are expected to be active?
- Under the influence of an electrical field, how much does the current activity vary with the changes in bearing operating point?
- How does debris particle concentration level affect the electrical breakdown events in a bearing?
- What are the differences in breakdown events arising due to different types of particles?
- Do the electrical breakdowns events influence the ability of the bearing to withstand additional electrical stress?
- What are the electrical properties, such as, relative permittivity, electrical conductivity and electrical breakdown strength of typical bearing lubricants?

1.3 Main contributions of the thesis

The following contributions have been made in the thesis:

1. The mechanical bearing has been treated a system of multiple sub-components to have a deeper understanding of current conduction through the bearing. An equivalent electrical circuit model has been proposed and experiments are carried out to quantify components of the circuit model using standard electrical characterisation techniques.
2. Experiments on running bearings are carried out to characterise the electrical properties in two possible states of the bearing, i.e., insulating and conducting states. The results show that all bearings exhibit these two states and the switching in between the states is a function of the bearing operating point and electric field strength.
3. Electric field dependent current conduction in bearing is investigated in range of 3.7 V/µm to 44.6 V/µm. A bearing under normal operation is fully conducting at electric field strength of higher than 29 V/µm. If the bearing has limited lubrication, the bearing is fully conducting between 20 to 25 V/µm.
4. Apart from measuring bearing capacitance at multiple operating points, a ball per ball capacitance measurement technique is performed for the first time to further the scope of standard bearing capacitance measurements technique.
5. In normal bearing operation, if electric field strength across the bearing is near the lower range (3 to 5 V/µm), the bearing is electrically insulating. In literature, this state is characterised by capacitance and capacitive current flows through the bearing. By measuring of dielectric loss during bearing capacitance measurements, bearing resistance in insulating state is for the first time experimentally quantified and presented using the ball per ball measurement technique.
6. The flow of ohmic current through the bearing is studied considering multiple plausible electro-physical mechanisms that can arise during normal operation. In literature, studies are performed with focus on only one of the mechanism, i.e., field dependent current conduction.
7. Asperity contacts cause significant ohmic current conduction at dimensionless speed of lower than 12000 corresponding to a speed of 800 rpm in the test bearing type 608. Above this threshold, the influence of the asperity contacts is negligible and result in ohmic current conduction for less than 1 % of the duration of measurement.
8. Particle-initiated breakdowns are not only investigated at proposed acceptable contamination level of 150 mg/L by Elforsk [40], but also at different concentration levels in the range of 7.5 mg/L to 150 mg/L. As particles form a bridge inside the bearing, all the voltage developed across the bearing is discharged though this path. For dust particles, this threshold is found to be too high and leads to ohmic current conduction for 10.7 % of the time. A recommendation to Elforsk from a bearing currents perspective is to reduce the contamination level to 30 mg/L in environments prone to dust particles, since it results in ohmic conduction for less than 1 % of the duration of measurement.
9. Particle contaminants used in tests that are metallic in nature, for example aluminium powder have ohmic current conduction of about 1 % at a concentration of 150 mg/L.
10. Ohmic current conduction due to electrical breakdown of oil film increases as the electric field across the bearing is increased from 3.4 V/µm to 44 V/µm. A normally operated bearing with adequate lubrication is found to have an inception level for ohmic current

conduction at 29 V/µm, while the same bearing with limited lubrication is found to have a lower inception field level of 14 V/µm.

11. The bearing is also found to exhibit *memory effect* or hysteresis due to after passage of large number of ohmic current conduction pulses and is not found to be reported in literature studies. The findings are presented in Chapters 8.2.2 and 8.5.2 of this thesis.

1.4 Methods

An experimental approach, utilizing different test setups for different types of bearings, was chosen in this work for obtaining information on the electrical state of bearings and lubricants for developing the electrical circuit model. Two types of bearings tested were deep groove ball bearing 608 and spherical roller bearing with cylindrical and tapered bore 22220 [41].

The electrical *insulating state* properties of the bearing are modelled as a parallel connection of bearing capacitance and bearing resistance in insulating state. The bearing capacitance is a function of the bearing geometry and lubricant properties, while the bearing resistance in insulating state represents all the dielectric losses in the bearing in the insulating state. The applied voltage along with the current through the bearing is measured to derive complex impedance, which is further used to find bearing capacitance and bearing resistance in insulating state.

The electrical *conducting state* properties of the bearing are modelled as a series connection of a switch and an equivalent bearing resistance in conducting state. An insulating state branch is connected in parallel to conducting state branch and is referred to as the insulating state branch in the equivalent electrical circuit model. The closed switch represents an electrical breakdown of the lubricating film and it can be caused by different conduction / breakdown mechanisms, such as:

- Asperity-initiated breakdown
- Particle-initiated breakdown
- Voltage and electric field dependent breakdown

The bearing resistance is the resistance of the bearing in conducting state, which is derived from the ratio of voltage across the bearing and the current through the bearing during the discharge or conduction process.

To study the voltage and electric field dependent breakdowns in a bearing, a current limitation resistor (approximately 1 kΩ) was used in series with the bearing in the test circuits to limit the amplitude of current flowing through the bearing during the discharge events. In this way, the effects of current induced damages on the bearing surface could be minimised, whilst evaluating voltage and electric field dependent breakdown characteristics of different tests objects.

Further on, electrical characterisation of bearing lubricants has been carried out using Frequency Domain Spectroscopy (FDS) and electrical breakdown strength measurement, in a statically bound test setup. FDS is a non-destructive test method and has historically been used in the field of transformer and cable diagnostics. The FDS measurements have been carried out using Insulation Diagnostics Analyser IDAX 300 [42] and IDA 200 where the complex impedance was derived as a function of swept frequency. The measurements were used to evaluate complex permittivity and temperature dependent DC conductivity of the bearing lubricants. Additionally, the 50 Hz AC breakdown strength of the lubricants were experimentally measured using ramping tests on small gaps of 0.1 and 0.2 mm.

The insulating state properties of bearing such as bearing capacitance, bearing resistance in insulating state and dielectric loss factor (tanδ) in a running bearing have been characterised using a measurement technique called AWIS (Arbitrary Waveform Impedance Spectroscopy). The method uses measurement of voltage across the test object and current through the test object to determine the complex impedance.

Surface analyses of bearing were carried by using an optical profiler WYKO surface morphology microscope.

The particle-initiated breakdown was studied as a function of different particle types, such as Arizona test dust, fine toner particles, aluminium powder and fine iron powder at five different concentration levels in the lubricant, varying between 7.5 mg/L and 150 mg/L. The particle counting for investigating the size and distribution of externally added particles was carried out according to standard method ISO 4406, using 1.2 µm membrane for particle-contaminated lubricant samples as well as cleanliness analysis MP A27, using 5 µm Nylon membrane for dry particle samples.

Finally, calculations of the film thickness and viscosity index were done using SKF Galaxy [43] toolbox. It applies the elasto-hydrodynamic film thickness formula of Hamrock and Dawson [44] and can be used for different types of bearings at different operating conditions of loads, speeds, temperatures and lubricant properties.

1.5 Limitations

The system aspects are not considered in this thesis since the performed literature review revealed existence of extensive work already present on system level studies. The effects of vibrations, eccentricity and misalignment on the current activity were also not taken up here due to limitations of the slip ring used in the test bench. The current activity in the bearing was investigated at a high dV/dt of 0.08 kV/µs, which is considerably less than the dV/dt (2 to 10 kV/µs) found in IGBTs. This limitation was introduced due to a lack of actual power switching devices (such as IGBTs) in the test setup. The temperature of the lubricant was not monitored for the miniature ball bearing of type 608 and hence lubricant temperature is not included as an operating point in the further presented results and discussions.

1.6 Outline of thesis work

In this thesis, Chapter 2 contains the review of scientific research in the field of bearing currents. The failure statistics for bearing in wind industry and in other sectors are presented first. Different damage modes relevant to the bearing failures due to the presence of particles and electric field-initiated breakdowns are considered. The origin of the common mode voltage, shaft voltage and the parameters of the stray capacitive network which form the common mode circuit in a machine are discussed. The origin of different bearing currents and their conduction paths in a drive train assembly, which could damage the bearing are also presented. The mitigation techniques for reducing current induced bearing damages, along with the present understanding of electrical properties of the bearing is presented. The electrical and mechanical properties of bearing lubricants found in literature are listed to allow comparison with the values obtained in this work.

Chapter 3 discusses the parameters of the proposed equivalent electrical circuit model of the bearing and their significance, while Chapter 4 presents the test objects, setups and methods involved in the laboratory experimental investigations.

Chapter 5 is dedicated to characterisation of bearing lubricants. Properties of the lubricating films, such as calculated thickness and viscosity index obtained during different tests are reported.

Chapter 6 presents results and discussions of the measured bearing capacitance, while Chapter 7 shows results from measurement of bearing resistance in insulating state.

Chapter 8 is devoted to switching pattern analyses for investigating different mechanisms leading to breakdown of bearing electrical insulation in running conditions. The current activity as a function of varying operating points, such as rotational speed and mechanical load, are discussed. The chapter further reports on investigations of asperity-initiated breakdowns, particle-initiated breakdowns and voltage dependent breakdowns in a running bearing.

Chapter 9 shows results of measured bearing resistance in conducting state for different breakdown mechanisms. Chapter 10 presents analyses of electrically induced damages on a bearing installed in electrical generator of a wind turbine. Chapter 11 presents summary of the work followed by conclusions in Chapter 12 of this thesis. Possible future activities for continuation of this research are presented before the References and Appendix.

1.7 List of publications

I. Joshi, A.; Blennow, J., “Investigation of the static breakdown voltage of the lubricating film in a mechanical ball bearing,” Proceedings of the 23rd Nordic Insulation Symposium (NORD-IS 13), June 9–12, 2013, Trondheim, Norway, pp. 94–97, ISBN/ISSN: 978-82-321-0274-7

II. Joshi, A.; Blennow, J., "Electrical characterization of bearing lubricants," IEEE Conference on Electrical Insulation and Dielectric Phenomena (CEIDP), 2014, vol., no., pp.586,589, 19–22 Oct. 2014, DOI: 10.1109/CEIDP.2014.6995856

III. Joshi, A.; Blennow, J., “Elaborating electrical properties of bearings with focus on asperity-initiated insulation breakdowns during operation”, planned for submission in Journal of Renewable Energy, Hindawi Publication Corporation.

IV. Joshi, A.; Blennow, J., “Elaborating electrical properties of bearings with focus on particle-initiated insulation breakdowns during operation,” planned for submission in Journal of Renewable Energy, Hindawi Publication Corporation.

2 Literature review

Surface morphology of failed bearings is considered when relating different failure modes to their primary causes. Root-cause analysis of bearing failures have already been well documented [45-47]. To keep within the scope of the thesis, damages in bearing caused by lubricant contamination by abrasive particles and by passage of electrical current are discussed in this chapter. There are several other causes of bearing failures such as faulty mounting, overloading, misalignment, inadequate lubrication, rough treatment, excessive speed etc., but they will not be discussed here and more information can be found in [47-49].

2.1 Failure statistics of wind turbines and other rotating machines

A survey of failures in 1200 electrical generators of wind turbines, taking place between 2005 and 2011 in America, had revealed that bearing failures are the leading causes of downtime for turbines of size greater than 1 MW [50]. As illustrated in Figure 1, one found that 70 % of all downtimes in electrical generators rated between 1 MW and 2 MW were caused by failures in bearing, while for generators greater than 2 MW this rate was 58 %. The root cause of these failures have been attributed to transient shaft currents and improper maintenance. Other listed causes were worn slip ring brushes, stator winding temperature sensor failure, encoder failure, fan failure.

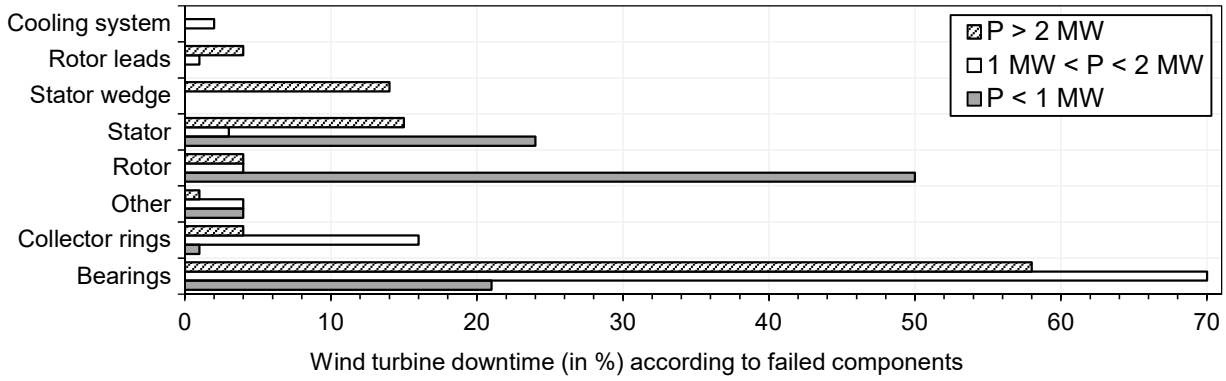

Figure 1. Causes of failures in 1200 wind turbine generators presented by K. Alewine and W. Chen in [50]. Failures in bearings are leading cause of downtime in wind turbine generators rated higher than 1 MW.

An update in this study was published in 2014 [51] and included data from a total of 2068 failed wind turbine generators during the period 2005 to 2013. It showed that failed bearings continue to be the leading cause of downtime in wind turbines. Bearing failures accounted for roughly 37 % of all failures, which is much higher than failures in any other component [51], as shown Figure 2. The bearing failures deemed to appear because of three main factors, which include; 1) inherent vibrations and loading problems; 2) transient shaft currents; and 3) poor maintenance strategies. In the conclusion, emphasis was put on mitigating transient shaft currents and on adapting improved grounding schemes along with use of insulated bearings in the system. In wind turbines, top three systems that account for highest failure frequency are electric systems, gearbox and generator. Failures in gearbox and electrical generator of wind turbine are also considered most expensive and account for 27 % of all failures and are equivalent to 0.6 failures per turbine sub-system per year.

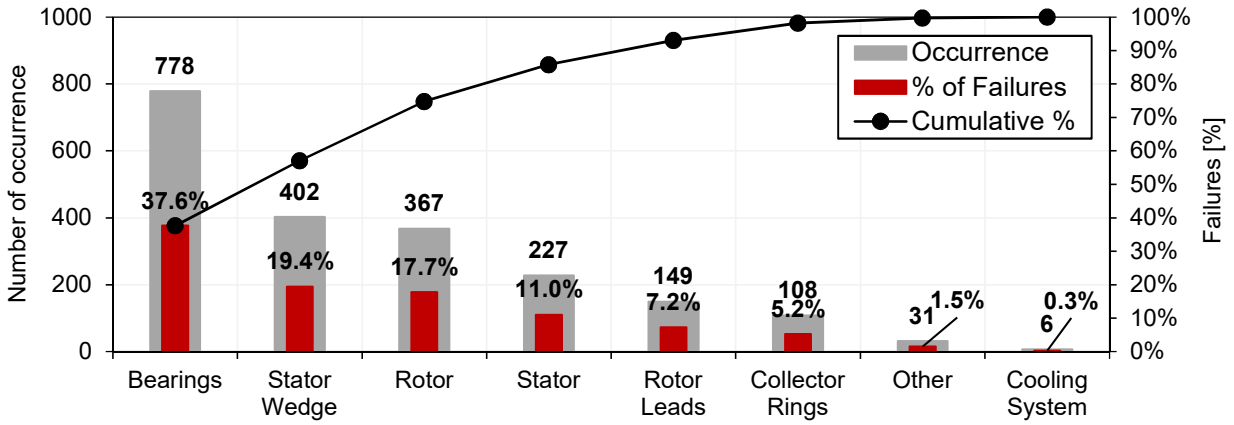

Figure 2. Failures statistics of 2068 wind turbine generators, having rated power in range of 660 kW and 3 MW, during the period 2005–2013. Failures in bearings not only remain leading cause of downtime in generators in wind turbines, but also in other applications. Image reproduced from [51].

In the wind power industry context, similar conclusions are found in [52], while [53] indicated that bearing failure rate within wind turbines is marginally higher than bearing failures in other industrial applications. IEEE surveys also showed that in large motors 42 % of all failures were due to bearings, as compared to 50 % found in wind sector [54-56]. This comparison is shown in Figure 3. Higher bearing failures in wind turbines compared to other industrial applications is consistent with the higher failures rates of electrical generators. In wind turbines, the failure rate of electrical generators is reported by Windstat to be 0.10 per generator per year [57], which included data for more than 6000 modern onshore wind turbines located in Denmark and Germany over a period of 11 years. In other industrial applications, the failure rates in generators is reported to be between 0.03 per generator per year to 0.07 per generator per year [54-56, 58, 59] and in large motor reliability survey of IEEE on industrial and commercial application [60, 61].

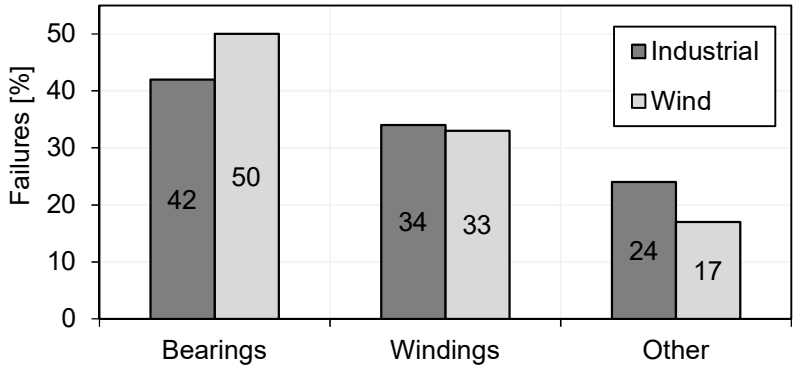

Figure 3. Percentage failures in machines due to different sub-assemblies. Data on industrial machine failures is collected from IEEE large motors survey parts I, II [54, 55] and III [56] and data on failures within wind generators is reported by K. Alewine in [50].

In other applications, such as petrochemical industries and refineries in the North Sea, bearing failures account for about 51 % of total failures [62], shown in Figure 4, claiming that the cause for bearing failures was due to mechanical breakage followed by overheating in bearings that caused high levels of vibrations and persistent overloading within drive systems.

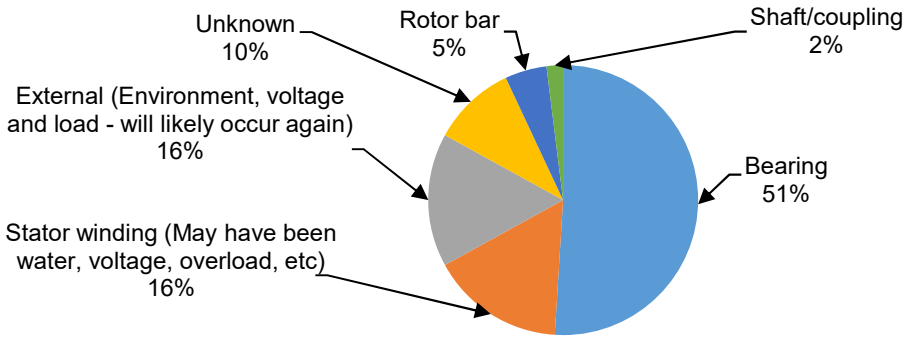

Figure 4. Distribution of failed components in induction motors in offshore and chemical industry reported in [62].

Yet another survey on low voltage and medium voltage induction conducted by P. J. Tavner [63] shows that 95 % of failures in low voltage AC induction motors (less than 750 kW, squirrel cage induction motors) resulted due to failure in the bearing sub-assembly.

An investigation [64] by Shaft Grounding Systems Inc. on failures of 1150 Adjustable Speed Drive (ASD) regulated AC motors installed for clean room application showed that 25 % of the motors failed within 18 months of operation due to bearing current damage. The cause for damage was claimed to be due to electrical discharges in bearings. Such drives operate at fixed speed, continuously without stops and typically have a carrier frequency of 12 kHz or higher for reducing motor noise. It is also reported that for bearings running for more than 18 months, more than 65 % of the bearings had failed at an average age of 24 months.

2.2 Damage modes in bearings

Bearings can be damaged due to several different factors such as shaft currents, debris, contamination, water intrusion (also moisture), temperature, fatigue etc. These factors have their own characteristic features and wear rate and results in a distinguishable change of bearing surface morphology after failure [20, 45, 48-50, 65]. In other words, the morphology of failed bearing surface can well be associated with the root cause of the failure.

2.2.1 Damages due to abrasive wear

If primary cause for damage is abrasive debris and contaminants in lubricant, the damage on the bearing surface looks like an ‘arrow’, as investigated in [66] and indicated in Figure 5. Rolling elements in bearings are designed to operate in Elasto-Hydrodynamic Lubrication (EHL) regime, where a thin film of lubricant (0.2 to 20 μm) is maintained between the rolling elements and the raceways. Since the sizes of the abrasive particles are mostly larger than the film thickness, this results in damage to the bearing surfaces. The direction of motion of the bearing element is in direction opposite to the arrow shown in Figure 5. It shows that the debris entering the lubricant film yields a three-body abrasion and results in formation of the large sized crater. This impact also causes a rupture of the debris particle into smaller ones, which rolling form in continued smaller craters (the tail of the arrow in the figure.

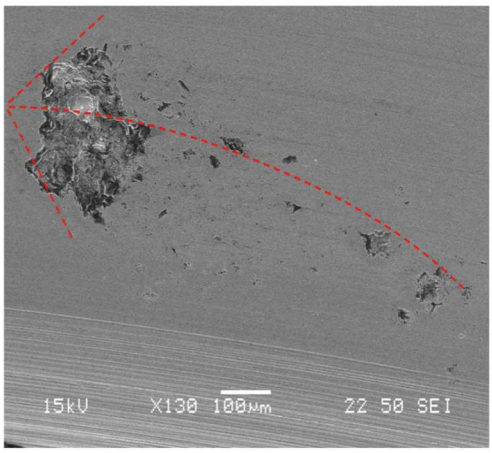

Figure 5. Scanning electron microscope image of surface wear due to particle contamination as illustrated by S. Schnabel in [66]. Image used with written permission of the author.

Damage in the bearing due to abrasive wear from contamination also may result in loss of mass from the balls, inner and outer raceways. In a study investigating this effect due to contamination by diamond abrasive particles of 2 to 4 µm in a deep groove ball bearing, analyses of the lubricant showed that 78 % of the total mass loss occurred from the balls. The inner and outer raceways suffered 21 % and 1 % loss respectively [67, 68]. In reality, industrial applications often face problems of solid contaminants that originate from ambient environments like salts, dust, silicon dioxide, aluminium oxide and due to human handling. The latter brings in bio-contaminants, like perspiration and fingerprints containing potassium chloride crystals).

2.2.2 Damages due to passage of current

The primary causes of bearing surface damage such as electrical pitting, electrical fluting, formation of micro-craters, formation of washboard pattern on raceways, degradation of lubricants, re-hardening of bearing steel have been linked to excessive passage of currents through bearings [69]. The damage due to current discharges (popularly referred to as EDM currents and stands for Electrical Discharge Machining currents) also has its signature look as

- Micro craters on the bearing surfaces, Figure 6.
- Frosting on surfaces as a wear damage, Figure 7.
- Formation of large, dark-coloured melt craters [70], Figure 7
- Discolouration of lubricant [71] (charring of carbon molecules)
- Corrugation pattern (or fluting pattern) on raceways, Figure 7

Appearance of large and small sized craters on the surface of balls and the raceways of the bearing are common outcomes of exposing bearing to electrical discharges. These result is localised melting of the surfaces due to the heat generated by the flowing current.

Figure 6. Damages on the bearing's ball due to electrical discharges form micro-crater on the ball, giving it a matte finish.

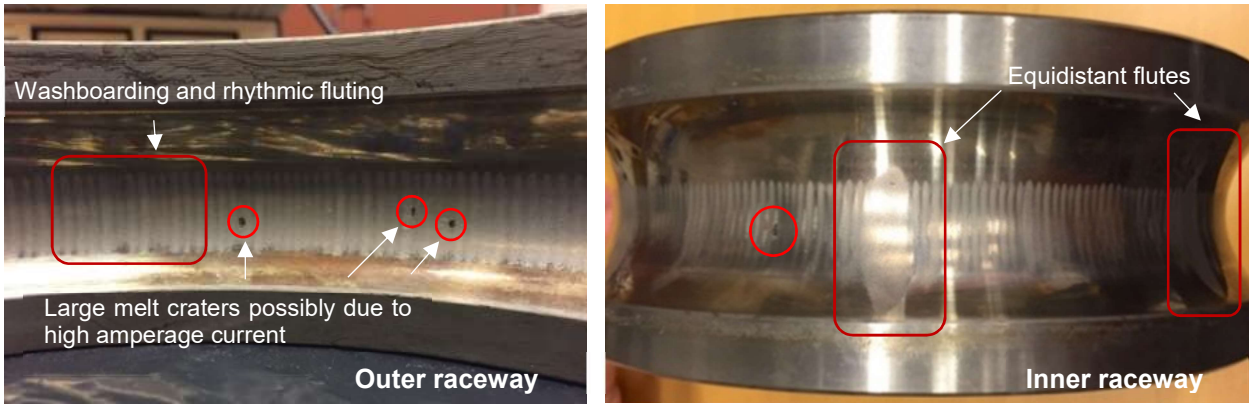

Figure 7. Wind turbine bearings damaged under operation. Damages on bearing's outer raceway (left) and inner raceway (right) due to electrical discharges, i.e., passage of electric current. Rhythmic and equidistant flutes are generated on the raceways due to occurrence of bearing current activity in conjunction with loading.

Literature studies have also confirmed discolouration of lubricant due to repetitive EDM events in a synthetic test bench [71, 72]. It was observed in these studies that 32000 EDM events at an applied voltage of 120 V led to dark discolouration of lubricant sample, which was transparent before the tests. This discolouration is not observed when the lubricant was exposed to 32000 EDM events at a lower applied voltage of 12 V. The changes in lubricant were observable in the visible spectrum of light, while no changes could be detected by means of infrared transmission spectroscopy. Thus, to investigate lubricant deterioration, determination of its electric breakdown voltage, dielectric spectroscopy, particle counting, dissolved gas analysis, total acid number and moisture content

analysis should be preferred to get a complete understanding of the changes in bearing's electrical insulating capability due to electrical stress.

The emergence of corrugation pattern on the raceways occurs after frosting damage, which looks like a glazed matt finish on the raceways of the bearing. Under-loading, the corrugation pattern may appear under the influence of electric field [73]. Another study [74] attributes appearance of the corrugation pattern (also known as fluting or washboard pattern) to bearing currents. The latter study related the degree of corrugation to current density and duration of its passage through the bearing. This relation is in Figure 8 showing the dependence of the time to corrugation on current density, using calculated Hertzian contact area for the bearing. The relation is of logarithmic dependence and the corrugation pattern on the raceways may show up in 5 hours when the current density equals to 2 A/mm^2, whereas for the density of 1.4 A/mm^2 the corrugation pattern appears after 500 hours of operation.

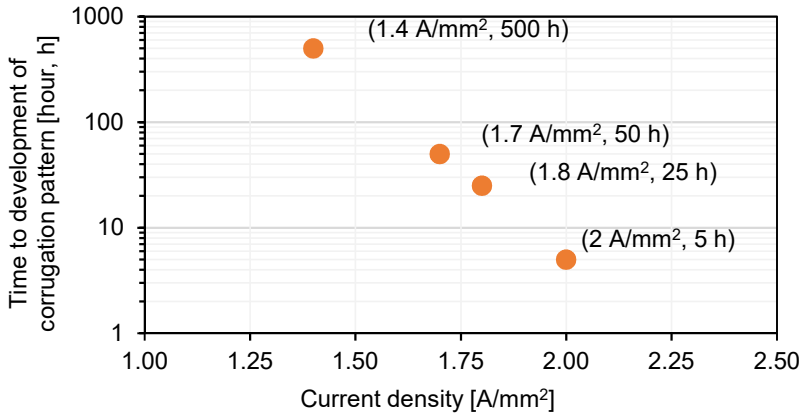

Figure 8. Time leading to development of corrugation pattern as a function of current density presented in [74]. The time to development of corrugation pattern is shown on a logarithmic scale.

2.3 Common mode voltage and current, common mode equivalent circuits

2.3.1 Common mode voltage and current

A *common mode voltage* (V_{CM}) appears due to inexact commutation to zero level during switching of the IGBT converters. The wave shape of common mode voltage is defined by the modulation scheme of the back to back AC-DC-AC converter and changes three times faster than the switching frequency of the power electronic switch, as shown in Figure 9. Since the switched output of the instantaneous value of the three line to ground voltages (V_{AG}, V_{BG} and V_{CG}) is not zero, V_{CM} is given by arithmetic mean of V_{AG}, V_{BG} and V_{CG}. The amplitude of V_{CM} can vary between ± $V_{DC}/2$ and ± $V_{DC}/6$ and is given by equation (1) as,

$$V_{CM} = \frac{V_{AG}+V_{BG}+V_{CG}}{3} = \pm\frac{V_{DC}}{2}, \pm\frac{V_{DC}}{6}. \quad (1)$$

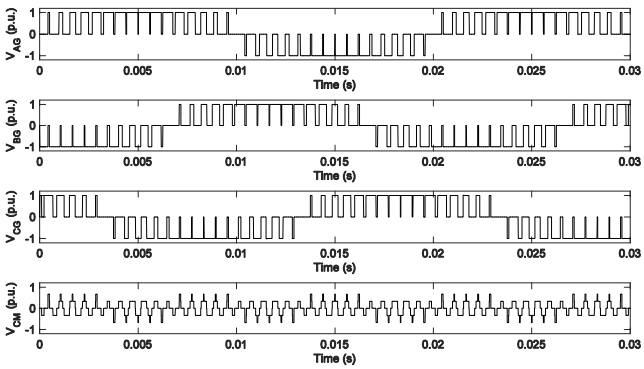

Figure 9. Common mode voltage (V_{CM}) is generated at the neutral of converter because the instantaneous sum of all the three phase voltages to ground is not zero. All voltages are shown in per unit (p. u.) value.

Due to the use of modern semiconductor switches, the common mode voltage has high voltage derivatives (dV/dt of up to 8 to 10 kV/µs) due to commutation times of the switch and DC link voltage. The DC link voltage can be up to 1 kV for wind turbines and could be even higher in modern wind turbines. The commutation times of a switch could be ranging from a few nano seconds to a few 100 micro seconds. Thus, the frequency content of the current pulses could range up to several megahertz. On a component level, typical rise times of modern IGBT is about 50 ns, but when measured within the system, the total rise time due to the IGBT can be measured up to 150 ns to 200 ns due to the impedance within the system.

The last trace in Figure 9 shows a typical shape of a common mode voltage. When the common-mode voltage makes a transition from one voltage level to another, a proportional *common mode current* flows to ground, via the stray capacitance formed between the machine winding and the grounded machine frame, due to formation of current loops in the system. The frequency of the current depends on the switching frequency of the power electronics, while the amplitude of the current pulse is proportional on the voltage derivative, since $i(t) = C \cdot dU(t)/dt$. Electrical connections are made using cables, which also form a part of the common mode equivalent circuit LC filters connected at the rotor side and the grid side converters to reduce the effect of high dV/dt and hence V_{CM}.

2.3.2 Stator-fed and doubly-fed induction generators in wind turbine

Wind turbines are at times connected in Stator-fed (SFIG, also sometimes called as singly-fed) connection, where the power is fed in to the grid through a converter on the stator-side. In this configuration, the common mode voltage is coupled to the shaft of the generator through the parasitic coupling between the rotor and the stator windings and between the rotor and the frame.

For enhanced speed control, the machine can be doubly-fed through an inverter at the rotor side in conjunction to grid-side converter. The configuration is termed as doubly-fed inverter generator (DFIG) and consists of a back to back AC-DC-AC inverter arrangement. In this arrangement, a shaft voltage could be imposed from two sides of the machine, the rotor side converter and by the stator side. Both arrangements are shown in Figure 10. Amplitude of the shaft voltage depends on the coupling capacity of the stray capacitances inside the machine.

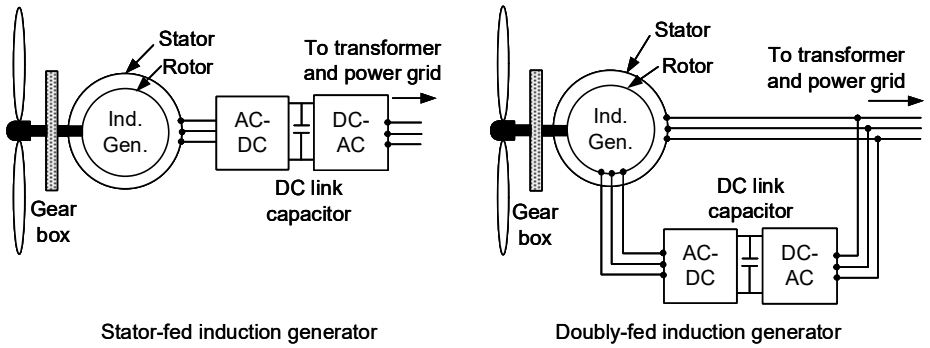

Figure 10. Simplified schematics of wind turbines in SFIG (left) and DFIG (right) arrangements. The converter is attached to stator-side for stator-fed arrangement, while it is attached to the rotor-side for doubly-fed arrangement.

2.3.3 CM equivalent circuit for stator-fed induction generator

The stray capacitances in the machine are influential when the high frequent V_{CM} is present in the system. Since the stray capacitances and the bearing capacitance form a common mode equivalent circuit, capacitive current flows and the common mode voltage is the driving energy source, as shown in Figure 11. The current could flow to the ground path through these capacitances and may take path offered at lower impedance and could be a result of improper grounding scheme [75]. The stray capacitances within stator-fed machines are denoted as C_{SWF}, C_{SWR}, C_{RF}, C_{B1}, C_{B2} shown and discussed below.

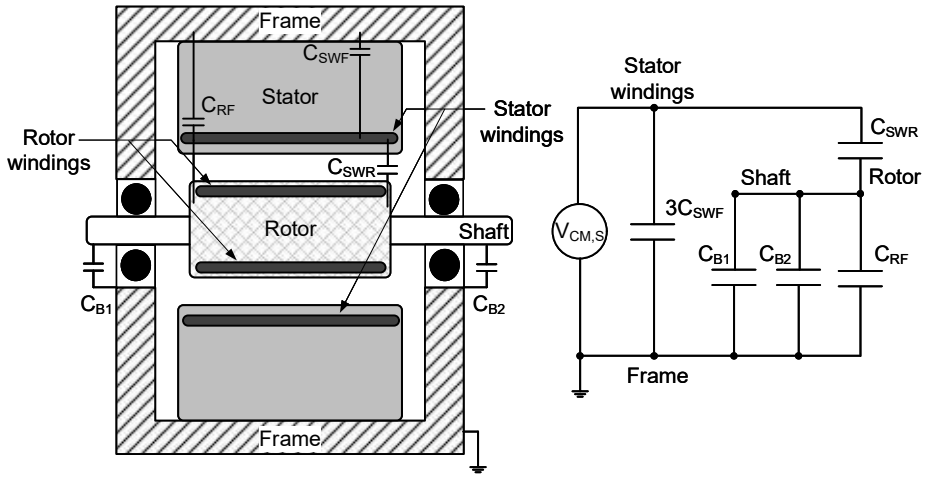

Figure 11. Stray capacitive coupling (left) within stator-fed machine elements that cause coupling of common voltage on shaft and corresponding electrical representation of the common mode circuit (right) formed as investigated by Erdman, Busse et al. in [76].

The capacitive couplings between the different parts of machine elements such as rotor core, stator windings and machine frame form a capacitive network, as shown in Figure 11. The drive-end and non-drive-end bearings is represented by an equivalent bearing capacitance C_{B1} and C_{B2}. The stator winding to rotor capacitance induces shaft voltage, which could possibly result in possibly harmful bearing currents. More detailed information about the common mode circuit is discussed below.

- **Bearing voltage ($V_{Bearing}$) -** It is defined as the voltage measured between the inner and the outer raceways of a bearing.

- **Shaft voltage (V_{Shaft}) -** It is generated on the shaft of machine through the linking of common mode voltage, V_{CM} through a network of stray capacitances between machine elements, investigated in [30, 77]. As per standards V_{Shaft} is measured between the two ends of the shaft of a rotating machine [78], arising due to electromagnetically developed voltages in the shaft, given by equation (2) as,

$$V_{\text{End-to-en shaft voltage}} = V_{\text{Bearing,Drive End}} - V_{\text{Bearing,Non-Drive End}}. \quad (2)$$

- **Stator winding to frame stray capacitance (C_{SWF}) -** It is formed between the stator winding and the grounded frame of the machine and is a result of two capacitances; the capacitance of winding insulation and the capacitance of slot wedge. It is the largest stray capacitance within the machine and most part of I_{CM} flows through it.

- **Stator winding to rotor stray capacitance (C_{SWR}) -** This stray capacitance is formed between the stator winding and the rotor in the machine. It is a function of the rotor length, length of slot tooth, number of slots and gap of air between the stator windings and the rotor. In relation to C_{SWF}, the value of C_{SWR} is relatively small, but is quite important since it determines the magnitude of shaft voltage in the machine.

- **Rotor to frame stray capacitance (C_{RF}) -** Stray capacitance between rotor and stator frame completes the charging path by forming a loop for current flow, which was started by charging of rotor by C_{SWR}. The value of C_{RF} is typically ten times more than the value of C_{SWR}. The voltage formed on the shaft due to presence of C_{RF} is in literature termed as *voltage along the shaft* [36].

- **Bearing capacitance (C_{B1}, C_{B2}) -** Bearing is in capacitive mode at high speeds and the load of the operation is carried out by a thin film of lubricant and it forms the smallest capacitance in common mode circuit.

- **Bearing Voltage Ratio or (BVR) -** It is defined as the ratio between the bearing voltage and the common mode voltage. Various studies have concluded that higher bearing voltage ratio leads to a higher amplitude bearing current activity across the bearing [1, 2, 36]. BVR is commonly used to understand the electrical stress on the bearing due to stray capacitances and is defined in [76, 79] and is described for stator-fed machines by equation (3) as,

$$\text{BVR} = \frac{\text{Bearing voltage}}{\text{Common mode voltage}} = \frac{V_B}{V_{CM,S}} \approx \frac{C_{SWR}}{C_{SWR}+C_{RF}+C_{B1}+C_{B2}}. \quad (3)$$

The quantification of machine stray capacitances as a function of machine size of up to 600 kW is reproduced in Figure 12 from [76]. BVR highly depends on the values of C_{SWR} and parallel C_{RF} in the common mode equivalent circuit, since other capacitances are smaller in their comparison.

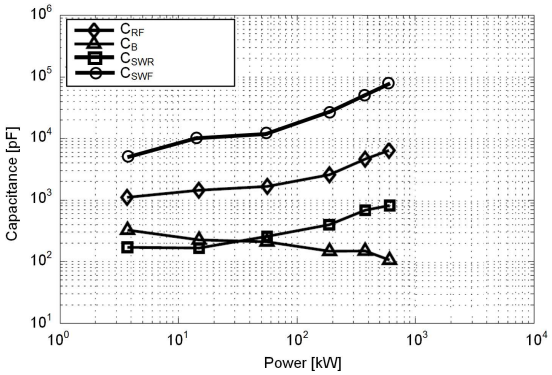

Figure 12. Stray capacitances within a machine as a function of machine size as investigated by Busse, reproduced from [76].

The stray capacitances are responsible for inducing many possible current paths not only within the generator, but also between the machine and components on the main shaft, if a path of lower resistance is offered through the bearing.

The stray capacitance within the electrical machine depends on its power, but not on its type, i.e., asynchronous, synchronous or permanent magnet rotors have the same stray capacitances. Electrical machines outside wind sector are dominantly stator fed, while wind turbine generators often work in doubly-fed or rotor-fed configuration. In DFIGs, the rotor windings are brought out of the machine and are connected to an AC voltage source through slip-ring connections from the rotor-side converter. Due to this difference in design compared to stator-fed induction generator, the stray coupling between the inverter fed rotor-winding and the rotor (C_{RWR}) is of importance in the common mode equivalent circuit of DFIGs.

2.3.4 CM equivalent circuit for doubly-fed induction generator

A generic schematic of wind turbine drive train assembly showing major components on the nacelle of the wind turbine such as blades, gearbox, electrical generator and converter are shown in Figure 13. Typical values of the stray parasitic capacitances for stator-fed machines has been shown in Figure 12, which have been reproduced from [76] and discussed in Chapter 2.3.2.

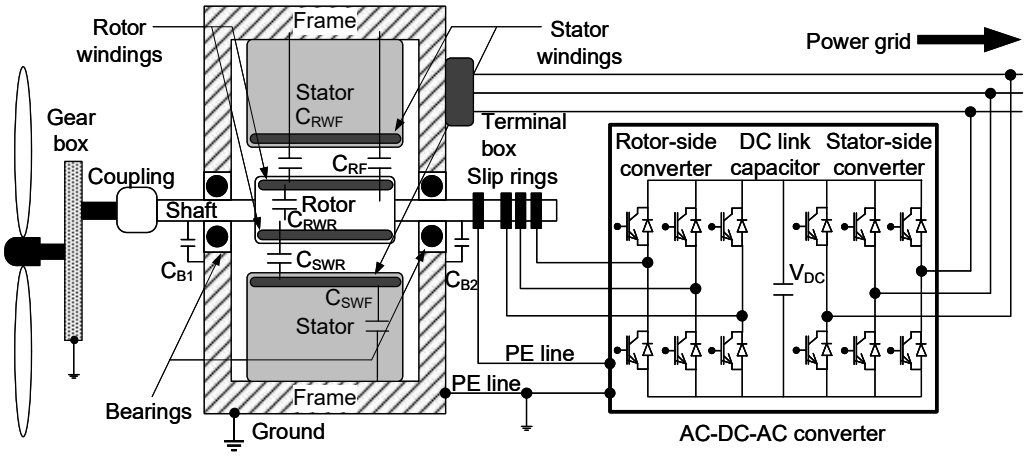

Figure 13. A schematic of electrical connection of the electrical generator of wind turbines, connected to the electrical grid in doubly-fed induction generator (DFIG) mode.

The common mode equivalent circuit is now modified and also consists of capacitive coupling between the rotor-fed windings and other parts of the machine. For rotor-fed, the common mode equivalent circuit is shown in Figure 14. The additional capacitive couplings are discussed below:

- **Rotor winding to rotor stray capacitance (C_{RWR}) -** Stray capacitive coupling between the inverter-fed rotor windings and rotor is represented by capacitance C_{RWR}. The flow of HF stray current through the bearings is possible when the current takes the path from rotor, through the bearings and then grounded via the stator frame, thus completing the current loop.
- **Windings to stator stray capacitance (C_{RWF}) -** Parasitic coupling between the converter-fed rotor windings and the frame plays an important role in wind turbines, since rotor may be grounded through the shaft coupling by the gearbox assembly, as shown in Figure 13. This causes the bearing current flowing though windings frame grounding currents may complete path to ground via the bearings. If an isolating coupling is used in a wind turbine generator, it is not likely to cause a concern in wind application.

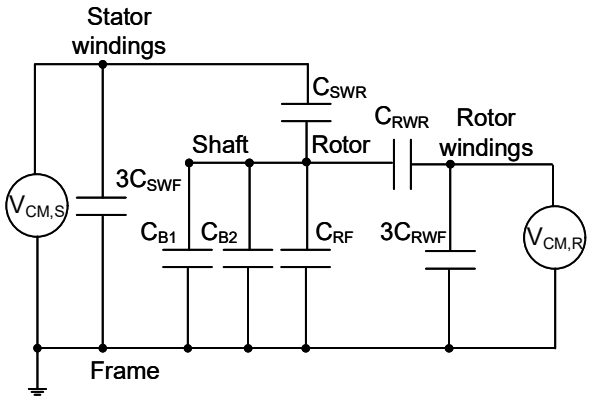

Figure 14. Common mode equivalent circuit for doubly-fed wind turbines.

In DFIG, total shaft voltage can be analytically shown to be a superposition of individual shaft voltages arising due to common mode voltages of the rotor-side and stator-side converters. The effect of the stronger rotor side coupling is investigated in [80] and the superimposed shaft voltage is given by equation (4) and (5) as,

$$V_{Shaft} = V_{Shaft,Stator-side\ converter} + V_{Shaft,Rotor-side\ converter} \tag{4}$$

$$V_{Shaft} \approx \frac{C_{SWR}}{C_{SWR}+C_{RF}+2C_B} V_{CM,S} + \frac{C_{RWR}}{C_{RWR}+C_{RF}+2C_B} V_{CM,R}. \tag{5}$$

The common mode circuit for rotor-fed wind turbine generators has a higher capacitive coupling compared to stator-fed machines. In DFIG, the amplitude of the shaft voltage and hence the corresponding bearing currents is higher because the coupling capacitance between the shaft and the neutral of the back to back converters is stronger. The coupling capacitance is hence decided by the isolation layer between the rotor core and rotor windings and is thus determined by a large surface, which has permittivity greater than that of the air gap (relative permittivity of the material is 3). The capacitive coupling in DFIG is found to be approximately 10 times higher compared to SFIG. In SFIG, the coupling capacitance is decided by the stator-winding to rotor capacitance (C_{SWR}) which is relatively small and is determined by air gap (relative permittivity is 1) between

stator and rotor. As an example, it is reported that the measured coupling capacitance between stator-fed windings and rotor of a 1.5 MW DFIG wind turbine generator is 9.21 nF, while the coupling capacitance between rotor-fed windings and rotor is 121 nF [2].

An analytical study [1] investigated and reported values of machine stray capacitances of induction generators of a 2 MW wind turbine configured in both stator-fed and doubly-fed modes. The stray capacitances were evaluated based on machine geometry and electrical properties of materials used in its construction. In stator-fed machines, the winding to rotor coupling capacitance is 0.81 nF, while in doubly-fed machines is 177 nF. It is also reported that this difference in stator-fed and doubly-fed configurations corresponds to direct increase in peak amplitude of bearing currents from 0.2 A to 4 A. A higher value of capacitive coupling will cause higher values of shaft voltage and results in higher amplitude bearing currents in the system. Similarly, higher values of DC link voltage will result in high amplitude of bearing currents in the system. As an example, the DC link voltage in wind turbines is typically around 600V up to 1000 V for a 1.5 MW wind turbine generator, hence the common mode voltage in such a system can be as high as 575 V [2].

2.4 Types of bearing currents

Different kinds of bearing currents can flow within the drive train system that could origin uniquely and could exist independently of the other. In a systematic approach, harmful effects of different types bearing currents are quantified in [36], using a lumped circuit model of electrical machines [77]. This section assesses the classifications of bearing currents, along with their typical amplitudes and frequency content.

2.4.1 Ohmic bearing currents

At low rotational speeds of the bearing, the resultant contacts (asperities, debris) between the bearing surfaces causes discharge of voltage between the inner and the outer raceways of the bearing. Ohmic bearing currents are not source or origin dependent and are because of low resistance ohmic contact. The path offered for the current in this case is because of metal to metal (asperity) contact and could also occur in case wear-debris and particles form conducting bridges between the inner and outer raceways of the bearing. Ohmic bearing currents may also occur in case of starvation of lubricant [81]. Starvation means lack of lubricant in the load zone, resulting in load carried by the solid surfaces. In case of debris/particles, three body abrasion mechanism creates high temperatures [16], which could further deteriorate the bearing. The amplitude of the ohmic bearing current is not so large and the peak amplitude is typically below 200 mA [82].

2.4.2 Capacitive bearing currents

The source of the capacitive bearing current is the dV/dt of the power switches and the passage of current during the commutation from one voltage level to the other. The frequency of the capacitive bearing current hence depends on the switching frequency of the power electronic switches. The amplitude of bearing voltage depends on the coupling capacitances of the common mode equivalent circuit and the amplitude of the common-mode voltage. Since the frequency of the current ranges from several 100’s of kHz to a few MHz and capacitance of the bearing is quite small (up to few 100’s of pF), capacitive bearing currents flow through the low impedance path offered by the bearing, given by equation (6) as,

$$I(t)_{B,Capacitive} = C_B . \frac{dV(t)_{Bearing}}{dt}. \quad (6)$$

As investigated in [36], the amplitudes of the capacitive bearing currents is small at room temperature and is in the range of 5 to 10 mA. At temperatures in the range of 70 °C to 90 °C, the amplitudes could reach up to 200 mA, but are still considered harmless.

2.4.3 Electrostatic discharge bearing currents

Electrostatic discharge current flows due to discharge of parasitic stray capacitance of the machine through the bearing, also popularly referred to as Electrostatic Discharge Machining (EDM) type of bearing currents. The working principle of an EDM type bearing current is similar to the EDM process commonly used in machining, but since it is not controlled, the physical process leads to electrical erosion in the bearing. The bearing could withstand high frequent nature of shaft voltage up to 30 V for short duration at 20 °C, which results in capacitive charge build up across the bearing [36, 77]. In an event of a discharge, the energy of the discharge current creates localised melting on steel surfaces, leading to formation of a crater in its path of propagation through the bearing surfaces and charring of grease [70]. Electrostatic discharge currents are a cause leading to bearing failures in small to medium sized machines.

The discharge event is typically very quick and is in order of a few 10's of nano-seconds. The lubricant film that is formed between the balls and the raceways of the bearing is reported to have a threshold voltage between 5 V to 30 V at 20 °C [36, 77]. During normal operation, the bearing lubricant temperature is normally between 50 °C to 90 °C. At higher temperatures, the reported threshold voltage is reported to be lower, between 5 V and 15 V [27, 36, 77], possibly due to reduction in film thickness. Moreover, statistical wear-rate during bearings during operation could reduce the breakdown voltage over time. The peak amplitude to electrostatic discharge currents can range between 0.5 A and 3 A and increases with size of the machine and are reported to be dominant cause for bearing damage in small machines [36]. In stator-fed machines, majority of the charge supplied during an electrostatic discharge current is through the rotor to frame capacitance, C_{RF} (90 to 95%), while very low charge is contributed by windings to rotor stray capacitance, C_{SWR} (5 to 10 %) [36, 80]. The energy of discharge (W) can be given by equation (7) as,

$$\text{Energy of discharge (W)} = \frac{C_{RF} V_{Bearing}^{\ 2}}{2}. \quad (7)$$

In rotor-fed machines, the effective coupling capacitance of the common mode equivalent circuit is about 10 times higher than in stator-fed machine, leading to dangerous levels of shaft voltages and higher failures rates in bearings of DFIG wind turbine. A disruptive current is likely to flow through the bearing if C_{RF} has higher accumulated charge than the threshold breakdown voltage of the bearing. The actual electro physical phenomenon causing electrical breakdown of lubricating film is unclear. The damaging effect on the bearing could be a result of discharge of energy in a very short time and not a function of voltage or current in particular [70]. The breakdown of the lubricating film could occur due to several factors, which prohibit the maintaining of voltage across the bearing. The breakdown of the lubricating film can occur at lower voltage levels due to formation of micro-craters on the interacting surfaces, which amplified the local electric field stress in the lubricant and leads to an early breakdown [83].

Electrostatic discharge currents are reported to only occur when minimum film thickness (h_{min}) is greater than 0.1 μm and the oscillating frequency content of the electrostatic discharge currents is

in range of 1 and 10 MHz [84]. If the electric field strength falls below 30 V/μm, the occurrence of electrostatic discharge current is sporadic for 6210-type ball bearing. The frequency of occurrence of these currents increases drastically with an increase in electric field strength, which implies that physical condition for an electric breakdown of bearing is no longer given. The resistance of bearing during an event of electrostatic discharge is reported to be 3 Ω ± 1.5 Ω and may vary from case to case. The limits for these type of current is reported to be independent for the motors with rated power between 30 kW and 290 kW. In the current thesis, the breakdown of lubricating film of the bearing due to shaft voltages has been investigated for electric fields ranging from 2 V/μm up to 30 V/μm, for a bearing with h_c calculated in the range of 0.5 μm up to 1 μm.

2.4.4 Circulating bearing currents

In large electric machines, due to the capacitive coupling between the stator winding and the grounded frame (C_{SWF}), the high frequency capacitive current (I_{CM}) flows from stator windings to the grounded frame of the machine and could have frequency content in the order of several 100's of kHz. The flow of I_{CM} generates a HF circulating flux around the circumference of the machine due to an effective asymmetry between two ends of stator windings which leads to flow of current to grounded frame. Thus, a circular time varying magnetic flux is generated in the stator core, around the main shaft of the generator. An asymmetric circular time varying magnetic flux induced a potential between the two ends of the main shaft. The HF circulating flux from the stator induces the HF flux to the rotor windings due to mutual inductance. This leads to the generation of HF shaft voltage along the ends of the shaft, which is due to inductive couplings between in the machine elements. The combination of capacitive current and inductive coupling within the electrical machine generates a HF shaft voltage at the two ends of the shaft. If the HF shaft voltage exceeds to dielectric breakdown strength of the bearing, or if a low resistive path is offered (particle/debris), HF circulating current flows through the bearing and circulates in a loop in the machine. The loop in which the HF circulating currents flow is through the frame of stator, drive end bearing, shaft, non-drive end bearing and finally finishing the loop back to the frame. The HF circulating current have been reported by Lipo, Chen and Novotny in [85] and the detailed analytical modelling of the phenomenon of this type of bearing currents is discussed by Mütze in [36]. The peak values may reach up to 20 A and are dependent on the size of the generator [36]. They can be mitigated by use of symmetric machine construction and use on insulating bearing to break the current path.

2.4.5 Rotor ground currents

If the electrical generator is grounded through drive train system, a part of total HF currents may flow as rotor ground currents. The ground currents may flow from rotor to shaft to the connected gearbox and to the ground. The peak amplitude of these currents is highly dependent on size of the generator and the grounding impedance of the rotor and the stator housing. The rotor ground currents are harmful to the bearings of the electrical generator and could cause short time of bearing operation. For machines with rated power of 500 kW, the grounding currents can reach peak values up to 90 A [36].

2.5 Electrical model of bearing reported in literature

For understanding the bearing current problem, much research has been done keeping in mind the system level perspective [1, 10, 38, 86, 87]. Literature review has shown that there is very little

understanding on breakdown of the lubricating film inside the bearing on a component level. It is claimed that the occurrence of the electrostatic discharge currents is understood to be sporadic below electric field strength of 30 kV/mm at film thickness of 0.2 μm [84]. A common manner to represent the electrical breakdown event in a bearing, is by electrically modelling it as a switch that closes in an event of electrical breakdown of lubricating film in the bearing [1, 77, 82, 84, 86]. The electrical breakdown event of the bearing is assumed to occur due to different assumptions chosen by different authors and has been largely regarded as an unexplained phenomenon.

In a simple version of the common-mode circuit model proposed by Busse et al in [76], the bearing model forms a part of the common-mode equivalent circuit model along with the converter and the machine. The bearing model is represented by the capacitance C_b, a non-linear impedance Z_l and bearing resistance during the event of an electrical discharge (R_b), shown in Figure 15. C_b is shown to be variable since the bearing capacitance is a function of electrical properties of lubricant and the geometric separation between the tribological parts. The authors describe the non-linear device to represent the charging and discharging of the shaft, i.e., in other words, the occurrence of electrical breakdown events in the bearing. The authors propose that the metallic bearing elements such as raceways and rollers represent resistances which are having effective resistances $R_{inner\ raceway}$, $R_{outer\ raceway}$ and $R_{ball,i}$ respectively. Each roller is having a layer of lubricating film around itself, which is represented by $C_{ball,i}$, which forms near the inner and outer raceway respectively. This forms of an effective capacitance $C_{gap,i}$ between each set of balls, which results in 'n' parallel capacitors. Furthermore, Z_l is added to the model to account for abnormal mechanical and electrical occurrences in the bearing. The nature of breakdown of the voltage across the bearing is termed a statistical and is dependent on the collapse of Z_l, which is to be determined through experiments. This breakdown of the bearing is hence said to be dependent on the position of the ball along with the condition of bearing surfaces and the lubricant's electrical characteristics.

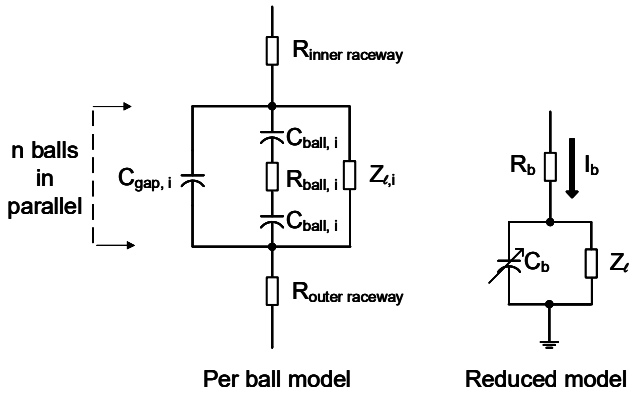

Figure 15. Ball per ball and reduced model of the mechanical bearing, adopted from [27].

The system level model proposed to describe the principle for the occurrence of electrostatic discharge current in the bearing can be illustrated by means of Figure 16, proposed by Busse et al [77]. The overall model consists of common-mode equivalent circuit of the converter and the machine and contains source impedances in series (Z_{SERIES}) and parallel ($Z_{PARALLEL}$). L_0 and R_0 are lumped parameters representing zero-sequence impedance of stator-windings. The common mode voltage appears at stator neutral (V_{sng}) and after voltage division, appears as the bearing voltage. The current flowing through the bearing (I_b) and the reduced model of the bearing itself is shown in the far-right branch in the circuit shown in the figure.

For the electrostatic discharge current to occur, it is proposed that three conditions must simultaneously be satisfied [77]. The first condition is to have a proper source of excitation (V_{CM}), which is the essentially a voltage source to ground (formed at 'V_{sng}' in Figure 16). The second condition is to have a capacitive coupling mechanism, which is provided by the stray capacitances (C_{swr} and C_{rf}) and the third condition is the rotor voltage build up across the bearing (C_{rf}).

At higher speeds, the film is formed and the impedance of the bearing (Z_l) is higher, reported to be in megaohm range. As the focus of majority of the studies has been kept on system level parameters and the emergence of different kinds of bearing currents, more emphasis can be given to elaborate the mechanisms with which the electrical breakdown events occur in the bearing. The motion of the bearing is complicated due to its dynamic nature and the variable nature of mechanical and electrical stresses and thus needs further elaboration. In the literature, the breakdown of bearing is also portrayed by a switch, but with arbitrarily chosen time of breakdown [36, 86]. The breakdown characteristics of lubricating film of bearing depend on many factors such as motion, magnitude of voltage across it, surface roughness of bearing, vibration levels, lubricant film properties, oil cleanliness among others.

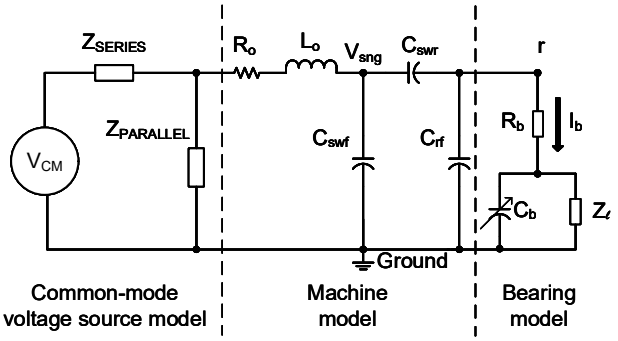

Figure 16. The common mode equivalent circuit model as proposed by Busse, Erdman et al in [27, 77] showing significant coupling capacitances in a motor. The bearing is modelled as a variable capacitance and a non-linear impedance of the lubricating film acting like a dielectric.

In [39] experimental investigations are reported on the non-steady nature of electrical breakdown events of bearing under the influence of discharge bearing currents and HF voltage. The currents were simulated using a signal generator to produce voltages at frequencies of 300 kHz and 1.5 MHz. The breakdown of the bearing was studied on two motors MA-15 (15 kW, frame size 160 mm) and MB-75 (75 kW, frame size 280 mm) and the speed of the motor was varied up to 3000 rpm. Motor MA-15 has bearing type 6309 C3, while motor MB-75 has bearing type 6316 C3. Figure 17 shows bearing voltage (V_b), bearing current (I_b), bearing impedance (Z_b) and angle of Z_b for motor MA-15 running at a speed of 210 rpm (left column). The peak value of V_b is at 10 V when the bearing is in capacitive mode and withstands the applied voltage. The capacitive mode can be seen to prevail from 0 to ~70 µs and the current through the bearing is non-existent and is near the zero line. The bearing impedance is showing a high value which is in the range of 1 kΩ to 1.2 kΩ, while the phase of the current is leading the voltage by ~90° as seen in the final trace. The calculated bearing capacitance in the insulating state at 210 rpm, is found to be 0.29 nF. Around the ~70 µs time, the bearing enters the resistive state until ~200 µs time mark. This is exhibited by sudden drop in V_b and flow of current I_b through the bearing. The minimum bearing resistance in ohmic state is found to be 2.3 Ω. It can be seen from the phase of Z_b, that the bearing has entered the resistive phase, where the phase shift between the voltage and the current is nearly ~0°. The

transition of the bearing from capacitive state (no breakdown) to ohmic state (breakdown) is dependent on the certain operating points such as speed and load, which the authors have termed as 'Transition Activity, TRA'. It can also be seen from Figure 17, at speed of 210 rpm, the two electrical breakdown events in the bearing last for a duration of approximately 150 µs to 170 µs. The bearing impedance during the extent of electrical breakdown event increases until the bearing again enters the capacitive mode (insulating state). Similarly, for motor MB-75, at a higher rotational speed of 450 rpm, the breakdown events inside the bearing can be observed as a function of bearing voltage, current and impedance of the bearing. The calculated bearing capacitance in the insulating state at speed of 450 rpm is found to be 0.83 nF, while the minimum bearing resistance in ohmic state is found to be 5.3 Ω. A change in speed from 210 to 450 rpm has resulted in a 186 % increase in bearing capacitance.

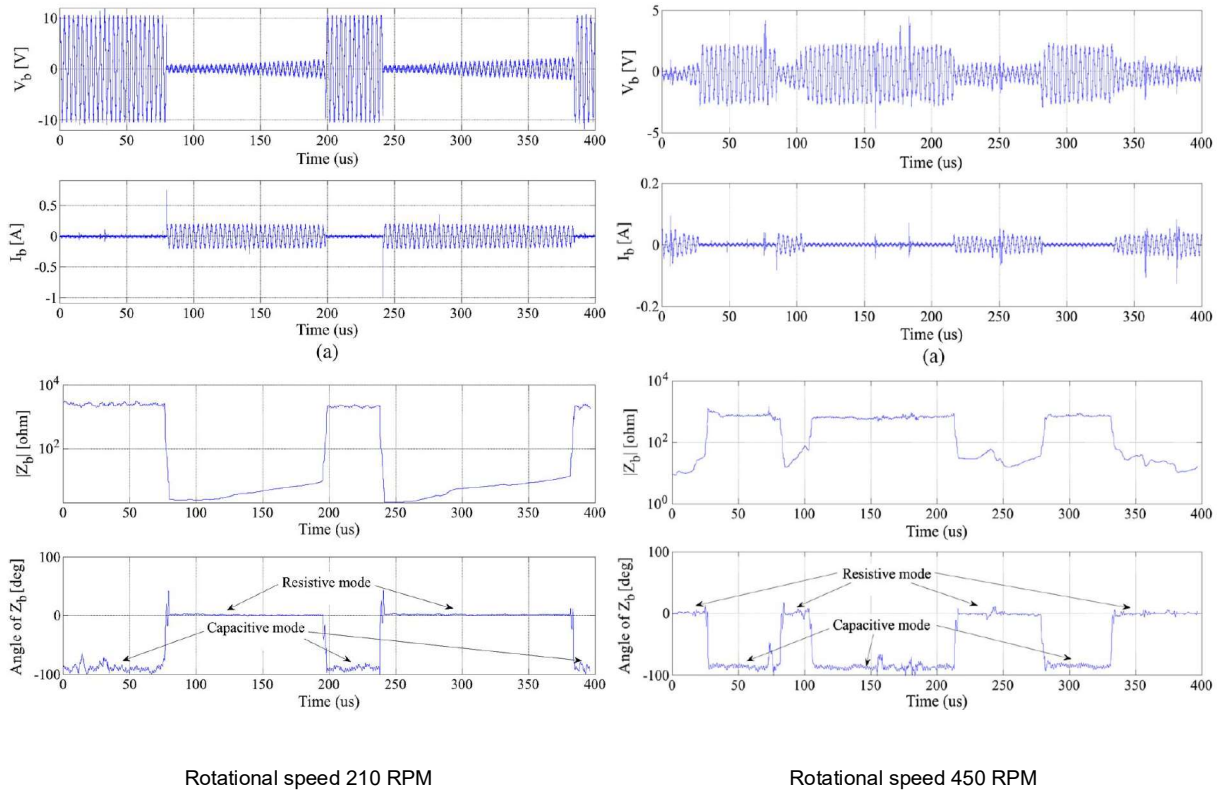

Figure 17. Transition of bearing from capacitive mode to resistive mode in a measurement window of 400 µs performed on two motors, a 15 kW motor (left) and a 75 kW motor (right) as reported by Niskanen, Mütze and Aloha in [39].

The bearing capacitance calculated in [39] varies between 0.1 and 0.9 nF, while it increases with an increase in bearing temperature. At a given temperature range of ~25 °C, the bearing capacitance also decreases from 0.36 nF to 0.12 nF as the speed is increased from 240 to 2000 rpm, as can be seen in Figure 18. It can be observed that only a 5 °C in temperature will change the capacitance by 25 % and rate of temperature increment is different for different speeds. The measurement for the bearing type 6309 C3 installed in motor type MA-15, under the influence of 300 kHz voltage signal, is reproduced using the raw data presented in [39] and is shown in Figure 18.

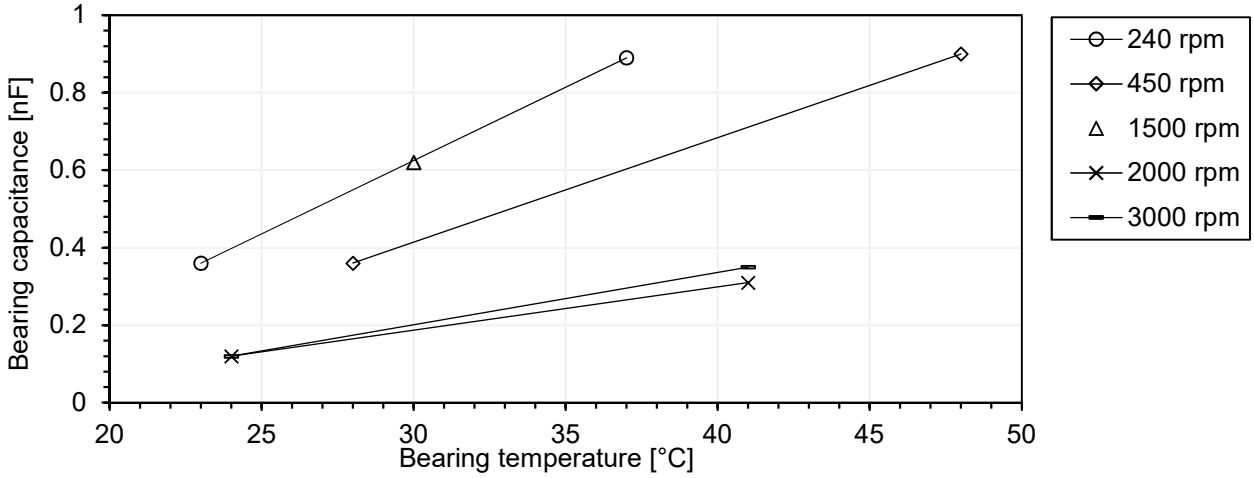

Figure 18. Calculated bearing capacitance as a function of bearing temperature and speed reproduced from raw data presented in [39] for motor MA-15 under the influence of a 300 kHz voltage signal source.

The changes in bearing capacitance for the larger motor, MB-75 installed with bearing type 6316 C3 also follows the same trend and the results again reproduced from raw data is presented in [39] and are shown in Figure 19. Both the results exhibit a decrease in bearing capacitance with an increase in speed, while, higher bearing temperatures have led to an increase in bearing capacitance. This due to inverse relation of film thickness of the lubricating film in the bearing with respect to film thickness, which is basically approximated using standard equation for capacitance calculation for parallel plate capacitors. The relation is reproduced from work presented by Schnabel in his licentiate thesis [66] and is given by equation (8) as,

$$C_B \approx \varepsilon_0 \varepsilon_r \int_{x=0}^{x=l_{contact}} \frac{A_{gap}(x)}{h(x)} dx, \tag{8}$$

where

ε_0 is permittivity of vacuum in F/m,

ε_r is relative permittivity of bearing lubricant,

$A_{gap}(x)$ is area related to the real area of contact and

$h(x)$ is local surface separation between the tribological surfaces.

In conclusion to their work [39], the general outcome was that the transition activity in bearing increases with an increase in temperature and the amplitude of the applied voltage and can be momentarily seen in Figure 17. Bearing stays longer in resistive mode at lower speed of 210 rpm, while it stays longer in capacitive mode at speed of 450 rpm. Although, it is stated that the current conduction and breakdown mechanisms in rolling element bearings are only partially understood now.

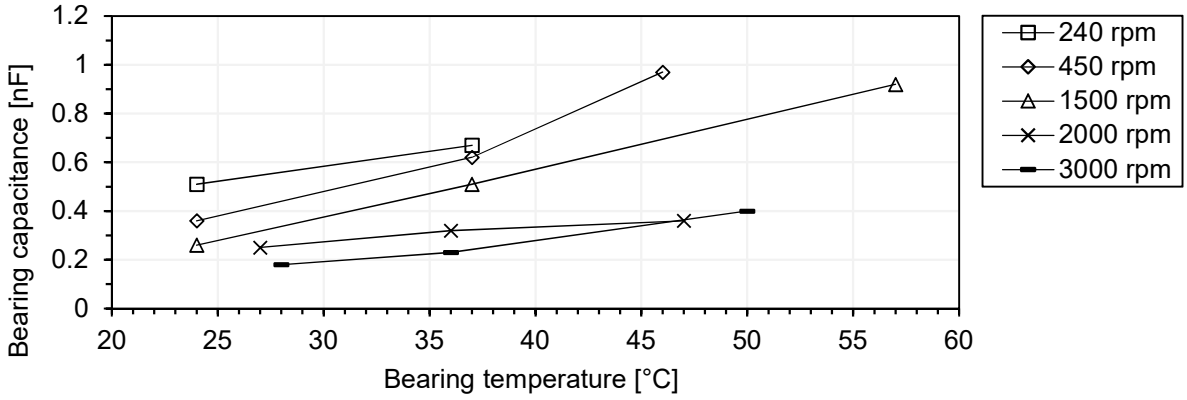

Figure 19. Calculated bearing capacitance as a function of bearing temperature and speed reproduced from raw data presented in [39] for motor MB-75 under the influence of a 300 kHz voltage signal source.

A method for monitoring of wind turbine bearings in patented in [88]. The condition of lubricant is determined through application of voltage to the bearing raceways and monitors the breakdown voltage. If the condition of the lubricant is good and a thick film is formed, the breakdown voltage will be high. The patent says that the layer of lubrication is insulating up to a certain level of applied voltage. Once a certain threshold value of applied voltage is reached, a breakdown of bearing results until the bearing starts to behave in insulating mode again. The patent hints that the breakdown voltage of the bearing may be high, when the temperature is low and it reduces with an increase in speed and/or load on the bearing. Thus, the condition of the bearing can be monitored during the running condition and the quality can be assessed using reference measurements. Alarms can be raised if critical levels are crossed and maintenance can be scheduled.

2.6 Mitigation techniques to improve bearing life

The techniques to mitigate modern bearing current activity and to avoid damages on the bearing surface due to bearing currents will be discussed in this section. On a broad scale, mitigation techniques can be seen to be formulated considering one of the two school of thoughts. The first approach tries to eliminate or reduce the bearing current activity at the inverter side by reducing the influence of V_{CM}, while the second approach tries to eliminate the bearing current activity at the machine end by adding components and methods to dissipate V_{Shaft} to ground or by shielding the bearings from its influence.

In the first approach, reduction is achieved using chokes or common mode (CM) filters and shielded cables. They filter-out high frequency bearing currents that can lead to a decrease in amplitude of the bearing current. However, filters cannot avoid the build-up of voltage across the bearing due to V_{CM}, hence they cannot be used to mitigate the electrostatic discharge current through the bearing. Filters help in reduction of amplitude of bearing currents, but cannot eliminate them. Multi-level converter with higher number of intermediate voltage levels helps control and reduce V_{CM}, but have trade-offs in increased total harmonic distortion (THD) and cost. Another method to reduce shaft voltage is by reducing the DC link voltage and changes in the modulation scheme of the power switches.

In the second approach, the modifications are done to bearing elements, lubricant, as well as in shaft couplings. Hence it relies on use of ceramic bearings, shaft voltage rings and brushes,

insulated bearings, conductive and low impedance grease, insulated shaft couplings and electrostatically shielding the motor.

Ceramic (hybrid) bearings provide a way to create a high impedance path through the bearing by using ceramic elements instead of steel elements. Ceramic elements offers high ohmic resistance (50 MΩ) and the bearing is able to withstand DC electrical stress of up to 1000 V [89].

Shaft grounding brushes - Electrostatic discharge type of bearing current can also be mitigated by redirecting the energy of discharge through a parallel path outside the bearing. Carbon brushes and shaft-rings discharge the voltage on the shaft to ground though a path which parallel to bearing [90] and avoid build of bearing and shaft voltage. Carbon shaft grounding brush is used combination with insulated bearing to ground the shaft voltage and break the flow of bearing currents to the attached grounded assembly. In literature [2], shaft voltages of about 531 V were measured on an ungrounded shaft of a 1.5 MW wind turbine generator, while V_{Shaft} of about 26 V were measured when the shaft was properly grounded. The shaft grounding brush accumulates dust and under the influence of grease and moisture develops a higher impedance path to ground, thus resulting in residual shaft voltage which can be up to few 10's of volts. Presence of dust and moisture around the brush can increase the contact impedance and thus needs regular servicing for correct functioning.

Balls in insulated bearings are coated with insulating materials (such as aluminium oxide, silicon nitride), to provide a high impedance path to the incoming bearing currents. The coating has a thickness of up to 250 µm and can be applied to both the outer ring and inner ring of the bearing. However the modification fails to address the high frequency bearing currents, since the insulation coating acts like a capacitor for high frequency bearing currents and lets them pass through the bearing.

A conductive grease is a blend of grease with conductive nanoparticles, which increase in dielectric conductivity of the grease. Use of conductive grease facilitates the passage of continuous current through the inner and the outer ring of the bearing, without initiating the destructive discharge process through the lubricant, thereby resulting in continuous discharge of developed voltage across the raceways of the bearing. Nevertheless, the use of conductive grease leads to agglomeration of the added particles in certain portions of the raceway of the bearing [91]. It has also been found experimentally that the conductive grease loses its electrical conductive properties after a period of about 40 hours [92]. Investigations have shown that damage caused on the bearing surface by use of low impedance grease (Klüberlectric BE 44-152) looked different to another standard lubricant (Castrol SafeCoat 66), but no explanations were presented for the observed difference [91]. Nevertheless, the threshold voltages for discharge current activity measured by use of low impedance grease did not differ significantly from the threshold voltage for discharge activity when using normal lubricant [91].

Electrostatically Shielded Induction Machine (ESIM) reduces the electrostatic discharge current in the machine [79] by electrostatically shielding the rotor of the machine, although it is not very cost-effective. Modification of the generator design could reduce the stray capacitive coupling of the common mode voltage to the shaft of the machine.

The most effective way to reduce bearing current activity is to use insulating bearings on both drive end and non-drive end of the machine, followed up by shaft grounding brush. Although this

solution does not completely suffice since for large machines, rotor ground currents could essentially flow via lower resistance paths and could damage other components along the shaft.

2.7 Characterisation of lubricants

Electrical and mechanical properties of lubricants are relevant for electrical characterisation of bearing as a component. The electrical properties of lubricants can be characterised by their relative permittivity (ε_r), DC conductivity (σ), dielectric loss (tan δ) and by electrical breakdown strength (E_{BD}). These parameters are measured as a function of electrode geometry, electrode gap spacing, frequency of applied voltage and temperature of the lubricant. Mechanically, one of the performance indicators of the lubricant can be expressed in terms of viscosity ratio (κ) and calculated lubricant film thickness during operation.

2.7.1 Electrical properties of lubricants

- **Relative permittivity and dielectric dissipation factor**

Relative permittivity (ε_r) provides a measure of a medium to store electrical energy under the influence of electric field. Typically, lubricants contain 90 % of mineral or synthetic oil, which is electrically insulating. In addition, lubricants may contain up to 10 % of additives, which provide additional capabilities, like sustaining extreme pressure, temperature, wear etc. Hence, different greases could have vastly different dielectric properties due to its manufacturing and composition. As an example, in a literature study [93], three different kinds of lubricants designed for operating range between -20 and 120 °C were studied. The grease samples were all general purpose industrial greases that are adopted in traction motor applications, where high pressures are to be sustained by the lubricant. The lubricants were grease based and consisted of lithium thickener. The values shown in the table are reproduced from the original work and are permittivity values obtained at temperature range between 30 °C and 90 °C.

Table I. Relative permittivity (ε_r) of grease samples investigated in [93]. The greases are classified per type and relative permittivity is presented at 1 kHz.

	Grease A	Grease B	Grease C
Base oil	Paraffinic mineral oil	Highly refined mineral oil	Hydroxystearate
ε_r at 1 kHz	5–15	2.16–2.36	3.1–3.3

The relative permittivity (at 1 kHz) of the Grease A changed between 5and 15 as the temperature increased from 30 °C, to 90 °C. This variation in Greases B and C was much less in the given temperature range.

Dielectric dissipation factor (tanδ) is a measure of all the dielectric losses in an insulating medium. The measurement of tanδ provides among others information regarding degradation in dielectric medium. Measurements of tanδ are for example commonly used in assessing degradation of oil impregnated systems (e.g. transformers or cables) [94]. A higher tanδ may also results from additives of ionic nature in the lubricant [93]. tanδ values in frequency range between 10 Hz and 10 kHz for the test samples shown in Table I indicate that Grease A has higher losses than Greases B and C, shown in Figure 20. The tanδ slope of Grease A (left, Figure 20) is-1, indicating that the losses are dominated by the conduction mechanism.

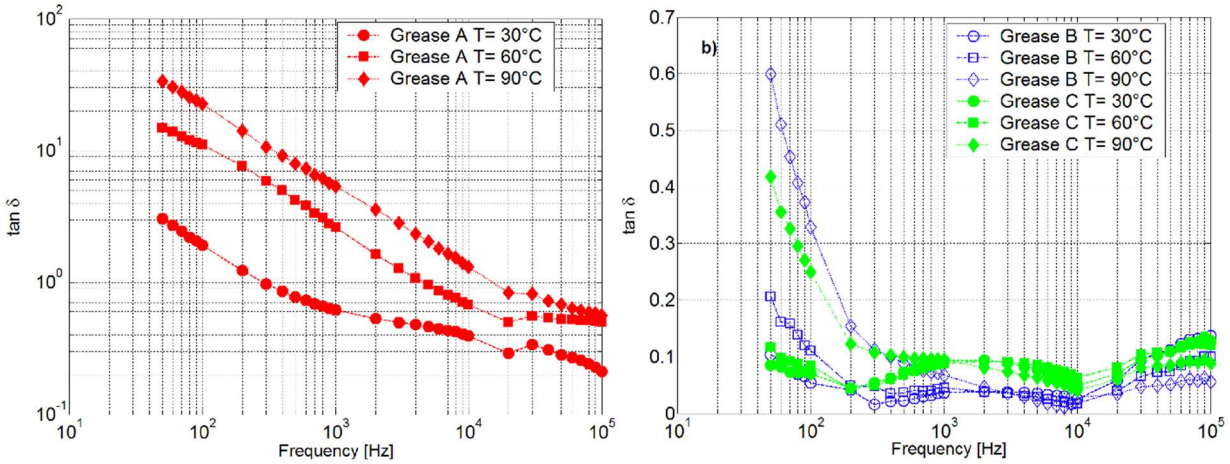

Figure 20. Tanδ of lubricant Greases A, B and C reported in [93] at different temperatures. Dielectric loss factor is significantly higher for Grease A compared to Greases B and C.

- **Electric breakdown voltage and breakdown field strength**

In context of bearing currents, the breakdown field strength for lubricants is reported to be at about 15 kV/mm [27, 77], obtained based on the ASTM D 877 procedure in a statically bound condition and gap length of 2.5 mm. Breakdown strength values are not reported for shorter gaps. It is claimed that a thin lubricating film within a rotating bearing breaks down when the voltage across it exceeds about 30 V_{peak} for a film of up to 2 µm [27, 36], which also correspond to a breakdown field strength of 15 kV/mm. However, the electric field across the thin film bearing lubricant under the influence of common mode voltage is said to be in the range of 3 kV/mm to 45 kV/mm.

The electrical breakdown strength of the lubricants described above was evaluated using two different types of applied voltage. A point-plane geometry was used, where the highest electric field strength in the gap spacing appears near the tip of the needle electrode and reduces along the length of the gap. The first breakdown tests were performed according to the UNI-4291 standard, where a sinusoidal voltage of 50 Hz was applied. The gap distance was varied between 0.35 and 0.175 mm and mean values of 6 successive tests were found. The tests were also conducted as a function of temperature of the lubricant and the results are tabulated in Table II.

Table II. Breakdown voltage, gap spacing and electric breakdown strength (E_{BD}) of lubricants tested in [93]. The electric field strengths reported here are highest expected values in the gap.

Temperature (°C)	Gap (mm)	V_{BD} Grease A (kV)	V_{BD} Grease B (kV)	V_{BD} Grease C (kV)	E_{BD} Grease A (V/µm)	E_{BD} Grease B (V/µm)	E_{BD} Grease C (V/µm)
30	0.35	3.5	>5.4	4.8	10.1	>15.4	13.9
60	0.35	1.6	4.6	2.1	4.5	13.2	6.0
90	0.35	1.4	3.7	2.1	4.0	10.5	6.0
30	0.175	2.6	4.4	3.7	15.1	25.4	21.1
60	0.175	1.3	2.6	1.5	7.7	14.8	8.6
90	0.175	1.1	2.4	1.5	6.8	13.7	8.5

The breakdown tests were also performed using square voltage for the gap of 0.175 mm, using the point-plane electrode system. Using a square voltage of 10 kHz, the breakdown voltages of Greases

A, B and C are 1.5 kV, 3 kV and 2.4 kV respectively. The breakdown performance is reported to for tests under non-uniform electric fields, through a cylindrical test cells using a point-plane electrode setup. The point electrode is a cone characterised by an aperture of 30 or 60°, while the plane is a circumference with radius of 2.5 mm. The corresponding inhomogeneous E-field strengths are evaluated by the author of this thesis to be 8.5 V/µm , 17.1 V/µm and 13.7 V/µm for Grease samples A, B and C respectively. As a comparison, square voltage at 1 kHz caused breakdown at 1.4 kV, while sinusoidal voltage at 50 Hz caused breakdown at 2.6 kV for a 0.175 mm gap.

Thus, at short gaps, the breakdown field strength of 15 kV/mm could vary depending on the type of lubricant and thus the condition for field dependent breakdown in bearings could vary significantly. The evaluation of the greases also shows that Grease B exhibited lowest losses (tanδ) and from the analyses above, it is visible that it had the highest electric breakdown strength when compared to greases A and C. It is also worth noting that grease B also had lowest permittivity (ε_r) compared to the other two lubricant samples.

- **Mechanisms of breakdown in liquids**

This sub-chapter summarises electro-physical mechanisms leading to breakdown in lubricants inside bearing. As lubricants contain several external materials, such as ionic additives, gas bubbles, globules of water and conducting particles, different theories are proposed to understand the cause for their breakdown. The main mechanisms discussed here are breakdown due to gaseous inclusions, solid contaminants and electronic breakdown of liquids.

Breakdown of lubricant due to gaseous inclusions (cavity breakdown) - Impurities with lower breakdown strength compared to lubricant, such as gas bubbles (or other gaseous inclusions), break before the lubricant and trigger a total breakdown [95-100]. The electrostatic force on the gas bubbles cause it to elongate in the direction of the electric field and enhances the process. This also leads to decomposition of the lubricant. On the other hand, in context of the bearing application, due to high pressures in the loaded zone (GPa range), the gas bubbles are likely to be pushed out of the zone. For transformer oil, an increase in pressure up to 40 kPa has little or no effect on the conduction and breakdown process in the oil [101].

Lubricant breakdown due to solid contaminants -

If the relative permittivity of the solid particles is greater than that of the lubricant, the particle will move in direction of stronger electric field [102, 103], thus forming a stable chain which causes breakdown between the electrodes after reaching a critical length. On the other hand, impurities that cause local field enhancements, such as conducting particles and lead to local breakdowns, thus contributing to a total breakdown of lubricant. Solid contaminants in lubricant can be quantified by particle counting tests according to standard ISO 4406:99.

Electronic breakdown in liquids - This type of breakdown requires extremely high electric fields across the liquid. In context of the bearing, rotation will result in redistribution of the bulk liquid and may change the physical condition of the lubricant in the discharge channel. The theory of electronic breakdown in liquids is applicable to homogeneous liquids characterised by high levels of purity. The breakdown voltage depends on the field, gap separation, cathode work-function and the temperature of the cathode. In addition, the liquid viscosity, the liquid temperature, the density and the molecular structure of the liquid also influences the breakdown strength of the liquid [102,

103]. Since commercially available lubricants are considered impure, this theory is not applicable here.

2.7.2 Mechanical properties of lubricants

The properties of lubricant are affected by different operating parameters, such as mechanical load, rotational speed and lubricant viscosity

- **Running-in and lubrication regimes:**

When bearings are to be installed for the first time in any machine, a running-in procedure is recommended since it secures the useful life of the bearing. The bearing surfaces contain certain level of surface roughness, which changes after the 'running-in' of the bearing. A running-in process on a fresh bearing is performed for typically 4 to 48 hours. A running-in is a process where a fresh bearing experiences significant amount of friction resulting in wear and is performed at relatively slower rotating conditions, so that the frictional movement does not cause considerable high change in temperature during normal operation [41]. The wear caused by 'running-in' is on the contrary, a positive type of wear compared to wear arising due to fatigue. The surface roughness decreases, or in other words the surfaces get smoother after the running-in process. The lubricant is usually changed or filtered out after this process since it contains wear debris from the bearing surfaces.

Depending on the operating condition of the bearing, lubricant film thickness changes. The operating condition (such as speed and load) along with properties of the lubricant (such as viscosity ratio, κ) can be interpreted using Gumbel number (Gu) and is given by equation (9) as,

$$\text{Gumbel number (Gu)} \approx \text{Speed} \times \frac{\text{Viscosity}}{\text{Load}}. \tag{9}$$

The frictional behaviour of a lubricated contact is preferably quantified by coefficient of friction (μ), which is the ratio between the tangential force and the applied normal load. In general, coefficient of friction strongly depends on the relative speed between tribological surfaces, the high-shear lubricant viscosity in the contact and the sustained normal load (all the three are grouped in the Gumbel number). When the coefficient of friction and lubricant film thickness (h) are plotted as a function of increasing Gumbel number, a Stribeck curve is obtained, as shown in Figure 21. The Stribeck curve can be split into three regions, as shown in the figure.

The first region is characterised by high friction; this occurs at low rotational speeds of the bearing. In this region, the film thickness is quite low and the operation of the bearing in this region results in frequent asperity contacts. High operating temperatures are here characteristic and the bearing is said to be in boundary lubrication regime. As the speed is increased, the friction reduces, at the same time the film thickness starts to increase. The bearing is said to operate in mixed lubrication regime. Finally, at high speeds, a thick film of lubricant is formed between the tribological surfaces. In this region, the lubricating film carries the complete load of the interacting surfaces and the bearing is said to operate in Elasto-Hydrodynamic Lubrication (EHL) regime and further proceeds to enter hydrodynamic lubrication regime. This region of operation is optimal for long life of bearing and thus preferred.

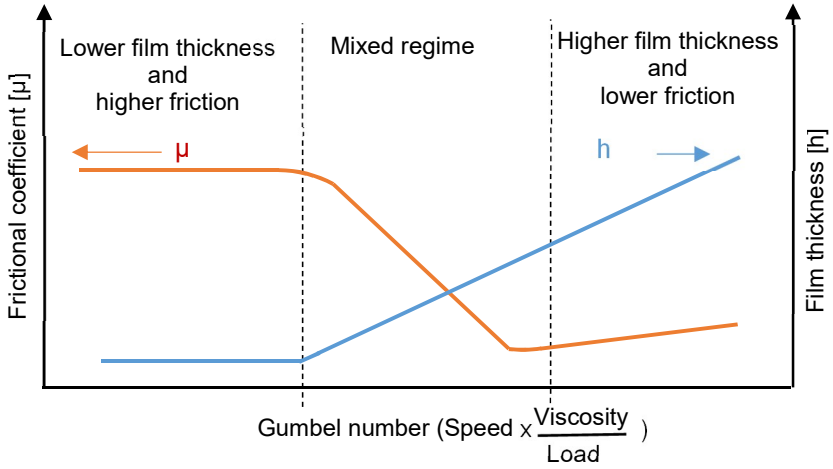

Figure 21. Typical Stribeck curve showing the variation in frictional drag (expressed as the friction coefficient) with the Gumbel number for a lubricated contact. Film thickness increases with an increase in speed. Image used with permission.

- **Viscosity ratio and lubricant film thickness:**

The viscosity ratio κ is an indicator of separation of the rolling element and the raceways. Lubricants with higher viscosity ratio have higher oil film thickness [41]. It is calculated as the ratio of operated viscosity of the lubricant to the rated viscosity and given by equation (10) as,

$$\kappa = \frac{V}{V_1}, \tag{10}$$

where

V is actual operating viscosity of lubricant (given in mm^2/s) and
V_1 is rated viscosity of lubricant depending on bearing mean diameters and rotational speed (given in mm^2/s).

A film thickness calculation tool (SKF Galaxy), provided by SKF AB, Göteborg is used to calculate film thicknesses as a function of lubricant properties and specific bearing geometry. The film thickness calculations are based on equation provided by Hamrock and Dowson, while the film thickness for point contact is based equation provided by Dowson given in [44]. The film thickness for line and point contact can be evaluated using equations (11) and (12) as,

$$H = \frac{h_C}{R_X} = 3.63\left(1 - e^{-0.68\,k}\right) G^{0.49}\, U^{0.68}\, W^{-0.073} \text{ and} \tag{11}$$

$$H = \frac{h_C}{R_X} = 2.65\, G^{0.54}\, U^{0.7}\, W^{-0.13} \tag{12}$$

where,

H is dimensionless film thickness,
h_C is central or average film thickness,

R_X is equivalent radius in rolling direction, $\frac{1}{R_X} = \frac{1}{R_{x1}} + \frac{1}{R_{x2}}$,
k is ellipticity ratio, a/b, where ‘a’ and ‘b’ are major and minor semi-axis of Hertzian contact,
G is material parameter, which is a function of reduced modulus of elasticity,
U is speed parameter, which is a function of average surface speed, absolute viscosity at temperature, reduced modulus of elasticity and equivalent radius in rolling direction and
W is load parameter, which is a function of normal load, reduced modulus of elasticity and equivalent radius in rolling direction.

3 Equivalent electrical circuit model of the bearing

In this chapter, the equivalent electrical circuit model of the bearing proposed in this thesis is discussed. Based on what was discussed in Chapter 2, we have chosen to model the bearing as electrically insulating (parallel $R_{B,Ins.}C_B$ branch) and electrically conducting (closed switch in series with a small resistance, R_B during conducting state), as shown in Figure 22.

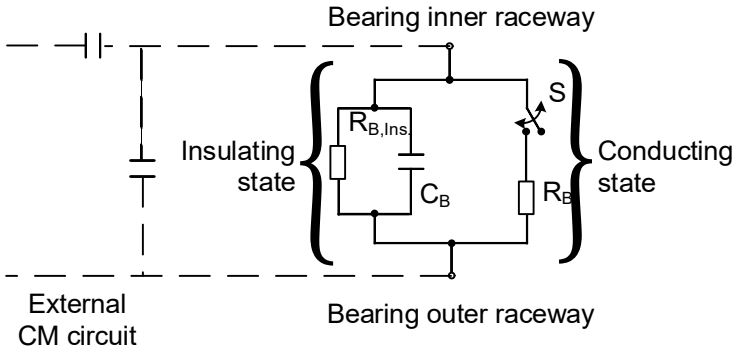

Figure 22. Electrical circuit model of mechanical bearing. The left branch, consisting of the parallel '$R_{B,Ins.}C_B$' branch represents *insulating state* and the right branch represents *conducting state* which includes a closed switch, S in series with a small resistance during conducting state, R_B.

3.1 Bearing in insulating state

It is well known that as soon as bearing's speed goes beyond few 100's of rpm, the lubrication enters in EHL regime and bearing is having a thin layer of lubrication around itself. Thus, the ball or the rolling element slides on this thin layer of lubricating film, avoiding friction between interacting metallic surfaces, which reduces wear. Under these operating conditions, the bearing behaves like a capacitor and is represented as an "Insulating state" within the electrical circuit model. In the equivalent circuit model of the bearing the switch is open and the bearing is represented by an impedance, consisting of the parallel branch representing *bearing resistance in insulating state* $R_{B,Ins.}$ and *bearing capacitance* C_B.

Within the model, the *bearing capacitance* C_B is the capacitance of the bearing between the inner and outer rings, which includes lubricant film thicknesses at inner and outer rings along with ball per ball capacitances. The overall capacitance of the bearings is measured between the inner and the outer ring, thus also including effect of cage or retainer inside the bearing. The *bearing resistance in insulating state* $R_{B,Ins.}$ is the equivalent resistance between inner and outer rings of bearing and it represents total dielectric losses in the bearing. This includes the effect of conductivity of the lubricant and possible resistive effects of particle bridges and ionic species (additives in lubricant). It is derived from imaginary part of measured complex capacitance of the bearing under application of low voltages. In addition, if polarisation losses exist, $R_{B,Ins.}$ will be frequency dependent.

3.2 Bearing in conducting state

In presence of voltage, when a low conducting path is offered through the bearing, the voltage across the raceways is discharged and the bearing starts conducting current through it. The bearing can lose its insulating state properties due to several reasons, such as asperity contact, excessive electric field strength or debris/contamination while rotating, as illustrated in Figure 23. This state of the bearing is termed as "conducting state". The conducting state is quantified by how often and for how long the electrical current is conducted through the bearing under a given operational condition.

The *Switch* in the model represents transition between the two states of the bearing; either the bearing acts mainly as an insulator (open switch) or as a conductor (closed switch). When the switch is open, the AC part of the current is dominantly capacitive, while when the switch is closed, the current flow becomes resistively, in phase with the voltage across the bearing. The switching action depends on the breakdown mechanisms and thus involves influences of film thickness, breakdown strength, voltage level and voltage shape, type of particles and their concentration, asperity contacts etc. *Resistance* R_B is the remaining resistance in conduction state, which can be dependent of discharge mechanism type (asperity, particle, electrical), contact area, discharge resistance, time of contact etc. The transition of bearing from insulating state to conducting state or vice versa is often referred as fritting.

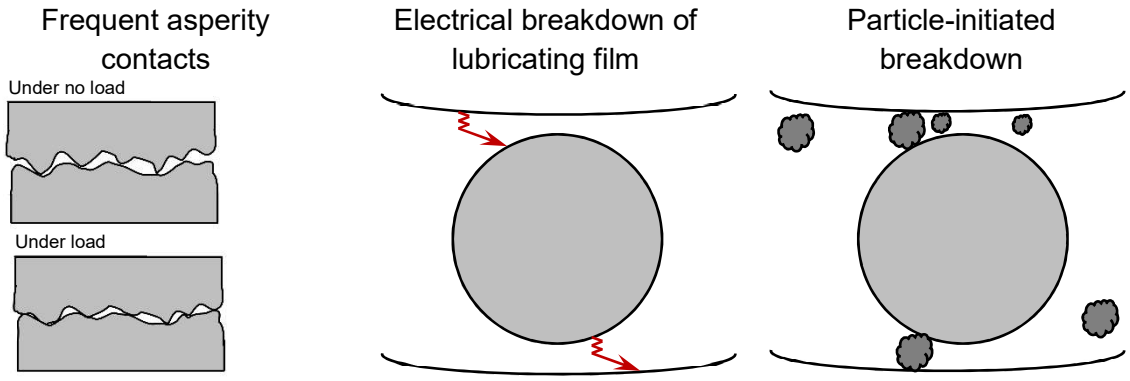

Figure 23. Plausible ways the electrical insulation of the bearing could breakdown.

3.3 Hypothesis for failure of bearing due to bearing current activity

Although root cause analysis itself requires an in-depth understanding of the primary and secondary reasons of bearing failure, the exact cause within such complicated system (electrical and mechanical stresses during operation in combination with wear due to debris and different types of contaminants) cannot be pinpointed to one factor. Primary cause of increased vibrations in a bearing is related to change in surface morphology of its tribological surfaces. Formation of large and small sized craters (size of up to 1 mm in diameter) on bearing surfaces have been linked to the passage of electric current [69, 91, 104, 105].

The formation of micro-craters on the tribologically interacting surfaces leads to frosting on the raceways. It has also been shown that corrugation patterns emerge on top of this frosting area when the bearing is unloaded [106]. At lower loads, the corrugation pattern yields uneven film thickness

for the rollers, as experimentally verified in [106]. Changes of local morphology and in lubricant thickness cause in-turn a change in bearing capacitance over time [106-108]. The film thickness is in order of several 100's of nm to a few μm and is extremely small in comparison to the interacting surfaces, namely the radius of the rolling element and either of the raceways. It has been claimed [83] that a change in pressure in the loaded region of the lubricant is also accompanied by a change in the lubricant film dielectric constant.

Small micro-craters are hard to detect through vibration sensors and hence goes undetected in the Condition Monitoring System (CMS). Further deterioration may thus continue to occur in the frosted region with appearance of higher amounts of surface peaks and lead to loads being carried by asperities, resulting in observable vibrations after prolonged operation in such conditions. An excessive amount of wear debris in lubricant, especially when they start intruding the load carrying film, results in abrasive wear on bearing surfaces. This further leads to increase in local temperature at tribological surfaces and causes further damages on the surface. The combination of higher temperature and electrical stress (excessive voltage and leakage current) leads to further deterioration of these affected surfaces causing electrical pitting and electrical fluting along the raceways, thus intensifying the vibration levels [70].

Lubricants when operated outside their prescribed temperature limits also lose their properties, which can occur in the loaded zone. Emergence of corrugation pattern or washboard pattern on the raceways has also been observed within bearings under the influence of different types of electric currents [69, 74]. These changes in the morphology of bearing surfaces leads to higher levels of vibrations and noise during operation.

This type of failure propagation causes higher levels of vibrations during operations and ultimately leads to faulty operation of the rotating shaft, which can cause further damage to the components along the shaft. Thus a damage in bearing can ultimately result in a run-away type of behaviour, leading to wind turbine downtime. A schematic development of such a failure propagation is graphically illustrated in Figure 24.

In the figure, the blocks with double-lined frame refer to detectable changes in bearing, through the use of external sensors. The bearing currents within the drive train system of the wind turbine can also cause damage to the gearbox assembly, if a low impedance is provided to earth. The winding frame ground current can flow from the rotor through the bearings to the shaft and shaft coupling to the gear box assembly which is grounded. Within CMS of rotating machines, temperature and vibration monitoring of bearings is quite standard since increase in level of either is considered to be a sign of the deterioration. Vibrations have been particularly the frequent cause of failures and several reports claim that early failures can be detected by using CMS that implement vibration sensors, such as accelerometers [109, 110]. Online or offline analyses of bearing lubricant are also recommended. An increase in bearing temperature could also be an early sign of bearing failure. Nevertheless, vibrations and temperature monitoring in wind turbines are today considered as the state of the art [20, 111, 112].

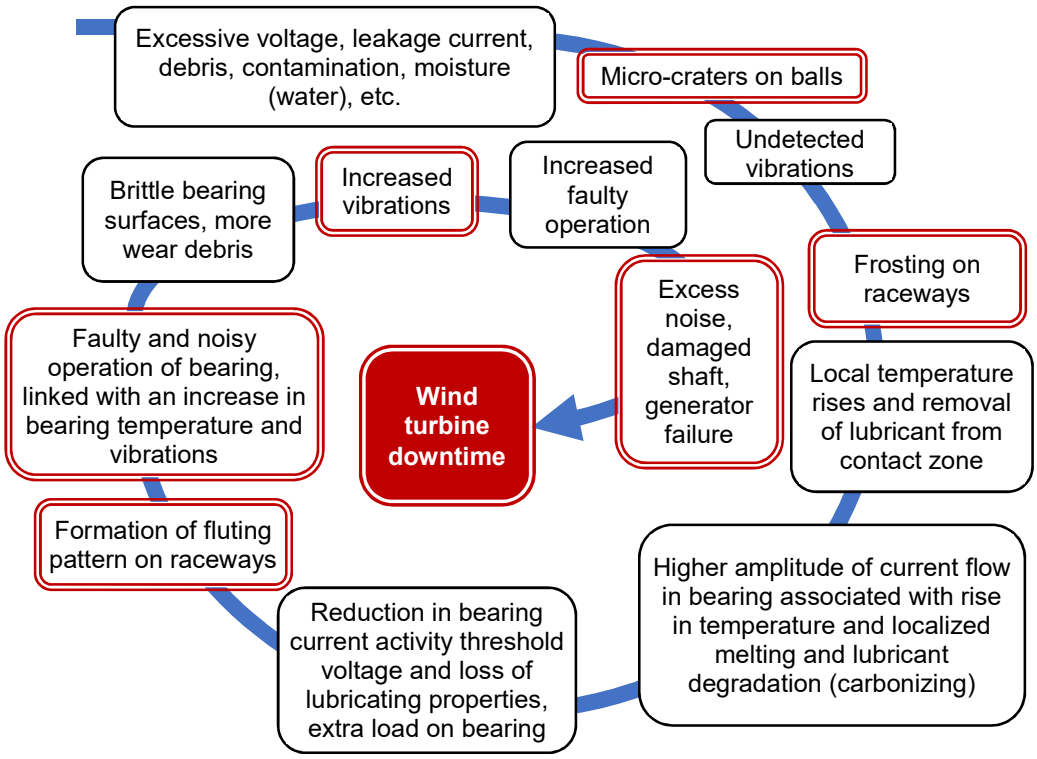

Figure 24. Possible way of damage propagation leading to wind turbine downtime. Formation of micro-craters seem to be primary source of damage [69], while increased levels of vibrations and temperature within the bearing along with formation of corrugation pattern on the raceways are secondary damages [74] due to external factors. Corrugation pattern might also result due to effect of low loads on the bearing [73].

4 Test setups and methods

In this chapter, the tested bearings, lubricants, test benches and test circuits used for characterisation of their electrical properties are described along with different methods of analyses. Four experimental setups have been used to understand the behaviour of the bearings, including methods of analyses of bearing capacitance (C_B), bearing resistance in insulating state ($R_{B,Ins.}$), insulation breakdowns in bearing (switching pattern analysis) and equivalent bearing resistance in conducting state (R_B). The measurement of electrical properties of lubricant such as DC conductivity and complex permittivity has been done by means of Frequency Domain Spectroscopy (FDS) measurements, while the 50 Hz AC electric breakdown strength of liquid lubricants has been quantified in a short gap arrangement of 0.1 mm and 0.2 mm.

4.1 Test objects

Two different types of bearings have been characterised under running condition in the tests benches, i.e. a miniature deep groove ball bearing of type 608 and a spherical roller bearing with tapered bore of type 22220. In analysis of commercial lubricants, five different types were selected based on application range and additives. Two lubricants were liquid oil based and the remaining three lubricants were greases. The liquid lubricants was chosen to facilitate mixing with different particles to investigate the particle-initiated breakdown of bearing insulation.

4.1.1 Bearing type 608

Bearing of type 608 is a high-speed deep groove ball bearing having 7 balls. It has an outer diameter of 22 mm and inner bore of 8 mm with normal internal radial clearance. This corresponds to a minimum radial clearance of 2 µm and maximum internal radial clearance of 13 µm. It is a miniature ball bearing and has limiting speed of 48000 revolutions per minute (rpm), while the static load rating is 1.37 kN and the dynamic load rating is 3.45 kN. The bearing is designed to handle axial load, while a radial load of 1 N can be expected to be present on each ball due to the weight of the shaft in the laboratory setup. The bearing was lubricated with a self-preserving lubricant. The bearing consists of outer raceway, inner raceway, balls, cages and seals, as shown in Figure 25.

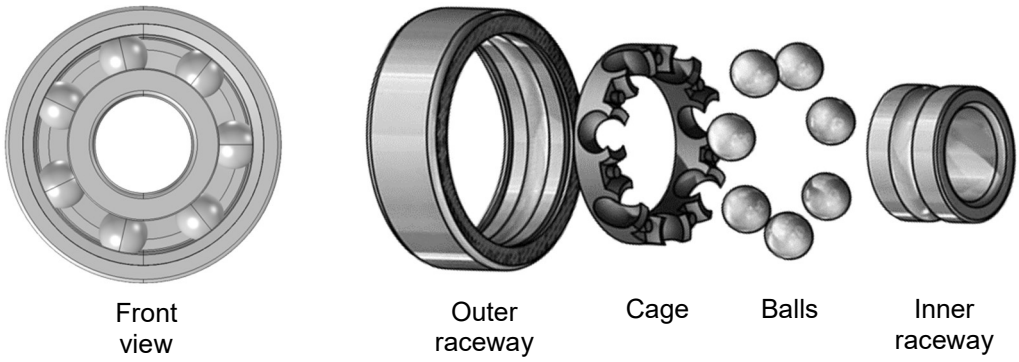

Figure 25. Schematic view of 608 bearing (left) and the exploded view (right) showing outer raceway, cage, balls and the inner raceway. CAD drawing (left) is obtained from SKF knowledge base.

4.1.2 Bearing type SKF 22220

Bearing of type 22220 is a spherical roller bearing with cylindrical and tapered bore. It has two rows, each row containing 19 rolling elements of maximum diameter of 41 mm, shown in Figure 26. Only one row of the bearing was utilised. The outer diameter of the bearing is 180 mm, while the inner bore is of 100 mm. The limiting speed is 4500 rpm, while static and dynamic load ratings are 490 kN and 425 kN respectively.

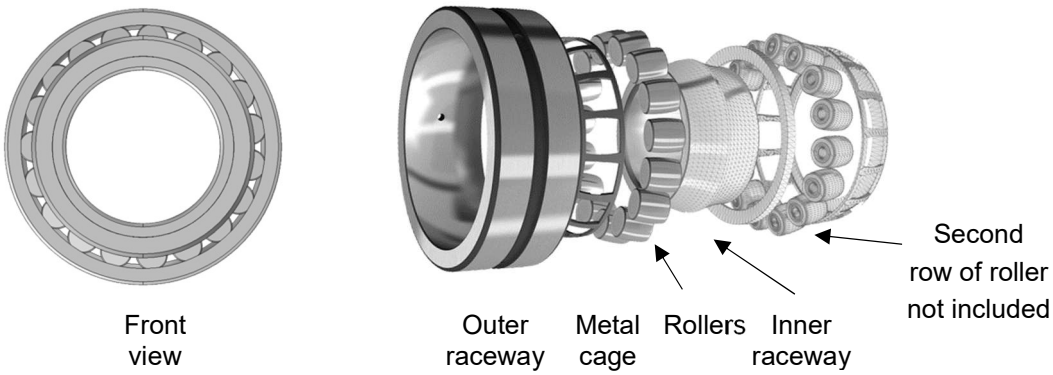

Figure 26. Schematic view and exploded view of 22220 bearing showing its different elements. CAD drawing is obtained from SKF knowledge base.

4.1.3 Bearing lubricants

Sample A is fresh sample that contains zinc-free additives that provide oxidation stability along with other desired properties, such as protection against rust and corrosion, low foaming and excellent demulsibility. It is a transparent liquid with a very light tint of yellow and resembles an additive free lubricant which is more close to a base oil. Two more versions of Sample A, namely A+ and A5 were prepared in laboratory environment to offer degradation after running-in A+ and electrical breakdowns in A5. The process of running-in results in inclusion of wear particles in the sample, while electrical breakdowns cause chemical degradation in form of carbonisation of the oil, which gave it a blackish yellow colour. Fresh Sample A lubricant was also chosen to be mixed with different particles of various concentrations to prepare Samples A1, A2, A3 and A4. The particle types and their concentration levels and sizes are listed in Table IV.

Sample B is a lubricant with nanoparticle additives that provides wear resistance to bearing and is assumed to contain much higher additives than Sample A. Sample B has a yellow colour.

Sample C is selected due to its wide area of application in wind turbines and is a grease designed especially for wind power plants for their operating range, mechanical stability and load carrying capacity. Sample C+ is a specimen obtained from the field, from the main bearing of a wind turbine. The lubricant sample was earlier exposed to operating conditions, such as high ambient moisture, rotation and mechanical load. This has resulted in changes of the colour and probably the chemical composition of the grease. The virgin Sample C is of peanut-butter colour, while the degraded Sample C+ has a dark brown colour.

Sample D is commonly used in rolling bearing applications and is regarded as a general purpose grease used in electric motors, escalators, conveyors, fans, etc., [43]. The grease is of mineral oil base thickened with lithium soap, having a red brown colour.

Information on the base oil type, additives and the base oil viscosity at 100 °C and 40 °C of the lubricant samples are summarised in Table III and Table IV.

Table III. Lubricant samples according to type, base, additives and application.

Sample	Type	Base oil	Additives	Base oil viscosity (mm^2/s)	
				40 °C	100 °C
A, A+	Oil	Hydro-treated mineral oil	Acrylic copolymers	100.0	11.4
B	Oil	Semi synthetic, mineral base oil and polyalphaolefins	Nano particles to improve surface roughness	320.0	31.2
C, C+	Grease	Fully synthetic	Li-soap thickened	320.0	30–40
D	Grease	Mineral oil based, Li soap thickened	Oxidation stabilizers, pressure additives, water and rust resistant additives	110.0	11.0
E	Grease	Not available (N.A.)	Corrosion/rust inhibitors	12.5	N.A.
+ refers to sample aged due to operating conditions					

Table IV. Type, concentration and size class of particles that are intermixed with the test lubricant A to form different versions of test lubricants.

	Sample A1	Sample A2	Sample A3	Sample A4
Particle	Arizona test-dust	Toner	Aluminum	Iron
Particle concentration (mg/L)	150, 75, 30, 15, 7.5	150, 75, 30, 15, 7.5	150	150
Particle size class	5.5–100 μm	8–10 μm	160 μm	Fine dust

4.2 Test setups

The test benches and the mechanical operating points for tests are presented in this section.

4.2.1 Test setup for bearing of type 608

A small scale test bench, previously constructed for studies of the breakdown voltage of a bearing exposed to different types of voltages [91] has been utilised for experiments. It is shown in Figure 27. The bearing under test was mounted on a shaft together with a hybrid bearing, SKF hybrid bearing 608, with ceramic balls, which provides control over the discharge activity in the tested bearing. The shaft is brought into rotation through a belt wheel and an insulating belt driven by a permanent magnet motor. The rotational speed is varied up to 4000 rpm. Various levels of mechanical load can be applied by changing the position of the block. The axial load is varied between 4 N and 40 N. The radial load is approximately 1 N on each bearing. The test voltage is applied to the shaft by means of a slip ring contact. A grounded U-girder, electrically insulated from the bearing housing, provides a solid foundation to the setup. The bearing under test is placed in a housing that accommodates a bath of liquid lubricant. The tests were carried out with lubricants listed in Table III and Table IV.

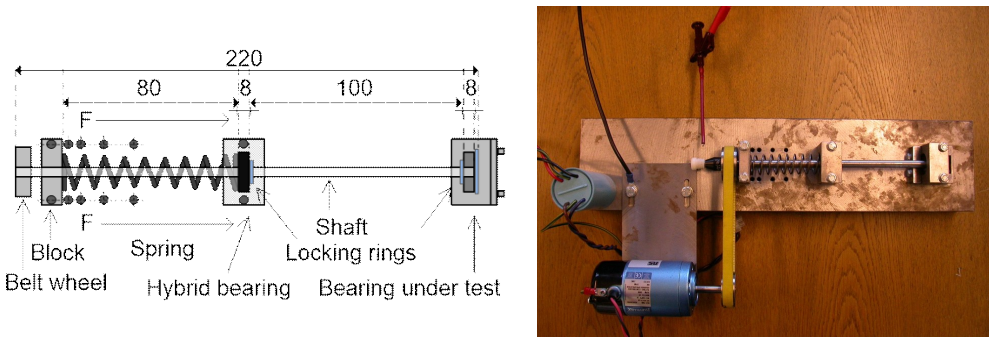

Figure 27. Dimensions of test bench for bearing type 608. All measures in mm.

4.2.2 Test setup for bearing of type 22220

Test bench LAD100 was used to test 22220 bearing, which was lubricated with Sample A. The test bearing is positioned on an electrically isolated plate and is mounted on a vertical shaft, shown in Figure 28. Since the inner ring of the bearing was connected to the rotating shaft, the circuit was completed by grounding the top of the rotating shaft. The rotational speed of the bearing was varied between 400 and 800 rpm in steps of 100 rpm. The applied axial load on the bearing was 5 kN and 10 kN, while the bearing was not radially loaded.

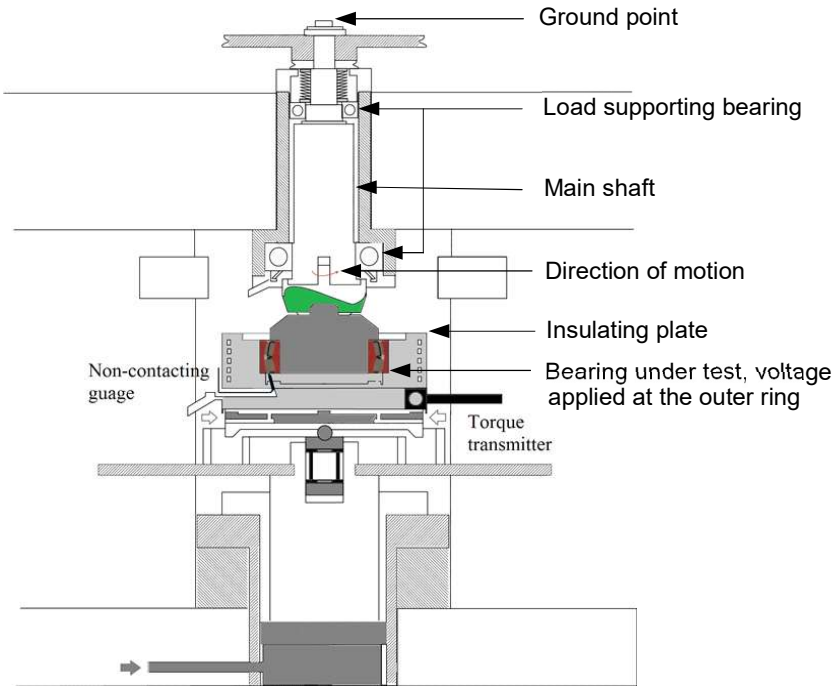

Figure 28. View of test rig for bearing 22220. The bearing is mounted on an electrically isolated plate and support bearings along the vertical shaft.

4.3 Characterisation methods

The methods used in measurement of parameters of the equivalent circuit model of the bearing are discussed in this section. The test circuit in which the bearing is connected and the test voltages applied are also presented along with data analyses methods.

4.3.1 Measurement of C_B and $R_{B,Ins.}$

Bearings under test of type 608 and 22220 were connected in electrical circuits to measure their properties o in the insulating state, i.e., C_B and $R_{B,Ins.}$. These test circuits are shown in Figure 29. Arbitrary Waveform Impedance Spectroscopy (AWIS), a methodology to measure complex impedance of dielectrics has been used [113].

The bearings were supplied from a voltage source V_0 and the voltage across the bearing and the current through it were measured using a RC shunt. The applied source voltage V_0 was a sinusoidal voltage of low magnitude, typically at 0.5 V_{peak} and 1 V_{peak}, to avoid insulation breakdown in the bearing. It was supplied from Agilent 33210A function generator. The frequency of the voltage was chosen to be 1 kHz. The measurements were taken in a 10 to 20 s windows and results are presented as an average value of six measurements. This way the resolution and accuracy of measurement is increased, by reducing the noise levels.

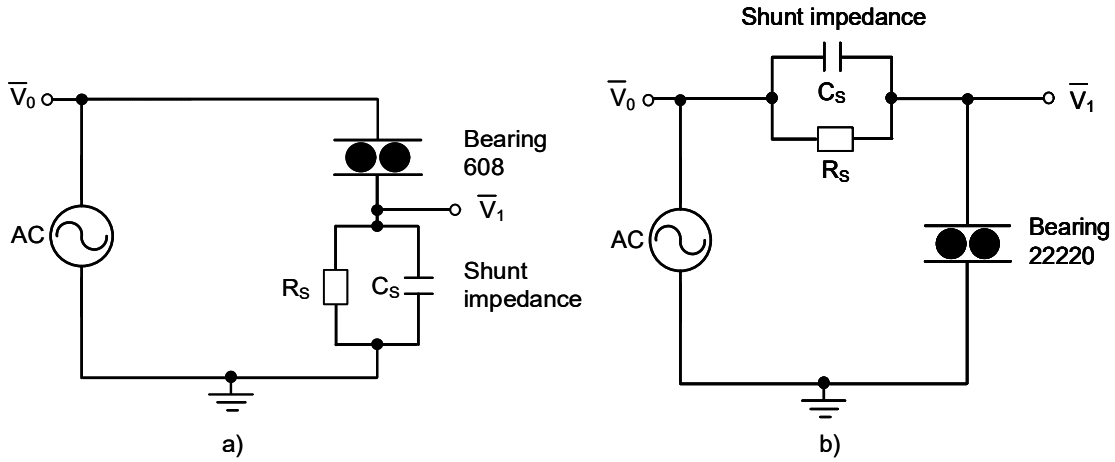

Figure 29. Electrical test circuit to measure bearing capacitance and bearing resistance in insulating state for bearing type 608 (a) and 22220 (b).

The shunt impedance is evaluated using equation (13),

$$\bar{Z}_{Shunt} = \frac{1}{\frac{1}{R_S} + j\omega C_S} = \frac{R_S}{1 + j\omega R_S C_S} \tag{13}$$

Here, $\omega = 2\pi f$, where f is the frequency of applied voltage. The choice of the shunt parameters depends on the bearing impedance during the measurement. The shunts are calibrated up to 5 kHz using standard air capacitors of type 1403-K (1 pF) and 1403-D (100 pF) to make sure that attenuation does not occurs due to incorrect transfer function of the shunt.

Table V- Parameters of the RC shunts used during experiments.

	bearing 608 + Sample D	bearing 608 + Sample E	bearing 22220 + Sample A
R_S	820 kΩ	570 kΩ	32 kΩ
C_S	280 pF	120 pF	160 pF

Phasor voltages and their phase difference are measured at points V_0 and $V_1$by means of National Instruments NI-USB 6251 data acquisition card. The sampling rate was set at 200 kHz. The bearing voltage for bearing type 608 is equal to the difference in phasor (V_0 - V_1), while for bearing type 22220 is equal to V_1.

The current for bearing type 608 is given by equation (14) as,

$$\bar{I}_{\text{bearing}} = \frac{\bar{V}_1}{\bar{Z}_{\text{Shunt}}}. \tag{14}$$

The current for bearing type 22220 is measured differentially and is given by equation (15) as,

$$\bar{I}_{\text{bearing}} = \frac{\bar{V}_0 - \bar{V}_1}{\bar{Z}_{\text{Shunt}}}. \tag{15}$$

For bearing type 608 the impedance is given by equation (16), while for bearing type 22220 it is given by equation (17) as,

$$\bar{Z}_{\text{bearing}} = \frac{\bar{V}_{\text{bearing}}}{\bar{I}_{\text{bearing}}} = \frac{(\bar{V}_0 - \bar{V}_1)}{\bar{V}_1}\bar{Z}_{\text{Shunt}}, \tag{16}$$

$$\bar{Z}_{\text{bearing}} = \frac{\bar{V}_{\text{bearing}}}{\bar{I}_{\text{bearing}}} = \frac{\bar{V}_1}{(\bar{V}_0 - \bar{V}_1)}\bar{Z}_{\text{Shunt}}. \tag{17}$$

The total measured bearing impedance is used to evaluate the values of C_B and $R_{B,Ins.}$. The total impedance of the bearing in insulating state is a parallel connection of C_B and $R_{B,Ins.}$ given by equation (18) as,

$$\bar{Z}_{\text{bearing}} = \frac{1}{\frac{1}{R_{B,Ins.}} + j\omega C_B}. \tag{18}$$

The values of C_B and $R_{B,Ins.}$ are approximated by equating the total impedance of the bearing to the total complex capacitance, which consists of a real and an imaginary part, as given in equation (19). The real part of the total capacitance is then approximated to be equal to C_B, while the imaginary part is approximated to be equal to $R_{B,Ins.}$ given respectively by equations (20) and (21) as,

$$\bar{C}_{\text{Total}} \approx \frac{1}{j\omega\,\bar{Z}_{\text{bearing}}} = \frac{1}{j\omega\left(\frac{1}{R_{B,Ins.}} + j\omega C_B\right)} \approx C_B - \frac{j}{\omega R_{B,Ins.}}, \tag{19}$$

$$C_B \approx \text{Re}(C_{\text{Total}}), \tag{20}$$

$$R_{B,Ins.} \approx -\frac{1}{\omega\,\text{Im}(C_{\text{Total}})}. \tag{21}$$

The ratio of the imaginary part to the real part of the total complex capacitance provides the dielectric dissipation factor, tanδ according to equation (22) as,

$$\tan\delta = \frac{\text{Im}(\bar{C}_{\text{Total}})}{\text{Re}(\bar{C}_{\text{Total}})}. \tag{22}$$

4.3.2 Switching pattern analysis and measurement of R_B

Two different voltage sources were used to perform experiments for analysing the switching patterns in the bearings. A DC voltage was applied using stabilised power supply LK 31, manufactured by CE-BIT Elektronik AB, for flexible increment of voltage across the bearing. The AC voltage was applied using Agilent 33210A 10 MHz function generator. For bearing type 608, additional tests were performed using a DC voltage supplied by standard rechargeable AA batteries, with internal resistance for one battery in the range of 0.1 to 0.2 Ω [114].

The DC voltage was applied to bearing type 608 through a current limiting resistor (981±2.5 Ω), to avoid current induced damages on the bearing surface. The purpose was to statistically study the insulation breakdowns in the bearing and not the effects of current induced damages. A shunt resistor of 81±0.5 Ω was connected between the bearing under test and ground for the experiments. The values of current limiting resistor and shunt resistor were chosen so that the amplitude of the discharge current pulses was clearly distinguishable from the noise level (0.1 mA).

For bearing 22220, the test voltage was also applied though a current limiting resistor (996±2.5 Ω), which also acted as a shunt resistor. This arrangement was forced by complex connection at the test bench LAD100 (see Figure 28). The voltage was applied to the outer housing of the bearing through the current limiting resistor, while the circuit was completed by grounding the top of the shaft, as it can be seen in Figure 28 and Figure 30. The applied voltage and the voltage V_1 were measured by means of DAC NI-USB 6251 at an aggregate sampling rate of 1 MS/s for two channels. Thus, the effective sampling rate per channel was 500 kS/s. As a complement, an oscilloscope (Tektronix DPO 4034) with significantly higher sampling rate of 2.5 GS/s was used for detailed studies.

The bearings were connected in a test circuits shown in Figure 30, where the bearing voltage was (V_1 - V_2) for bearing of type 608, while for bearing of type 22220 the bearing voltage was V_1. In the event of a breakdown, a current proportional to the total resistance in the circuit flue through the bearings. The conduction current ($I_{bearing}$) was evaluated by equation (23) for bearing of type 608 and by equation (24) bearing of type 22220 as,

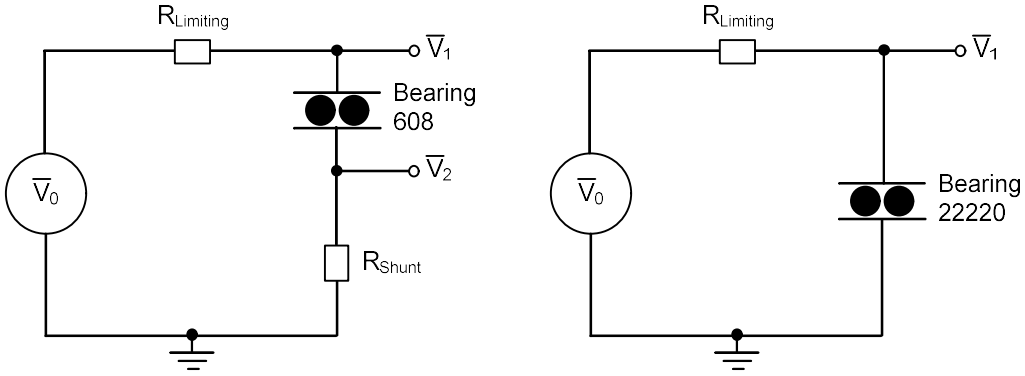

Figure 30. Test circuit for analysing the switching pattern and resistance in conducting state, R_B during breakdown and conduction in bearings under test.

$$I_{bearing} = \frac{\overline{V_2}}{R_{Shunt}} \text{ and} \tag{23}$$

$$I_{bearing} = \frac{(\bar{V}_0 - \bar{V}_1)}{R_{Limiting}}. \quad (24)$$

The current activity in the bearing is found to initiate at a certain threshold value of bearing voltage, henceforth referred to as the inception voltage. Once the inception voltage is surpassed, the bearing current activity increases and has a characteristic of longer current pulses. The bearing current activity is also found to extinguish below a certain value of bearing voltage and is henceforth referred as the extinction voltage for bearing current activity.

A current pulse is represented by the closed switch in in the electrical circuit model of the bearing and the bearing is said to be in conducting state. The time in conducting state is denoted by pulse duration. The threshold value of recording a current pulse is set at 1 mA. The value is chosen since it should be higher than the noise level in the measurement circuit, but it should also be as close to 0 as possible for increasing measurements accuracy. The duration the current pulses is recorded along with the measurement of time between successive pulses.

By analysing all the current pulses in a given measurement at a given operating point in a statistically significant manner, a complete picture of current conduction characteristics in the bearing is provided. The time between successive current pulses is shown as Δt in Figure 31 and is a measure of the time for which bearing is in high impedance state, providing insulation and withstanding the voltage across it. The number of current pulses (insulation breakdown events) is given in per second values. Similar method to quantify and analyse the awaiting times to breakdown events in bearing have been presented in [39, 115, 116].

To make comparable analyses with the information about the pulse duration and time between immediate discharges (Δt) for different voltages, 300 sample points were selected at random from the entire measured data to represent the mean values at given operating points of speed, load and applied voltage level.

To quantify how much percentage of time the bearing was found in the conducting state, a term called 'Time of Conduction' (ToC) is introduced and refers to the time during the bearing's electrical insulation is in breakdown or conducting state, expressed in a percentage value. The time of conduction is given by summation of pulse duration of all the current pulses during the measurement, presented in a percentage value of the total duration of measurement, given by equation (25) as,

$$\text{Time of Conduction, ToC (in \%)} = \frac{\sum \text{Pulse duration}}{\text{Measurement window}} \times 100. \quad (25)$$

Time of Conduction (ToC) can be used as an indication to compare the current conduction characteristics at the different operating points.

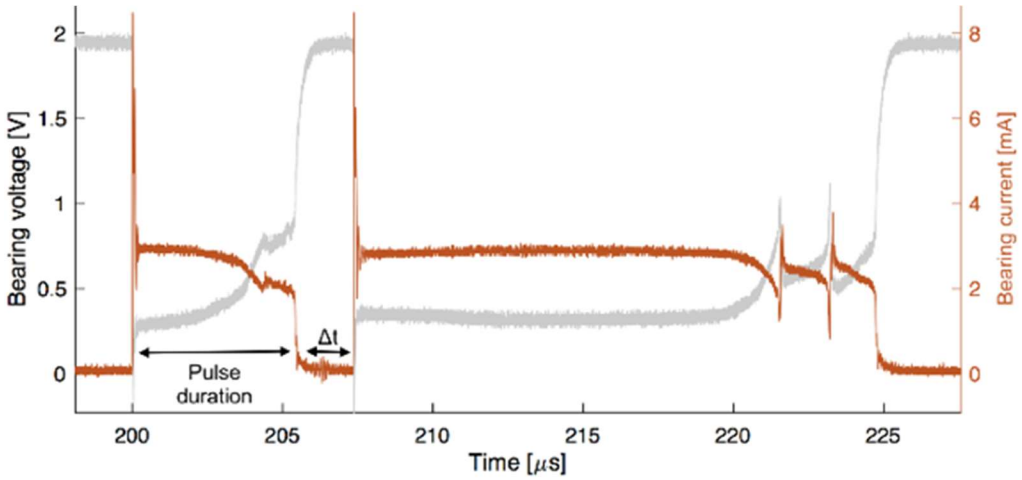

Figure 31. Oscilloscope trace showing a bearing current pulse (orange) and the corresponding drop in voltage across bearing (grey).

In the event of a breakdown the equivalent resistance of the bearing in conducting state is measured using the instantaneous values of bearing voltage and bearing current. During the discharge, the voltage across the bearing drops to a small value and its equivalent value consists of combination of bearing resistance in insulating state ($R_{B,Ins.}$) and bearing resistance (R_B). Since the bearing resistance in insulating state was found to be rather high in comparison to the bearing resistance, we neglect it and assume the measured resistance in conducting state of bearing (R_B) to be given by equation (26) as,

$$R_B = \frac{\overline{V_B}}{I_{bearing}}. \tag{26}$$

4.3.3 Electric characterisation of lubricants

The lubricants are electrically characterised by analysing their complex permittivity, using frequency domain spectroscopy (FDS) measurements and by determining electrical breakdown strength.

- **Relative permittivity and DC conductivity**

A three-terminal test cell consisting of two concentric stainless-steel cylindrical electrodes and a guard ring was used to determine complex impedance of tested lubricants. The cell is designed to characterise 40 ml of liquid or semi liquid dielectric medium and its geometrical capacitance (C_0) is 60 pF. The distance between the electrodes in this cell is fixed at 2 mm. The voltage is applied through a high voltage electrode and the responding current is measured through a second electrode, while the guard electrode is grounded. The test cell is shown in Figure 32 (right) while the insulation diagnostics analyser IDAX 300 [42], is shown to the left.

Figure 32. IDAX 300 [42] (left), used in FDS and Tettex oil test cell (right).

A relatively low test voltage of 5 V_{RMS} was applied to reduce dissociation of ionisable substances at high electric fields (> 1 kV/cm) [117]. The frequency was swept from 1000 Hz to 0.0001 Hz. The measurements were done between a temperature of 35 °C (308 K) and 80 °C (353 K), considering the operating range of lubricants. The complex capacitance, $\bar{C}(\omega)$ is given by equation (27) as,

$$\bar{C}(\omega) = C_0\bar{\varepsilon}_r(\omega) = C'(\omega) - jC''(\omega). \tag{27}$$

Similarly, complex permittivity of the dielectric can be given by equation (28) as,

$$\bar{\varepsilon}_r(\omega) = \varepsilon_r'(\omega) - \varepsilon_r''(\omega). \tag{28}$$

Dissipation factor can be expressed as ratio of imaginary and real part of the measured complex capacitance; and also for complex permittivity. The relations can be given by equation (29) as,

$$\tan\delta = \frac{C''(\omega)}{C'(\omega)} = \frac{\varepsilon_r''(\omega)}{\varepsilon_r'(\omega)}. \tag{29}$$

The complex permittivity is given by the ratio of real part of complex capacitance and C_0, which corresponds to geometric capacitance of an empty test cell and is given by equation (30).

$$\varepsilon_r'(\omega) = \frac{C'(\omega)}{C_0}. \tag{30}$$

The imaginary part of complex capacitance represents the conductivity losses in the lubricants, given by equation (31) as,

$$\sigma(\omega) = \frac{C''(\omega)\varepsilon_0\omega}{C_0}. \tag{31}$$

From the relation shown in equation (32), it is seen that conductivity is temperature dependent and this Arrhenius-type dependency can be expressed using lubricant's activation energy (E_{DC}) and a constant σ_0 as,

$$\sigma(T) = \sigma_0 e^{\frac{-E_{DC}}{kT}}, \tag{32}$$

where

T is absolute temperature and
k is Boltzmann constant in electron-volt.

- **Electric breakdown strength of lubricants**

The AC 50 Hz breakdown voltage (V_{BD}) of the different samples of oil lubricants was measured at gap distances of 0.1 and 0.2 mm of standard shaped electrodes for oil testing of diameter 3.5 cm at room temperature. The results are further reported in their root mean square (RMS) values. The circuit used for measuring breakdown strength of lubricants is shown in Figure 33. The voltage was ramped at a constant rate of 50 V/s was applied from a signal generator Agilent 33210A, a power amplifier Brüel & Kjaer of model type 2706 and a transformer through a 1 MΩ current limiting resistor. The breakdown events were recorded using a Pearson current monitor 2877 connected to a digital oscilloscope Tektronix 4034 with a bandwidth of 350 MHz. The breakdown voltage was averaged for six consecutive tests. The oil was stirred in between tests to disperse bubbles and breakdown by-products formed near the electrode during preceding breakdowns.

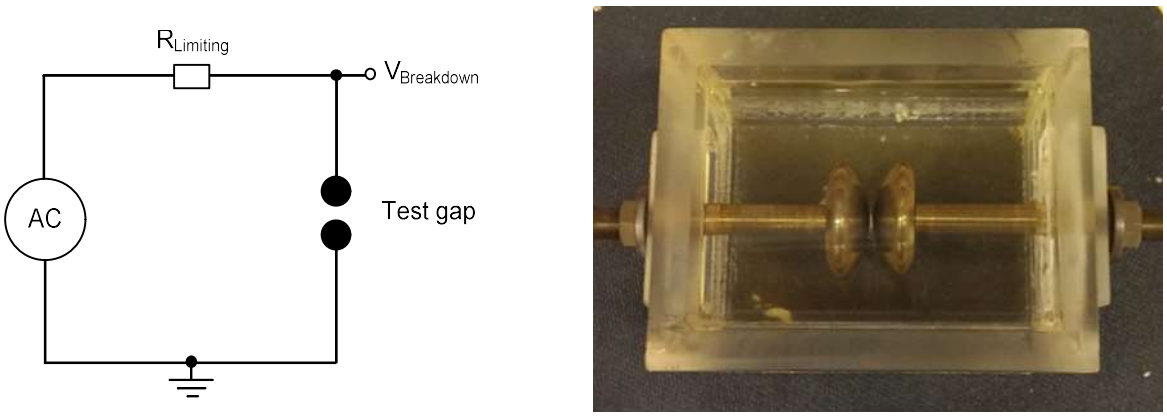

Figure 33. Electrical circuit connection of the liquid breakdown test setup, along with photo of the test cell. The test gaps were set 0.1 and 0.2 mm.

5 Characterisations of lubricants

5.1 Mechanical characterisation

5.1.1 Calculated film thickness (h_c)

The lubricant film thickness during operation is dependent on lubricant's chemical, thermal and physical properties and the operating conditions. The film thickness calculations in this thesis are done using SKF Galaxy tool provided at SKF AB, Göteborg. The program uses different models to evaluate the film thickness, depending on the lubrication regime and the input parameters such as lubricant properties, operating parameters etc. The models used are according to Elasto-Hydro Dynamic) EHD theory, Hydro-Dynamic (HD) piezoviscous theory and is automatically selected based on the input parameters provided during calculation. The film thickness is calculated for a rolling element, both at the inner raceway ($h_{c,inner}$) and at the outer raceway ($h_{c,outer}$) contacts. The output is provided in form of calculated deformation and stress on bearing surfaces, oil film thickness and viscosity ratio.

The information provided by the calculated lubricant film thickness will be used in electrical circuit modelling to relate the measured parameters of the electrical circuit model to evaluated physical properties. For example, in insulating state, the capacitance can be related to the lubricant film thickness to establish a correlation between the evaluated capacitance through measurements and the calculated film during the operation. The film thickness will also be used to evaluate the conducting state of the bearing, in order to approximate the apparent electric field strength in the lubricant at which we have the electrical breakdown of the bearing during operation. The film thickness varies depending on how much lubricant is applied in the bearing, for example, an adequately lubricated bearing will have a higher film thickness around the rollers, while a scarcely lubricated bearing will have a much lower film thickness. Adequate lubrication was applied to the bearing, except for tests with pre-lubricated bearing of type 608. The film thickness calculations for bearing type 608 are first presented, followed by film thickness calculations of bearing type 22220.

- ► Bearing type 608 lubricated with Sample A (oil)

The bearing of type 608 has a radial load of 1 N on each bearing due to the weight of the shaft. An axial load is applied to the bearing from a loaded spring and is adjusted between 4 and 40 N. The equivalent dynamic bearing load with an axial load of 4 N and radial load of 1 N is calculated to be 9.8 N, while the equivalent dynamic bearing load with an axial load of 40 N and radial load of 1 N is calculated to be 80 N [41]. The rotational speed of the bearing is varied up to 4000 rpm, for the film calculations. The film thickness using lubricant Sample A is shown at both inner and outer rings of the bearing as a function of rotational speed and axial load, shown in Figure 34. Film thickness at the outer contact is slightly larger than that at the inner contact for the bearing under test. Detailed information about lubricant Sample A is presented in Table III.

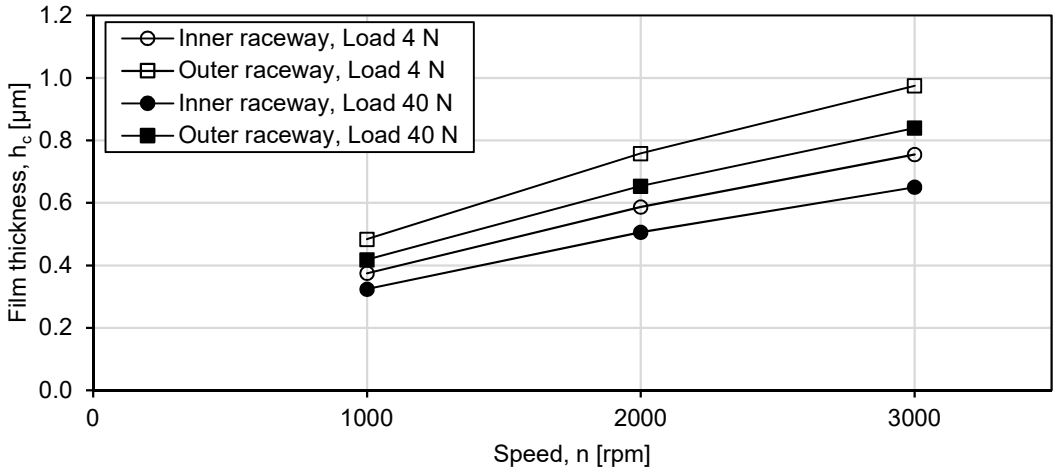

Figure 34. Film thickness (h_c) calculated for deep groove ball bearing of type 608 lubricated with Sample A. The film thickness at the inner and the outer raceway contacts is shown as a function of different rotational speeds and axial loads. For these calculations, temperature of the operation was set at 20 °C.

The film thickness changes with the bearing operating temperature and is found to decrease with an increase in temperature. The calculations show that the reduction in total film thickness as a function of increasing temperature, at 20 °C, 40 °C and 60 °C is shown in Figure 35. It can be seen that as the lubricant temperature increases, the film thickness reduces significantly for a given operating point. A higher temperature will lead to a lower viscosity and form a thinner film. This is observed for both grease and oil lubricated bearings. The lubricant temperature can increase due to high friction between metallic parts of the bearing and at extreme operating conditions. Faulty bearing operation such as eccentricity in rotation and high amount of debris could also indirectly lead to an increase in lubricant temperature.

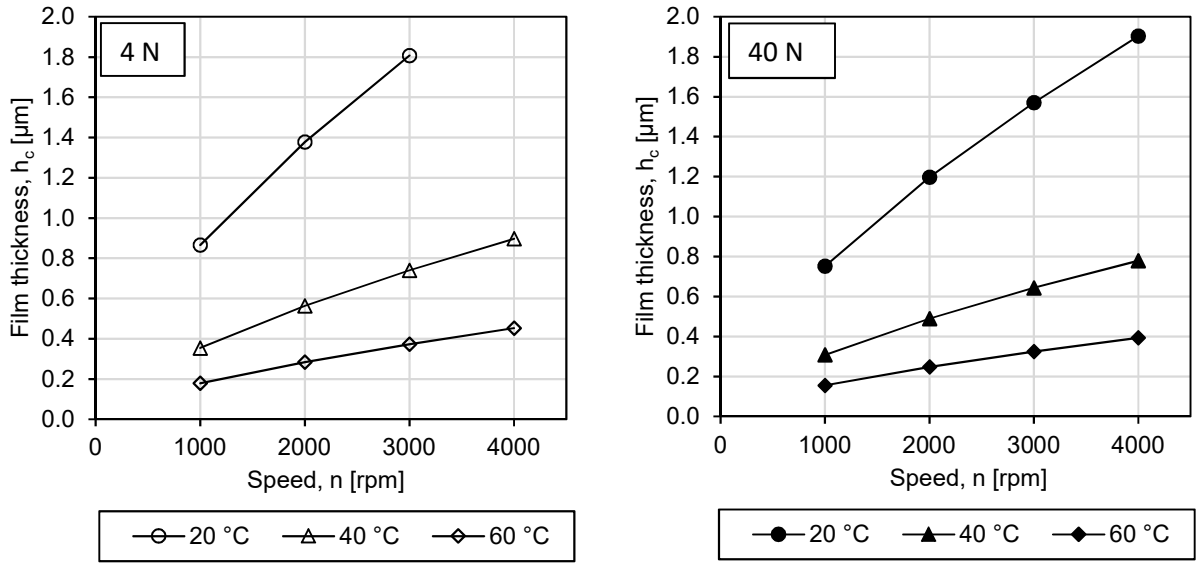

Figure 35. Total film thickness ($h_{c,inner}$ + $h_{c,outer}$) at different temperatures for bearing type 608 lubricated with Sample A, shown as a function of speed. Total film thickness is presented for an axial load of 4 N (left) and 40 N (right).

► Bearing type 608 lubricated with Sample D (grease)

Lubricant film calculated for bearing type 608 lubricated with Sample D at speeds between 200 rpm and 3000 rpm and at two load settings at 20 °C is shown in Figure 36. Lubricant Samples A and Sample D offer almost identical film thickness across the speed range. Film thickness is calculated at speeds below 1000 rpm since lubricant Sample D was used in investigations of asperity contact-initiated breakdowns, later presented in Chapter 8.1.4.

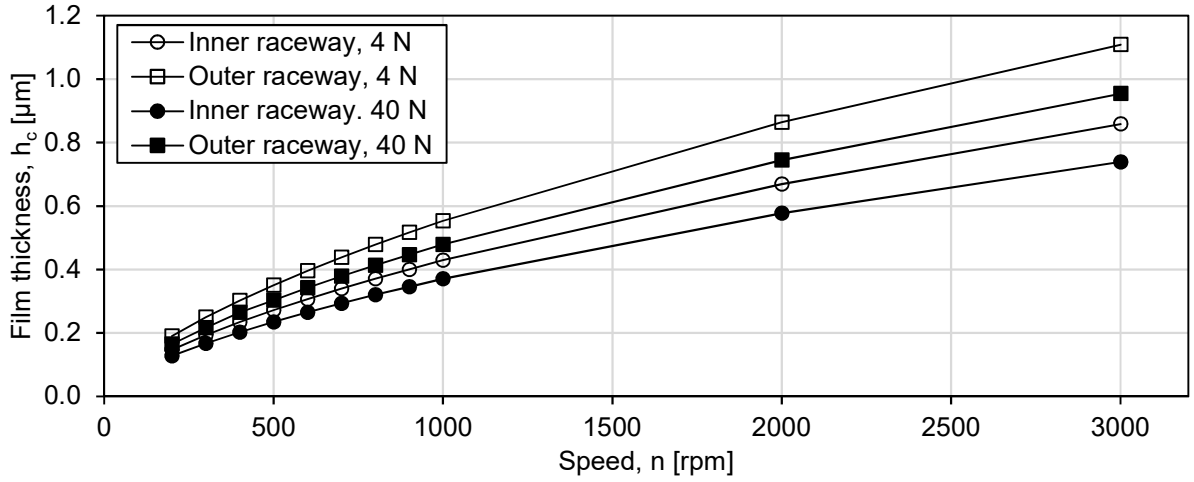

Figure 36. Film thickness for bearing type 608 lubricated with Sample D at inner and outer raceways as a function of different operating points, calculated at 20 °C.

The total film thickness ($h_{c,inner} + h_{c,outer}$) as a function of different operating points and at different temperature is presented in Figure 37.

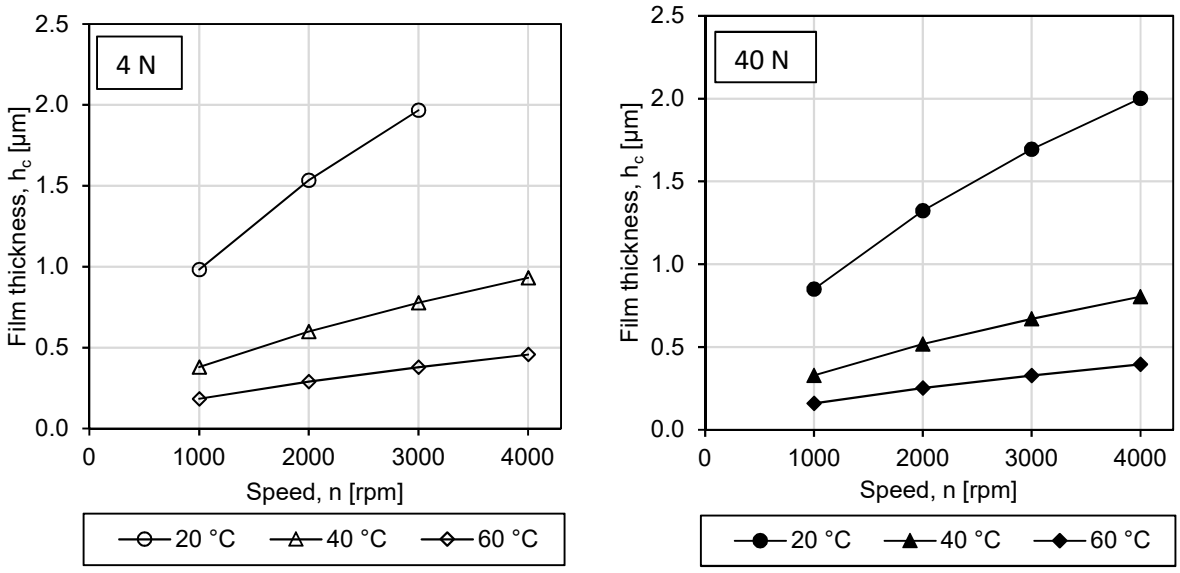

Figure 37. Total film thickness ($h_{c,inner} + h_{c,outer}$) calculated at different temperatures for bearing type 608 lubricated with Sample D, shown as a function of speed. Total film thickness is presented for an axial load of 4 N (left) and 40 N (right).

► Bearing type 608 lubricated with Sample E (grease)

The film thickness of the pre-lubricated bearing was also evaluated at different load settings. The static axial and radial loads during operation was used to calculate equivalent radial load during operation and used to determine the film thickness at temperature of 20 °C and lubricated with Sample E. The results are presented in Figure 38. The evaluated film of bearing pre-lubricated with corrosion inhibitor grease is much smaller in comparison with the film thickness of the same bearing lubricated with other lubricant samples. The total film thickness at a temperature of 20 °C for Sample E, at loads of 4 N and 40 N are shown in Figure 39. At the given operating points, the rise in temperature for bearing type 608 is insignificant (up to 5 °C), hence results are presented only at 20 °C.

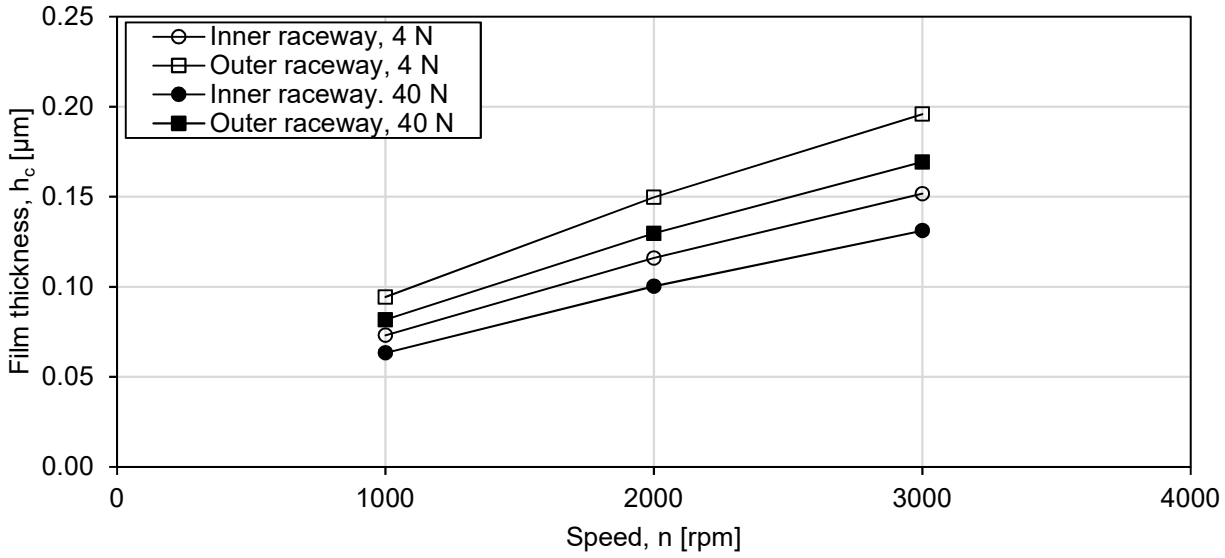

Figure 38. Film thickness calculated at different speeds and loads for pre-lubricated with Sample E bearing of type 608, calculated at 20 °C.

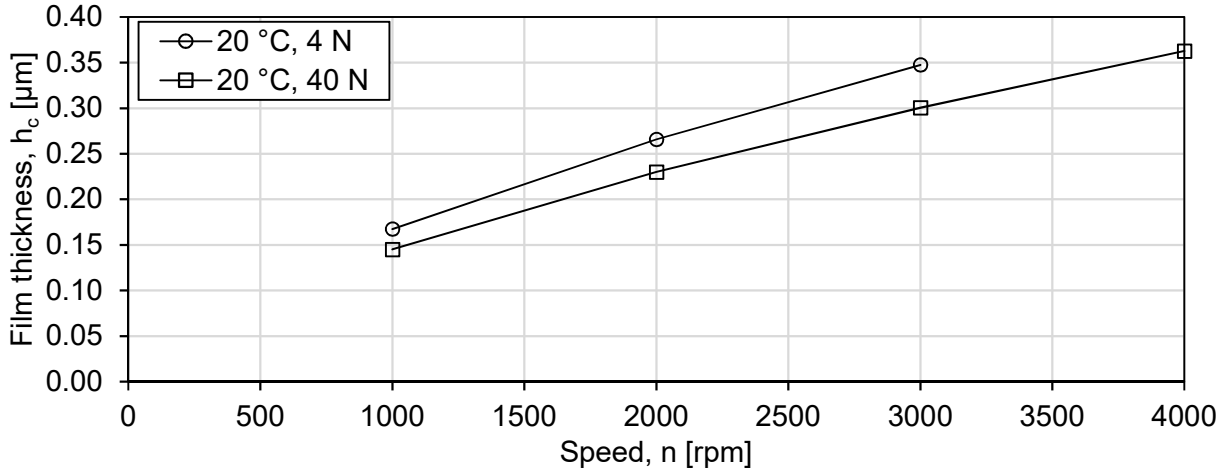

Figure 39. Total film thickness ($h_{c,inner}$ + $h_{c,outer}$) calculated for pre-lubricated with Sample E bearing of type 608, calculated at temperature of 20 °C and at loads of 4 N and 40 N respectively.

► Bearing type 22220 lubricated with Sample A

The film thickness is calculated at both, the inner ring contact and at the outer ring contact, but is here presented as total film thickness, as their sum. It can be observed that the film thickness reduces significantly as the temperature of the bearing reaches 50 °C and above, shown in Figure 40. At a given temperature, an increase in speed causes an increase in film thickness. On the other hand, at a given temperature, an increase in load causes a slight decrease in film thickness, as given by equation (11). Thus, the simulated film thickness is almost identical, both at the inner ring contact and the outer ring contact.

Simulations show that lubricating film reduces drastically as temperature increase. It can be observed that at higher speeds a larger film thickness can be expected, given that the temperature is kept constant. An increase in axial load from 5kN to 10 kN on the bearing slightly reduces the simulated film thickness. For a larger bearing (22220), a bigger film thickness can be expected compared to the small bearing of type 608.

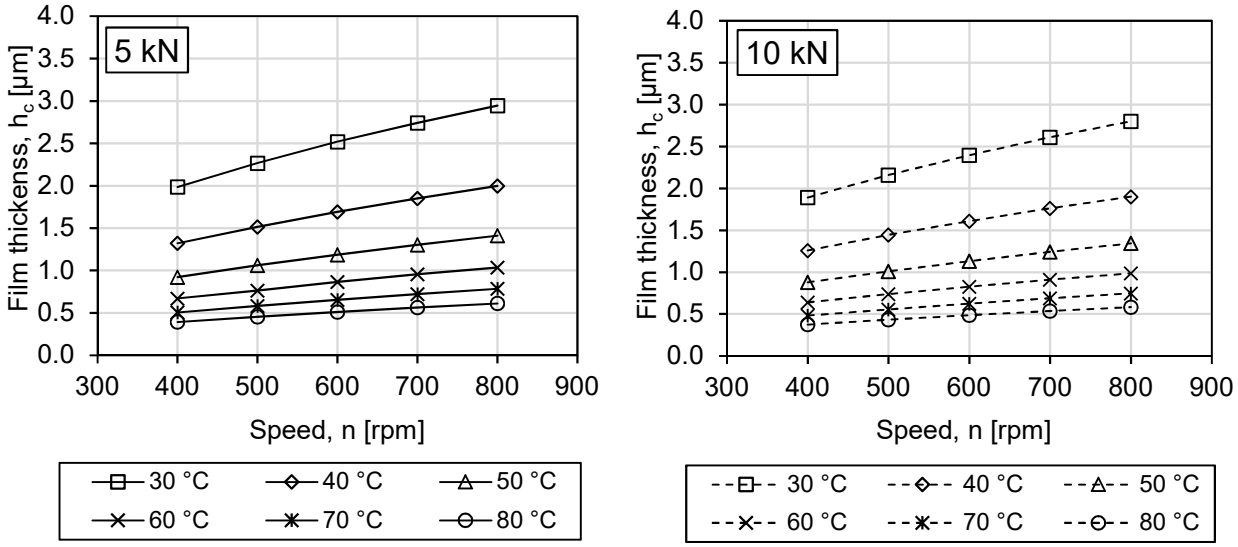

Figure 40. Total film thickness ($h_{c,inner} + h_{c,outer}$) for bearing type 22220 lubricated with Sample A as a function of speed, presented at different temperatures. Total film thickness at axial load of 5 kN is shown on the left graph, while total film thickness at axial load of 10 kN is shown on the right one.

5.1.2 Calculated viscosity ratio (κ)

The viscosity ratio (κ) (see equation 10) is a function of bearing speed and lubricant viscosity. A minimum viscosity ratio of 1 is required to assure separation of the balls and the raceways. A higher viscosity ratio ensures larger separation during operation and is thus desirable for correct functioning of the bearing. In experiments performed here, for both the bearings, type 608 and type 22220, viscosity ratio was found to be above 1, thus assuring separation between the rollers and the raceways.

5.2 Electrical characterisations

5.2.1 Relative permittivity (ε_r)

The relative permittivity for all lubricant samples was calculated based on the measurement of real part of the complex capacitance, using the methodology described in Chapter 4.3.3, while the compositions of lubricant samples are elaborated in Table III and Table IV.

Electrical properties of virgin Samples A, B, C and D are first shown, followed by comparison with the degraded Sample A+, C+ and A5. The relative permittivity of the lubricants is presented at a temperature of 50 °C as a function of swept frequency from 0.1 mHz to 1 kHz and is calculated according to (20). The climatic chamber used in experiments has a stable operation at higher temperatures than at temperatures close to room temperature. The relative permittivity at frequency of 46 Hz for oil Samples A and B is 2.16 and 2.25, while that of grease Samples C and D is 3.82 and 4.40 respectively, at 42 Hz as shown in right side graph of Figure 41. The relative permittivity of samples tends to increase at lower frequencies and may be attributed to an increase in dipole mobility, as shown in left side graph of Figure 41. The relative permittivity of oil Sample A decreases from 2.16 at 40 °C to 2.12 at 80 °C, at 46 Hz. The permittivity of Sample A reduces slightly with increase of 10 °C in lubricant temperature. Similarly, relative permittivity for Sample B reduces from 2.26 at 40 °C to 2.21 at 80 °C.

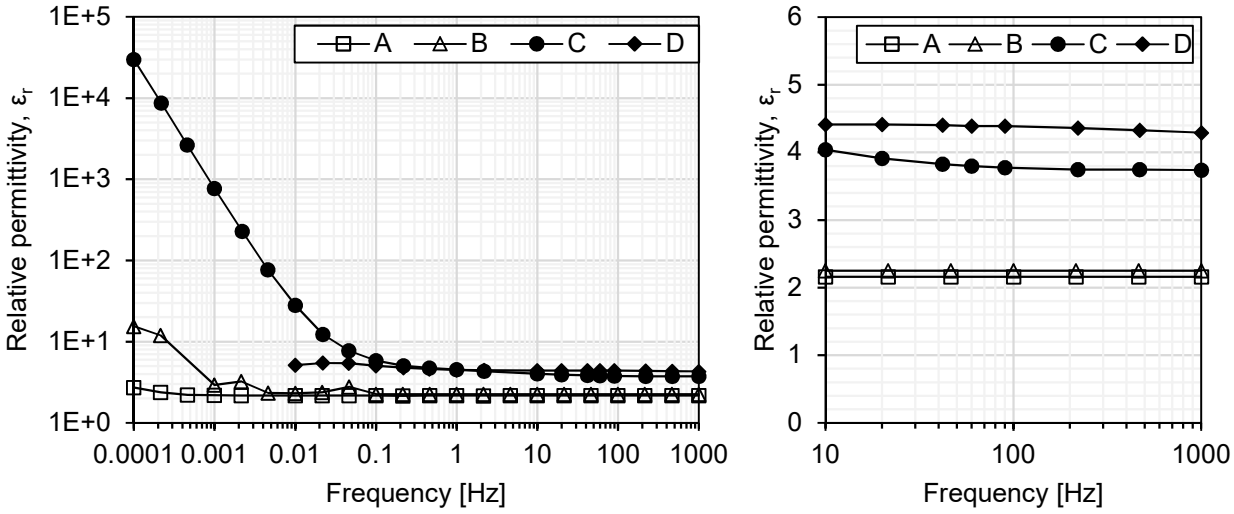

Figure 41. Relative permittivity of Samples A, B, C and D over the used frequency range, measured at 50 °C. Figure on right presents magnified data in frequency range of 10 Hz and 1 kHz.

Effect of temperature on grease Sample C is shown in Figure 42. The increase in relative permittivity for a used sample at higher temperature could be attributed to changes in chemical structure of the lubricant, which has been exposed to mechanical operating conditions and ambient conditions of the operation such as moisture and contaminants etc. The permittivity of Sample C changes from 3.83 at 20 °C to 4.52 at 80 °C, at 42 Hz. The permittivity of Sample C+ changes from 3.46 at 20 °C to 5.06 at 80 °C, at 42 Hz. Thus, due to degradation the resultant change in relative permittivity with temperature for Sample C+ is slightly higher than change of relative permittivity with temperature for Sample C.

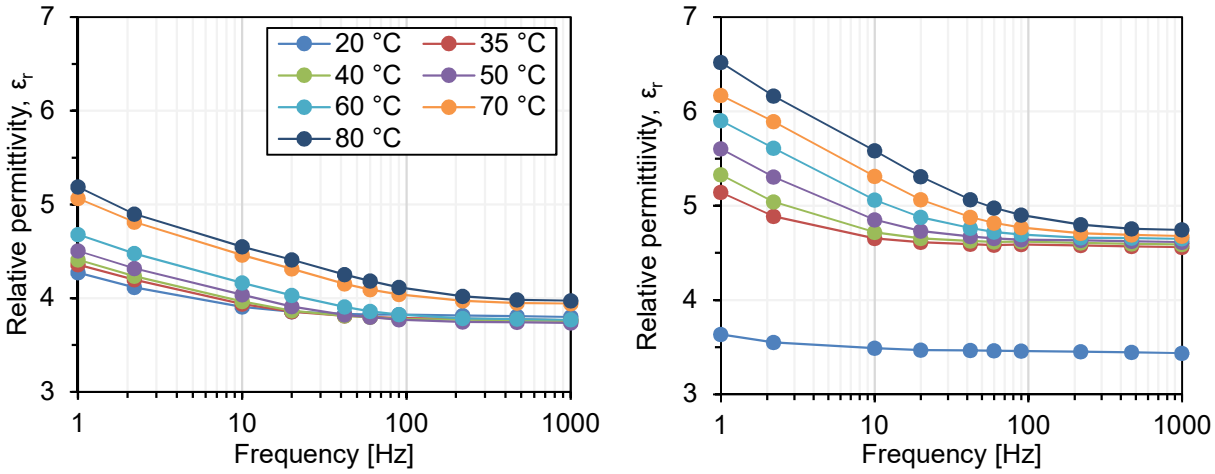

Figure 42. Effect of temperature on fresh lubricant Sample C (left) and used lubricant Sample C+ (right). The used lubricant Sample C+ obtained from wind turbine has higher relative permittivity at higher temperatures compared to Sample C.

Relative permittivity in oil Samples A+, A1, A3, A4, A5 is found to be slightly lower than the Sample A ($\varepsilon_r = 2.16$). The relative permittivity of Sample A+ is 2.15, while of Samples A1, A3, A4 and A5 is 2.13, measured at frequency of 42 Hz and at temperature of 50 °C and is shown in left-side graph of Figure 43. The reduction in permittivity is most likely attributed to changes in geometric capacitance C_0 (given by equation 30) of the test cell due to accumulation of the particles on the bottom electrode due to gravity.

On the other hand, grease Sample C+ has a higher relative permittivity of 4.67, when compared to Sample C ($\varepsilon_r = 3.82$), measured at 42 Hz and temperature of 50 °C, shown on the right-side graph of Figure 43. In literature [93], the reported dielectric properties of lubricant having similar composition to the test lubricants of this thesis are found to be in a similar range. The increase of permittivity in these lubricant samples with temperature is similar to the increase found in this thesis.

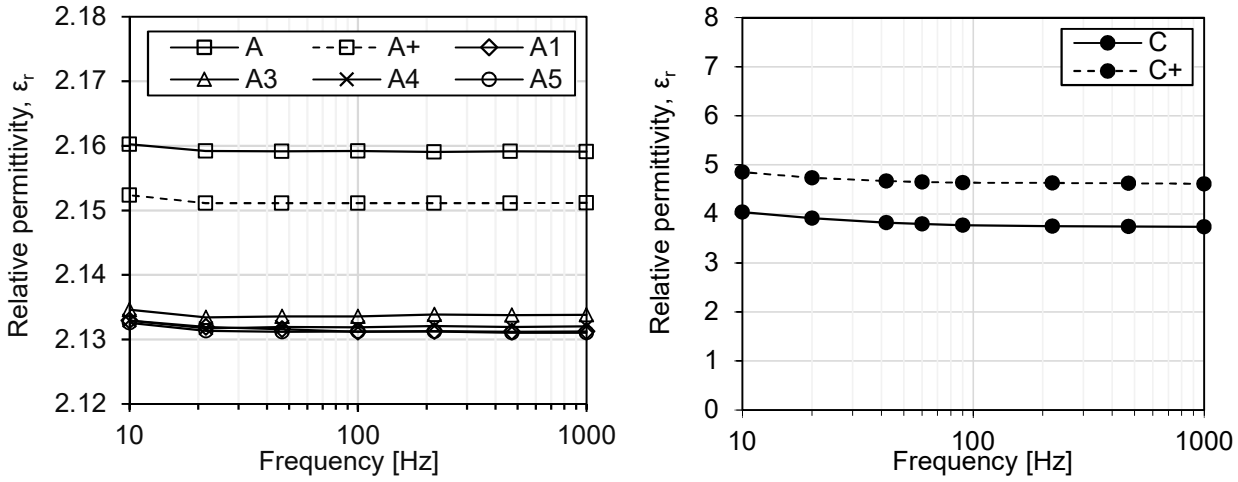

Figure 43. Relative permittivity of lubricant samples A and C measured at 50 °C (shown in the range of 10 Hz to 1 kHz).

5.2.2 Dielectric dissipation factor tanδ

Plotting dielectric dissipation factor tanδ as a function of frequency can provide an insight into the loss mechanisms operating in the dielectric material under test. If the plot of tanδ as a function of frequency sweep from 0.1 mHz to 1 kHz yields a slope of -1, the losses in the material can be said to emanate from conduction processes, as seen in the case of liquid oil lubricant Samples A and B, shown in Figure 44. If losses origin from other physical mechanisms, such as interfacial polarisation and dipole polarisation, distinct peaks are visible at different frequency ranges. A Maxwell-Wagner (MW) peak is visible for Sample C in Figure 44 and is caused by interfacial polarisation. Similar MW peaks are also observed in Oil-In-Paper (OIP) insulation system in transformers and generally occurs between 0.1 Hz and 0.01 Hz, characteristic of low moisture condition in OIP insulation systems. In diagnostics of oil based insulation systems in electrical equipment, a high level of tanδ is in general an indication of degradation processes. Sample D shows similar characteristics to Samples A and B, but the data are available only down to 0.01 Hz and no MW peak is visible.

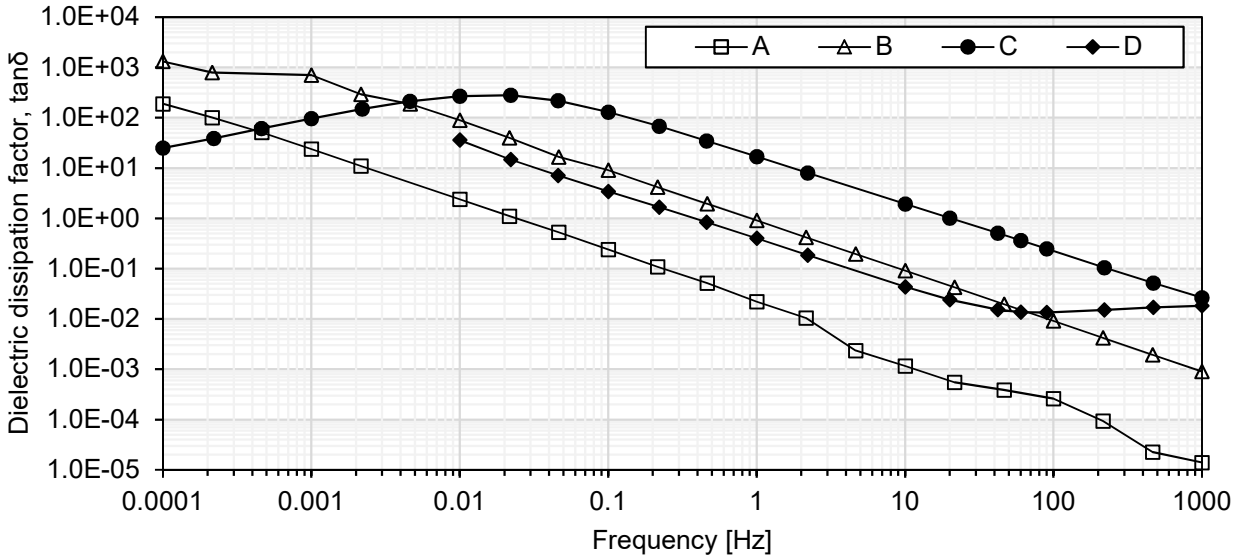

Figure 44. Tanδ plotted in the frequency range of 0.1 mHz to 1 kHz at a temperature of 50 °C for tested lubricant samples.

Samples A and B are highly refined mineral oils, but due to unique manufacturer formulation, the dielectric dissipation factor is orders of magnitude apart. The tanδ for Sample A measured near power frequency and at temperature of 50 °C is 3.8 x 10^{-4}, while tanδ for Grease B is 1.9 x 10^{-2}.

Presented in literature [93] results of tanδ up to 10^5 Hz for Samples B and C are shown earlier in Figure 20 in Chapter 2.7.1.

Samples with particle contamination (A1, A3, A4 and A5) show a slightly lower loss compared to Samples A and A+, shown in Figure 45. At the same time tanδ increases after the running-in process, Thus, the running-in process not only changes the lubricating properties of the lubricant but may also affect the physical structure and chemical composition of the insulation and is not exclusively affected by the presence of wear debris in the lubricant.

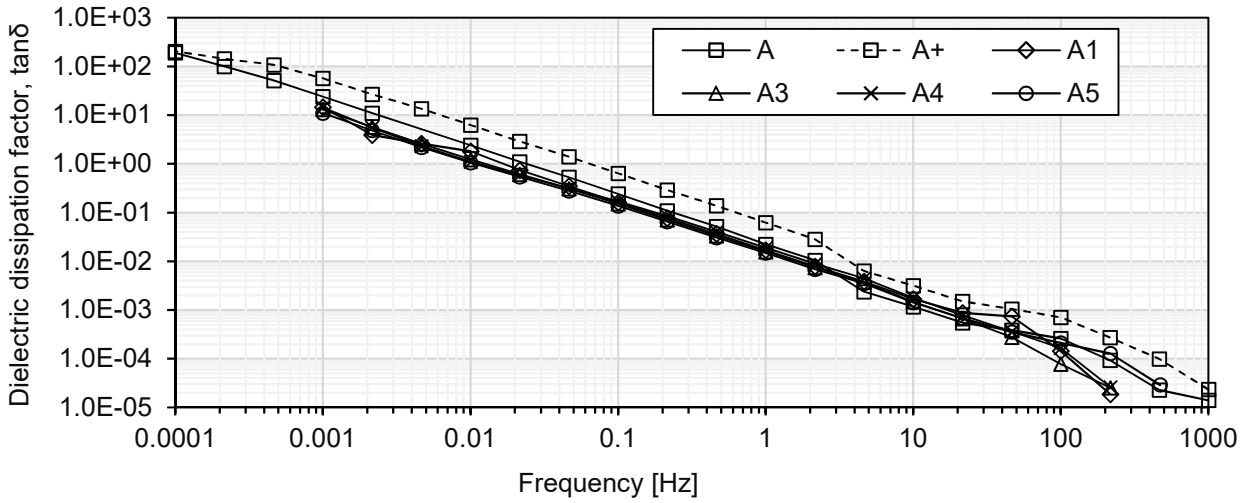

Figure 45. Tanδ of various oil lubricant samples of type A, shown at 50 °C.

5.2.3 DC conductivity (σ)

DC conductivity is derived from the dielectric spectroscopy measurements, using the imaginary part of the complex capacitance, using equation (32), where the derived temperature dependent conductivity is presented as a function temperature, ranging between 20 °C (293.15 K) and 80 °C (353.15 K). Degradation in an insulation medium will generally lead to a higher conductivity in the sample, however for lubricants, conductivity is also influenced by the additives in the lubricant.

Measurements on grease samples reveal additional polarisation in the low frequency region (between 0.1 Hz to 0.1 mHz), which can be attributed to free ions, debris or moisture content in high viscous grease [117, 118]. This effect can be accounted for in the model proposed in Chapter 3.2 by adding additional parallel RC branches, representing different time constants according to the theory by Debye. However, from the perspective of a rotating bearing, events occurring at these low frequencies (or the corresponding long times) are not of practical interest and therefore we choose not to extend our proposed model.

The imaginary parts of the complex capacitance at 50 ℃ (323 K) for all the samples are presented in Figure 46. It should be noted that the imaginary part of all lubricant samples are straight lines with -1 slope and thus the losses are due to conductivity only and then DC conductivity can be calculated per equation (32). The conductivity of the samples was calculated as a function of temperature and the activation energies were also evaluated.

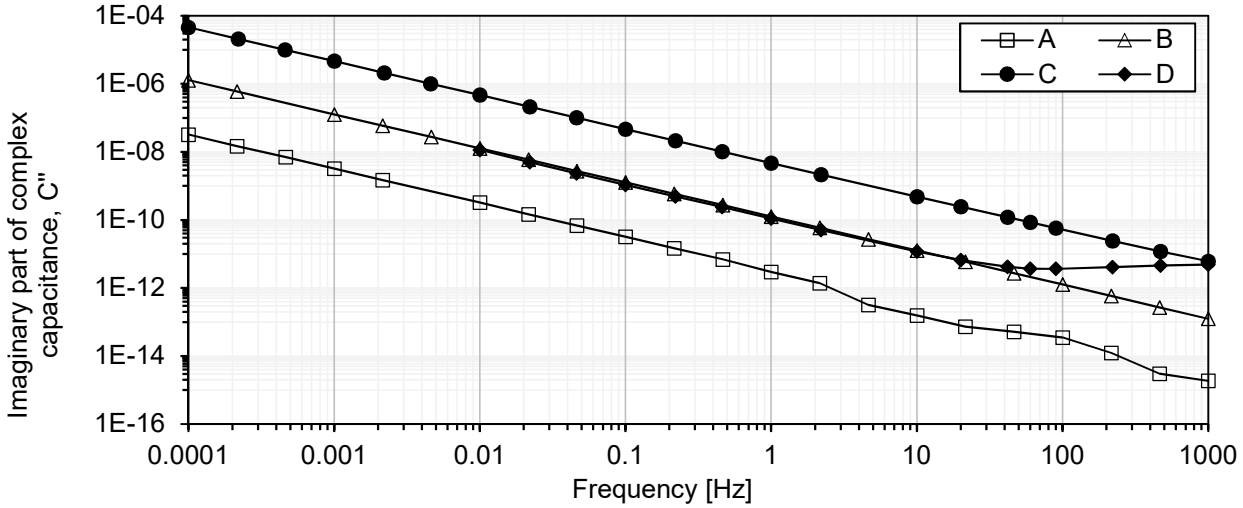

Figure 46. Imaginary part of complex permittivity for all lubricant samples at 50 °C (323 K).

The conductivities are presented in Figure 47. After 48 hours run-in of Sample A (i.e. Sample A+) an increase in DC conductivity from 2.9 pS/m to 7.6 pS/m, measured at 0.1 Hz at a temperature of 50 °C. The increase in conductivity could not only be attributed to increased particle density in Sample A+ due to debris after usage, as suggested in [118], but also to changes in physical and chemical properties of the lubricant after the running-in process. Sample B, with wear resistant nanoparticle additives, exhibit higher conductivity 114 pS/m, compared to virgin Sample A. The grease samples show even higher conductivities, Sample C 4202 pS/m while the used Sample C+ has a conductivity of 2446 pS/m. Sample C is lubricant with extreme pressure additives and these additives cause increase in DC conductivity. After the lubricant has been put inside a bearing, the effect of the additives could possibly diminish under operation. These could be the reason for significantly lower DC conductivity in Sample C+. DC conductivity of grease Sample D is found to be 96 pS/m. The respective activation energies are found in Table VI.

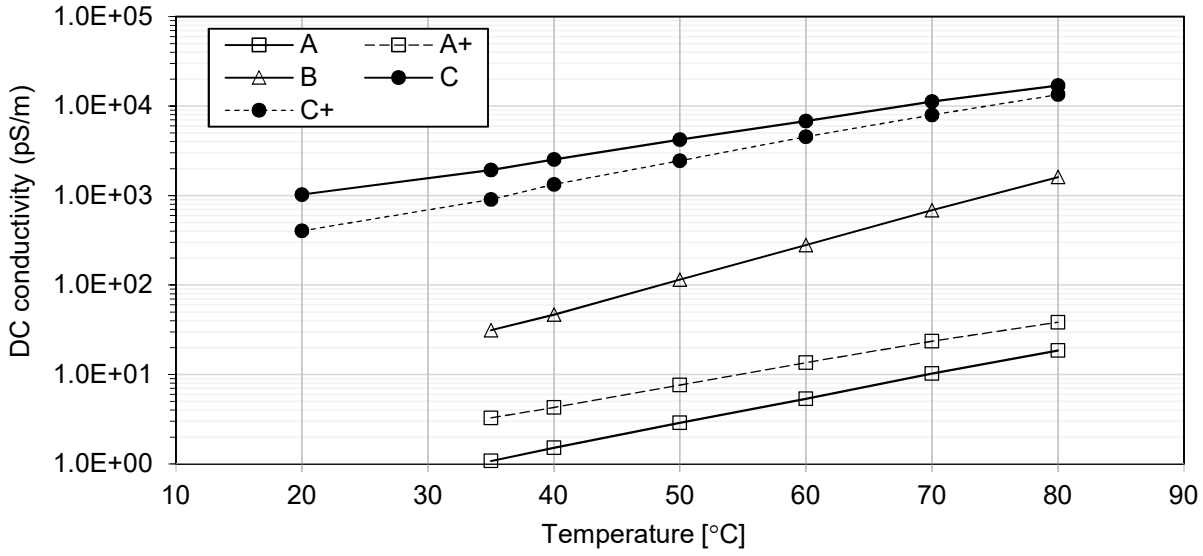

Figure 47. Variation of DC conductivity for lubricant samples measured as a function of temperature.

Table VI. Activation energy of lubricant samples.

Sample	A	A^+	B	C	C+
E_{DC} (eV)	0.25	0.22	0.35	0.18	0.24

5.2.4 Electric breakdown of lubricants

The electric AC breakdown strength of liquid oil Samples A, A+ and B was measured along with reference breakdown strength of transformer oil (Nytro Lyra X). The breakdown voltages are presented as root mean square (RMS) values of the voltage and the measurements were made at power frequency, 50 Hz. Due to the high viscosity of grease Sample C and D, it was not practically possible to fill the narrow gap (0.1 and 0.2 mm) of the test cell, thus making sure that no air bubbles were present and therefore breakdown tests were not performed. The mean values of breakdown voltages for the different samples along with their error bars indicating standard deviation are presented in Figure 48. The breakdown voltage of fresh but un-dried transformer oil was found to change linearly for the electrode distances. Sample A also shows a linear increase in breakdown voltage with gap distance. Sample B with nanoparticle additives show a higher breakdown strength than Sample A without additives.

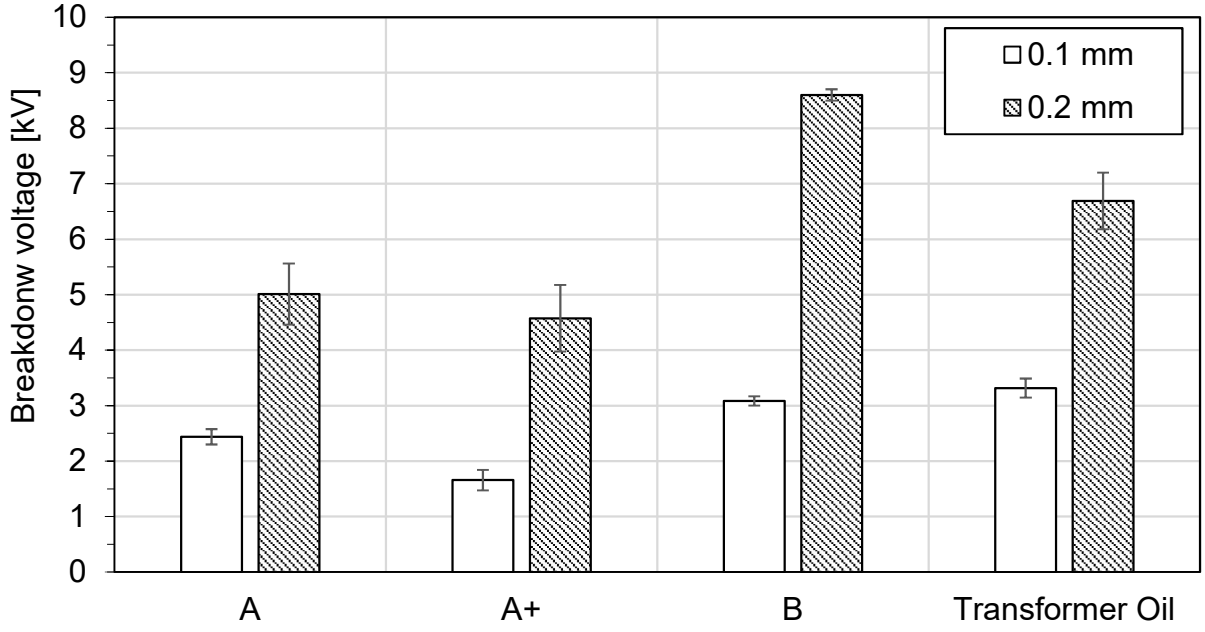

Figure 48. Breakdown voltage for liquid oil samples measured for short gaps of 0.1 and 0.2 mm.

The corresponding breakdown field strength of test samples is given in Table VII below. Breakdown field strength of Sample A is found to be approximately 25 kV/mm at gaps of 0.2 and 0.1 mm. On the other hand, breakdown field strength for run-in Sample A+ is found to reduce with gap distance, compared to fresh Sample A. The breakdown field strength is 22.8 kV/mm at 0.2 mm and 16.6 kV/mm at 0.1 mm. Sample B is found to have a slightly higher breakdown field strength compared to Sample A. The breakdown field strength is found reduce with gap distance and is found to be 43 kV/mm at 0.2 mm and 34.9 kV/mm at 0.1 mm. As a comparison, breakdown field strength of transformer oil was also investigated and found to be approximately 33.2 kV/mm at both 0.1 and 0.2 mm.

Table VII Breakdown field strength at gap distances of 0.1 and 0.2 mm

	Breakdown field strength at gap distance (kV/mm)	
Test sample	0.1 mm	0.2 mm
A	24.4	25.0
A+	16.6	22.8
B	34.9	43.0
Transformer oil	33.2	33.4

In literature, 50 Hz breakdown voltage of lubricants is reported to be around 15 kV/mm [27]. This data was recorded based on the ASTM Standard D 877 procedure in a statically bound condition and gap of 2.5 mm (6 kV/mm). The provided by lubricant manufacturer data are not reported for shorter gaps. It is however claimed that a thin lubricating film within a rotating bearing breaks down when the voltage across it exceeds about 30 V for a film of up to 2 μm [27, 36], which would correspond to a breakdown field strength of 15 kV/mm. It is also shown in literature review that breakdown voltage of lubricants varied up to 13 kV/mm [93] for gaps of 0.35 mm at 30 °C, while it drastically increased up to 25.4 kV/mm for shorter gaps. The summary of the electrical breakdown strength of three different types of greases is shown in the literature review part in Table II.

6 Bearing capacitance, C_B

The bearing impedance is evaluated when bearing is said to be insulating, which occurs only at low magnitudes of applied voltage and at operating points that provide adequate film thickness between tribological elements. The amplitude of applied sinusoidal voltage was kept at 0.5 V_{Peak} and was applied to the bearing at a frequency of 1 kHz and the corresponding current was measured using AWIS technique, elaborated in Chapter 4.3.1. Bearing capacitance, C_B and bearing resistance in insulating state, $R_{B,Ins.}$ are evaluated from the obtained measurements using steps discussed in equations (16) through (24).

Bearing capacitance of a bearing in running condition is assumed to be a function of bearing geometry, physical, chemical and material properties of individual bearing components and operating parameters. Analyses are first presented for bearing of type 608, followed by investigations to establish relation between the evaluation of the measured capacitance, film thickness and viscosity ratio for bearing type 22220.

6.1 Bearing type 608

The bearing was lubricated with lubricant Sample D, while the speed of the bearing is varied between 200 and 4000 rpm and the axial load is varied at 4 N and 40 N. In general, capacitance is found to be decreasing with an increasing in speed of the rotating bearing. The capacitance also slightly increases with an increase in load on the bearing. A stable value of capacitance is found at higher speeds of 1000 to 4000 rpm, shown in Figure 49. It corresponds to a bearing in full film regime for the bearing type, since the viscosity ratio at 40 °C is calculated to be 5.0 at 2000 rpm.

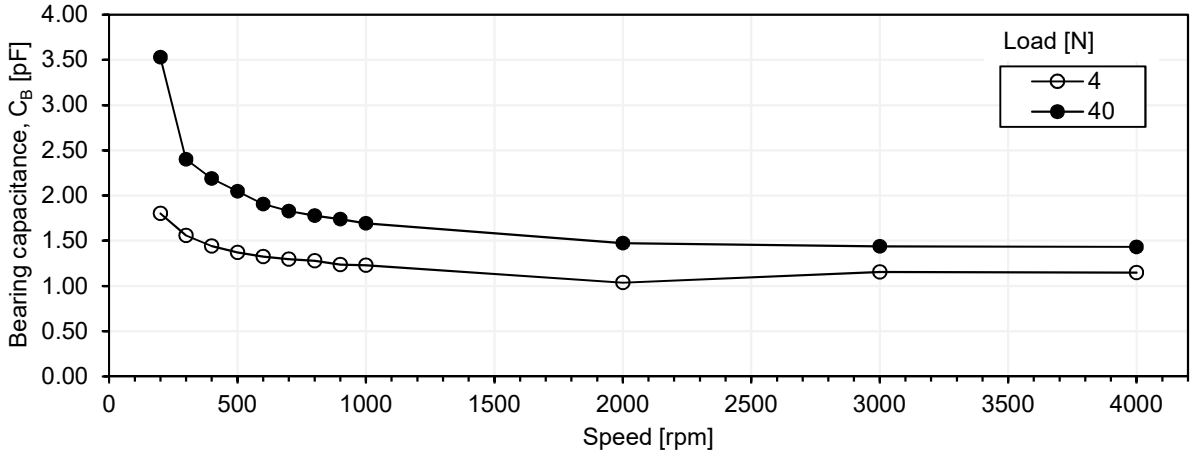

Figure 49. Bearing capacitance, C_B (in pF) evaluated at different operating points for a steel ball bearing of type 608 fitted with cage lubricated with Sample D. At lower speeds the lubricant film is not fully developed, which results in a thinner lubricating film and relatively unstable value of C_B.

Within the speed range of 2000 to 4000 rpm and at a load of 4 N, the mean value of C_B is evaluated to be 1.1 pF, whereas at a load of 40 N, the mean is found to be 1.4 pF. This mean is evaluated using average of the measured C_B at speeds of 2000, 3000 and 4000 rpm. It is also observed through these tests that at a given load, C_B reduces with an increase in speed (200 to 4000 rpm), while the calculated lubricant film thickness (h_c) increases with an increase in speed. As an example, at a

load of 4 N, the evaluated C_B and the calculated value of $(1/h_c)$ at 40 °C, have a direct positive correlation, with a value of coefficient equal to 0.96. Thus, under these conditions, C_B is found to be inversely proportional to h_c. At nominal speeds, C_B increases by about 30 %, as the axial load is increased from 4 to 40 N.

It is worth noting that the lubricating film thickness during operation is dependent on several parameters such as i) speed, ii) load, iii) material, iv) ratio of radii of interacting surfaces and v) the angle at which lubricant enters the loaded zone and is here evaluated using the formulation given in the EHL theory [41, 119]. As concluded by this theory, the lubricant film thickness is most influenced by the speed parameter, as can be seen from equations (16) and (17). Such considerations are always done with caution, since the material parameter is influenced by operation that in turn changes the load and the speed parameters.

However, between 200 and 1000 rpm, the test bearing is assumed to be in *boundary* or *mixed* lubrication regime, which corresponds to an evaluated film thickness of less than 0.5 µm. In this speed range the bearing is not in fully insulating state, resulting in appearance of frequent current pulses, but C_B is evaluated to range between 1.80 and 1.22 pF for an axial load of 4 N; and between 3.53 and 1.69 pF at axial load of 40 N.

6.1.1 Modified bearing type 608

To better understand the capacitive behaviour of bearing type 608, some of the steel balls were replaced by ceramic balls. With one steel ball and six ceramic balls, the mean value of C_B is evaluated to be 0.38 pF at axial load of 4 N for speeds above 1000 rpm. With two steel balls and five ceramic balls, mean value of C_B is evaluated to be 0.50 pF, while with four steel balls and three ceramic balls, C_B is evaluated to be 0.78 pF, shown in Figure 50.

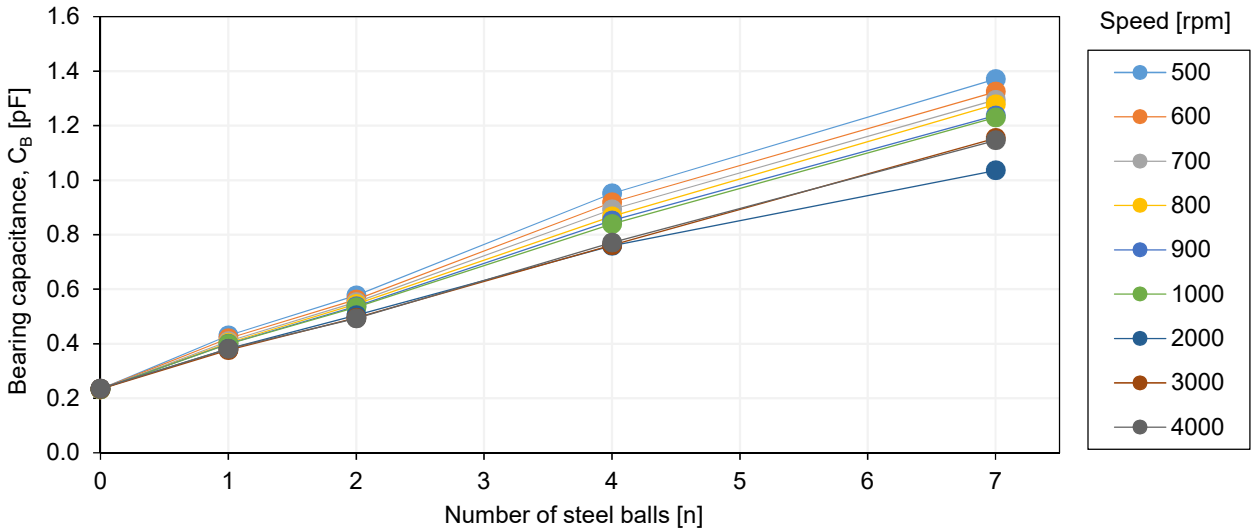

Figure 50. Bearing capacitance, C_B (in pF) increases linearly with respect to the number of steel balls in the bearing. An axial load of 4 N is applied.

At speeds higher than 500 rpm, as the number of steel balls in the bearing is increased, the bearing capacitance increases nearly linearly, as represented by equation (33),

$$C_B(n) = C_B(0) + \left(\frac{C_B(N) - C_B(0)}{N}\right) \cdot n, \quad (33)$$

where
$C_B(n)$ is the capacitance with n steel balls,
$C_B(0)$ is the total capacitance of a bearing with all ceramic balls,
N is equal to 7, the number of balls in bearing type 608 and
$C_B(N)$ is the total capacitance of a bearing with all steel balls.

The experimentally evaluated values of the capacitance are in good agreement with equation 33 and the percentage deviation between the two values is less than 9 %, when n = 1, 2 and 4.

6.2 Bearing type 22220

For bearing type 22220, a constant film thickness could be expected at a given range of operating conditions and temperature, hence the capacitance is measured when the bearing lubricant reaches steady state at the set temperature, Figure 51. The measurements are done at temperatures of 55±5 °C, since the temperature is maintained by an external water cooling mechanism. Once the measurement is completed, the operating parameter is changed and same procedure is repeated. The rotational speed of the bearing was varied between 400 and 800 rpm, while the mechanical load on the bearing was 10 kN.

The capacitance of a standard bearing 22220 lubricated with Sample A is found to decrease with an increase in speed. It is ranging from 4.1 nF at 400 rpm to 3.5 nF at 800 rpm, for a fixed mechanical load of 10 kN. The capacitance shows a step-wise decrease with an increase in speed of the bearing from 400 to 800 rpm in steps of 100 rpm. But as the speed is stabilising at a measurement point, the capacitance is found to be gradually increasing. It was found out in the above investigations that the bearing capacitance was more influenced by bearing temperature than the rotational speed of the bearing. An increase in rotational speed of the bearing from 400 to 800 rpm caused the lubricant temperature to steadily increase from ~52 °C to ~61 °C. The following comparison shows the increase in speed, lubricant temperature and the evaluated bearing capacitance all overlaid on the same graph. It is important to notice that the lubricant temperature initially increases from 52 °C and increases steadily as the speed is increased from 400 to 800 rpm in steps of 100 rpm. At 800 rpm, the lubricant temperature plateaus at 61 °C even as the rotational speed of the bearing is reduced back to 400 rpm, shown in Figure 51 and Figure 52.

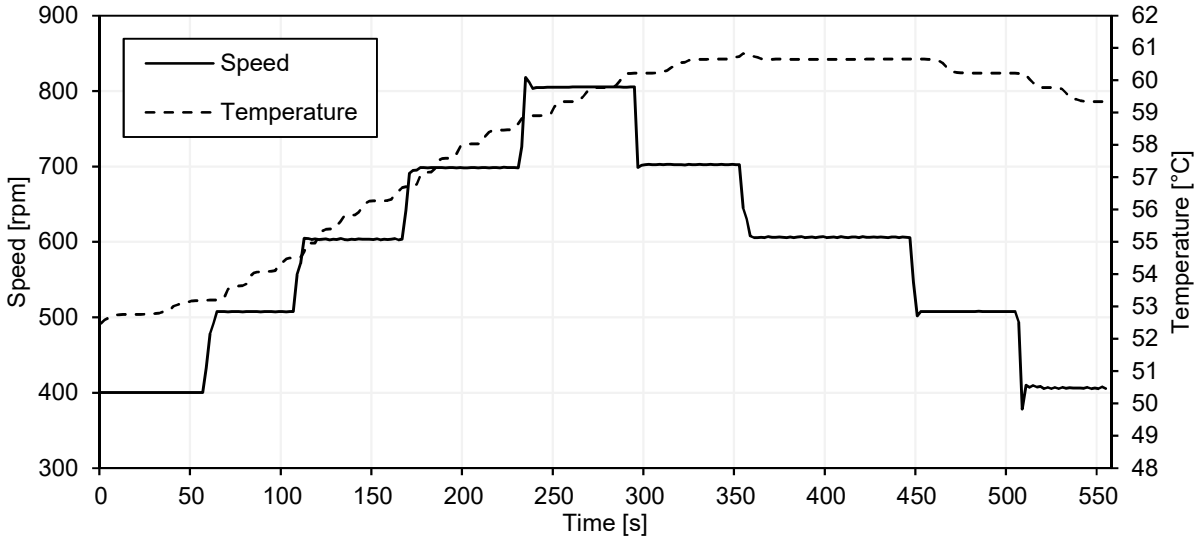

Figure 51. Temperature change at the outer ring of bearing type 22220 during step-wise increase and decrease of its speed. Mechanical load on the bearing is 10 kN. Time (in seconds) of the test is shown on x-axis.

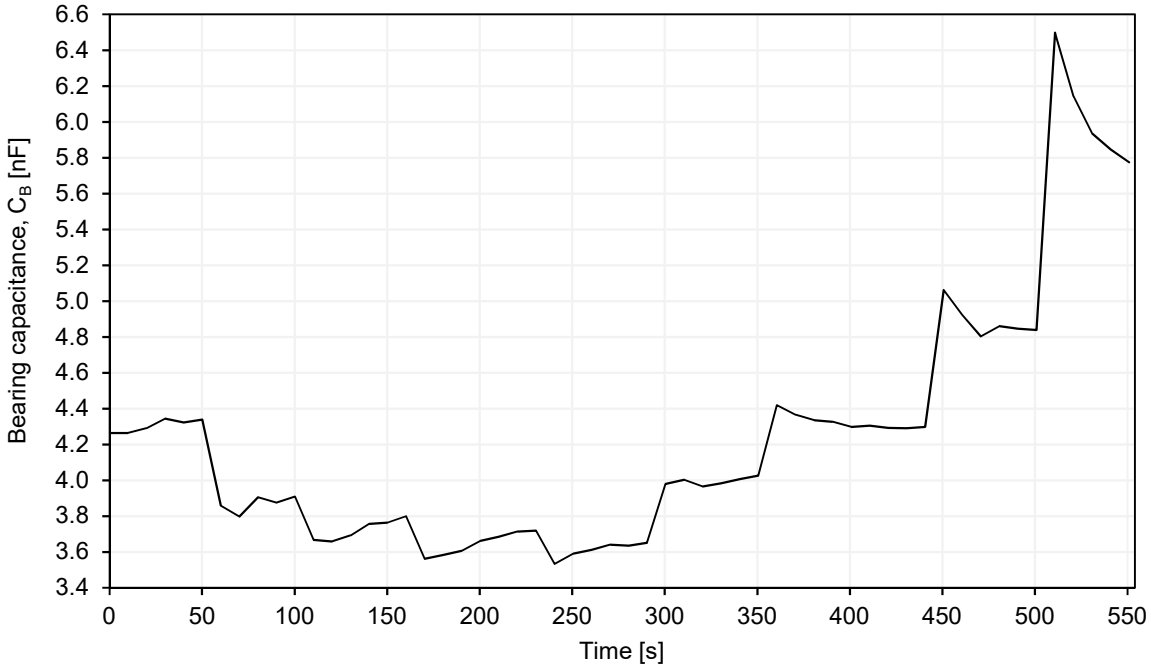

Figure 52. Changes in measured capacitance, C_B (in nF), of bearing type 22220 during the total measurement sequence presented in Figure 51.

The observed decrease in bearing capacitance is shown in Figure 53. The bearing capacitance is shown here as an average value during the operating point. The temperature of the bearing increased from 52.5 °C to 60 °C. Due to this change in temperature during operation, the total film thickness decreases from 0.67 µm to 0.53 µm as speed was increased from 400 to 800 rpm. The total film thickness is shown after multiplying with a scalar factor of 10 in Figure 53. At the same time, the calculated viscosity ratio increased from 2.4 to 3.5.

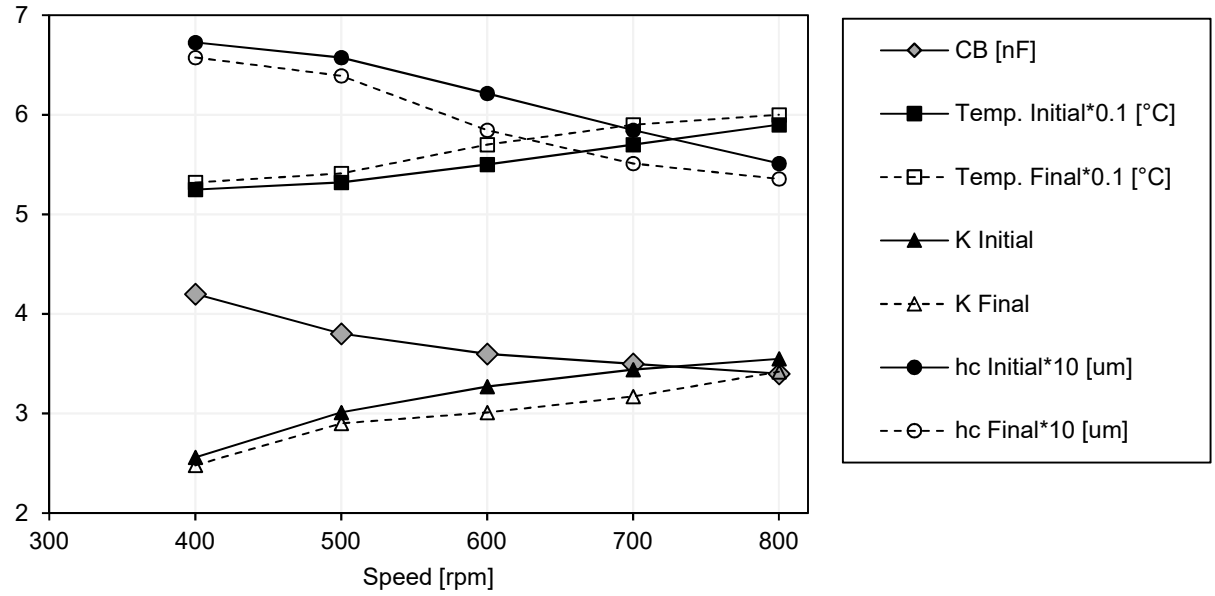

Figure 53. Change in evaluated parameters plotted as a function of increasing rotational speed from 400 to 800 rpm. The plotted parameters such as measured temperature (Temp., in °C) and calculated lubricant film thickness (h_c, in µm) have been scaled and are appropriately plotted in different units, as provided in the legend box. K (Kappa, κ) is the calculated viscosity ratio given by equation (10) at the given operating point.

In the test, after reaching a speed of 800 rpm, the speed was reduced in steps from 800 to 400 rpm, shown in Figure 54, but due to the operating conditions, the temperature stayed at about 60 °C. Due to the increase in operating temperature, the measured C_B increases from 3.4 nF to 6.0 nF. During this operating point, the calculated film thickness is around 0.53 µm, while the calculated viscosity ratio reduces from 3.55 to 1.91. The increase in C_B at constant temperature could be attributed to reduction in viscosity ratio due to shear thinning.

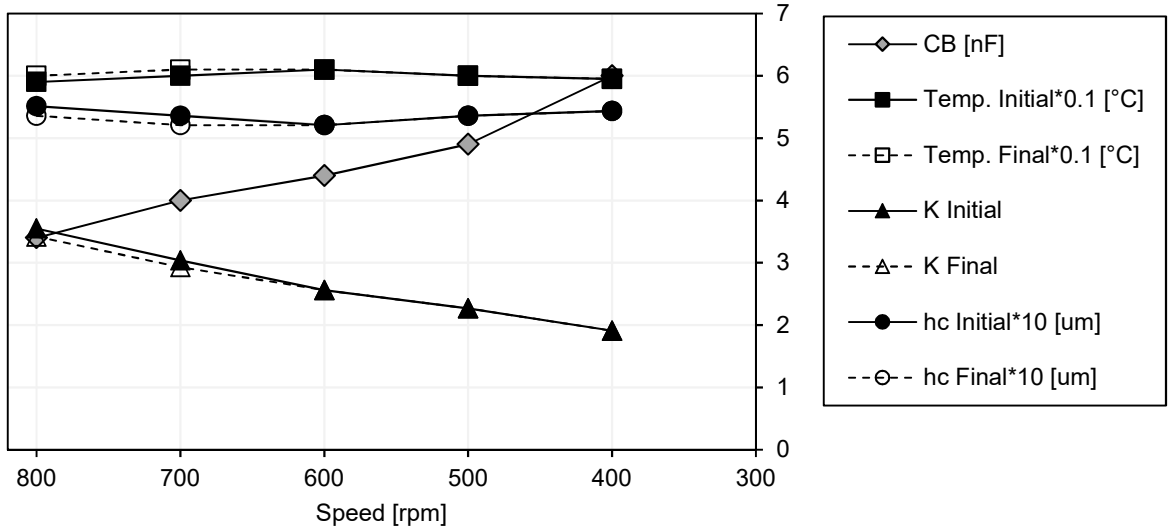

Figure 54. Change in evaluated parameters plotted as a function of decreasing rotational speed from 800 to 400 rpm. Parameters are shown after multiplying with a scalar factor to accommodate all information in the same figure.

The findings of investigations presented in Chapter 6 are summarised below:

1) The bearing can be electrically modelled as an equivalent circuit including a parallel branch of C_B and $R_{B,Ins.}$.
2) The analyses revealed dependence of the calculated values of C_B on the bearing operating point. A stable value of C_B was found once the bearing (of type 608) operated in EHL regime (above 1000 rpm).
3) C_B decreases with an increase in speed and decrease in load of the bearing. At lower rotational speeds, the film thickness is lower and results in higher bearing capacitance. Bearing capacitance has a relatively lower value at higher speeds due to formation of a thicker lubricating film around the rolling elements. This is under the assumption that the changes in temperature inside the bearing negligible. In larger bearing the temperature has a significant effect and the changes in the measured capacitance and film thickness is more pronounced.
4) The relation between C_B and the calculated film thickness (h_c) is almost inversely proportional, having a direct positive correlation of 0.96.
5) The decrease in capacitance with number of ceramic balls suggest that the total capacitance in between the inner and outer ring of the bearing consists of individual ball capacitances connected in parallel to each other.
6) For bearing type 22220, C_B is found to decrease with an increase in speed of the bearing.
7) At a fixed speed, load of operation results in steady increase of lubricant temperature. The monitoring of capacitance of bearing type 22220 has also shown that at a given operating point its capacitance is temperature dependent. As the temperature increases, the capacitance tends to increase.

7 Bearing resistance in insulating state, $R_{B,Ins.}$

In the equivalent circuit model, the bearing resistance in insulating state, $R_{B,Ins.}$ represents all types of losses in the bearing. $R_{B,Ins.}$ is characterised when the bearing is in insulating state and can conveniently be evaluated based on measurements of the dielectric dissipation factor (tanδ). In the parallel representation of the proposed equivalent electric circuit model, tanδ can be expressed as $1/\omega\, R_{B,Ins.}C_B$.

The AWIS measurements are performed using a sinusoidal voltage of 0.5 and 1 V_{p-p} applied at 1 kHz. The lubricant in a running bearing is not a typical dielectric, due to the large variation in temperature and pressure during its operation. The occurrence of frequent asperity contact at lower speeds also increases frictional heating and hence increases temperature in the contact zone and the surrounding dielectric, accompanied with a flow of higher resistive current.

7.1 Bearing type 608

The speed of the bearing was varied between 200 and 4000 rpm, while the load on it varied at 4 and 40 N. The bearing was lubricated with Sample D. The respective variation of the lubricant film thickness is shown in Figure 36. The value of tanδ at 1 kHz is found to be rather constant over the whole speed range and ranges between $37 \cdot 10^{-2}$ and $40 \cdot 10^{-2}$ up to the speed of 4000 rpm, which means that the current in the capacitive branch could be 2.5 times larger than in the resistive branch. Thus, effect of $R_{B,Ins.}$ cannot be excluded in the electrical circuit model of a bearing in insulating state. At speeds lower than 500 rpm, rather larger values of tanδ (temporary maximum value of approximately 0.8) were recorded at both loads of 4 and 40 N and are assumed to result from frequent asperity contacts, which is manifested through a flow of larger resistive current. Asperity contacts at very low speed of 200 rpm could increase the bearing temperature by a few degrees. Higher temperature in the dielectric could also result in increase in electrical conductivity of the insulation medium and hence in higher tanδ. When the bearing is in insulating state, stabilised average value of tanδ is found to be $40 \cdot 10^{-2}$, which is significantly higher than in conventional dielectric medium. This level of dielectric dissipation factor was also reported for bearing lubricants in [93].

As load on the bearing is increased from 4 to 40 N, tanδ increases slightly by 5 %. A higher load is accompanied with an increase in pressure in the lubricating film, hence increasing temperature at the interface of the solid and the lubricant. During operation, the measured tanδ is significantly larger in comparison to the summation of losses reported for each component in the bearing separately, such as the lubricant itself as well as for the cage material and bearing materials.

In a separate test by use of FDS, the value of tanδ in the lubricant Sample D at 50 °C, measured at 1 kHz is $1.15 \cdot 10^{-2}$. In literature, tanδ in the cage material is reported to be 0.2 at 100 Hz, at 75 °C [120, 121] and increases significantly (up to 0.9) at higher temperatures. The increase in the dielectric loss factor could be credited to operating conditions, which bring about changes in distance in between the bearing surfaces which act as electrodes during the measurements. The operating condition may also create localised high temperature conditions during bearing operation on lubricant and hence would explain high values of tanδ. The ionic current flow could be amplified due to temperature increase and local electrical field enhancements due to nano and micro-asperities.

A stable value of $R_{B,Ins.}$is evaluated at nominal speeds, i.e., at speeds higher than 2000 rpm, as seen in Figure 55. For a bearing with all steel balls, at an axial load of 4 N, $R_{B,Ins.}$ has a mean value of 368 MΩ. At an axial load of 40 N, $R_{B,Ins.}$ has a lower mean value of 278 MΩ. It is observed that at a given load, as the speed increases, $R_{B,Ins.}$ increases gradually to attain a stable value. As an example at load of 4 N, it was seen that if the speed of the bearing is increased from 200 to 4000 rpm, the value of $R_{B,Ins.}$ increased from 0.8 MΩ to 350 MΩ. The change in $R_{B,Ins.}$ is more pronounced at lower speeds and relatively less at higher speeds, which is attributed to a more stable lubricating film.

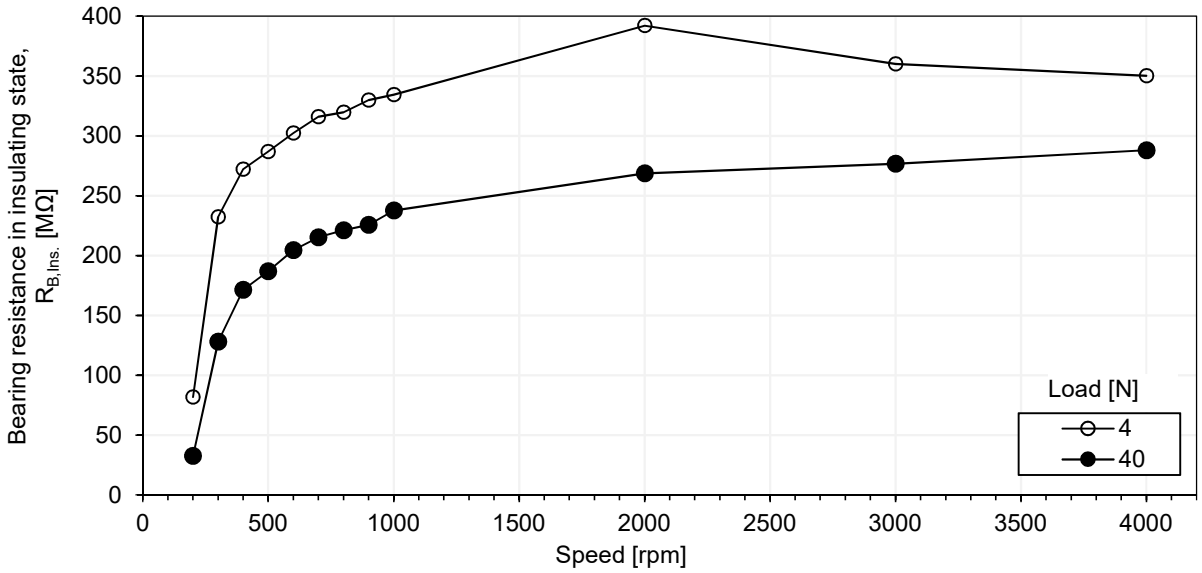

Figure 55. Bearing resistance in insulating state, $R_{B,ins}$. (in MΩ) evaluated for bearing type 608. The evaluated values are rather stable at speeds greater than 2000 rpm, measured at frequency of 1 kHz.

7.1.1 Modified bearing type 608

If steel balls are replaced by silicon nitride ceramic balls, the value of $R_{B,Ins.}$ also increases significantly. The value of $R_{B,Ins.}$ decreases with the number of the remaining metallic balls in the modified test bearing, as shown in Figure 56.

At speeds higher than 1000 rpm, with n number of steel balls in the bearing, the bearing resistance in insulating state can be approximated by equation (34),

$$R_{B,Ins.}(n) \approx \frac{N \cdot R_{B,Ins.}(N) \cdot R_{B,Ins.}(0)}{n \cdot R_{B,Ins.}(0) + (N-n) \cdot R_{B,Ins.}(N)}, \quad (34)$$

where

$R_{B,Ins.}(n)$	is the modelled resistance with n steel balls,
$R_{B,Ins.}(0)$	is the total resistance of a bearing with all ceramic balls,
N	is equal to 7, the number of balls in SKF bearing 608 and
$R_{B,Ins.}(N)$	is the total resistance of a bearing with all steel balls.

The modelled and the experimentally evaluated values are in good agreement and the percentage deviation between the two values is less than 10 %, when n = 1, 2 and 4.

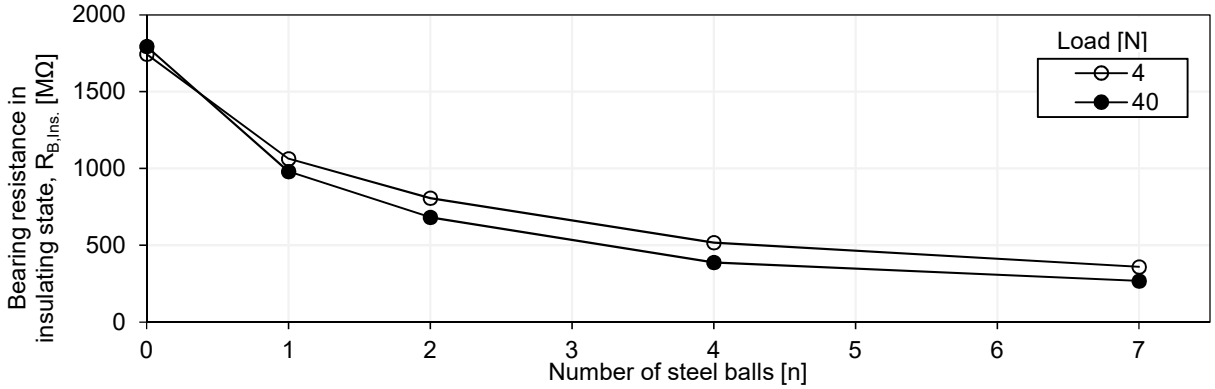

Figure 56. The bearing resistance in insulating state, $R_{B,Ins.}$ (in MΩ) decreases with number of steel balls in the modified test bearing.

7.2 Bearing type 22220

Spherical rolling element bearing of type 22220 with cylindrical and tapered bores is lubricated by immersing in an oil bath with Sample A. The testing procedure involves step-wise speed increment at a fixed load setting. The rotational speed is step wise increased from 400 rpm to 800 rpm in steps of 100 rpm, while the load is fixed at 10 kN. Each step lasts at least 50 s, but does not exceeds 100 s. After attaining speed of 800 rpm, the speed is stepwise decreased by 100 rpm down to attain 400 rpm, shown in Figure 57.

The measured bearing resistance in insulating state ($R_{B,Ins.}$) is shown in Figure 58. Tanδ of the bearing is found to become higher values when the speed of the bearing is stepwise increased, shown in Figure 59. After the momentary increase, it tends to stabilise once the speed is constant. Tanδ for this bearing at speeds of 400 rpm is $3.4 \cdot 10^{-2}$. As the speed is increased to 800 rpm in steps of 100 rpm, tanδ reaches value of $2.47 \cdot 10^{-2}$. After stabilising, the mean value of tanδ more than doubles, reaching $7.24 \cdot 10^{-2}$ at 600 rpm and, as the speed is decreased from 600 to 500 rpm, the mean value of tanδ again doubles to $13.55 \cdot 10^{-2}$. Same pattern is repeated when the speed is decreased from 500 to 400 rpm, mean value of tanδ is found to be $29.43 \cdot 10^{-2}$. The peak value of tanδ is found to be $38 \cdot 10^{-2}$ and is significantly higher than that of conventional dielectric medium. This implies that at the measured frequency of 1 kHz, current in the capacitive branch (C_B) could be as much as 2.6 times larger than the current in the resistive branch ($R_{B,Ins}$). The peak value of tanδ was found when the bearing attained temperature of 61 °C during the test. This indicates that losses in bearing type 22220 could origin from frictional losses, resulting in lubricant temperature increment.

It should be noted that for thin film of insulating liquids (30 µm) tanδ as high as $2 \cdot 10^{-2}$ have been reported [119]. The high pressure and temperature conditions during operation could also temporarily cause changes in phase, viscosity and structure of the lubricant and hence possibly explain rather higher values of tanδ compared to the dielectric properties of same lubricant in a statically bound condition. Under high pressure, the oil in the hydrodynamic contact area could transfer into a glassy state. At extremely high electric field strengths (greater than $2 \cdot 10^8$ V/m), the charge injection could also occur, due to Fowler-Nordheim (FN) injection at the metal-liquid interface.

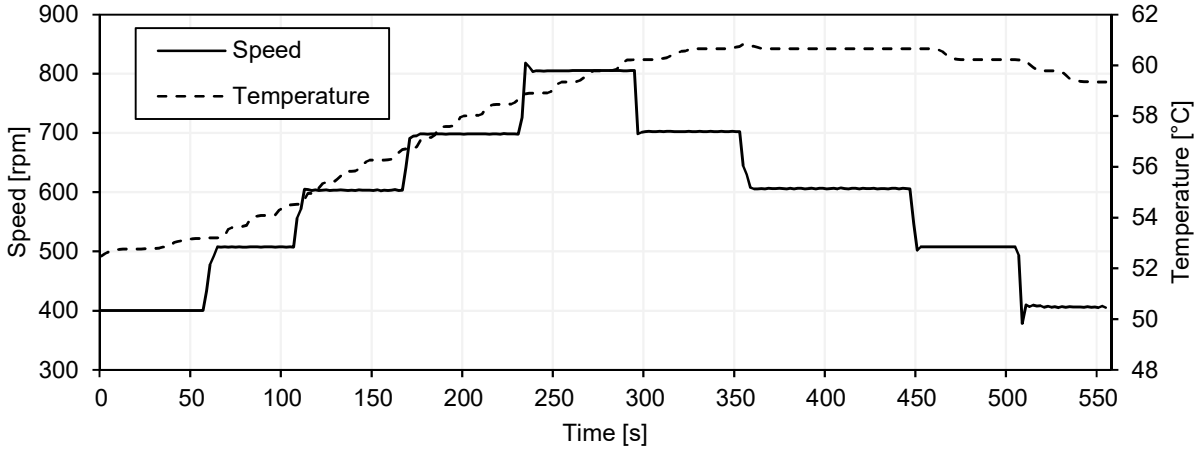

Figure 57. Changes in speed and the corresponding change in temperature of bearing type 22220 (measured at outer ring of the bearing).

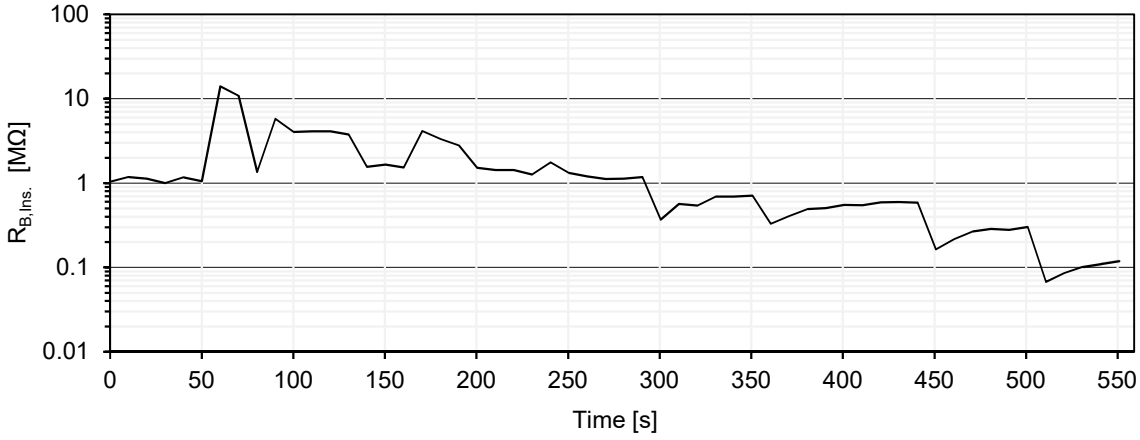

Figure 58. Bearing resistance in insulating state, $R_{B,Ins.}$ (in MΩ) of bearing type 22220 at different operating points. $R_{B,Ins.}$ is plotted on a log scale to indicate its subtle changes with respect to speed.

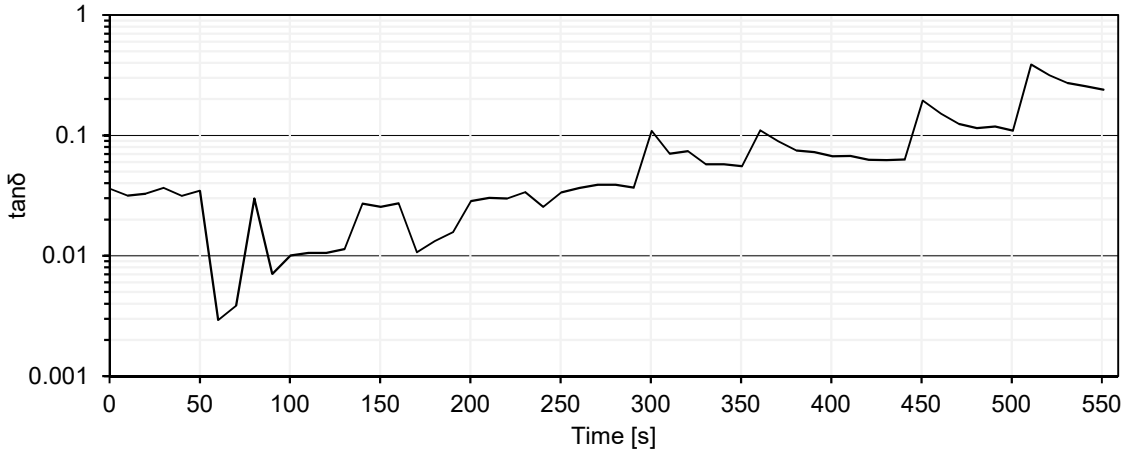

Figure 59. Dissipation factor of bearing type 22220 at the different operating points shown on a log scale.

Findings of the investigations presented in Chapter 7 can be summarised as follows:

1) C_B and $R_{B,Ins.}$ levels depend on the dimension of the dielectric lubricating film between the rolling elements. The performed analysis showed the dependence of the calculated value of $R_{B,Ins.}$ on the bearing operating point.
2) A large value of $R_{B,Ins.}$ indicate that the lubricating oil is electrically insulating, whereas ageing of oil or presence of inclusion particles and debris reduces this resistance and thus yields an increased level of the dissipation factor.
3) In running conditions, the current flowing through C_B could be 2.5 times higher than the current in $R_{B,Ins.}$ for bearing type 608, whereas it could be 2.6 times higher in case of bearing type 22220. This implies that while electrically modelling a running bearing in insulating state, the equivalent circuit must consist of C_B in parallel with $R_{B,Ins.}$.
4) A stable value of $R_{B,Ins.}$ is found in EHL regime. For the bearing of type 608 the stable value of $R_{B,Ins.}$ is measured once it operates above 600 to 800 rpm.
5) The character of bearing resistance change with number of steel balls suggest that it does not consists of individual resistances between the raceways. $R_{B,Ins.}$ does not scale linearly with increase in number of steel balls. On the other hand, dissipation factor tanδ of a running bearing is found to be significantly higher than that of the lubricant measured under statically bound conditions. Both of these trends could be credited to the dynamic motion of a running bearing and thus the resulting changes in electrode setup (high voltage and ground corresponding to inner and outer raceways).
6) Continuous monitoring of $R_{B,Ins}$ of bearing type 22220 has shown that at a given operating point, as the temperature increases, the bearing resistance tends to decrease, indicating higher dielectric losses. A step-wise change in speed results in step-wise change of $R_{B,Ins}$.
7) An increase in bearing speed results in a steady increase of lubricant temperature. If the speed is thereafter reduced, the measured value of $R_{B,Ins.}$ does not match the initial one, indicating that a standardised testing procedure should be developed and followed in such measurements.

8 Insulation breakdown analysis

The physical mechanisms causing insulation breakdown in bearings are investigated here by studying number of breakdown events and their duration under switching conditions. The breakdown of electrical insulation of the bearing can occur due to several plausible physical phenomena, out of which three will be discussed here, namely 1) insulation breakdowns due to asperity contacts, 2) particle-initiated insulation breakdowns and 3) electric field dependent breakdown. To discuss the mechanisms leading to breakdown in the bearing, we first define in Chapter 8.1 the features of the switching patterns used in the investigations. Thereafter switching pattern analyses of pre-lubricated unmodified bearing are presented in Chapter 8.2. Bearing of type 608 was predominantly used in these experiments, unless otherwise stated. Focus was kept on variation in operating points, applied voltages, types of voltage wave shapes etc. All the bearings were run-in before the tests.

Breakdown of bearing insulation due to asperity contacts is observable at lower speeds. Frequent metal to metal contact yields electrical discharges, wear in the bearing and rise in its temperature. During the investigations of the asperity contacts related breakdowns, the applied voltage was kept below the inception voltage of bearing current activity, while focus was given to lower rotational speeds. The results are discussed in Chapter 8.3.

If the bearing operates at high speed and a uniform film is formed across the rollers, presence contamination particles, wear debris etc., will cause discharges, which intensity is a function of the particle concentration, particle size, particle hardness and possibly their conducting nature. The investigations of particle-initiated breakdowns were thus conducted at high rotational speeds, where the bearing is normally found to be in insulating state. Successive tests with different particle types and concentrations in the test lubricant were conducted. Details of these investigations are presented in Chapter 8.4.

If high enough voltage (electric field) is applied to the bearing, the breakdown occurs in a very narrow window of voltage increment and it dependent on the lubricant film thickness. For these investigations a new bearing was lubricated with clean and fresh sample. The bearing ran at a high speed, which ensured adequate film thickness around the rollers, while voltage was gradually increased and the bearing current activity was monitored. The results are discussed in Chapter 8.5.

8.1 Electrical characteristics of switching pattern

Breakdown events of the lubricating film were investigated by studying current discharge characteristics during the above defined conditions by varying bearing operating point and applied voltage level. An increase in the applied voltage across the bearing (bearing voltage, V_B) above a certain level causes a partial breakdown of the lubricant film at voltage level, which is said to be inception voltage level ($V_{Inception}$).

In our analyses, the apparent electrical field strength (E or $E_{Apparent}$) in the lubricant is defined as the ratio between bearing voltage and lubricant film thickness

$$\mathrm{E\ or\ E}_{Apparent}(\mathrm{in\ V/\mu m}) = \frac{V_B}{h_{c,inner}+h_{c,outer}} \tag{35}$$

The analyses of bearing switching pattern can be performed in different ways. One of them involves defining the inception voltage at which the bearing current activity starts, the duration of current pulses and the time between the pulses. The apparent electric field at which the bearing current activity initiates and the percentage of time the bearing is found to be in the conducting state are other ways to describe the phenomenon.

The change in electrical nature of the bearing i.e., transition from high impedance state to a low resistive state is investigated by evaluating the percentage of time for which the bearing behaves resistively at a set voltage level V_B, given by equation (25). If V_B is gradually increased, the number of discharge events increases and reaches $V_{10\%ToC}$, where the bearing is conducting for 10 % of the time. This voltage level is associated with initiation of transition from insulating to conducting state. Similarly, the voltage level at which the bearing is in conducting state for about half of the time of test is termed as $V_{50\%ToC}$. At higher bearing voltages, the bearing will reach a critical voltage level ($V_{90\%ToC}$), during which the bearing is conducting for 90 % of the time. The breakdown of lubricating film can hence be elucidated by means of the following parameters associated with the discharge events:

- Inception voltage measurement
- Breakdown/conduction voltage levels $V_{10\%ToC}$ and $V_{90\%ToC}$
- Apparent electrical field strength between raceways of the bearing ($E_{10\%ToC}$ and $E_{90\%ToC}$)
- Duration of discharges
- Time between discharges
- Number of discharges occurring per second
- Time of Conduction, ToC

8.2 Study of insulation breakdowns in an unmodified bearing

A pre-lubricated with Sample E bearing of type 608 was chosen in these experiments. Sample E is a grease with corrosion and rust inhibitors. No additional lubrication was applied to the bearing. The operating point was set at a speed of 3000 rpm and load of 4 N. A DC voltage of up to 8 V was applied to the bearing in a stepwise increasing manner, where each step was of 1 V and lasted for about 10 s. As the electric field strength in the lubricating film exceeds the breakdown field strength, bearing quickly makes a transition from insulating to conducting state, resulting in initiation of bearing current activity, Figure 60. At certain voltage level a current activity starts and it is marked as inception voltage ($V_{Inception}$). On the other hand, if reducing the amplitude of voltage across the bearing, the bearing current activity stops at a certain voltage, which is henceforth referred as extinction voltage ($V_{Extinction}$) of bearing current activity.

The amplitude of the current pulse trace is controlled by the limiting resistance in the circuit. It is seen that the lubricating film repeatedly loses and recovers its insulating properties, indicating that the breakdown is a temporary event and does not present an irreversible feature.

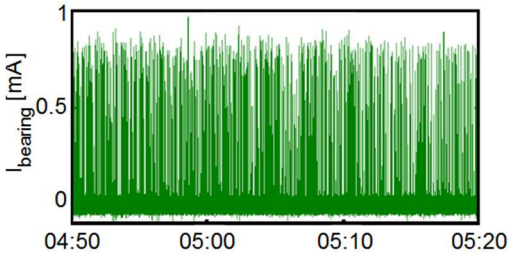

Figure 60. Current pulse trace recorded over 30 s when a voltage of 8 V was applied to a pre-lubricated bearing of type 608 running at 3000 rpm and axial load of 4 N. The x-axis shows time in minutes, indicating time passing from the commencement of test.

To study an individual breakdown phenomenon in the bearing, a high bandwidth oscilloscope with sampling rate of 2.5 GS/s was used. The breakdown event is temporary and the voltage across the bearing recovers shortly before occurrence of a second breakdown event. The applied voltage is 2 V, while the current amplitude momentarily reaches in oscillations a peak value of 8 mA before stabilizing at around 3 mA limited by the resistors in the circuit. The duration of breakdown and time between the successive discharges (Δt) are shown in Figure 61.

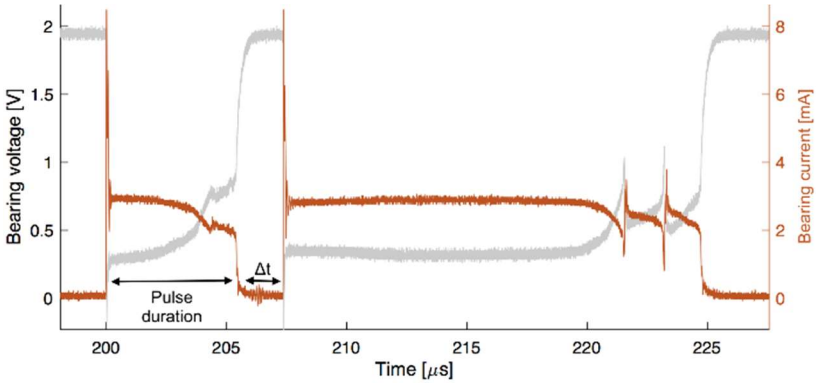

Figure 61. Bearing voltage (grey) and bearing current (orange). The figure shows pulse duration and time between two immediate pulses, denoted by Δt.

8.2.1 Study of discharge events and current pattern analyses

In case the applied voltage is near the inception voltage of bearing current activity, the number of discharges will be few. This will be accompanied by current pulses of very small durations and larger times in between successive current pulses. As the applied voltage is increased, the number of discharge current pulses will increase and will be accompanied with longer duration pulses. This section investigates the relation between the number of discharges and the current pattern analyses in bearing of type 608.

The DC voltage applied across the bearing (V_B) was set at four different levels (4.0 V, 6.6 V, 7.9 V and 10.6 V). AA batteries connected in series were used for this purpose. The rotational speed varied at 3000, 2000 and 1000 rpm, and the mechanical load was 4 N and 40 N.

The data obtained for duration of discharges (pulse duration) and time between discharges are shown using frequency distributions. The bin size of the distributions is taken by the smallest value of time in the measurement, thereby the distributions represent all the data, including the smallest value of the measured time. To make the results comparable, they are presented in number of

lubricant film breakdowns (or discharges) per second. The x-axis on these plots shows the time-related information of the discharge current, such as time between discharges and duration of discharges in micro-seconds. The values on y-axis represents the number of times per second the above-mentioned time durations are recorded. Each measurement was carried out for a window of 30 seconds.

The data for the bearing operated at rotational speed of 3000 rpm and mechanical load of 4 N are shown in Figure 62. Up on application of 4 V across the bearing at this operating point, the resultant electric field strength between the inner and the outer raceway of the bearing is calculated to be 11.5 V/µm (equation (35)). This results in a few discharges during the measurement window (once in every 4 or 5 second, shown in Figure 62, top left plot. The duration of discharges ranges up to 20 µs, as shown in Figure 63. The mechanisms of these discharges are not discussed as a part of the analyses. However, as is stated in [84, 122], for appearance of electrostatic discharge current in bearing, the film thickness needs to be higher than 0.1 µm and the applied electric field should be in a range of 20 V/µm to 50 V/µm. It is also mentioned in [84] that the occurrence of discharges below electric field strength of 30 V/µm is sporadic.

As the applied voltage was increased to 6.6 V, the electric field strength in bearing lubricant film increased to 19.0 V/µm. This field strength, close to 20.0 V/µm resulted in occurrence of a larger number of discharges, though the probability of harmful discharge events is still at electric field strength below 30 V/µm and at a temperature of 20 °C quite low [84]. In experiments conducted in current thesis, the damages were avoided due to introduction of current limiting resistor. The time between these discharges is up to ~100 µs and they last up to ~25 µs. At this electric field strength, the number of discharges is in the order of 10^3 s^{-1}, which is in accordance with findings of Tischmacher [84]. The results are shown in top right plots of Figure 62 and Figure 63 respectively.

When the applied voltage was increased to 7.9 V, the resultant electric field in the lubricant film was evaluated to be 22.7 V/µm. The increment in electric field strength in the lubricant film from 19.0 V/µm to 22.7 V/µm almost doubled the number of discharges per second. The time between discharges on the other hand had reduced to half, while their duration has not altered much. This is shown in bottom left plots of Figure 62 and Figure 63.

Finally, when the voltage across the bearing was set to 10.6 V, the resultant electric field strength in the lubricating film was 30.5 V/µm. This increment of the electric field in the lubricant resulted in reduction of the time between discharges by one order of magnitude, while on the other hand the duration of discharges has increased drastically by more than two orders of magnitude. The time between discharges drastically reduces from a few seconds (ranging up to 4 s) at applied electrical field strength of 11.5 V/µm to only a few microseconds (ranging up to 14 µs), when electrical field was 30.5 V/µm. There were altogether up to 4000 discharge events per second.

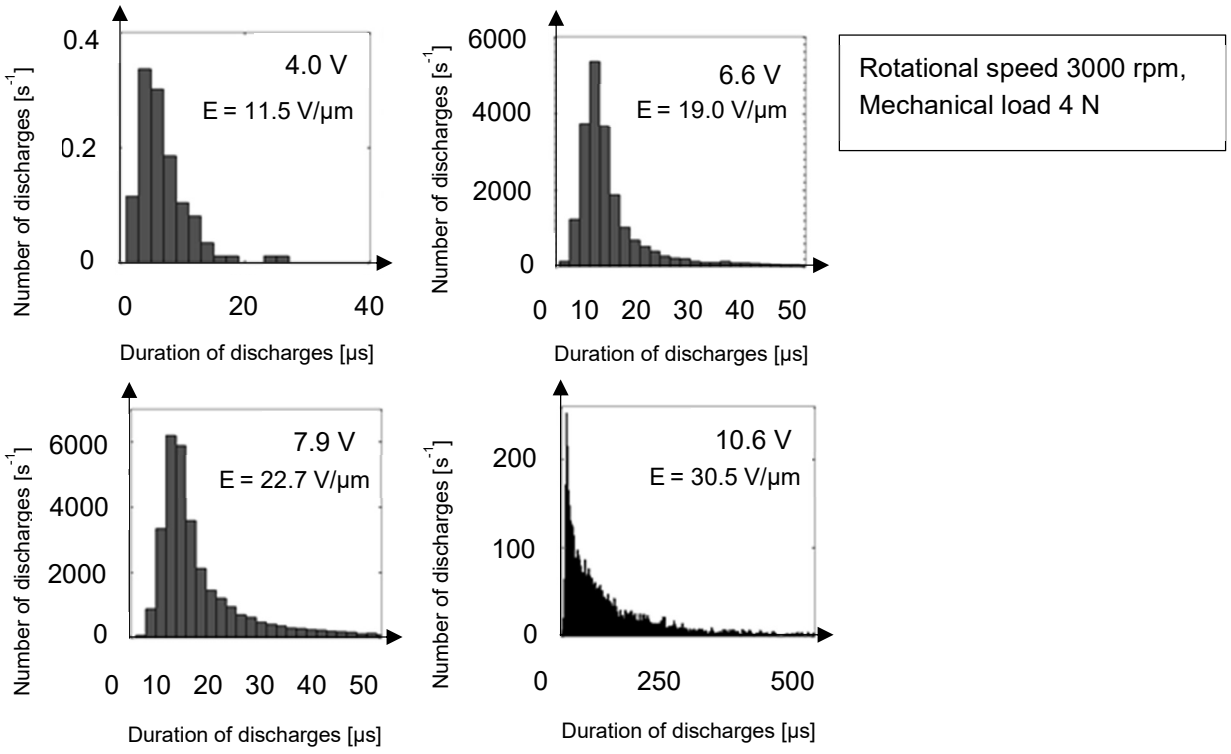

Figure 62. Duration of discharges (pulse duration) at rotational speed of 3000 rpm and mechanical load of 4 N for different bearing voltages.

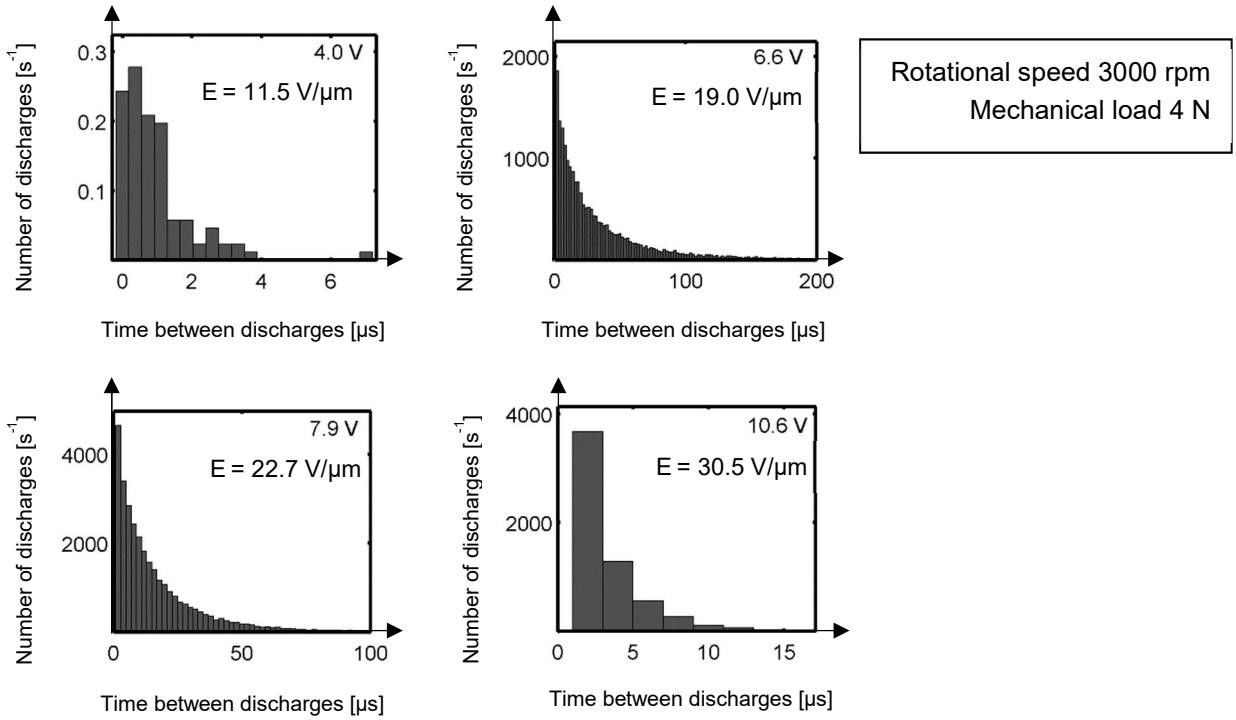

Figure 63. Time between discharges (Δt) at rotational speed of 3000 rpm and at mechanical load of 4 N for different bearing voltages.

A reduction in rotational speed of the bearing results in lower film thickness, thus yielding asperity contacts bearing the load. This may also result in an increase in lubricant temperature along with reduction in its viscosity. The reduction in film thickness of the lubricant is thus accompanied by more frequent discharge current events.

The discharge activity at rotational speed of 2000 rpm and mechanical load of 4 N is discussed next. On application of 4.0 V across the bearing at this operating point, the resultant electric field strength between the inner and the outer raceway of the bearing is calculated to be 15.1 V/µm. This is accompanied by more frequent flow of discharge current for a longer duration. The time between discharges range up to 50 µs and the duration of the discharges range up to 600 µs. The maximum number of discharges are around 7500 s^{-1} (shown in top left of Figure 64 and Figure 65). There is a steep increase in number of discharges at 2000 rpm compared to 3000 rpm.

As the applied voltage is increased to 6.6 V, the electric field strength in bearing lubricant film has increased to 24.8 V/µm. The time between these discharges is very short (below 10 µs) and the duration of discharges last from 10^3 to 10^4 µs. At this electric field strength, the number of discharges are 10^2 s^{-1}, indicating discharge current with long durations and short times between consecutive discharges. The lubricating film breaks down and recovers for a short time, which is again followed by discharge event. The distribution of the discharges is shown in top right plot of Figure 64 and Figure 65.

When the applied voltage is increased beyond 7.9 V, the resultant electric field in the lubricant film is evaluated to be 29.7 V/µm or higher. The increment of electric field strength across the lubricant makes the bearing to enter the resistive mode, i.e. it is in a full breakdown mode. The bearing mostly stays in conducting state, with 500 discharge events per second and the time of transition between the two states (Δt) is less than 6 to 8 µs. The state of the bearing is characterised by long discharge events, while recovery of the insulating properties of the lubricating film of the bearing is hardly seen. Thus, number of discharges are less in number (up to 100) and the duration of individual discharge has increased up to 15 ms, bottom left plot in Figure 65. Plots on bottom part show bearing in mostly conducting state, where the lubricating film of the bearing does not recover its insulating properties between discharges.

When mechanical load of 40 N is applied, the duration of discharges increases by one order of magnitude compared to duration discharges at 4 N. Distributions of discharge activity at mechanical load of 40 N and rotational speeds of 3000 and 2000 rpm are not shown here, but results on a broad scale are shown in Table VIII. At rotational speed of 1000 rpm, the bearing is in full breakdown mode and the discharge current flows through the bearing continuously. The discharges in the bearing at speed of 1000 rpm occur much more frequent and last longer even at lower electric field strengths, as compared to those observed at higher rotational speeds of 2000 and 3000 rpm.

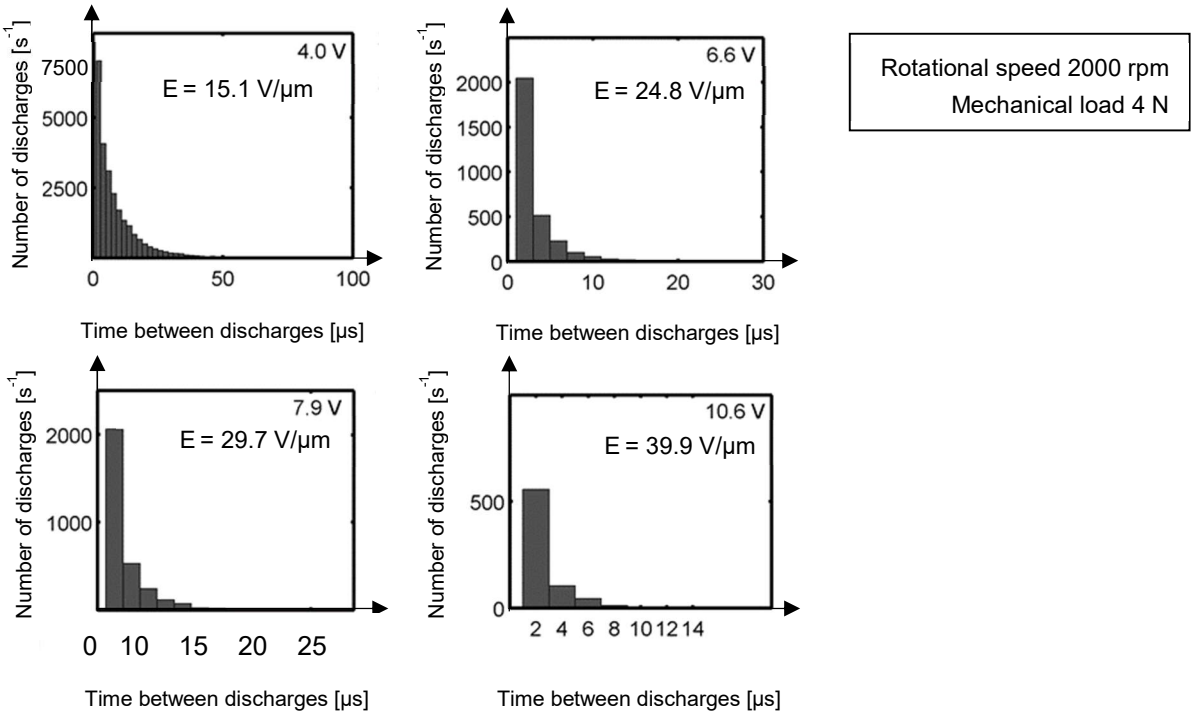

Figure 64. Time between discharges (Δt) for rotational speed of 2000 rpm at load of 4 N for different bearing voltages.

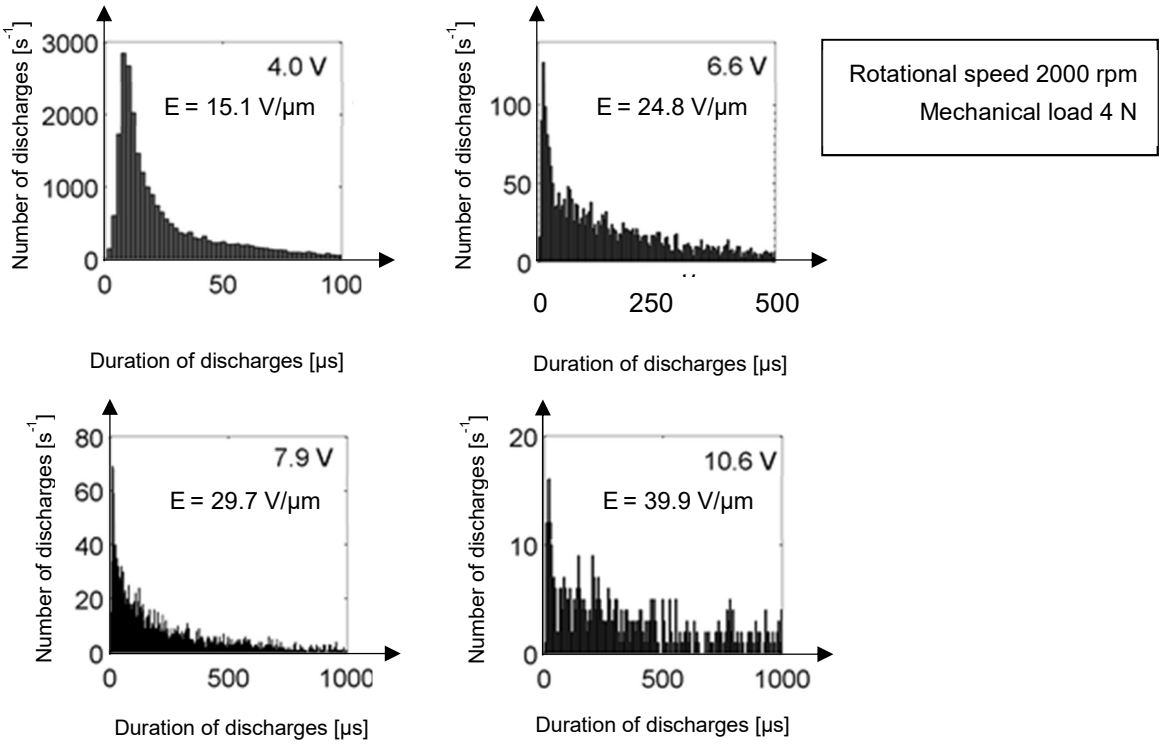

Figure 65. Duration of discharges at rotational speeds of 2000 rpm and constant load of 4 N, for different bearing voltages.

The following are the findings from the performed tests:

1) The bearing discharge activity at a high rotational speed (3000 rpm) is much less as compared to lower speeds (2000 and 1000 rpm), indicating the capability of forming thicker lubricant film and withstanding the applied DC voltage more effectively.
2) The discharge activity at a load of 4 N is also significantly reduced as compared to the load of 40 N. The higher load causes a slight deformation in the dimensions of the ball bearing steel (calculated to be ~0.04 μm) and thus change the physical dimension of the lubricant film during operation.
3) As the applied voltage is increased from 4 V to 10.6 V, the discharge current activity is found to strongly increase, occurrences of electrical breakdowns are more frequent and the current flows for longer time.

A broader look at results given above in the investigations are summarized in Table VIII.

Table VIII. Frequency of discharge and duration of discharge of the current pulses in the data at indicated bearing voltage.

Operating point		Frequency of discharges (Discharges per second, shown in powers of 10)				Duration of discharge (μs, shown in powers of 10)			
Speed (rpm)	Load (N)	4 V	6.6 V	7.9 V	10.6 V	4 V	6.6 V	7.9 V	10.6 V
3000	4	10^{-1}	10^{3}	10^{3}	10^{2}	10^{1}	10^{0}	10^{2}	10^{3}
2000	4	10^{3}	10^{2}	10	10	10^{2}	10^{3}	10^{3}	10^{4}
3000	40	10^{2}	10^{2}	10^{2}	10^{2}	10^{2}	10^{3}	10^{3}	10^{4}
2000	40	10^{2}	10^{2}	10	1	10^{3}	10^{4}	10^{4}	10^{4}

8.2.2 Study of memory effects due to insulation breakdown events

Memory effects due to insulation breakdown events are associated with changes of the electrical insulating properties of the bearing lubricant in the recovery process following the current activity. To study this effect, a step-wise DC voltage was applied to the bearing under current limiting conditions. The test bearing of type 608 was kept under a constant operational condition with rotational speed of 3000 rpm and a mechanical load of 4 N. The applied voltage was increased up to 6 V, in steps of 1 V, where each step lasted for 10 s. This was done to first find the inception voltage level and once this voltage level was reached, the applied voltage was step-wise reduced for determining the extinction voltage. In this particular case the bearing started to behave resistive (conducting state) at the voltage between 4 and 5 V, as shown in Figure 66. The film thickness was evaluated to be 0.3475 μm and the electrical field strength of 14.3 V/μm. After reaching voltage level of 6 V, the voltage was step-wise decreased to 1 V. It was found that the bearing started to behave capacitively (insulating mode) at a lower voltage of 3 V, which refers to electrical field strength of 8.6 V/μm. At 1 V, when the electric field strength in the lubricating film was 2.8 V/μm, the bearing was run for 4 minutes to observe if any discharges would appear. No discharges occurred in the bearing during this period.

The bearing was thereafter brought to a standstill and was grounded for 6 hours before commencing the next test. This was done to discharge any charged species that remained within the lubricant after the application of static voltage and possibly due to chemical recovery of the lubricant.

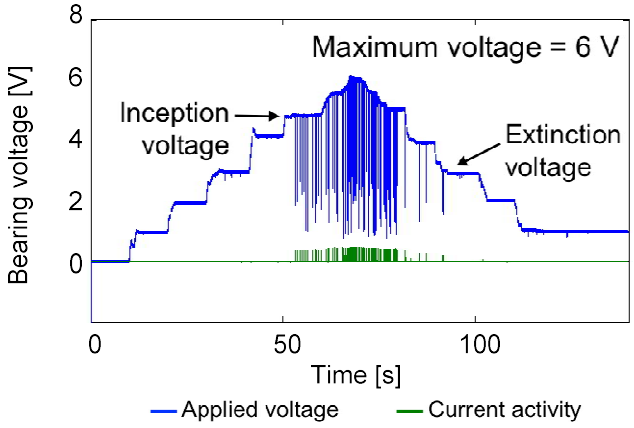

Figure 66. Current activity in bearing of type 608 during a step-wise voltage increase up to 6 V indicating their inception and extinction voltage levels. The current is shown in green, while the bearing voltage is shown in blue.

In the next test, the maximum applied voltage was increased from 6 to 8 V. The electric field strength in the lubricating film of the bearing corresponding to 8 V was 23 V/µm. The voltage across the bearing was increased and decreased in a similar manner as in the test shown in Figure 66. The inception voltage was again found to be between 4 and 5 V, corresponding to electric field stress of 14.3 V/µm. The current activity (in mA) is illustrated in the graphs of Figure 67, which present it at different instances of the test. The occurrence of bearing discharges gradually reduced after 19 minutes (bottom right). Once bearing discharges had been initiated, they could thereafter be maintained even at 1 V (E = 2.8 V/µm), i.e. well below the previously measured extinction level, but the bearing had gradually recovered after duration of about 19 minutes. This indicates that, after an intense current activity, a memory effect is present in the recovery of insulating properties of the bearing.

The bearing was brought to a standstill and was grounded for 6 hours before again commencing the same test procedure. The static voltage was increased to 8 V (E = 23 V/µm), like in the previous test and the discharges were monitored until they significantly reduced, but this time the voltage was kept constant at 2 V (E = 5.6 V/µm) instead of 1 V (E = 2.8 V/µm). The results are shown in Figure 68. At the voltage of 2 V across the bearing, the discharges were very frequent (top right, Figure 68). The discharge frequency gradually reduced after 19 minutes (bottom left, Figure 68), but it took almost one hour to reach a state of their seldom appearance.

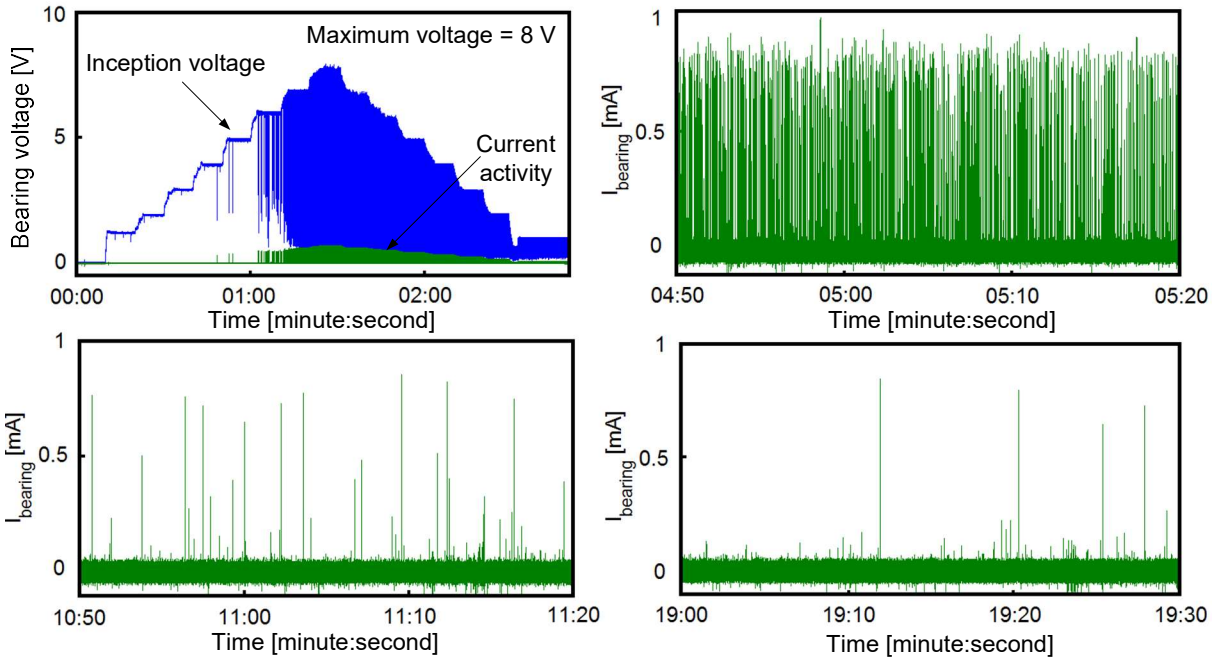

Figure 67. Current activity in bearing of type 608 during a step-wise voltage increase up to 8 V. The bearing current activity did not stop while reducing the voltage down to 1 V and it lasted for about 20 minutes.

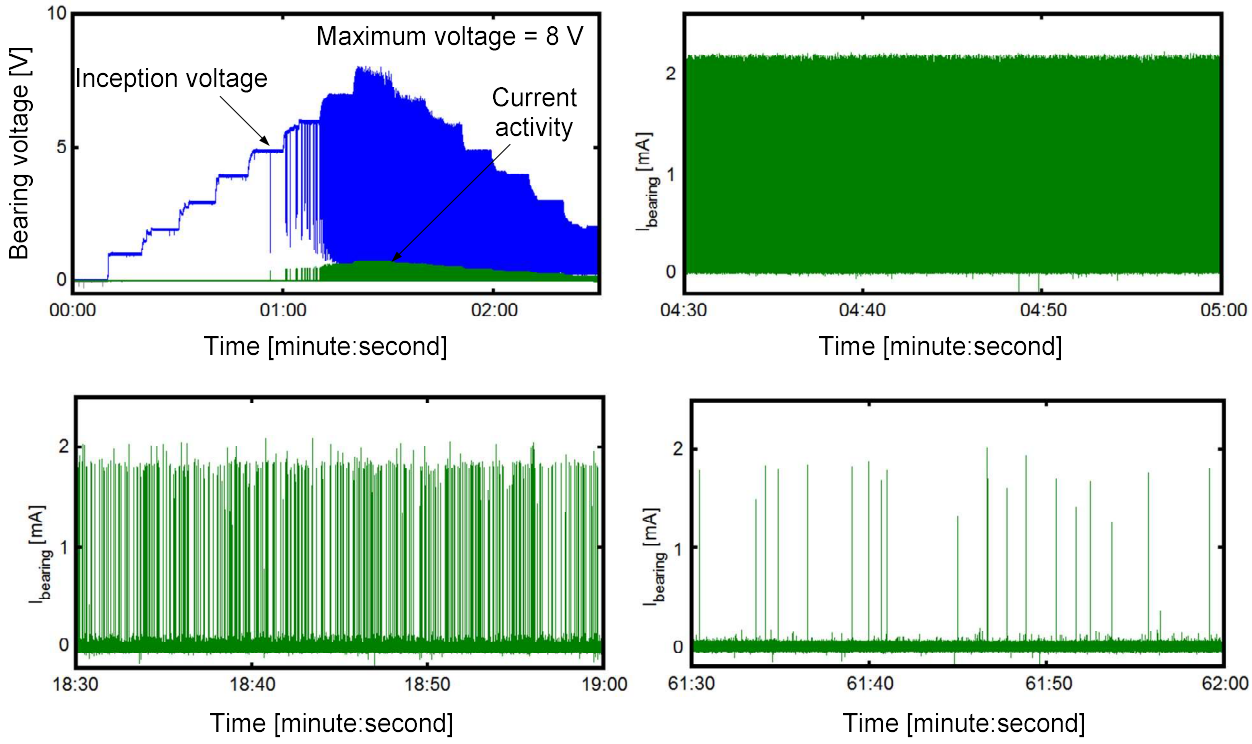

Figure 68. Current activity in bearing of type 608 during a step-wise voltage increase up to 8 V. The bearing current activity did not stop while reducing the voltage down to 2 V and it lasted for about 1 hour.

As the tests were repeated, the inception voltage was consistently found to be between 4 and 5 V (approx. 14.3 V/µm), provided that the shaft was grounded in between the tests, i.e. the discharging of bearing was effective. This recovery of the insulating properties of the lubricants could be attributed to its reversible recovery of viscosity after shear thinning during the operation [36]. More information about experiments related to this phenomenon can be found in [43], while further investigations into the memory effect in oil-lubricated bearing are discussed in Chapter 8.6.

The following findings summarise the outcomes of the above described tests:

1) The inception voltage for the bearing current activity in the tests is between 4 and 5 V, corresponding to electric field stress of 14.3 V/µm.
2) The extinction voltage for bearing current activity in the tests is between 3 and 2 V. Under the conditions of the test, inception voltage is found to be higher than extinction voltage.
3) Once the bearing current activity has initiated at a given voltage, an increase in voltage increases the occurrence of discharge activity.
4) The lubricant take time to recover after occurrence of intense current activity and is only able to partially withstand lower voltage levels.
5) The time to recover could be longer if bearing is exposed to higher voltage level of 8 V.
6) The lubricant cannot not completely recover after intense and repetitive bearing current activity, as seen by instant recovery shown in Figure 66, while an extended required time to recovery of 19 minutes (Figure 67) and 60 minutes (Figure 68). This is an indication of presence of a memory effect or hysteresis in recovery of the original properties. The memory effect is seen to occur if electric field stress across the pre-lubricated bearing crosses 23 V/µm (applied voltage = 8 V).

8.2.3 Study of insulation breakdown events for bearings of different sizes

To investigate the percentage of duration for which the discharge current flows in the bearing, the tests were conducted at different operating points (speeds and loads), under step wise increment of static voltage across the bearing. The conduction of a bearing at an operating point is presented in terms of ‘Time of Conduction, ToC’, which is calculated by summing up the individual duration of discharges and dividing it with the total duration of measurement, given by equation (25).

Two test bearings were used for these investigations, first tests were conducted on the bearing type 608 and later on the bearing of type 22220. The static DC voltage across the bearings was increased up to 15 V in steps of 1 V, followed by consistently performing the grounding and resting procedures between each test run. The voltage was applied to the bearing 15 minutes after it was set at desired rotational speed and mechanical load to keep consistently similar conditions during all the tests.

- **Transition of bearing type 608 from insulating to conducting state**

For the bearing of type 608, speeds of 1000, 2000 and 3000 rpm were chosen to be able to get various film thicknesses, while the axial load was at 4 and 40 N. The bearing made a transition from completely insulating, through a partially conducting state to a completely conducting state, as the applied voltage was increased at a given operating point. The transition occurred in a narrow window of voltage increment (approximately 2 to 3 V), as shown in Figure 69. However, the transition point depends on the operating point and occurs at lower voltage for lower speeds and

higher axial load. The experiments proved that an increase in speed of the bearing results in thicker film and thus in an increase of its insulating ability. At the same time an increase in axial load results in a decrease of film thickness and in lower insulating ability.

The limits for the time of conduction through the bearing are further classified in terms of $V_{10\%ToC}$ and $V_{90\%ToC}$, where the lower level is marked by the green area in Figure 69, while the upper one by the red area.

It can be found from Figure 69 that the $V_{10\%ToC}$ is distinctly different at different operating points because of different lubricant film thicknesses formed. It can also be observed that at different operating points the instant at which the bearing goes from partially conducting state to mostly conducting state differ as well. Since the voltage was increased in the same manner for all the operating points, the bearing operating at lower speed of 1000 rpm and higher load of 40 N is the first to reach the conducting state (very thin film during the operation). On the other hand, at speed of 3000 rpm and load of 4 N, the bearing reaches to the conducting state late, at much higher levels of the applied voltage.

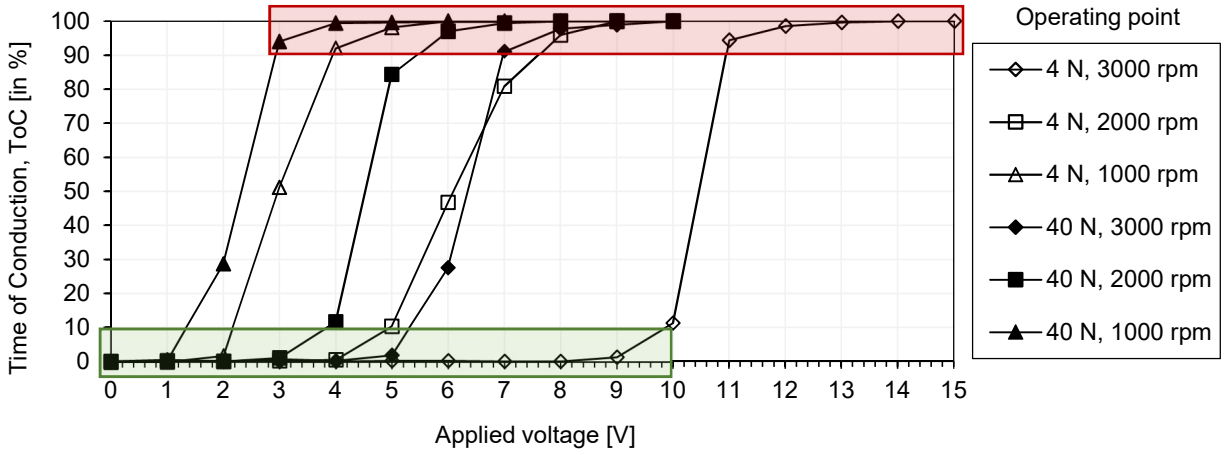

Figure 69. Relative time of conduction under different operating points (in %) for bearing type 608 during a step-wise voltage increase up to 15 V. The bearing always makes a transition from insulating to conducting state within a narrow window of voltage increment (2 to 3 V).

A plot against the apparent electric field strength $E_{10\%ToC}$ and $E_{90\%ToC}$ exhibits a more condensed region for the transition from partially conducting state to mostly conducting state, as shown in Figure 70. At low rotational speed of 1000 rpm; and mechanical loads of 4 N and 40 N, the bearing makes transition to mostly conducting state when the apparent electrical field strength is between 20.7 V/µm and 23.9 V/µm. At medium and high rotational speeds of 2000 and 3000 rpm; and at a mechanical load of 4 N, the bearing makes the transition to the mostly conducting state when the apparent electric field strength is between 28.5 V/µm and 31.5 V/µm. At medium and high rotational speeds of 2000 and 3000 rpm; and at mechanical loads of 40 N, the bearing makes the transition to the mostly conducting state when the apparent electric field strength is ~23.5 V/µm.

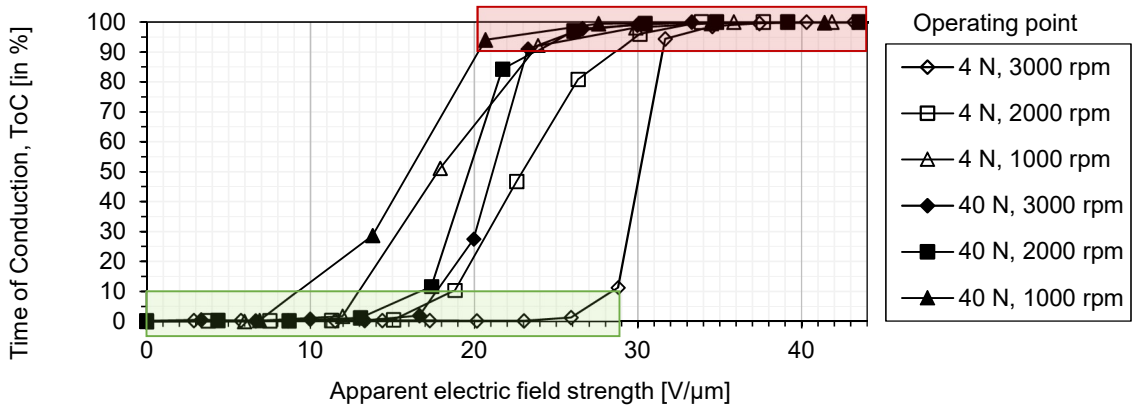

Figure 70. Relative time of conduction under different operating points (in %) for bearing type 608 plotted as function of apparent electric field strength. The shaded regions show the values of apparent electric field strength required for making the transition from partially insulating state ($E_{10\%ToC}$, lower box in green) to almost fully conducting state ($E_{90\%ToC}$, upper box in red).

To show the safe limits of bearing operation, the $V_{10\%ToC}$ and $E_{10\%ToC}$ values from Figure 69 and Figure 70 are respectively plotted as functions of rotational speed in Figure 70 and Figure 72.

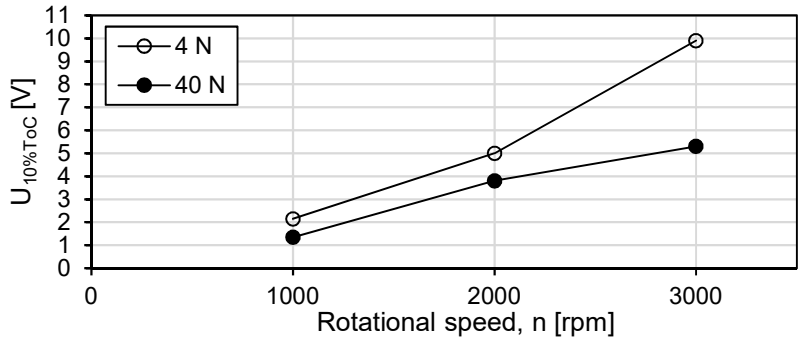

Figure 71. Voltage level leading to conduction for 10 % of time ($V_{10\%ToC}$) under mechanical loads of 4 and 40 N, regarded as safe operating point for bearing type 608, plotted as a function of rotational speed.

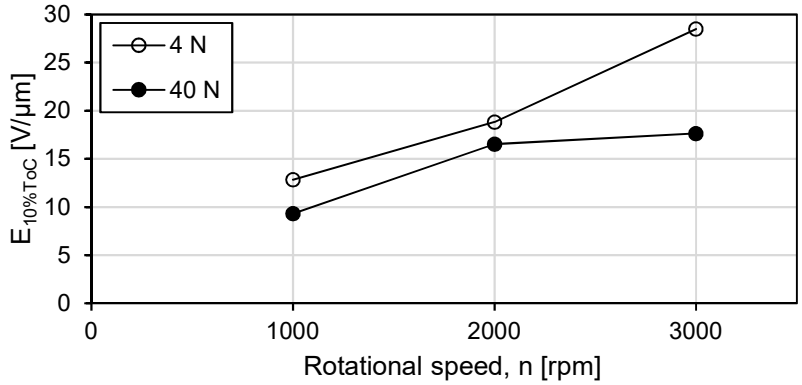

Figure 72. The apparent electrical field strength leading to conduction for 10 % of time ($E_{10\%ToC}$) under mechanical loads of 4 and 40 N, regarded as safe operating point for bearing type 608, plotted as a function of rotational speed.

The summary of the section findings are as follows:

1) The bearing operating at a given operating point can quickly transfer from an insulating state to a mostly conducting state, given that a high enough voltage is applied across it.
2) The voltage (field) level of his transition depends on bearing operating point; when thickness of the lubricating film is higher, the transition of bearing from electrically insulating to the conducting state occurs at a higher level of applied voltage.
3) The transition occurs at the apparent electric field strength ranging from ~10 to ~30 V/µm The field strengths below 10 V/µm are assumed to be safe for bearing operation.

- **Investigations on bearing type 22220**

To verify the validity of findings presented in previous sections, tests were conducted on a larger bearing of type 22220 immersed in an oil bath of lubricant Sample A. This sub-chapter presents results of measurements of lubricant temperature during the tests, which is used to calculate the film thickness at different operating points.

The temperature on the bearing can be monitored on the outer ring of the bearing. An increase in temperature can result from increasing load, from high friction, high speed, etc. and it leads to a change in lubricant viscosity and film thickness in running bearing. Due to this, an increase in speed of the bearing would not necessarily result in increase in film thickness. To elucidate these phenomena, tests were made at four different speeds and at two different load settings. Like investigations in Chapter 8.2.2, the applied voltage and the evaluated film thickness are used to calculate the apparent electric field strength at different operating points.

Results of bearing temperature, monitored at the bearing housing, are shown in Figure 73. At first, the test was performed with mechanical load of 5 kN at rotational speed of 400 rpm. It was thereafter followed by second test at rotational speed of 800 rpm. The mechanical load was then increased to 10 kN and tests were repeated at the same speeds. The temperature during these tests varied between ~46 °C and ~60 °C. For the start of tests at each operating point, the temperature was stabilized to ~50 °C - a tolerance of ±5 °C was allowed due to time constraints and the observed temperature increment is due to the load under operating conditions.

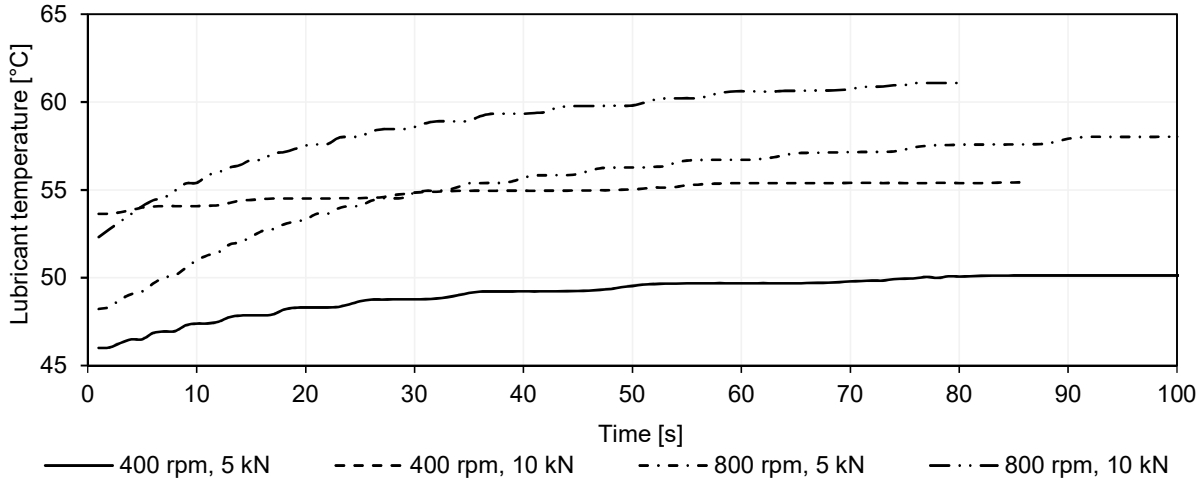

Figure 73. Temperature rise of bearing type 22220 at different operating points.

The lubricant film thickness of the bearing calculated for the different operating points are presented in Figure 74, where the error bars denote the minimum and maximum values of the thickness in the running bearing, considering the fluctuations in the temperature during the measurement (derived from Figure 73). The variation of the film thickness in regards to temperature is visible at higher loads, which results in reduction in viscosity ratio.

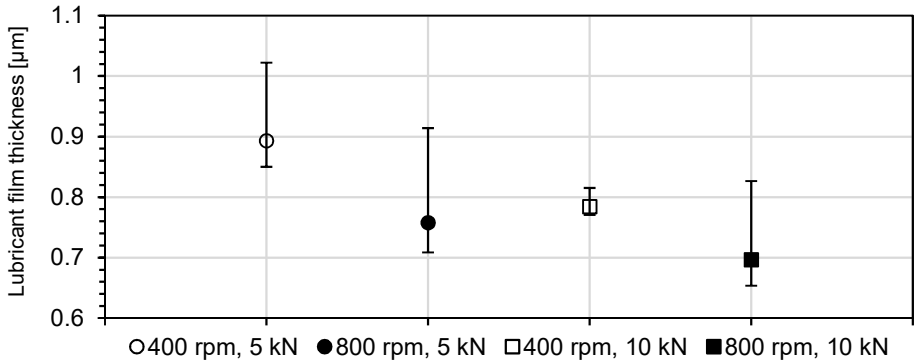

Figure 74. Calculated film thickness for bearing type 22220 at different operating points. The error bars indicate the changes of film thickness over the test duration.

The switching pattern analyses of the bearing were investigated by analysing the conduction current whilst the applied voltage was increased in the same manner at all the operating points. The applied voltage across the bearing was increased between 1 V and 10 V, in steps of 1 V, where each step lasted for about 10 seconds. The number of current pulses per second, pulse durations and the time between successive current pulses were monitored.

It is observed that at a fixed load, the occurrence of discharges per second nearly doubles as the speed increases from 400 to 800 rpm, as shown below in Figure 75. A possible interpretation of this observation is that an increased pressure during operation results in increased friction and eventually yields an increased temperature in the bearing. The rise in temperature is at the same time accompanied by a reduction in lubricant film thickness and a reduction of apparent electric field strength in the bearing. The number of discharges per second peaks at the point where the time of remaining in conduction state reaches 50 to 60 % and thereafter reduces. The number of current pulses become lower, but of longer duration. At the speed of 400 rpm and the load of 5 kN, the highest number of discharges per second occurs at the apparent electric field strength of 5.6 V/µm. Upon increasing the speed to 800 rpm the highest frequency of discharges occurs at the field of 10.5 V/µm. The same observation is made at the load of 10 kN, where the peak of the bell curve is attained at the field strength of 3.8 V/µm at 400 rpm and 7.2 V/µm at 800 rpm.

The values of the applied voltage and the apparent electric field strength at which the time of conduction reaches 50 % during the test are respectively denoted as $V_{50\%ToC}$ and $E_{50\%ToC}$. It is found that $V_{50\%ToC}$ increases with an increase in speed of the bearing. Interestingly, it can also be observed at all operating points that $E_{50\%ToC}$ depends on the operating condition and nearly coincides with the peaks of the bell-shaped curves as indicated by the blue vertical lines in Figure 76.

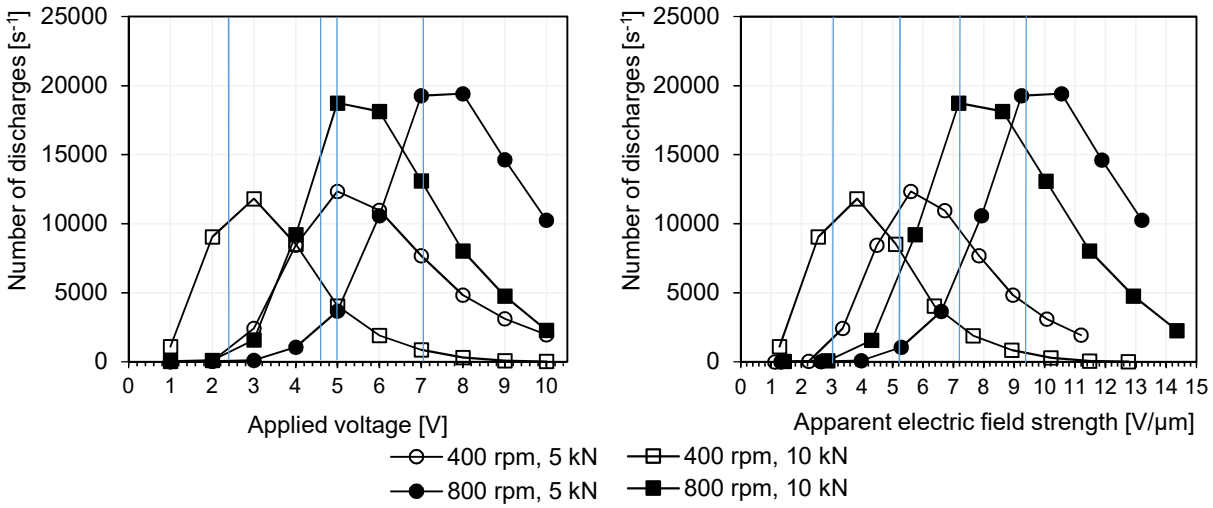

Figure 75. Number of discharges per second at different operating points as functions of applied voltage (left) and estimated apparent electric field strength (right) in the lubricating film of the mechanical bearing of type 22220.

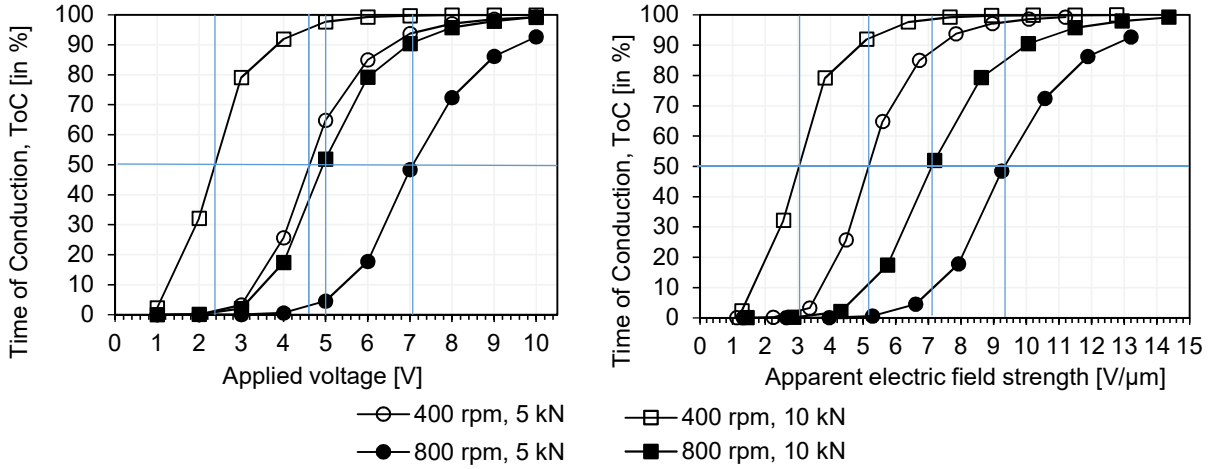

Figure 76. The time of conduction (in %) at different operating points, plotted as a function of applied voltage (left) and apparent electric field strength (right) in the lubricating film of the mechanical bearing of type 22220.

At a fixed speed, the changes in $V_{10\%ToC}$ and $E_{10\%ToC}$ as a function of different loads on bearing type 22220 are graphically presented in Figure 77.

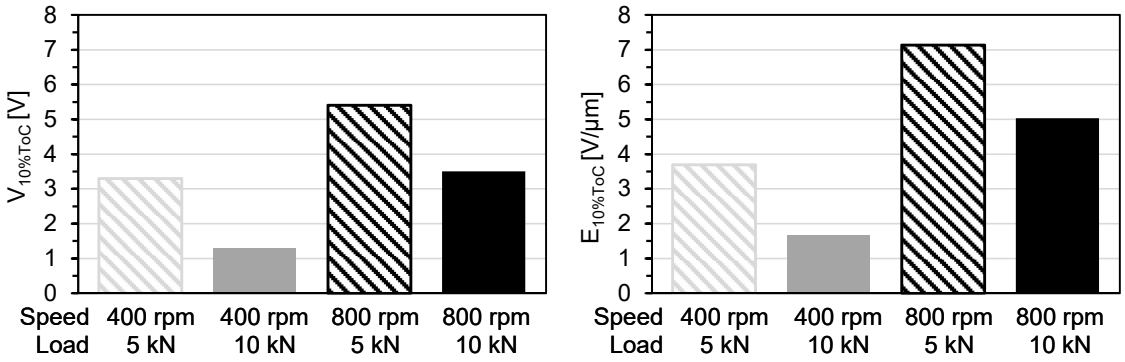

Figure 77. Applied voltage (left) and apparent electric field strength (right) at which the bearing type 22220 reaches 10 % time of conduction, shown as a function of different operating points.

A higher value of estimated electrical breakdown strength at higher rotational speed of 800 rpm, when compared to the field level at 400 rpm could be attributed to lower number of asperity contacts leading to a higher withstand voltage. At same time, lubricant film thickness at 800 rpm is calculated to be slightly smaller than at 400 rpm. Nevertheless, the measured discharge activity shows that the $E_{10\%ToC}$ is nearly doubled as the speed is increased from 400 to 800 rpm. Even as the film thickness has reduced when speed is increased from 400 to 800 rpm, the breakdowns arising due to asperity contacts could also have significantly reduced. Thus a higher speed causing lower asperity contacts, could have resulted in requirement of higher $E_{10\%ToC}$. Higher load setting of 10 kN leads to lower $E_{10\%ToC}$, thus at constant speed, a higher load reduces the distance in between the rolling element and the bearing raceways, hence resulting in reduction in field strength requirements for causing breakdowns. The breakdown phenomenon is governed by both asperity related breakdowns and field dependent breakdowns and the former cannot be completely neglected.

At a constant load setting, an increase in speed of the bearing reduces the asperity contacts, and should results in an increase in value of evaluated E-field and is seen in Figure 77. Whereas, at a constant speed setting, an increase in load on the running bearing results in reduction of distance in between the rolling elements. Thus, an increase in speed of the bearing at a fixed load results in large increase in breakdown electrical field strength of the lubricating film of the bearing (up to ~104 %). Whereas, an increase in load results in large reduction in electrical breakdown field strength of the lubricating film of the mechanical bearing (up to ~33 %).

Compared to bearing type 608, the transition of the larger bearing type 22220 takes place in a much wider window of voltage increment. For bearing type 608, the window of voltage increment was in the range of 1 to 3 V (see Figure 69), but in the case of bearing type 22220, the window is 5 to 6 V (see Figure 76).

In contrast to bearing type 608 value of electric field strength for transition from electrically insulating state to conducting state between 10 V/µm and 30 V/µm, the transition of bearing of type 22220 takes place below apparent electric field of 10 V/µm.

The pressure during operation could be another key factor for the early transition from insulating state to conducting state. The load applied the bearing type 608 (0.04 kN) is significantly less than the rated dynamic load is 3.45 kN. For bearing type 22220, the highest load applied is 10 kN, while

the rated dynamic load is 433 kN. Such high pressures lead to higher temperatures, due to higher friction and could more likely results in decrease in lubricant film thickness.

The findings of the experiments in this sub-chapter can be summarised as follows:

1) The aim of the experiments was to investigate if the conduction behaviour of a larger bearing type 22220 was similar to the smaller bearing of type 608.
2) At higher speeds, the transition of the bearing from an electrically insulating state to an electrically conducting state takes place at a higher voltage level. This is credited to reduction in asperity contacts at higher speeds and better separation in between bearing surfaces. Thus the breakdowns in the bearing could be assumed to be dominated more by electrical breakdown of the lubricant film and significantly lesser by breakdowns due to asperity contacts.
3) Similarly, at a higher load setting, the transition from insulating to conducting state takes place at a lower value of applied voltage. While this behaviour is similar to bearing type 608, some exceptions also appear as pointed below.
4) The transition of the bearing of type 22220 from an electrically insulating state to the electrically conducting state occurs at lower values of applied voltage. This is likely due to the line contact of the roller elements, which bring larger contact area and an increased likelihood of forming current paths in the lubricant.
5) The transition from insulating state to the conducting state occurs over a larger window of voltage increment, which contrasts with the bearing type 608.
6) The behaviour of bearing type 22220 is also found to be different compared with regards to the converging of the transition lines (compare Figure 70 and Figure 76).

- **Analyses of duration of discharges and time between discharges for bearing type 22220:**

As the apparent electric field strength in bearing increases at a fixed operating point, the pulse duration of the conduction current increases by several orders of magnitudes, from few micro-seconds at lower E-fields of 1.43 V/μm to several 10's of milliseconds at higher E-fields of 14.3 V/μm, as shown in Figure 78. The duration of discharges in the lubricating film of the bearing is here presented by a mean value along with standard deviation to show the spread of data. The time between successive discharges reduces drastically by several orders of magnitude as the applied voltage is step-wise increased, which is shown in Figure 79. The time between discharges decrease from 0.04 s to few micro seconds as the voltage is increased from 1 V to 10 V.

When the bearing reaches mostly conducting state, the duration of discharges increases drastically by two or three orders of magnitude, while the time between the discharges also drastically decreases. At a fixed level of applied voltage and load, the duration of discharges is shorter for a higher speed, whereas at set level of applied voltage and speed, the duration of discharges is longer for a higher load and can be seen in Figure 78.

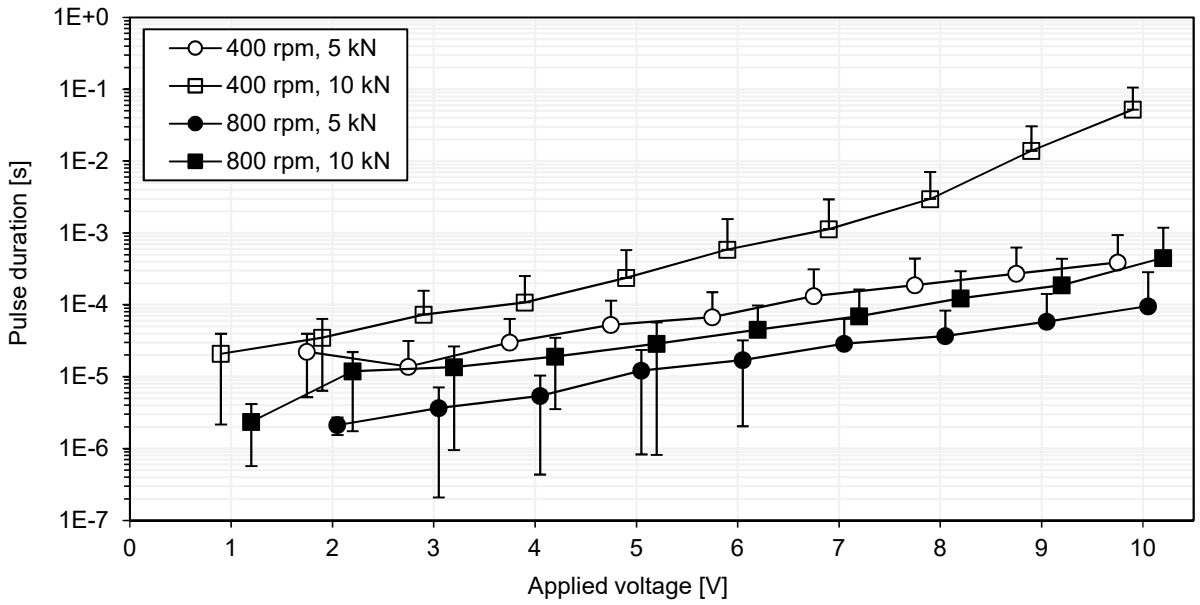

Figure 78. Current pulse durations as a function of increasing voltage within the bearing type 22220. Information is presented in form of mean value and standard deviation to show the spread of data.

At a fixed level of applied voltage and load, the time between successive discharges is longer for a higher speed, whereas at set level of applied voltage and speed, the time between discharges is shorter for a higher load on the bearing and can be seen in Figure 79.

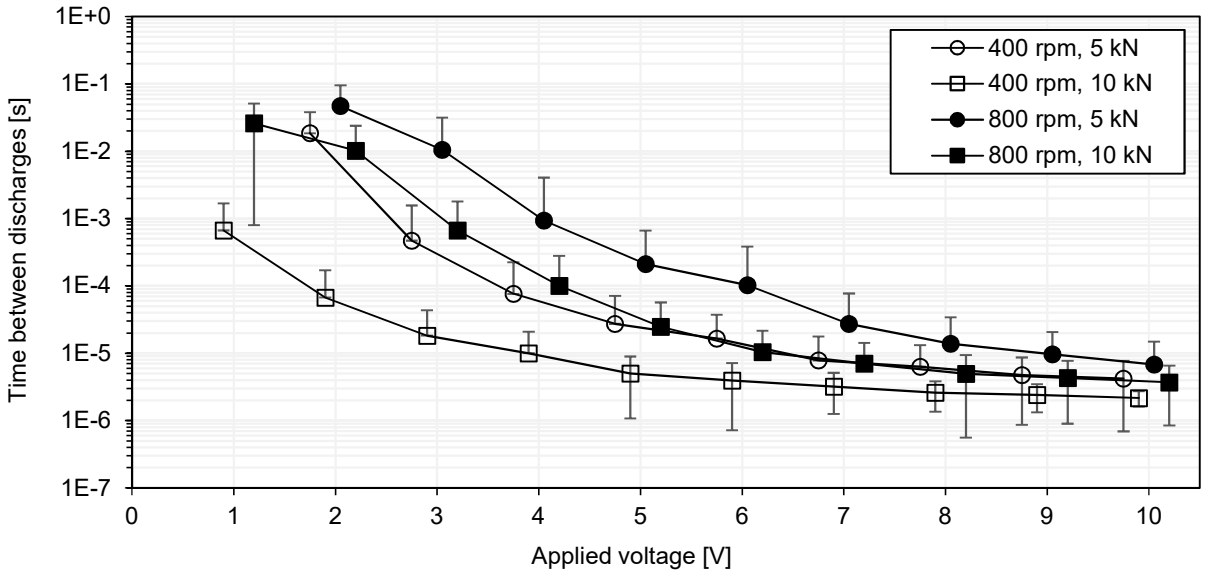

Figure 79. Time between discharges for the bearing type 22220. Information is presented in form of mean value and standard deviation to show the spread of data.

Summary of findings of time-based characteristics of discharge current conduction:

1) In comparison to bearing type 608, the characteristics of the discharge current pulses of bearing type 22220 behave in the same manner.

2) The duration of discharge current pulses is shorter (few microseconds) at lower values of applied voltage (1–4 V).
3) As the applied voltage is increased, the duration of the discharge current pulses increases by many orders of magnitude (to a few 100's of microseconds).
4) At higher speed setting, the discharge events are of shorter duration compared to a lower speed setting.
5) At a higher load setting, the discharge events are of longer duration than at the lower load setting accompanied with significant reduction in time in between successive discharge events. The changes in the duration of discharge events and the time in between successive events for bearing types 22220 and 608 can be compared in Figure 78, Figure 79 and Table VIII respectively.

8.2.4 Switching characteristics under alternating voltages

Study of bearing current activity for the bearing of type 22220 is also done under the application of alternating voltages. Voltages of different amplitudes and frequencies are applied and the responding current activity is monitored. To simplify the analyses, the operating point is kept at a fixed speed of 400 rpm and load of 5 kN. The bearing is lubricated with Sample A and immersed in an oil bath during the extent of the test, while its temperature has been monitored. The knowledge of temperature is used to calculate the film thickness and the field strength during the test.

The current activity in the bearing is analysed in the following sections by investigating following parameters:

- Inception voltage and corresponding electric field,
- Impact of applied voltage derivative (dV/dt),
- Impact of applied voltage polarity.

- **Types of alternating voltage used in the tests**

The applied alternating voltage (V) has been varied in its peak amplitude (V_{peak}) and in angular frequency ω. The shape of the applied voltage has been varied between sinusoidal, triangular and saw-tooth type, all of them not containing a DC offset. The peak amplitude of the voltages varied between 1 and 10 V_{peak}, in steps of 1 V while their frequencies were set at 25 Hz, 50 Hz, 1 kHz and 2 kHz. The voltage peak level and the frequency determined the dV/dt level.

- **Calculated lubricant film thickness during different tests**

Due to high load in the bearing, the temperature during operation generally tends to increase unless it is forced cooled. The temperature measured at the outer raceway of the bearing increased from 45 ˚C to 55 ˚C during the tests. The temperature variations during the tests at different frequencies and shapes of the applied voltage are shown in Figure 80. The film thickness at the inner and the outer raceways reduces with an increase in temperature and is shown in Figure 81. In the given temperature range, the total film thickness is calculated to vary between 0.6 μm and 0.9 μm, as shown in Figure 82. For these tests, the calculated viscosity ratio (κ) is always higher than 1, indicating a separation between the rollers and the raceways.

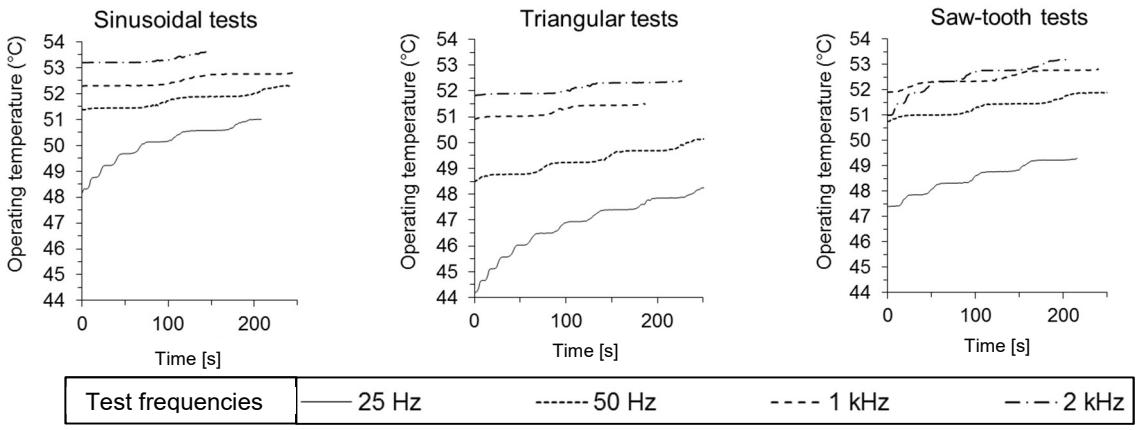

Figure 80. Bearing temperature recorded at its outer ring during tests with alternating voltages of different wave shapes and frequencies.

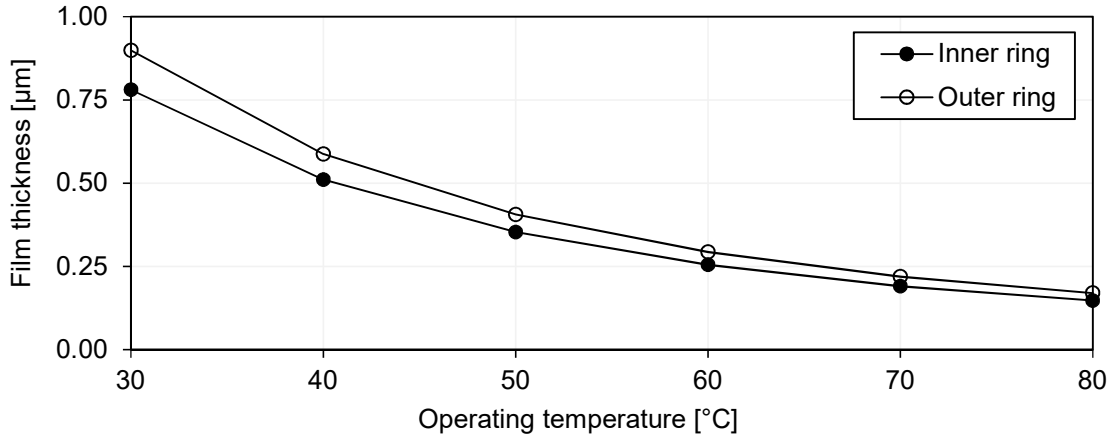

Figure 81. Film thickness at inner and outer ring in test bearing 22220 with lubricant Sample A operated at rotational speed of 400 rpm and mechanical load of 5 kN.

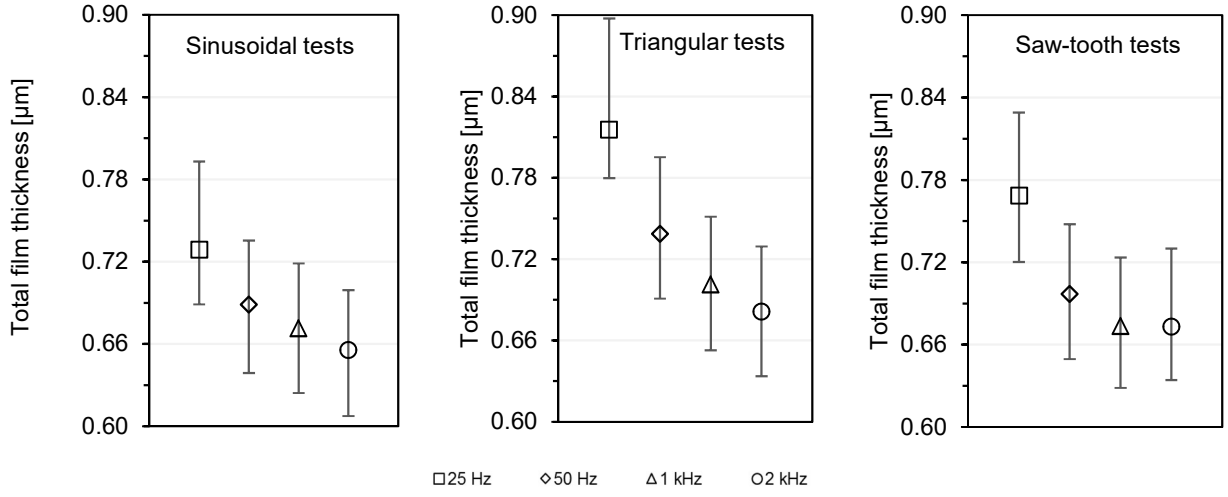

Figure 82. Average value of total film thickness during tests with alternating voltages of different wave shapes and frequencies. The bars show minimum and maximum attained thicknesses during the test while the symbols show average values corresponding to the average test temperature.

- **Extraction of voltage and current information from measured data**

The information from recorded data is extracted using a Matlab code that allows identification of the inception and extinction voltages, duration of discharges, time between discharges, etc. for both positive and negative cycles of the applied voltage. As an example, the raw data on application of alternating voltages of 6 V_{peak} at 50 Hz are shown in Figure 83.

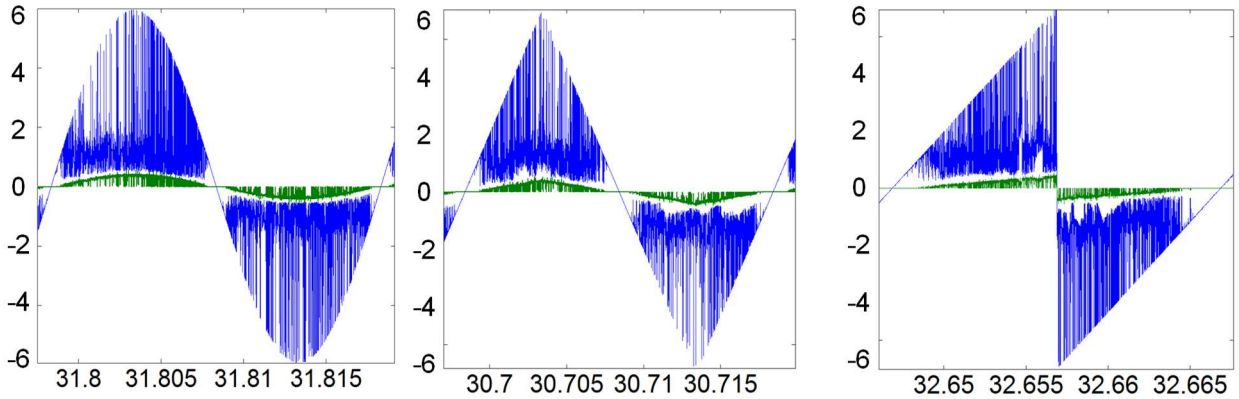

Figure 83. Bearing current activity (green) in lubricating film at V_{peak} of 6 V and frequency of 50 Hz at different voltage shapes (blue). It can be observed that the discharge bearing currents do not occur near the zero crossing of the alternating voltages. X-axis shows time in seconds for different measurements.

The pulse duration information is used to evaluate the percentage time of conduction (ToC) during the tests. To determine the presence of bearing current activity within a half period of applied voltage, a pre-set DC threshold value is used. A threshold of 0.2 mA for bearing current activity is taken and is higher than noise level of 0.1 mA. If the current exceeds the threshold, the start time of the current pulse is registered along with the instantaneous value of the applied voltage. Similarly, if the current reduces below the threshold, the end time of current pulse and the corresponding instantaneous value of voltage is also registered. The voltage information from the first current pulse in a cycle is saved as inception voltage, while the last current pulse provides the extinction voltage information. Similar data processing is carried out for negative cycles. Information from several cycles is used to secure a statistical significance of the measured quantities. The duration of the current pulses and time between successive current pulses are also saved using similar principle.

The measurement data were acquired using the same data acquisition card as in Chapter 4.2. The total measurement time for all the tests was chosen to be 10 s. To compare the data of different tests, a total of 100 points were chosen at random to evaluate the mean values and standard deviations of inception and extinction voltages. An example of mean inception voltages and their standard deviations for the tests with sinusoidal voltage at different peak levels at a frequency of 25 Hz is shown in Figure 84.

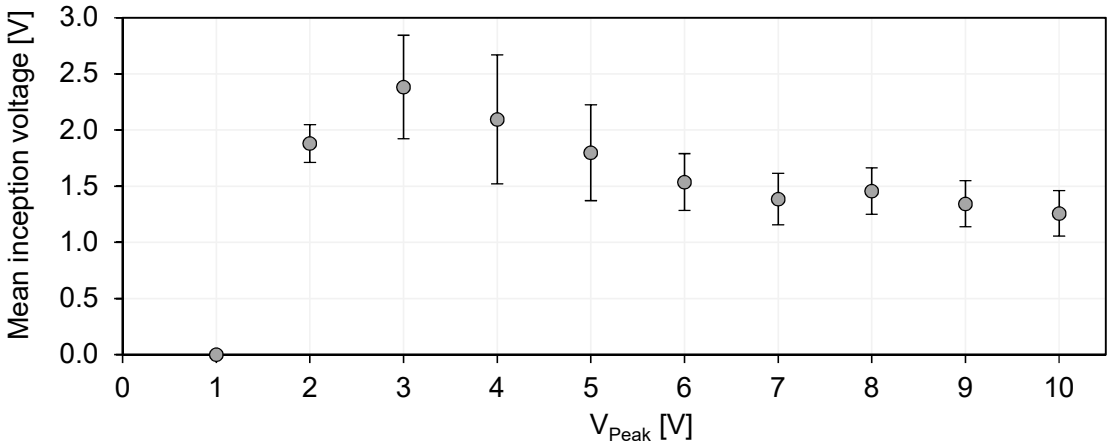

Figure 84. Mean inception voltage level along with its standard deviation for test with sinusoidal voltage of different peaks values at 25 Hz.

- **Results - Effect of amplitude, frequency and wave shape of applied voltage on inception voltage, time of conduction and inception electric field.**

The inception voltage of bearing current activity is shown as a function of amplitude, frequency and wave shape of the applied voltage in Figure 85. The mean inception voltage is generally found to increase up to a certain point and then reduce as the applied voltage is further increased.

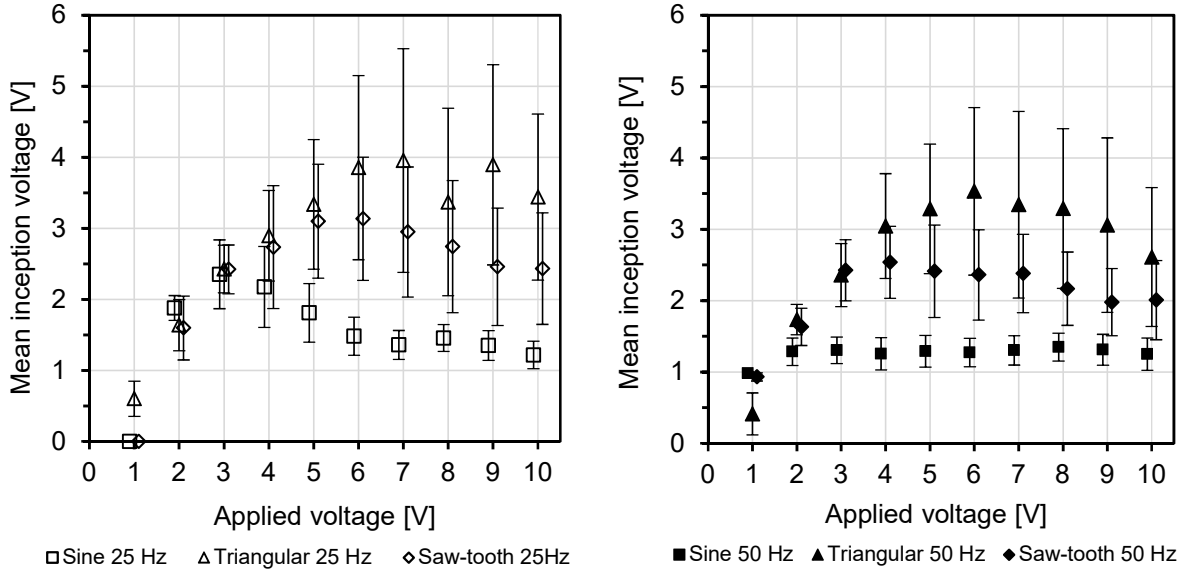

Figure 85. Mean inception voltage is shown as a function of different wave shapes, amplitudes and at frequencies of 25 and 50 Hz. Standard deviations of the data are shown as error bars. The inception voltage is higher for triangular and saw-tooth wave shapes in comparison to sinusoidal wave shape and could possibly arise due to higher film thickness during tests.

The reduction in inception voltage with increase in applied voltage is expected as the current activity in the bearing increases with higher voltage levels. Generally, an increase in frequency of applied voltage from 25 Hz to 50 Hz results in lower values of inception voltages. At the same time, the time of conduction (ToC) in the bearing at a 50 Hz is slightly higher compared to ToC at 25 Hz, as can be seen in Figure 86.

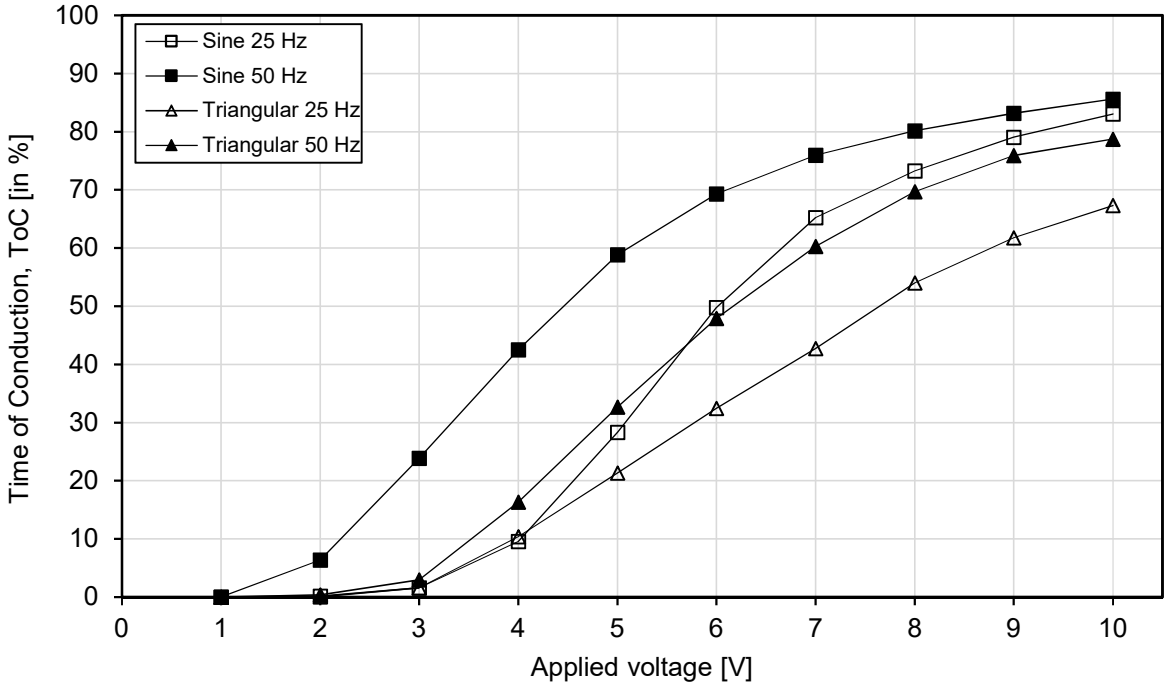

Figure 86. Time of conduction (ToC) for tests with sinusoidal and triangular voltages at 25 and 50 Hz. ToC is found to be higher at 50 Hz compared to 25 Hz at the same level of applied voltage (data represent positive cycles only).

At frequencies of 1 and 2 kHz, the mean inception voltage becomes slightly lowered for all the applied voltages compared to tests with frequencies of 25 and 50 Hz (shown in Figure 87). The inception voltage does not increase beyond a certain level, in this case around 4 to 5 V and thereafter lowers or stabilizes beyond this point. The bearing reaches higher ToC at lower levels of applied voltages at frequencies of 1 and 2 kHz in comparison to ToC shown in Figure 88.

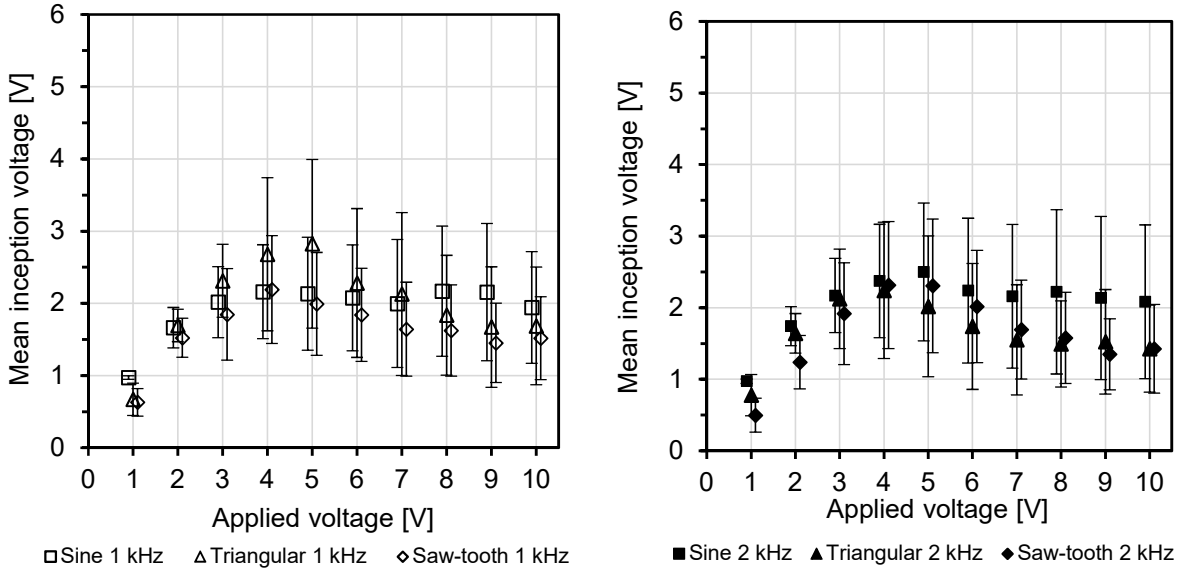

Figure 87. Mean inception voltage for different wave shapes, amplitudes and at frequencies of 1 and 2 kHz. Standard deviations of the data are shown as error bars.

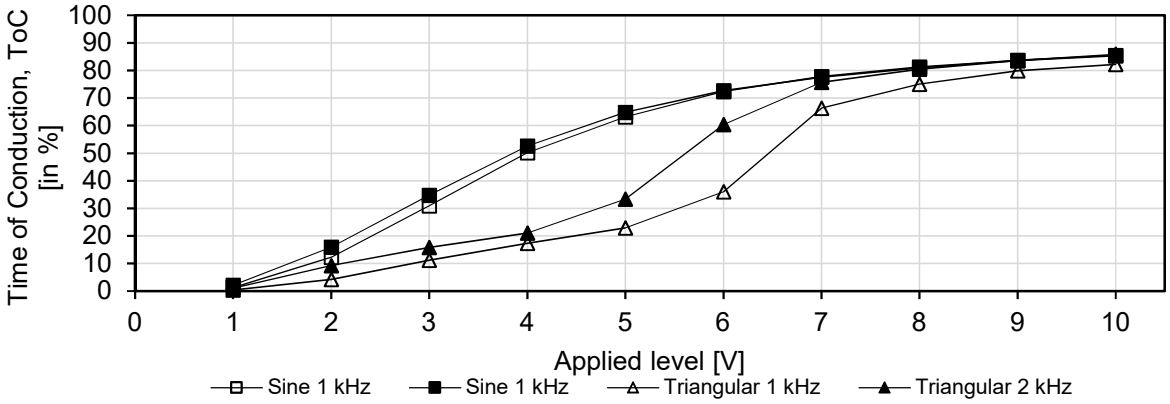

Figure 88. Time of conduction (ToC) for tests with sine and triangular voltages at 1 and 2 kHz. ToC is found to be slightly higher at 1 kHz compared to 2 kHz at the same level of applied voltage.

Within the applied voltage and frequency range, the dV/dt of a triangular voltage could be seen to vary from 100 V/s up to 80000 V/s. The inception electric field in this range of dV/dt can be seen to increase gradually until a peak point and further reducing for all the tests, as shown in Figure 89. The inception electric field is calculated using the film thickness information provided in Figure 82. The inception electric field is also lower at amplitudes voltage higher than 5 to 6 V. It can also be observed that inception electric field for bearing current activity is lower for higher frequency of applied voltage. The film thickness is taken to be the mean value given in Figure 82.

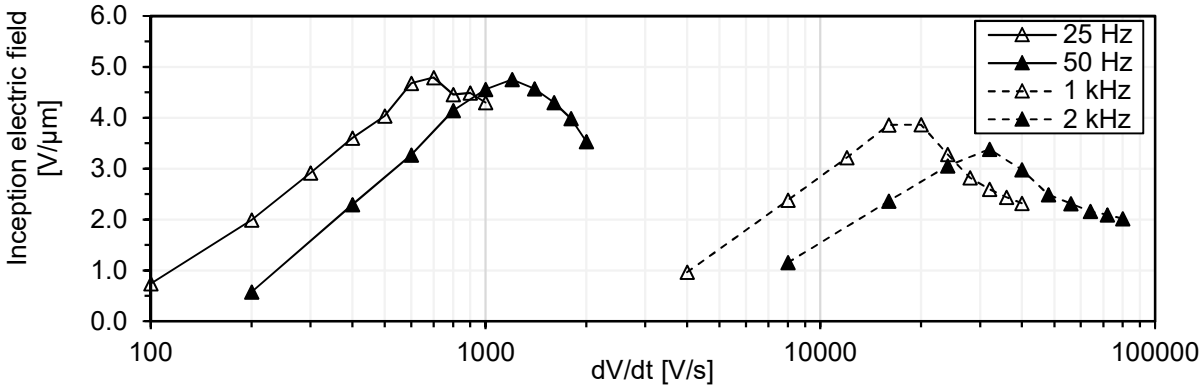

Figure 89. Inception electric field as a function of dV/dt of applied voltage.

- **Results – Effect of amplitude of applied voltage, frequency and wave shapes on pulse duration and time in between discharges.**

The pulse duration of the current pulses through the bearing increase about 2 orders of magnitude as the applied voltage is increased from 1 V_{peak} to 10 V_{peak}, as shown in Figure 90. Simultaneously, the time in between discharges reduces by several orders of magnitude. The increase in pulse duration is also reflected in time of conduction, which is shown in Figure 86 and Figure 88 respectively. As the frequency of the applied voltage is increased from 25 Hz to 2 kHz, a slightly higher value of mean pulse duration is found at a higher frequency. Similarly, as the frequency of the applied voltage is increased, the time in between discharges reduces by many orders of magnitude at a given voltage level.

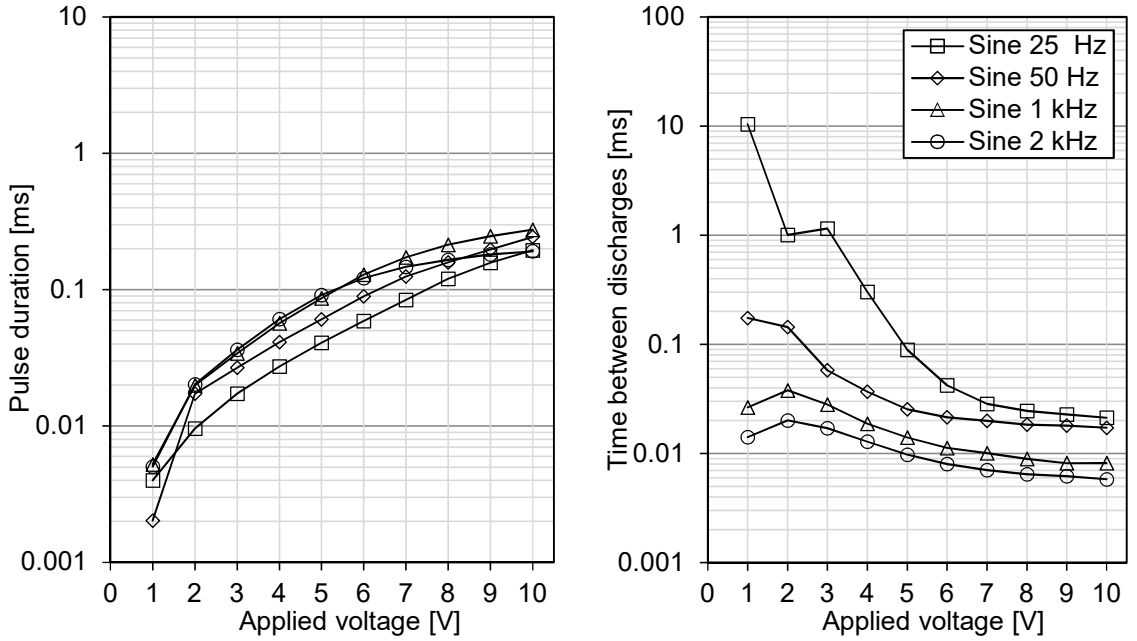

Figure 90. Pulse duration (left) and time between discharges (right) for tests with sinusoidal voltage (data represent positive cycles only).

The pulse duration and time in between discharges for triangular voltages are shown in Figure 91. The triangular voltages have more pronounced difference in between two frequency groups (lower frequency group of 25 and 50 Hz and higher frequency group of 1 kHz and 2 kHz).

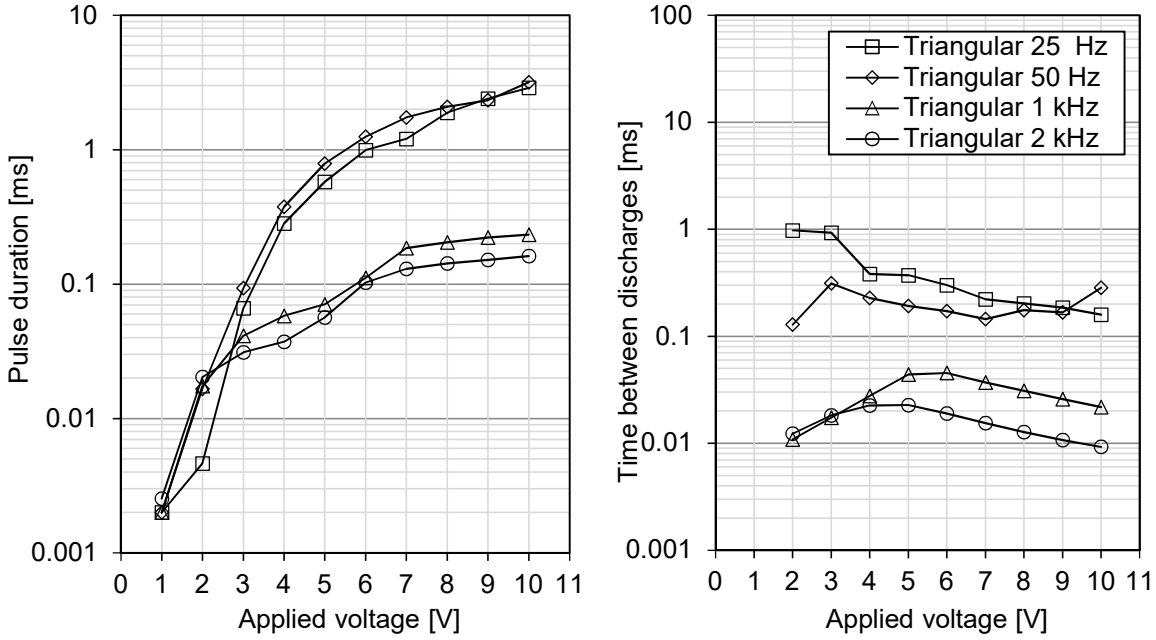

Figure 91. Pulse duration (left) and time between discharges (right) for tests with triangular voltage.

The tests with triangular voltages could be seen to have longer pulse durations at lower frequencies of 25 and 50 Hz when compared to sinusoidal voltages. The results shown in Figure 90 and Figure 91 are analysed for positive cycles only..

- **Results – Effect of polarity**

The analysis of the negative polarity of the applied voltage shows that a change in polarity does not affect the bearing current activity. The mean inception voltage, pulse duration and time in between pulses are in similar magnitude range and do not show wider differences. The mean inception voltage at the different tests is shown in Figure 92 and Figure 93.

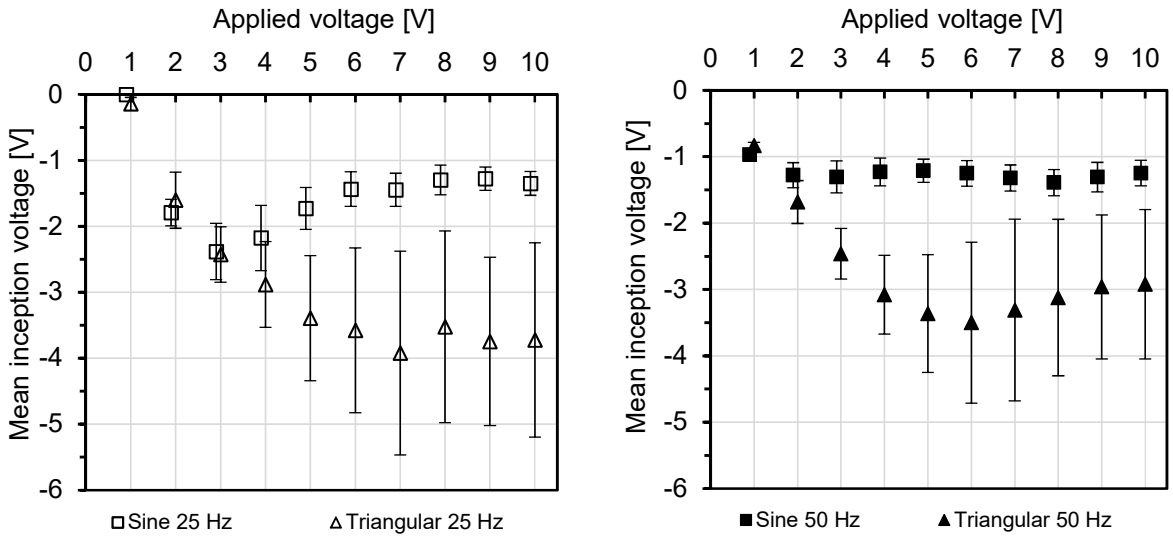

Figure 92. Mean inception voltages for negative cycles. The applied voltages are sinusoidal and triangular of 25 and 50 Hz. Error bars show standard deviations of the inception voltages.

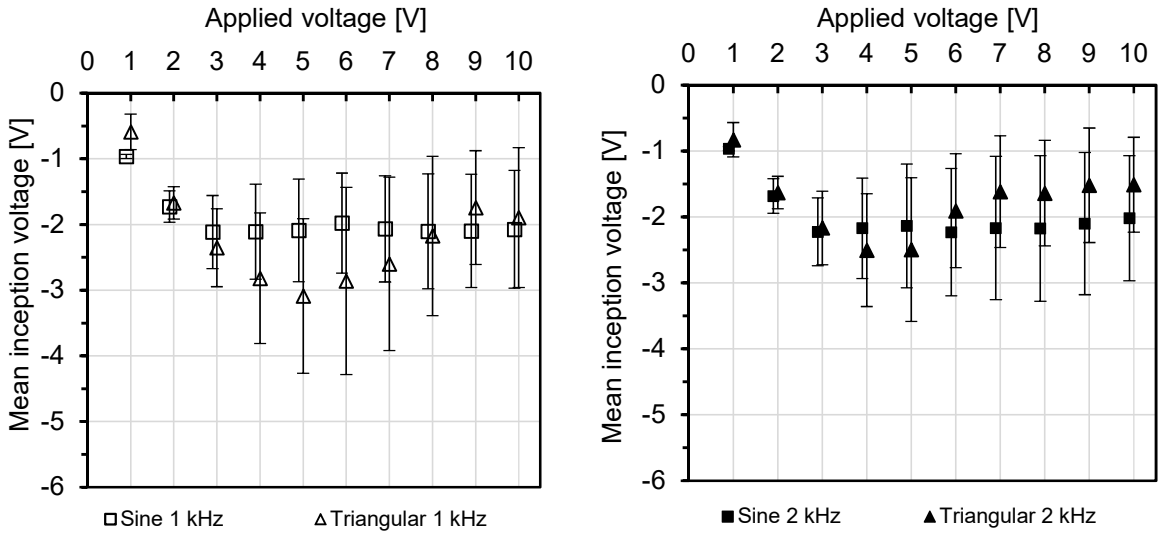

Figure 93. Mean inception voltage for negative cycles. At frequencies of 1 and 2 kHz the mean inception voltage is lower compared to 25 and 50 Hz.

Similarly, the pulse duration of the current pulses and time between discharges for negative cycles of sine voltage do not deviate much from the values measured at positive cycles, see Figure 94.

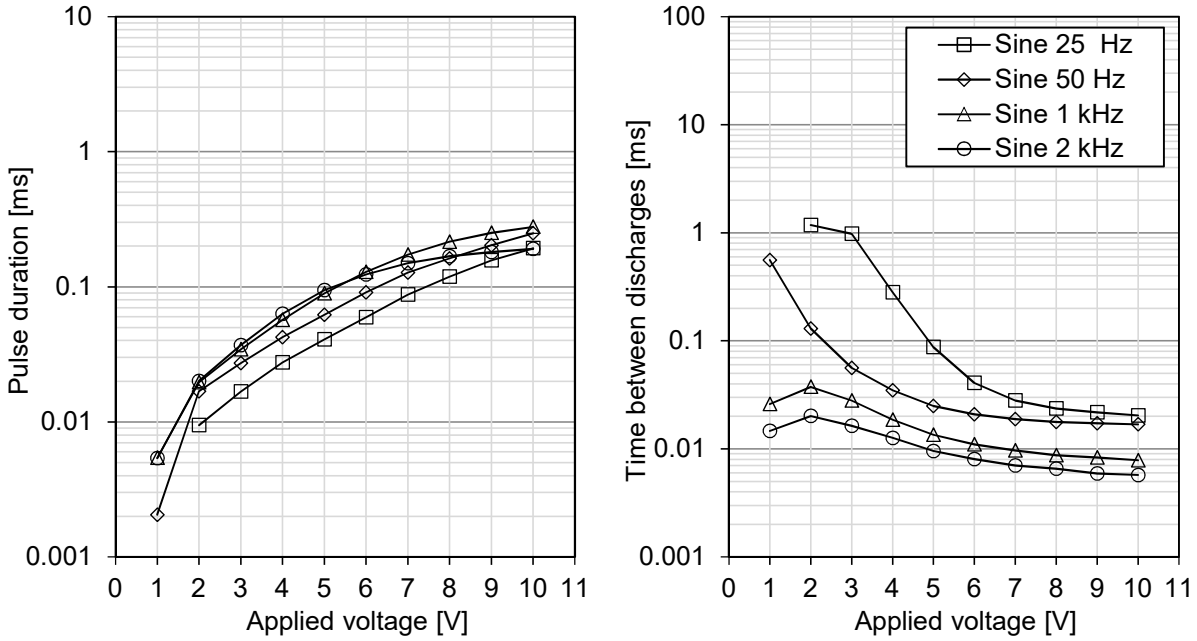

Figure 94. Pulse duration (left) and time between discharges (right) for tests with sine voltages. Data are shown for negative cycles of applied voltage only.

For triangular voltages, the pulse duration and time in between characteristics of bearing current in the negative cycles is similar as positive cycles, as shown in Figure 95. In addition, no memory effects were observed during the tests with alternating voltages.

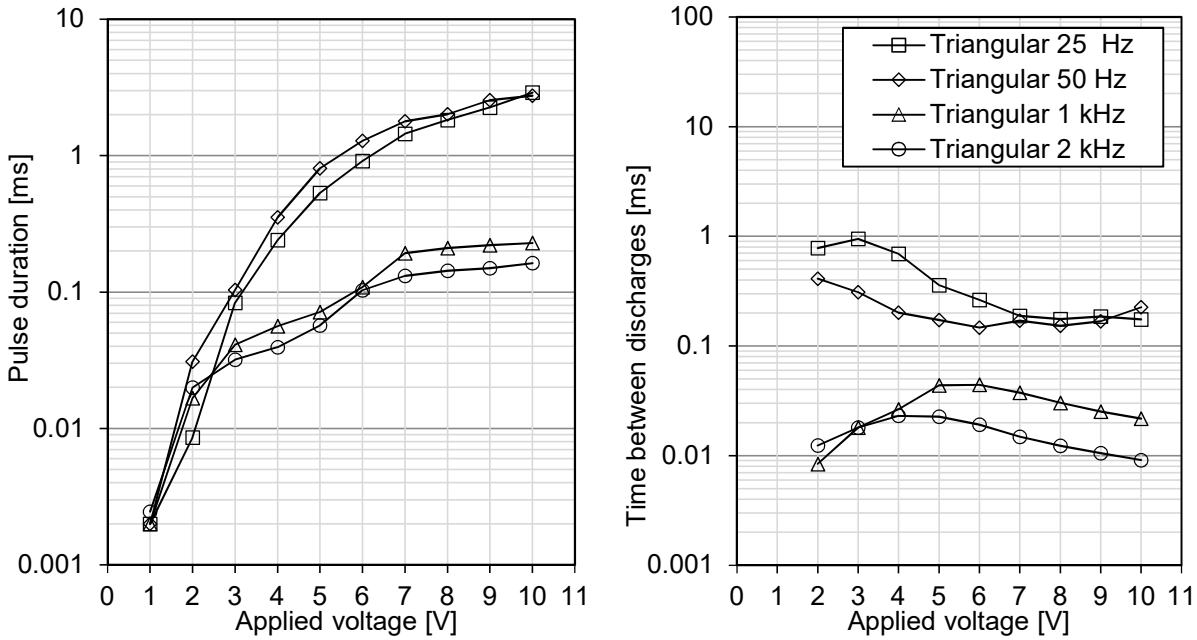

Figure 95. Pulse duration (left) and time between discharges (right) for tests with triangular voltages. Data is shown for negative cycles of applied voltage only.

Summarizing observations and plausible interpretations

- The initiation voltage for bearing current is found to be at about 1 to 2 V for the applied alternating voltages. At these low ampltudes the current pulses occur at the peak of the applied voltage.
- At higher voltages (3 V and above), the inception of bearing current acitivity takes place before reaching the peak level.
- The bearing current activity extingushes as the applied voltage nears the zero-crossing, which is also one of the reasons why the highest time of conduction (ToC) is found to be 89 % instead of 100 % observed at DC voltages.
- The inception voltage increases until a certain peak voltage level (4 to 5 V) and it decreases beyond this point.
- The mean inception voltage is found to be slightly lower at 1 and 2 kHz than at 25 and 50 Hz.
- The pulse duration of current throught the bearing increases with an increase in amplitude of the applied voltage while the time between the current pulses reduces by several orders of magnitude as the applied voltage is increased.
- The time of conduction is found to be slightly higher at 1 and 2 kHz than at 25 and 50 Hz.
- The inception electric field for bearing current activity increases until a certain point (4.7 V/µm) for 25 and 50 Hz, beyond which it reduces with an increase in dV/dt of the applied voltage. Similarly, for tests with frequency of 1 and 2 kHz, the inception electric field increases up to 3.3 V/µm and 3.8 V/µm respectively and reduces with a further increase in dV/dt.
- The polatiry of the applied voltage is seen to have no influence on the parameters of the bearing current activity, such as inception voltage, pulse duration and time in between discharges.
- Memory effects are not observed in tests with alternating voltages.
- The window of transition from insulating state to conducting state occurs approximately during the same range of applied voltage for all the tests. This seems to be a result of the fixed operating point of speed and load. It is also observed that the transition from insulating state occurs faster in case of DC voltage as compared to alternating sinusoidal voltages.

8.3 Breakdown mechanism - Asperity contacts

For the characterisation of asperity contacts at different operating points, bearing of type 608 was lubricated with Sample D. The bearing is smaller in size and hence is easier to run a number of tests since the cleaning and the mounting procedures are simplified.

For experiments to investigate asperities, the focus is kept on lower speeds, i.e., between 200 and 1000 rpm, although tests were also conducted for higher speeds (up to 4000 rpm). The mechanical load on the bearing is varied at 4 and 40 N and a fixed value of DC voltage of 5 V was applied in the test circuit. The analyses for asperity contacts are first shown for a standard bearing (all steel balls), after which the analyses of the modified test bearing with ceramic balls is discussed for elucidating the asperity contact importance. The purpose for modifying the bearing was to

investigate if the amount of current conduction state could directly be linked to the number of rollers in the bearing.

8.3.1 Bearing type 608

At lower speeds of less than 500 rpm, the bearing is in high friction or a mixed lubrication regime. This regime is characterised by frequent asperity contacts and the lubricant is unable to carry the load of bearing operation. Under these conditions, if a voltage is applied to the bearing, it will be discharged frequently and more than one ball can be in contact with the raceways, resulting in multiple current conduction paths through the bearing while their amplitude is limited by the values of limiting and shunt resistors in the test circuit.

To study the asperity contacts of an all steel bearing, histograms representing the measured pulse duration and time between pulses are shown in Figure 96 to Figure 98. In Figure 96 and Figure 97, the x-axis shows the values of pulse duration in microseconds, while the y-axis shows the insulation breakdowns normalized per second. In this way, the frequency of pulses is shown as a function of pulse duration.

At a fixed axial load of 4 N, when the speed is increased from a minimum speed of 200 rpm to maximum speed of 1000 rpm, the bearing becomes less and less conducting, as the speed is increased and is shown in Figure 96. This means that the pulse duration and the number of insulation breakdowns per second decreases and is attributed to the formation of an insulating lubricating film around the steel balls. As the axial load is increased from 4 to 40 N, the behaviour of the bearing does not change significantly.

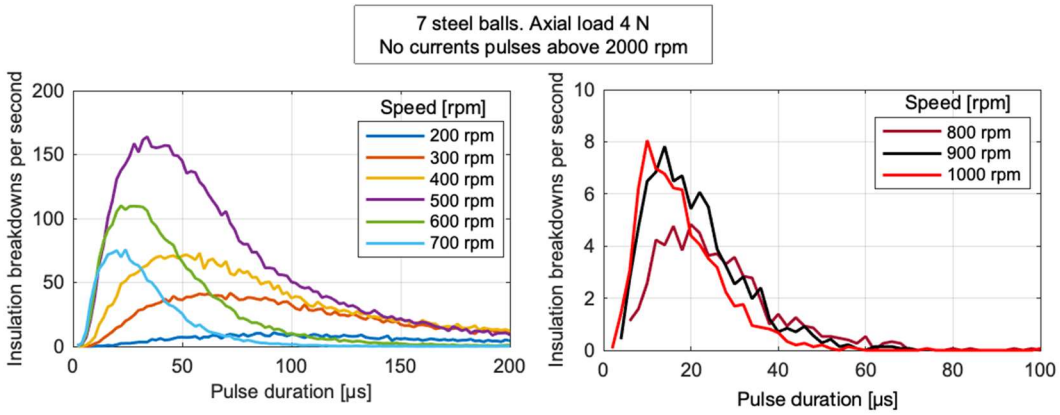

Figure 96. Distributions of current pulse duration at different speeds and mechanical load of 4 N. The applied voltage is 5 V DC. The x-axis shows the values of pulse duration while y-axis shows the frequency of asperity contacts (insulation breakdowns per second).

The interval between asperity contacts can be measured by measuring the time between current pulses (Δt), which increases with the increase in speed of the bearing, shown in Figure 98. This is a measure of frequency of the asperity contact events. The value of time between asperity contacts is much smaller at speeds lower than 800 rpm accompanied by higher number of insulation breakdowns per second. As the speed is increased beyond 800 rpm, the interval between asperity events increases accompanied by a reduction in frequency of occurrences and is evident from significantly lower time of conduction.

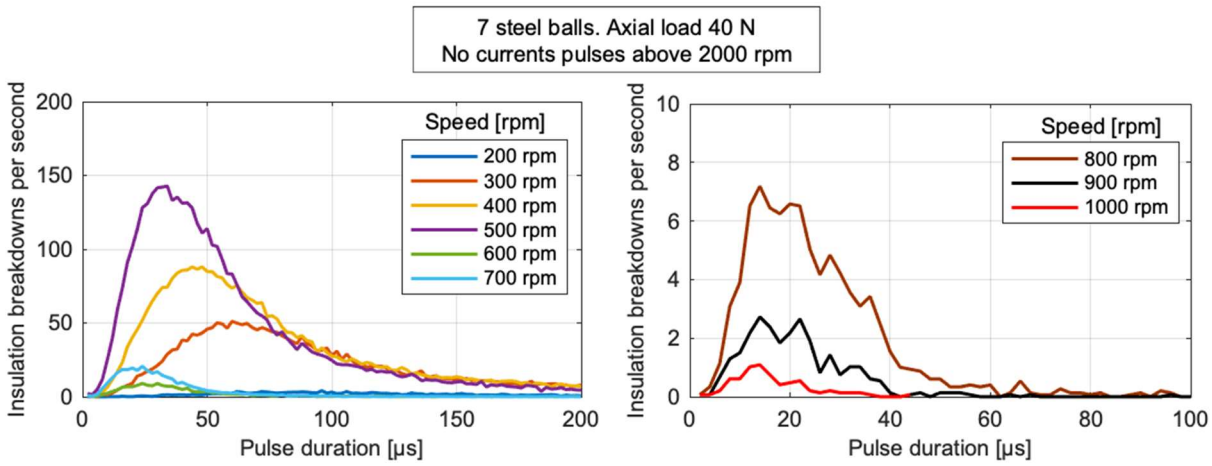

Figure 97. Distributions of current pulse duration at different speeds and mechanical load of 40 N. The applied voltage is 5 V DC. The x-axis shows the values of pulse duration while y-axis shows the frequency of asperity contacts (insulation breakdowns per second).

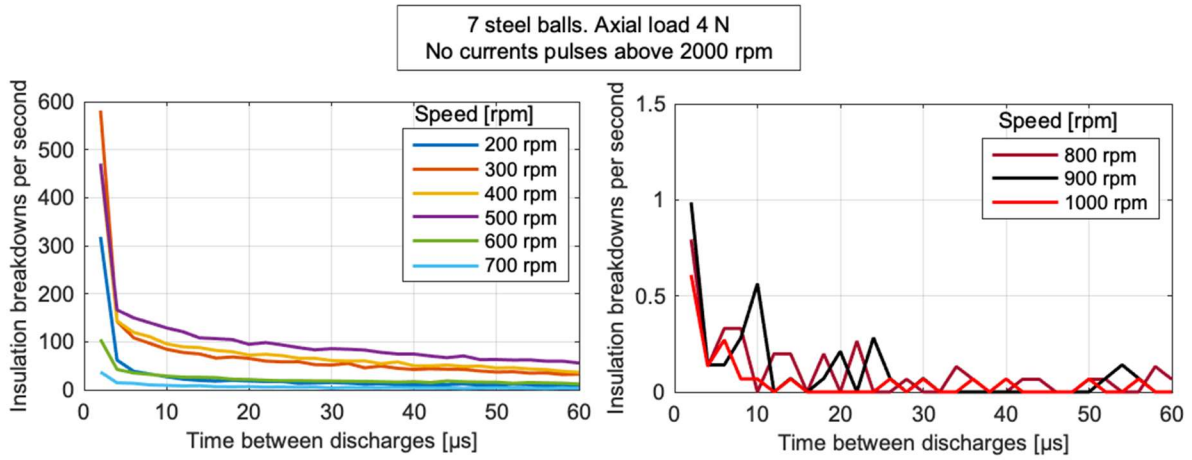

Figure 98. Distributions of time between current pulses at different speeds and mechanical load of 4 N. The applied voltage is 5 V DC. The x-axis shows the values of pulse duration while y-axis shows the frequency of asperity contacts (insulation breakdowns per second).

To elaborate the speed range until which the breakdown mechanism is dominated due to asperity contacts, the results are further discussed in terms of Time of Conduction, (ToC, in %) at different operating points. At an axial load of 4 N, it is observed from that when the speed was increased from 200 to 300 rpm, the ToC reduces from 90 to 75 %. As the speed is further increased, the ToC is 40 % at 400 rpm and 25 % at 500 rpm. Such large ToC is due to large pulse durations of the conduction pulses (not shown here). At a load of 4 N, the longest pulse measured is of 80 ms at speed of 200 rpm and 18 ms at 300 rpm. Above 600 rpm, the asperity contacts are again reduced and ToC is only about 2 %. Also, the pulse duration reduces as the speed is increased from 200 to 500 rpm. At speed of 800 rpm and above, the ToC is ~0.1%, hence this operating point could practically be considered to be the limit above which asperities on do not play any role in breakdown of bearing voltage. The ToC for the all-steel ball bearing at different operating points is shown in Figure 99. Rotational speed of 800 rpm corresponds to a dimensionless speed (d_m) of 12000, which is calculated using the relation given in equation (36) as,

$$\text{Dimensionless speed } (d_m) = \text{Rotational speed in rpm} * \frac{1}{2}(d + D), \quad (36)$$

where

d is bore diameter of bearing in mm and

D is outer diameter of bearing in mm.

Dimensionless speed parameter (d_m) could possibly be used to determine the operating point at which influence of asperity contacts to ohmic current conduction become negligible.

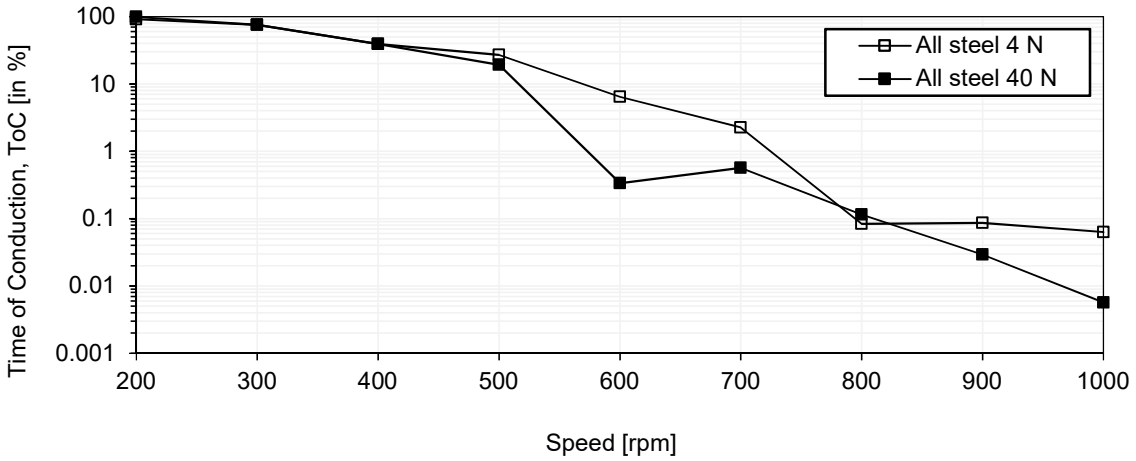

Figure 99. Time of conduction (in %) for all steel ball bearing at different operating points.

At an axial load of 40 N, the asperity contacts increase nearly linearly with the increase in speed and can be observed up to 800 rpm. The asperity contacts are very high at 200 rpm, resulting in ToC of more than 90 %. As speed is increased to 300, 400 and 500 rpm, the ToC respectively reduces to 75, 39 and 20 %, shown in Figure 99. At 800 rpm, the ToC is 0,3 %. There is only a minor difference between ToC results at low and high axial loads, since they are very small in comparison to the static load rating of the bearing, which is 1.4 kN. For bearing type 608, a speed of 800 rpm corresponds to a dimensionless speed of 12000, calculated using equation (36).

8.3.2 Modified bearing type 608

For the all steel ball bearing, the number of contacts has reduced by nearly half at the speed of 400 rpm compared to 200 rpm, as shown in Figure 99. To investigate this effect further, two modified bearings were prepared and tested, where the first one contained only one steel and the second one contained two steel balls. The results of the measurements of the ToC for the modified test bearings are shown in Figure 100 and remaining ball arrangements in the bearing is for the first case illustrated in Figure 101. The modification results in a periodically occurring asperities of shorter duration, compared to the all steel ball bearing. The focus is however kept on lower speeds, where the asperity contacts are dominating in the bearing breakdown.

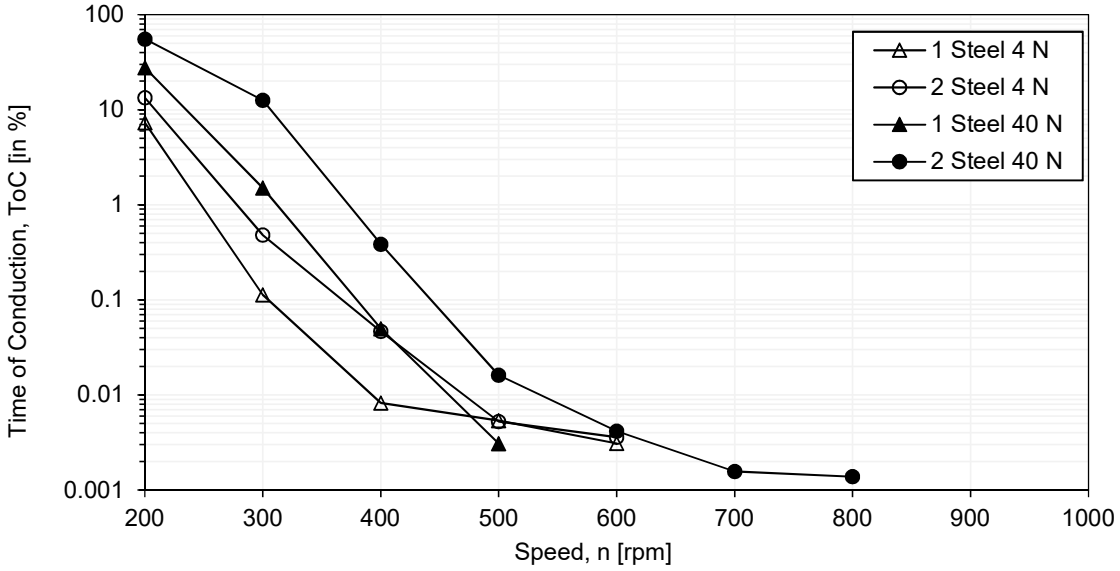

Figure 100. Time of conduction (in %) shown for 1 and 2 steel ball bearings at different operating points.

It can be observed in Figure 100 that at a speed of 200 rpm and a load of 4 N the ToC of the modified bearing with one steel ball is around 7 %, which is only half of that of bearing with two steel balls, which has ~14 %. This trend is also observed for higher load of 40 N, where ToC in the bearing with one steel ball at 200 rpm is ~27 %, which is half compared to bearing with two steel balls, ~55 %. Hence, we have demonstrated that in high friction regime, the number of asperity point contacts nearly doubles as the number of conducting balls doubles. At axial load of 40 N, for both the modified bearings, the number of contacts is higher than that at low axial load of 4 N.

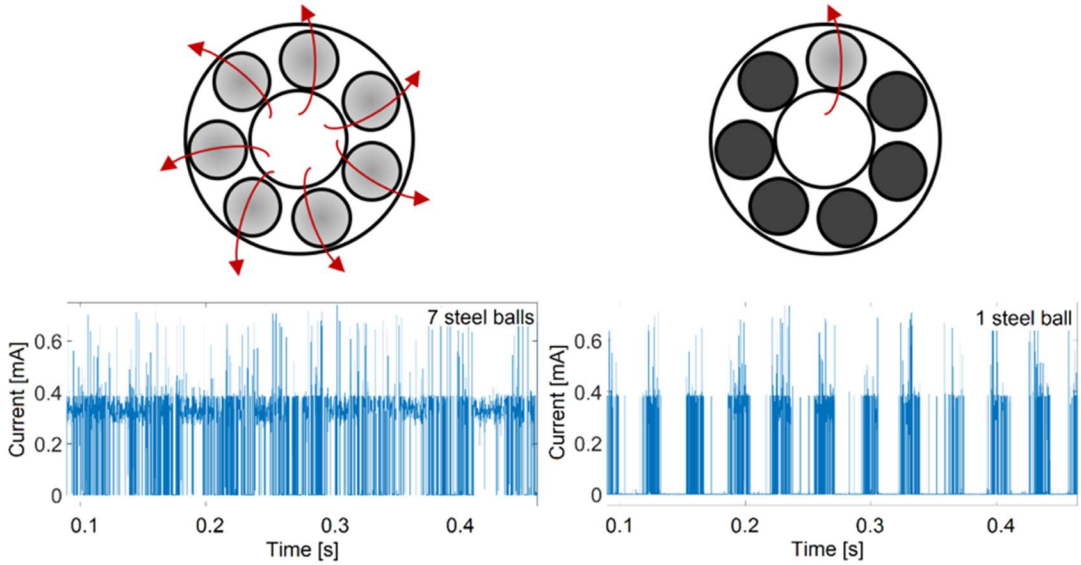

Figure 101. Current traces of all steel ball bearing (left) and one steel ball bearing (right) operating at a speed of 500 rpm and axial load of 40 N. It is observed that the current amplitude is frequently at a level of 0.4 mA, which corresponds to a conducting path through the bearing formed by the asperity contacts. Periodicity of shaft rotation is also visible in the right current trace.

The findings of the investigations of breakdowns due to asperity contacts are summarised below:

1) The breakdown of the bearing voltage is dominated by asperities at low speed of 200 rpm for bearing type 608. This speed corresponds to a dimensionless speed of 3000.
2) The pulse duration during the repeated breakdowns of bearing due to asperities reduces as the rotational speed is increased. Beyond the speed of 800 rpm (d_m = 12 000), the asperity breakdowns result in reduced Time of Conduction of less than 1% (ToC = 0.1 %). In the present investigations, the no conduction current was found to be at speeds higher than 2000 rpm, which corresponds to d_m of 30 000.
3) The loads during these investigations did not play here a significant role, but this can be investigated for larger bearings in the future.
4) The investigations using modified bearings that in high friction regime the number of asperity contacts nearly doubles as the number of conducting balls doubles.

8.4 Breakdown mechanism - Particle-initiated breakdowns

The breakdown of the electrical insulating properties of the bearing may also occur due to the presence of contamination particles, which can bridge the ball and the inner and outer bearing rings. The nature and the physical, electrical and chemical properties of the particles are certainly of important since they can be involved in abrasion of bearing surfaces. Their size will influence the possibility of the entering the loaded zone between the ball and the raceway, while the mechanical strength of the particle influences the wear on the bearing surface.

The breakdown of the electrical insulation in the bearing is investigated here by adding different particle types and their concentration, while their influence on the wear and damage of the bearing surface are not investigated.

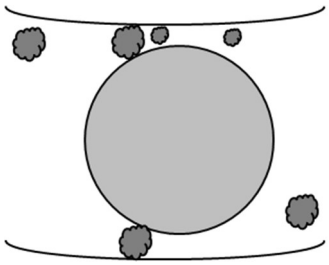

Figure 102. Illustration of a bearing in operation with contamination particles present in the lubricant.

The mass of the particle decides whether it will remain inside the bearing or will sink to the bottom of the lubricating bath. In our experiments, the lubricant samples once prepared, were not exposed to atmospheric air and were used immediately for experiments, assuming little or no oxidation process affecting them.

To study the influence of particle concentration, bearing 608 was lubricated with Sample A to obtain a high homogeneity of their dispersion. Particles of different types, size class, concentration and different electrical insulating ability were used. The maximum particle concentration was chosen to be 150 mg/L, which is a contamination threshold according to the recommendations provided by Elforsk [40] in a report on oil cleanliness in wind turbine gearboxes. Four different particles were used as specified in Table IX. For Samples A1 and A2, five different concentration

levels ranging from 150 mg/L to 7.5 mg/L were prepared, while Samples A3 and A4 were tested at a single concentration level of 150 mg/L.

Table IX. Composition of contaminated lubricants showing the base lubricant, particle contaminant type, particle concentration levels and range of particle size.

Contaminated test lubricant	Sample A1	Sample A2	Sample A3	Sample A4
Base lubricant	Sample A	Sample A	Sample A	Sample A
Particle contaminant	Arizona test dust	Toner	Aluminium	Iron
Particle concentration (mg/L)	150, 75, 30, 15, 7.5	150, 75, 30, 15, 7.5	150	150
Particle size	5.5–100 μm	8–10 μm	160 μm	Fine dust

For the experiments, five test bearings were prepared after a running-in process of the virgin bearings for 4 hours and a separate bearing was used for a given type of particle. Reference measurements with particle-free oil Sample A were conducted before the tests with particle-contaminated lubricant. For this, the bearing was disassembled, cleaned from the corrosion inhibitor grease, reassembled and lubricated with particle-free fresh lubricant Sample A. For all the tests in this section, the bearing was run at a fixed operating point, i.e. speed of 2000 rpm and axial load of 4 N, resulting in a calculated lubricant film thickness of 1.38 μm, at 20 °C. The film thickness between the inner and the balls is 0.59 μm, while the film thickness between the outer ring and the ball is evaluated to be 0.76 μm.

In the reference measurements, when all the bearings were lubricated with particle-free Sample A, no current activity could be detected up to voltage level of 5 V DC at the given operating point. Hence the reference level for all the experiments was at 0 % of ToC, which refers to a bearing in fully insulating state. Thus, we can conclude that the bearing does not show any asperity-initiated breakdowns as well as voltage dependent breakdowns at these conditions. Thus, the breakdowns occurring in the following tests can only be attributes as particle-initiated once and the ToC becomes a function of particle concentration.

For the main tests, the bearings were disassembled and the surfaces were cleaned with isopropanol (99.9 % pure), followed by use of a sonication process of its parts for 5 minutes. Thereafter the bearing was dried and reassembled in a clean environment, remounted on the test rig and lubricated with the desired type of lubricant sample. The cleaning procedure was repeated whenever changing the lubricant contamination level.

The measurements on the bearing were conducted within three stages; During first stage (Start 1), it was brought into rotation at the set operating parameters and a total of 5 measurements were conducted, where each measurement lasted for 30 s. Afterwards, the bearing was brought to a stop for a duration of 2 minutes to save the accumulated data and then the same procedure was repeated as the second stage (Start 2) and the third one (Start 3). Hence, a total of 10 to 15 measurements were done with each lubricant sample. This procedure was adopted to investigate the effect of start-stops on the bearing current activity.

8.4.1 Arizona test dust

Arizona test dust is used as a contamination medium due to its standardized chemical composition and particle size distribution. Arizona test dust is relevant to investigate particle-initiated breakdowns in bearings and have been widely used in reliability analyses [123, 124]. The details about the dust, such as photographs, size distribution and its chemical composition can be found in Appendix A

A trace of the bearing voltage and the current activity due to the use of lubricant containing Arizona test dust is shown in Figure 103. The hardness of the test dust is low in comparison to the bearing steel surface and hence when the test dust enters the pressurised lubricating film, it possibly form pellets and smaller particles under the contact stress.

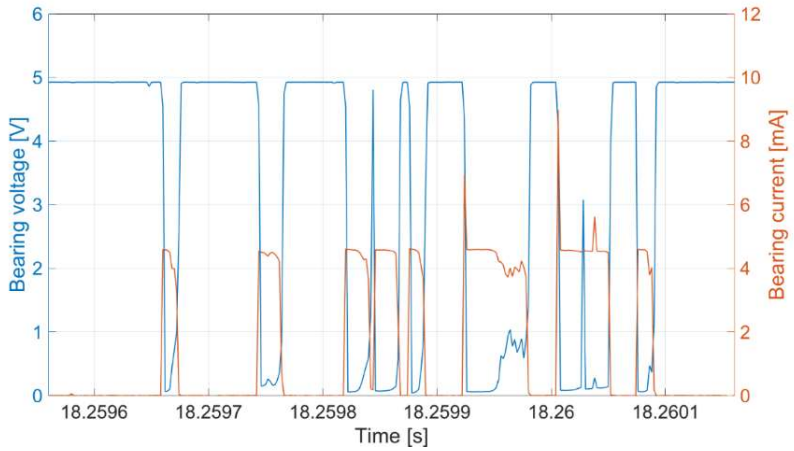

Figure 103. Voltage and current patterns in a bearing type 608 lubricated with Arizona test dust particles at a concentration level of 150 mg/L. The bearing voltage is shown in blue, while the bearing current activity due to particle-initiated breakdown is shown in orange. The measurement window is 600 µs.

The particle-initiated breakdown events are in Start 1 stage more frequent than in stages Start 2 and Start 3. At the particle concentration of 150 mg/L, the number of breakdowns is extremely high and the conduction current time has an average value of 9.51 % in Start 1 stage, with a standard deviation of 0.85. In Start 2 stage, the ToC drops to almost half the value, i.e. 4.5 % with a standard deviation of 0.42. This may indicate that the heavier particles are removed from the bearing and tend to accumulate at the bottom of the lubricant bath, thus resulting in a reduction of the current activity, as shown in Figure 104. The number of breakdowns (per second) within the five measurements in Start 1 stage has a mean value of 4722 breakdowns and reduces for the next five measurements of Start 2 stage, with a mean value of 2426.

The reduction in particle concentration to 75 mg/L halved the ToC compared to lubricant with 150 mg/L of Arizona test dust. In Start 1 stage with particle concentration of 75 mg/L, the average value of ToC is 4.26 % with a standard deviation of 0.28. The number of breakdowns per second within the five measurements in Start 1 stage has a mean value of 2287 and again reduces for the next five measurements of Start 2 stage with a mean value of 1415. In Start 2 stage, the ToC reduces to almost half with an average value of 2.51 % and standard deviation of 0.13. A further reduction

in particle concentration to 30 mg/L reduces the ToC to about 0.5 %, a reduction by factor 10 when compared to the ToC at 150 mg/L, shown in Figure 105.

Upon stopping and restarting the bearing, the ToC due to particles is approximately halved in all the tests with Arizona test dust. The ToC at particle concentration of 7.5 mg/L is found to be relatively higher compared to ToC at concentrations of 30 and 15 mg/L. The reason for this could be due to a relative inhomogeneity in dispersion of the particles in the lubricant. This can also be confirmed by the higher number of particle-initiated breakdowns per second, which is shown in the secondary y-axis of Figure 105. The variation of ToC in context the whole test sequence is relatively small and is less than the standard deviation of the five measurements in the first test with 150 mg/L.

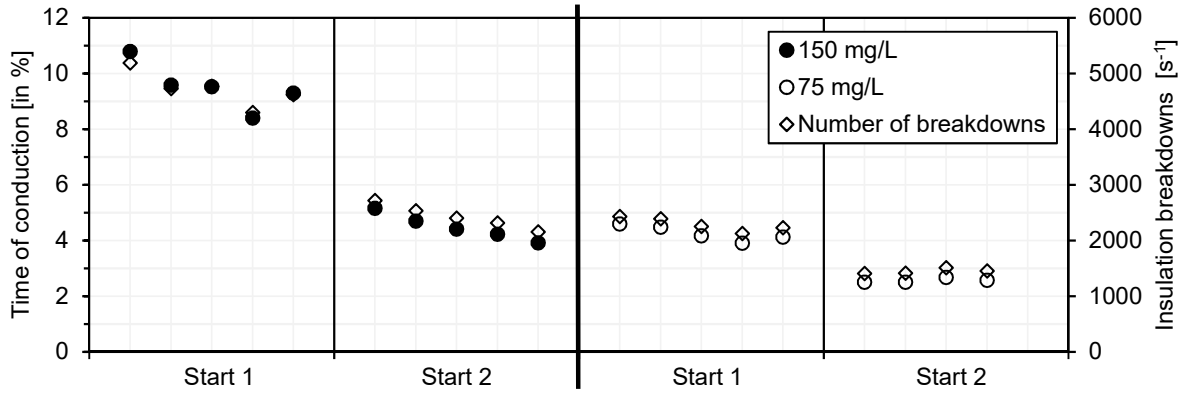

Figure 104. Time of conduction and particle-initiated breakdowns during Start 1 and start 2 stages of the test with lubricant contaminated with particle concentrations of 150 mg/L and 75 mg/L.

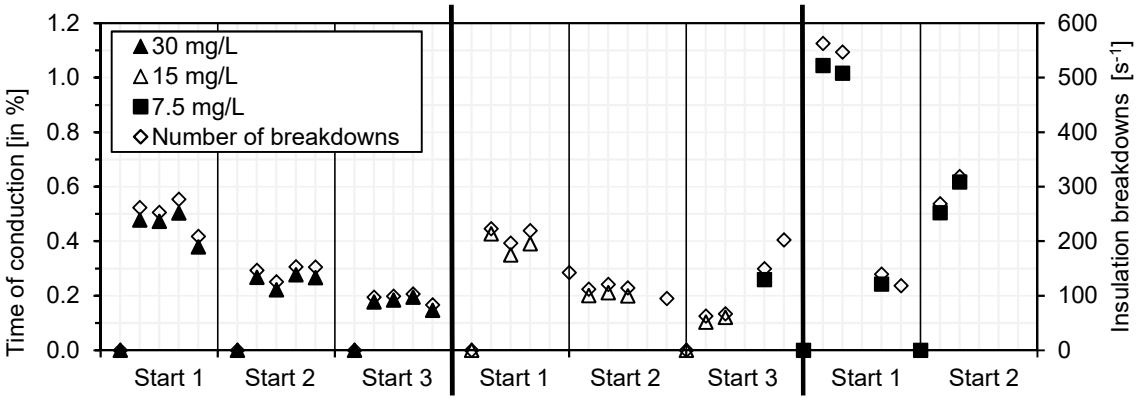

Figure 105. Time of conduction and particle-initiated breakdowns during Start 1 and start 2 stages of the test with lubricant contaminated with particle concentrations of 30 mg/L, 15 mg/L and 7.5 mg/L.

The particle size was analysed from a fraction of volume of the lubricant Sample A1, which had particle concentration of 150 mg/L. The lubricant was mixed for 5 min to assure its homogeneity and thereafter was filtered through a Nylon test membrane of size 1.2 µm using a vacuum filtration device. The results of the size distribution of the particles and count per 100 mL of oil sample according to oil cleanliness code ISO 4460 is presented in Appendix A It can be stated that the majority of the particles were in the range of 5 to 15 µm, while they could also be as large as up to 100 µm. Since majority of the particles were larger than the film thickness during bearing

operation, the result was a 3 body abrasion and possibly a little wear on the bearing surfaces [125], since the hardness of the Arizona test dust is lower than that of bearing steel.

8.4.2 Toner particles

Toner particles comprises mostly of a type of polymeric resin which acts as a binder (about 60 to 80 %) along with wax, carbon black particles (up to 20 %) and few additional ingredients listed in Appendix A. Printer toner particles could retain static electric charge and thus possibly agglomerate around air bubbles in the lubricant. Detailed information about physical and chemical composition of toner particles used in the tests, along with photos of dry and wet particles are provided in Appendix A. Due to Toner particles are considerably soft and have a melting point of around 60 to 70 °C, in this case the melting point (softening point) of the particles is reported to be 90 °C.

Toner particles of size range up to 15 µm were used at different concentration levels in lubricant Sample A (Sample A2). The particles were dispersed in the lubricant using by means of a sonication process that served as both degassing and dispersion mean. The sonication process might rupture the toner particles, but it is assumed that the energy of the process was too low to cause a milling effect on the toner particles, as can also be seen in microscopic images of dry and wet particles in Appendix A. It is however assumed that the load during operating conditions breaks the particle into smaller fractions as it faces 3 body abrasion in the load zone.

The breakdown initiated by toner particles is much shorter than breakdown initiated by the Arizona test dust particles, Figure 106. This can be credited to their smaller size. Since the film thickness is in sub-micron level, individual particles (majority of which are in the size class of 5 to 15 µm) are assumed to break down under pressure and cause particle bridges in between the inner and outer raceways of the bearing. This can be seen by comparing the pulse durations during the current activity, as plotted in Figure 103 and Figure 106 respectively. As it can be seen, the time between the current pulses is much larger compared to that during breakdowns initiated by Arizona test dust.

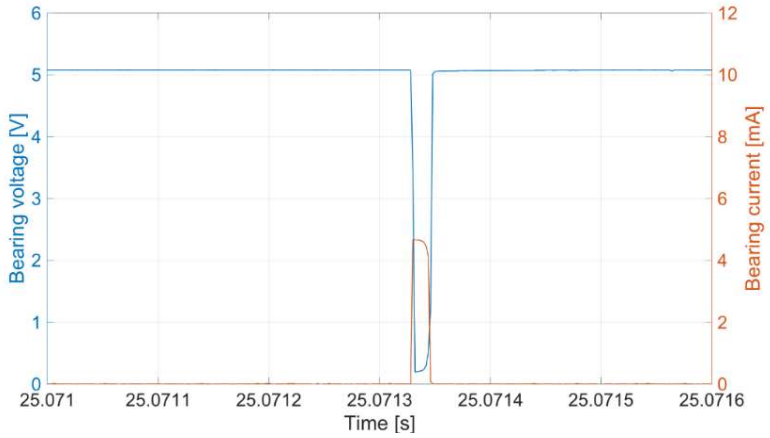

Figure 106. Voltage and current patterns in a bearing type 608 lubricated with toner particles at a concentration level of 150 mg/L. The bearing voltage is shown in blue, while the bearing current activity due to particle-initiated breakdown is shown in orange. The measurement window is 600 µs.

At concentration levels of 150 mg/L and 75 mg/L, the bearing showed significantly less ToC when compared to Sample A1. The ToC did not much with the start-stop sequences neither. This indicates that due to their light weight, the carbon particles do not sink to the bottom so easily and they stay in the liquid bulk. The ToC during three tests for 150 mg/L and 75 mg/L concentrations is showed in Figure 107. In the first case a continuous increase was observed within the first 5 test sequences of Step1 stage. The ToC had an average value of 0.03 %, which corresponds an average of 16 particle-initiated breakdowns per second. The ToC was thus around one order of magnitude lower than that of Arizona test dust at concentration of 7.5 mg/L.

After stopping and starting, the ToC in the Stop 2 stage did not reduce, but at times is found to be higher than the first one. The results suggest that the size and agglomeration due to static charging of the particle could trap the particles in the bearing even after stopping, thus prohibiting them to settle at the bottom of the oil-bath. This was not found in tests with heavier Arizona test dust particles, which are mostly of insulating nature. The toner particles tend to stay in place during the interval while the shaft and the bearing is not rotating. This is also visible in number of particle-initiated breakdowns in the bearing.

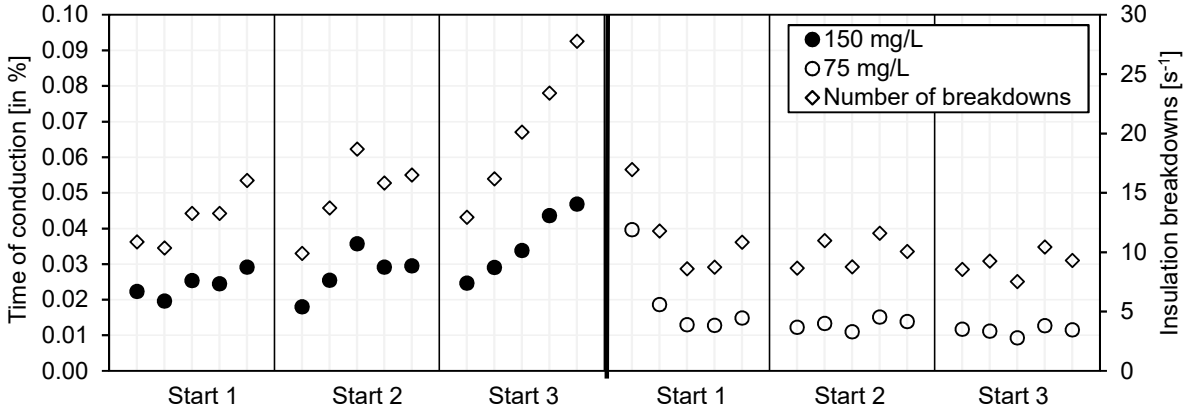

Figure 107. Time of conduction and particle-initiated breakdowns during Start 1, Start 2 and Start3 stages of the test with lubricant contaminated with toner particles at concentration levels of 150 mg/L and 75 mg/L.

The average ToC for all the tests run at particle concentration of 150 mg/L was 0.029 %, while for particle concentration of 75 mg/L was 0.014 %, which is almost half of the former. This is also reflected in higher number of particle-initiated breakdowns. When lubricated with less particle concentrations of 30, 15 and 7.5 mg/L the ToC has reduced by an order of magnitude to average values of 0.005, 0.006 and 0.004 % respectively, as shown in Figure 108. Thus, the ToC also reduced to about half. At such low concentration levels, the dispersion of particle in lubricant could have more influence over the breakdown events in the bearing than the particle concentration itself. The reduction in ToC is also reflected in number of insulation breakdowns per second.

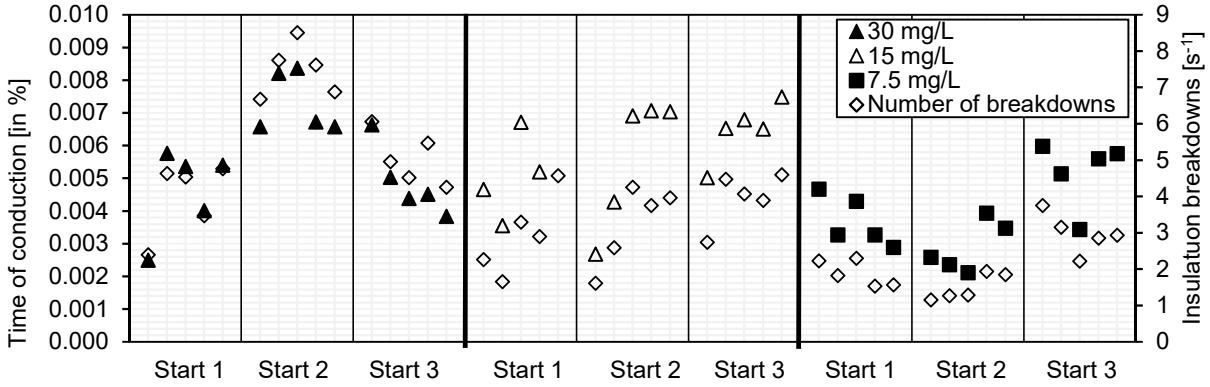

Figure 108. Time of conduction and particle-initiated breakdowns during Start 1, Start 2 and Start 3 stages of the test with lubricant contaminated with toner particles at concentration levels of 30 mg/L, 15 mg/L and 7.5 mg/L.

8.4.3 Aluminium powder

The aluminium fine power is visibly of larger diameter compared to the previous two contaminants. The size distribution and other relevant properties of aluminium powder is detailed in Appendix A. The aluminium particles are assumed to be not oxidised, since the lubricant sample were prepared and sealed. Particle concentration of 150 mg/L is used in tests.

A typical trace of breakdown due to aluminium particles is shown in Figure 109, where the bearing voltage during the breakdown and the corresponding current activity are shown. The current activity initiated due to aluminium particles is stronger than in the case of toner particles, but is lesser as compared to Arizona tests dust case. The breakdowns are also more complex, as the fluctuation in the current activity shows rises and falls of current during a single discharge event.

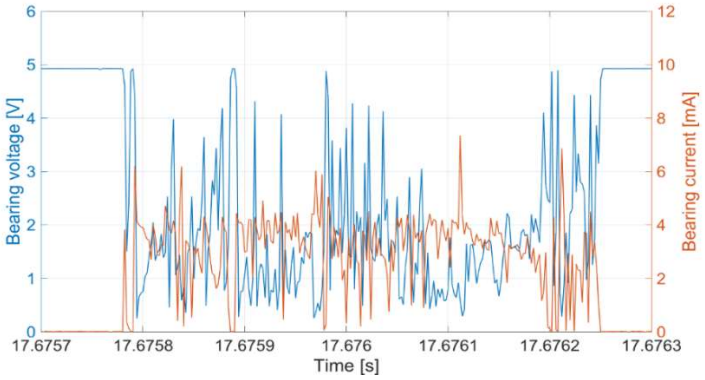

Figure 109. Voltage and current patterns in a bearing type 608 lubricated with aluminium particles at a concentration level of 150 mg/L The bearing voltage is shown in blue, while the bearing current activity due to particle-initiated breakdown is shown in orange. The measurement window is 600 µs.

The ToC has a mean value of 1.52 % for the first two tests of Start 1 stage, while it drops below 0.38 % for the last three tests. This corresponds to a sharp decrease in number of particles bridges formed between the inner and the outer raceway of the bearing. The number of recorded particle-initiated breakdown per second reduces from 845 in first test to 217 (average value of last three tests). In the subsequent tests after stopping and starting, the ToC reduced further to an average

value of 0.105 % in Start2 stage and after Start3 stage to 0.030 %. The drop of ToC could be attributed to the weight of the aluminium particles, which settle at the bottom of the lubricant bath. The decrease is also visible in the recorded number of insulation breakdowns per second, which is found to be at an average of 17 breakdowns per second in Start 2 stage and 3 breakdowns per second in Start 3 stage.

Figure 110. Time of conduction and particle-initiated breakdowns during Start 1, Start 2 and Start3 stages of the test with lubricant contaminated with aluminium particles at concentration level of 150 mg/L.

8.4.4 Iron powder

Fine iron powder was also used to check the conduction in the bearing. The method to prepare the bearing was similar to the previous cases. The ToC was studied for iron particles since they are fine in nature, like toner particles, but much finer than aluminium particles.

The breakdowns initiated due to iron particles are comparable to those caused by Arizona test dust in terms of the level of ToC. During the tests, that the ToC systematically reduced with each measurement, along with the number of particle-initiated breakdowns per second, which suggests that the iron particles in the bearing's loaded zone reduce steadily with time, shown in Figure 112.

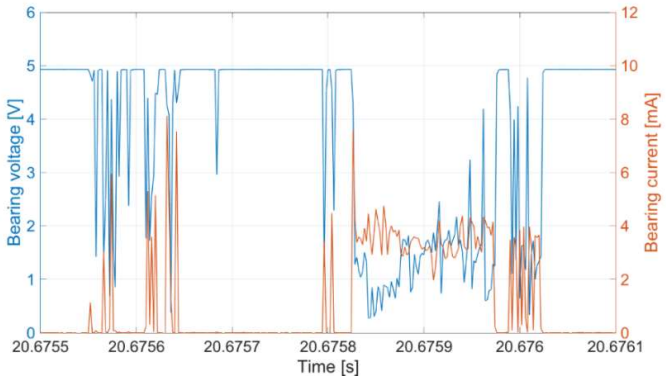

Figure 111. Voltage and current patterns in a bearing type 608 lubricated with iron particles at a concentration level of 150 mg/L The bearing voltage is shown in blue, while the bearing current activity due to particle-initiated breakdown is shown in orange. The measurement window is 600 µs.

The ToC was relatively high during for the first test of Start1 stage (about 8.24 % and 8258 insulation breakdowns per second), but subsequently dropped to lower value of 2.8 % (3278 insulation breakdowns per second) in the fifth test of Start 1 stage. After stopping and re-starting the second test run (Start 2 stage), the ToC starts with 2.03 % (2539 breakdowns per second) and ends at 0.52 % (652 breakdowns per second). In Start 3 stage, the ToC is 0.37 % (469 breakdowns per second) in first test and ends with 0.12 % (141 breakdowns per second) in last one.

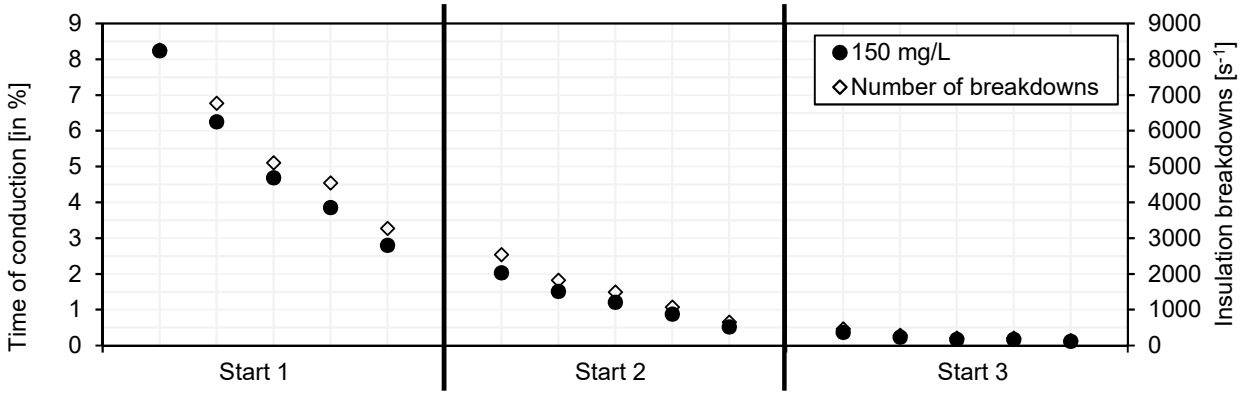

Figure 112. Time of conduction and particle-initiated breakdowns during Start 1, Start 2 and Start3 stages of the test with lubricant contaminated with iron particles at concentration level of 150 mg/L

- **Particle-initiated breakdowns due to electrical degradation in oil**

Electrically degraded lubricant was specially prepared by electric arcing and contained charred particles in the lubricant. Due to this, the oil was discoloured from transparent to dark-yellow with visible particles possibly originating from the electrodes and the carbonisation of oil. The bearing did not show any conduction when run with the degraded lubricant.

8.5 Breakdown mechanism - Voltage and field dependent breakdowns

The voltage and electric field dependent breakdowns were also studied by using bearings with different types of lubricants, yielding two different ranges of lubricant film thickness at a given operating point. The bearings were operated at a speed of 2000 rpm and an axial load of 4 N. For this investigation, the current activity in the bearing lubricated with grease E is compared with the current activity in the bearing lubricated with Sample A. The lubricating film thickness of the former is evaluated to be 0.266 μm and for the latter one 1.34 μm, both calculated at an assumption that the temperature during operation is 20 °C.

8.5.1 Bearing lubricated with Sample E

For comparison, the tests determining the transition of 608 type bearing from insulating state to conducting state is repeated. The bearing has ToC of 0.6 % at electric field stress of 15 V/μm. As stress is increased, the current conduction through the bearing increases drastically. The apparent electric breakdown field strength for the bearing pre-lubricated with Sample E is found between ~20 V/μm and ~28 V/μm. The breakdowns occur at low amplitudes of applied DC voltage, i.e. between 4 V and 7 V. The total lubricating film thickness is very small (comp. Figure 38), hence the high evaluated electric field strengths. The bearing current activity initiates at electric field strength of ~20 V/μm, while at ~28 V/μm the bearing makes transition to fully conducting state

($E_{90\%ToC}$). The bearing goes in conduction state in a narrow window of voltage increment, of 3 V. As each voltage level was applied for 30 s, the bearing goes from partially conducting to fully conducting state in about 150 s. The ToC at different voltage levels was earlier shown in Figure 69, but the ToC as a function of apparent electric field strength in the bearing is shown Figure 113.

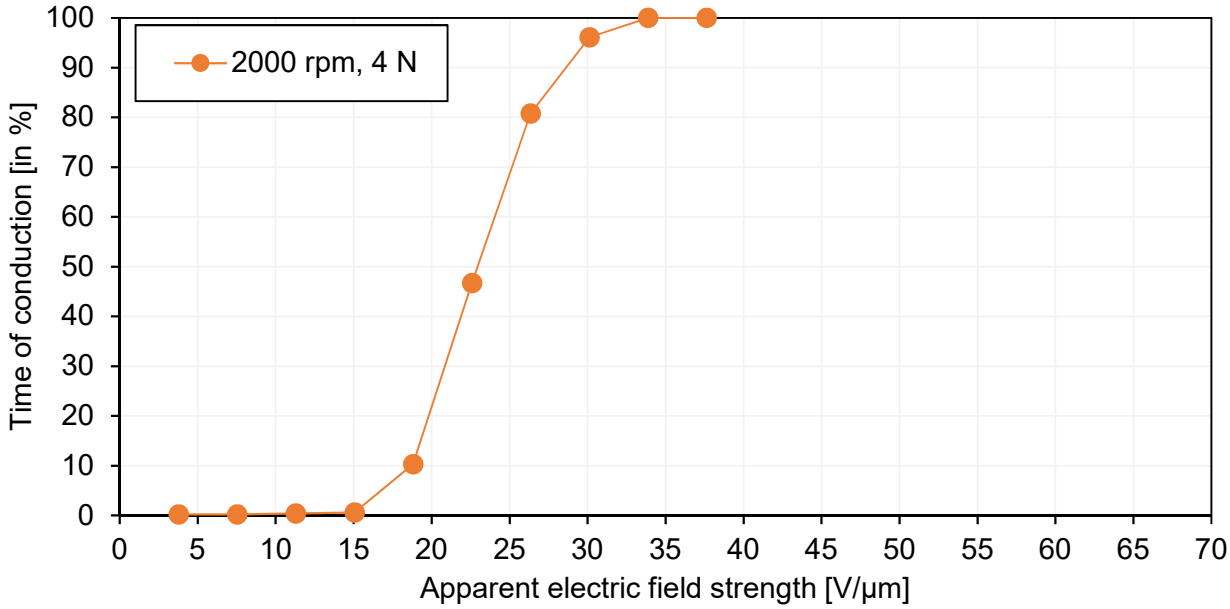

Figure 113. Time of conduction in a likely starvation regime for a pre-lubricated with grease E bearing type 608 operating at speed of 2000 rpm and axial load of 4 N. The transition of the bearing from insulating state to conduction state is shown by the orange line and occurs when electric field strength in the film is between ~20 V/µm and 30 V/µm.

8.5.2 Bearing lubricated with Sample A

A new test bearing was prepared after cleaning (see Chapter 8.4) and running-in process for 2 hours. The speed was set at 2000 rpm and the load at 4 N. The film thickness is calculated to be 1.34 µm at these operating conditions. After an interval of 30 s, a DC voltage was applied to the bearing in steps of 5 V and the bearing voltage and the bearing current activity was monitored and recorded using DAC. The ToC was calculated as an average value of 5 measurements, each lasting for 30 s and is shown in filled blue dots in Figure 114, while the empty dots show the ToC of the individual 5 measurements. The total measurement time spent on each voltage level is about 150 s. At 5 V the ToC has an average value of 0.0012 %. Thereafter the current activity gradually increases with each measurement at a given voltage level. At 30 V and 35 V, the estimated apparent electric field strength in the lubricant is calculated to be 22.3 V/µm and 26.0 V/µm. The ToC seems to increase four to five times at 35 V, compared to current activity at 25 V level. Thus the bearing current activity shows an increase with increase of the applied voltage, even when the bearing is not in fully conducting state (100 % ToC). At applied voltage of 35 V, although the ToC is still very low (< 0.08 %), the bearing can be said to be partially conducting every now and then.

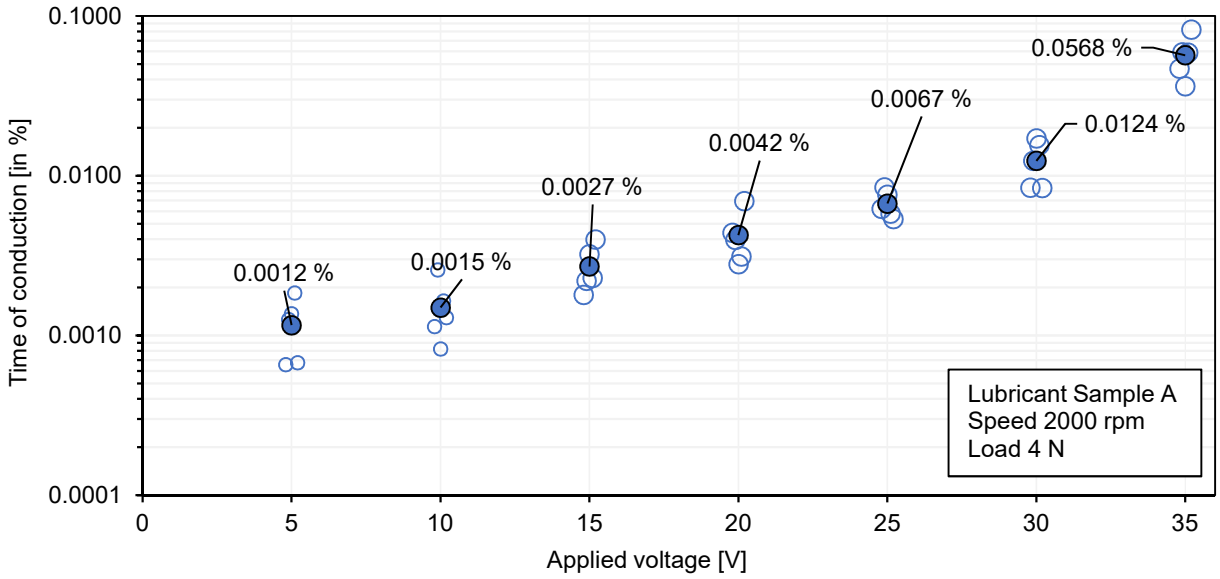

Figure 114. Voltage of time of conduction in bearing type 608 lubricated with Sample A. ToC on y-axis is shown in log scale.

As the applied voltage is 40 V, the electric field strength is 29.7 V/µm. At this high voltage level, the bearing current activity increases to 0.8 % in the first test that lasted for a duration of 30 s and was measured to be 16 % in the second test, which again lasted 30 s, shown in Figure 115. The bearing reached 86 % in ToC during test 3 and full breakdown state (of 94 and 96 %) in tests 4 and 5. At 40 V the bearing reached the mostly conducting state in a test lasting for 150 s, from 0.8 % to 96 % and the approximate electrical field strength in the lubricant was 29.7 V/µm. Thus, the bearing has gone from partially conducting state of less than 1 % ToC, to more than 90 % ToC within a few volts window. The apparent electric field strength for a bearing to reach a full conduction state is 29.7 V/µm when lubricated with Sample A, while it is ~28 V/µm for the pre-lubricated with grease Sample E bearing, shown in Figure 113. Thus, the breakdown phenomena at speed of 2000 rpm for both, the pre-lubricated bearing and a bearing immersed in oil bath can be assumed to be similar. In comparison, a pre-lubricated bearing 608 exhibited memory effect at electric stress of 23 V/µm at speed of 3000 rpm and load of 4 N.

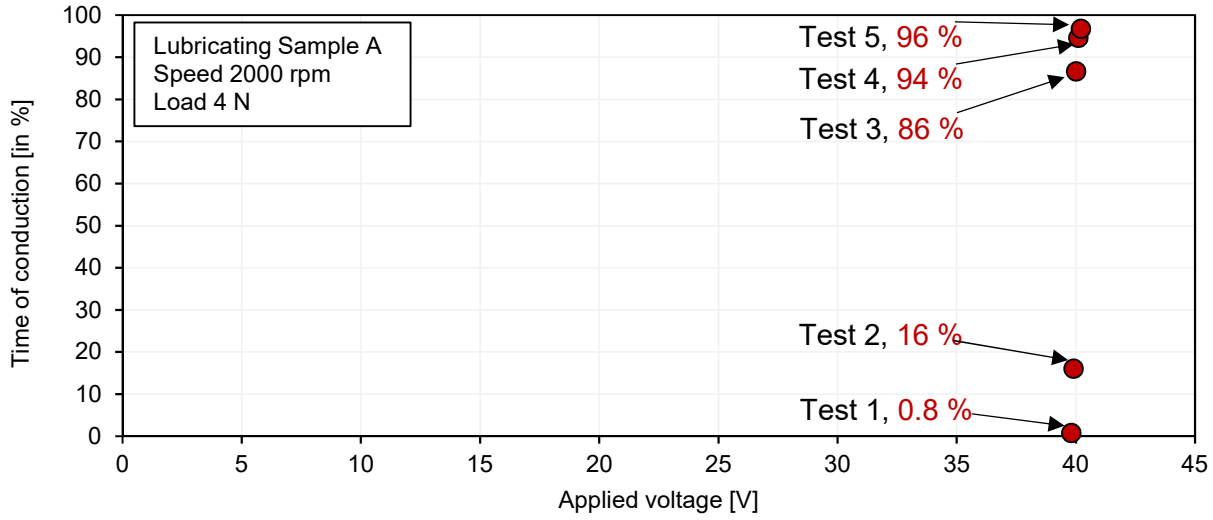

Figure 115. Full breakdown of bearing type 608 lubricated with Sample A occurring at 40 V.

Once the bearing was in fully conducting state, the applied voltage was step wise decreased in steps of 5 V. The bearing current activity was monitored for checking if a memory effect takes place in recovery of bearing's insulating properties. At 35 V, the bearing conduction state was at 82 % in the first test and then gradually increased to 93 % in the fifth test. Here, a strong memory effect is seen, as earlier discussed in Chapter 8.2.2. The whole measurement sequence is illustrated in Figure 116. Thus, in the considerations referring to the electrical circuit model of the bearing, the bearing clearly does not return to an *open switch* position after an intense current activity, even as the applied voltage is reduced.

The memory effect reduces the threshold voltage and the apparent electric field strength necessary for initiation of bearing current activity. As five tests were conducted at every voltage level, where each test lasted for 30 s; it was observed that the ToC increased from test 1 through 5 at a fixed value of applied voltage, as seen in Figure 116. This shows that the bearing conducts more and more after losing its insulating ability. At 30 V, the ToC is 42 % and increases for the next 3 data points up to 58 %, but again reduces to a value of 53 % at the last test point. As the voltage is further decreased to 25 V, the ToC now reduces instead of increasing. The approximate electric field strength in the lubricant at 25 V is 18.6 V/µm. The ToC in the first test of 30 s is 7 % and reduces to 2 % in the last test. At 20 V, the ToC is 0.1 % and has a standard deviation of 0.02, indicating that the bearing current activity in the five tests is rather steady. At 15 V, the ToC after intense current activity is 0.02 % higher than the ToC before the current activity. At voltage levels of 10 and 5 V, this difference is reduced to 0.004 and 0.05 % respectively. The memory effect is thus mainly seen in the red circled area of Figure 116, since a higher ToC is found in decreasing the applied voltage, compared to when applying step-wise increasing voltage.

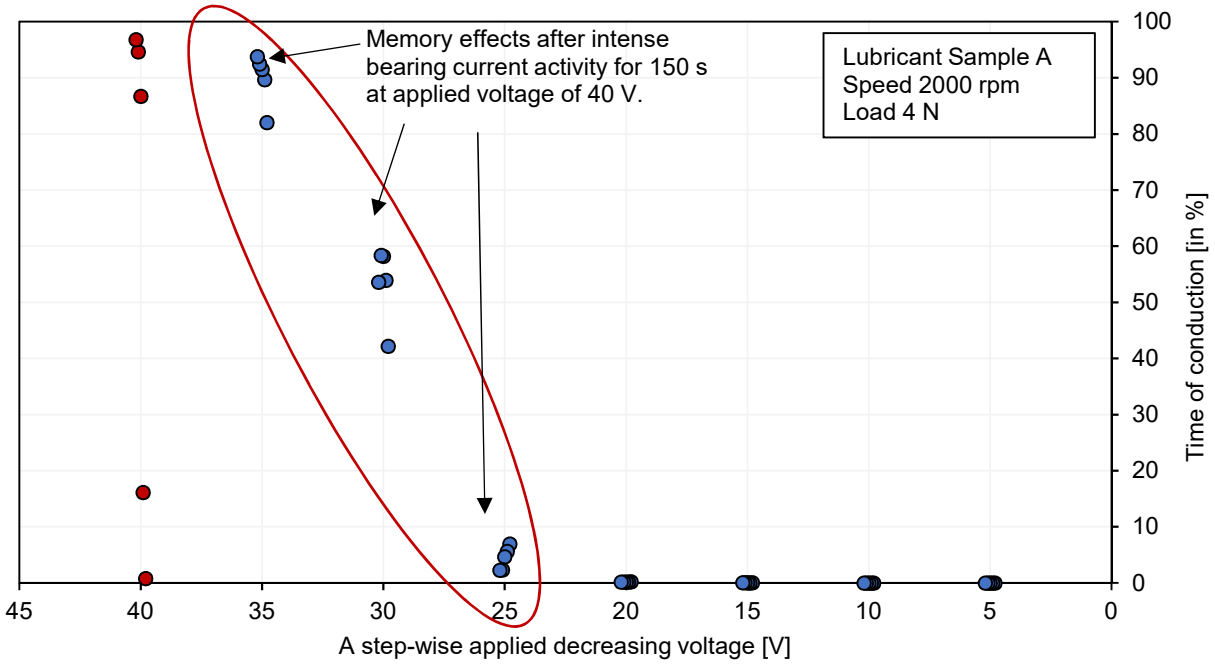

Figure 116. Memory effect in bearing type 608 lubricated with Sample A at step-wise decreasing DC voltage. After intense bearing current activity, the bearing also conducts at lower voltages, where bearing current activity was insignificant before the intense bearing current activity.

The criteria for breakdown in terms of estimated electric field strength show that the conduction sharply increases beyond the electric field strength of ~30 V/µm, a value also found during investigations earlier presented in Chapter 8.2. The current conduction through the bearing when presented in terms of ToC looks similar to current conduction in insulating liquids under the application of high electric fields.

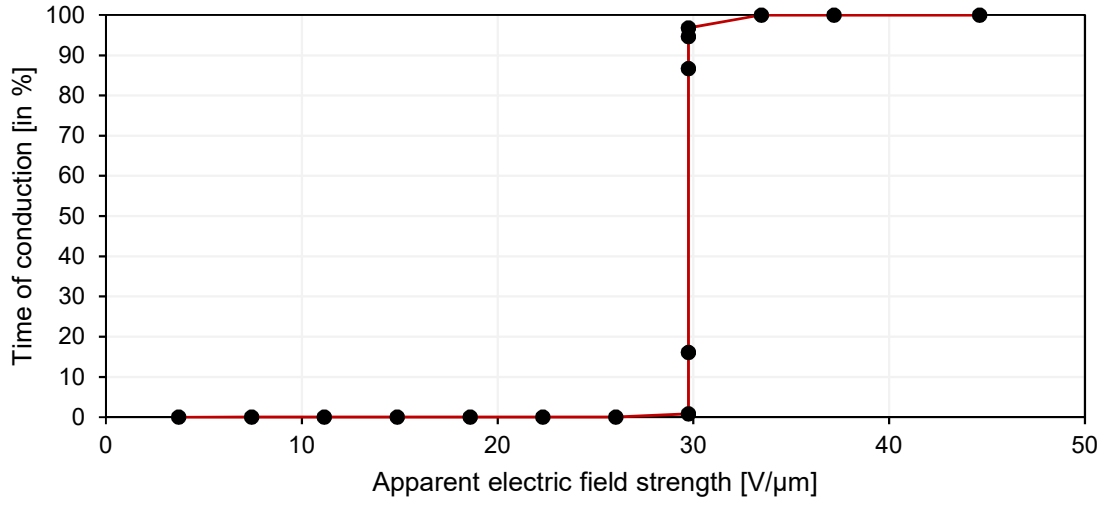

Figure 117. Field dependence of ToC in bearing type 608.

The breakdown mechanisms in liquid dielectrics still remains not completely understood and the present knowledge points towards two school of thoughts. The first theory attempts to explain the

breakdown in liquids as an extension of the theory of breakdown in gases, which is based on avalanche formation after ionisation of atoms due to collision by electrons under the effect of electric field. The electrons are injected in the liquid bulk through field emission due to electron tunnelling or by field enhanced thermionic effect, commonly referred to as Schottky effect. The second theory proposes bubble formation due to excessive overvoltage, also termed as negative discharges [96]. The breakdown electrical field strength of *high purity insulating oils* is in the range between 1 and 4 MV/cm (100 and 400 V/µm) [102]. The bearing is constantly rotating and its surface contains many micro asperities bringing in local enhancement of electric field. This results in injection of electrons in the lubricant due to field emission process, which take part in the discharge process. The increase in conduction current due to high electric field occurs at much smaller values of the average electric field (~30 V/µm).

In liquids, the mean free path of the travelling electron is much shorter than gases, in order of 0.01 µm and ionisation potential of 10 eV is necessary to ionise liquid molecules [103]. The electrons are emitted into pure liquids when electric field strength attains 10 V/µm and get multiplied by primary emission processes, similar to avalanche breakdown theory in gases. The breakdown voltage depends on the field, gap separation, cathode work-function and the temperature of the cathode. In addition, the liquid viscosity, the liquid temperature, the density and the molecular structure of the liquid also influences the breakdown strength of the liquid [102, 103].

9 Bearing resistance, R_B

In the proposed equivalent electrical circuit model, bearing resistance, R_B represents its resistance in conducting state. In the below presented investigations, instantaneous values of the bearing resistance are calculated for individual breakdown events, using the measured instantaneous values of bearing the voltage and current, as recorded during the breakdown. The measurements are performed at 5 V DC under current limiting conditions.

9.1 Bearing resistance during frequent asperity contacts

The amplitude of the applied voltage was kept constant to make the results at different operating points comparable. Bearing type 608 was used and was lubricated with grease Sample D. A low resistive paths were formed due to occurrence of asperity contacts at low speeds, while at high speeds, other mechanisms such as an electric breakdown of lubricating film, particles initiated breakdowns could lead to formation of the low resistance path.

It was observed in our experiments that the mean value of R_B during a discharge event varied stronger at lower speed of 200 rpm than at a higher one of 500 rpm. In the latter case the bearing resistance during the conducting state was rather constant, as can be seen by comparing the graphs in Figure 118.

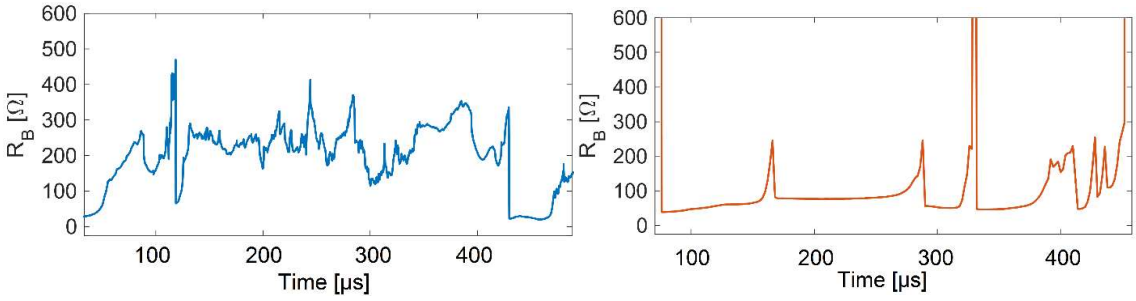

Figure 118. Example of time variations of instantaneous resistance of bearing type 608 at speeds of 200 rpm (left) and at 500 rpm (right).

For illustrating the behaviour of R_B during high friction regime of a bearing at an operating point, a large number of breakdowns is analysed and represented by means of box plots. Each discharge event is characterised by three parameters, the minimum value of R_B during the event, the median value of R_B during the event and the current pulse duration. The red markers at the centre of the box show the median value of R_B. The top and the bottom edges of the box indicate the 75th and the 25th percentiles respectively. The whiskers, which show ±2.7σ and thus cover 99.3% of the distributed data do not include the outliers., The latter could reach several 1000's of Ω, resulting in a strong change graph scale of the graph. The outliers could amount to up to 10 % of the number of points in the complete dataset.

The minimum and median values of R_B at load of 4 N and at different speeds is shown in Figure 119. The data are positive and skewed to the right, or have a positive skew as presented in Figure 119. In the opinion of the author, the minimum value of R_B could be an indication of the number of paths formed in the bearing during the instantaneous breakdown. As the speed increases, the

number of asperity contacts reduces, thus also reducing the number of instantaneous parallel current paths and yields an increase in the measured R_B.

The minimum value of R_B is much normally distributed, especially at lower speeds and is having a median value of 28 Ω at 200 rpm and attains a slightly higher value of 43 Ω at 1000 rpm. The increase of minimum value of R_B almost doubles at higher speeds. The duration of pulses due to asperity contacts are shown in right graph of Figure 119. The median value of pulse duration reduces from about 270 µs at 200 rpm to 16 µs at 1000 rpm, while the overall duration of conduction state reduces from a few 1000's of µs at 200 rpm to about 16 µs at 1000 rpm, a reduction by three orders of magnitude.

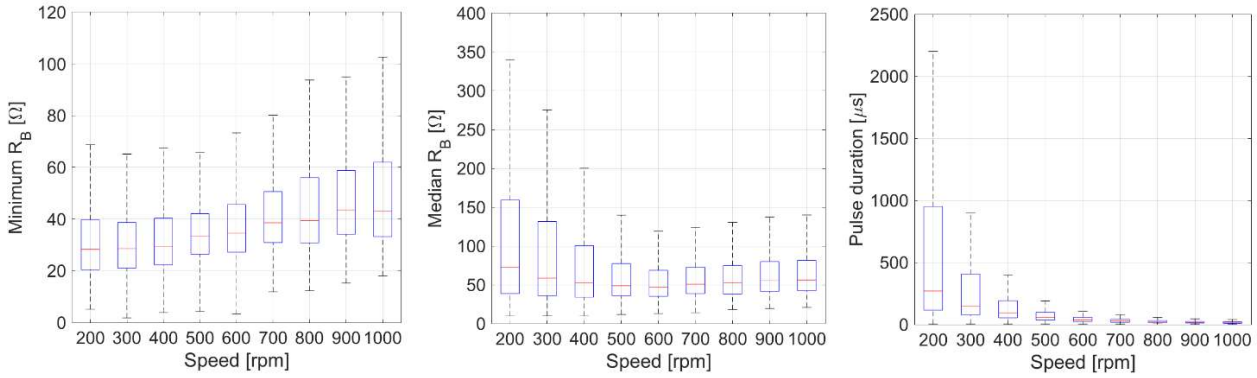

Figure 119. Box plots showing minimum (left) and median (centre) values of bearing resistance R_B at a fixed axial load of 4 N and at speeds up to 1000 rpm. Duration of breakdown pulses (right) is also displayed. No current activity was observed between 2000 and 4000 rpm.

The median value of R_B has largest values and spread at lower rotational speeds between 200 to 500 rpm, when compared to higher speeds. Larger spread in median value of R_B at lower speeds can be credited to loads carried by asperities, i.e., metal to metal contacts. The median value of R_B at speeds of 200 and 300 rpm was 72 Ω and 58 Ω respectively. At speeds between 400. 1000 rpm, the median value of R_B was in the range of 50 Ω.

At the higher axial load of 40 N, the dominating effect is visible clearly at speeds below 500 rpm. The minimum value of R_B almost reduced to half value when compared to measurements at 4 N. The median value of minimum R_B varied between 10 Ω at 200 rpm and 20 Ω at 1000 rpm, shown in left most plot of Figure 120. The decrease in bearing resistance at a higher load could be accredited to the increase in contact surface area, which is proportional to the axial loading on the bearing. This is also accompanied with almost doubling of pulse duration and is mainly observed at speed of 200 rpm.

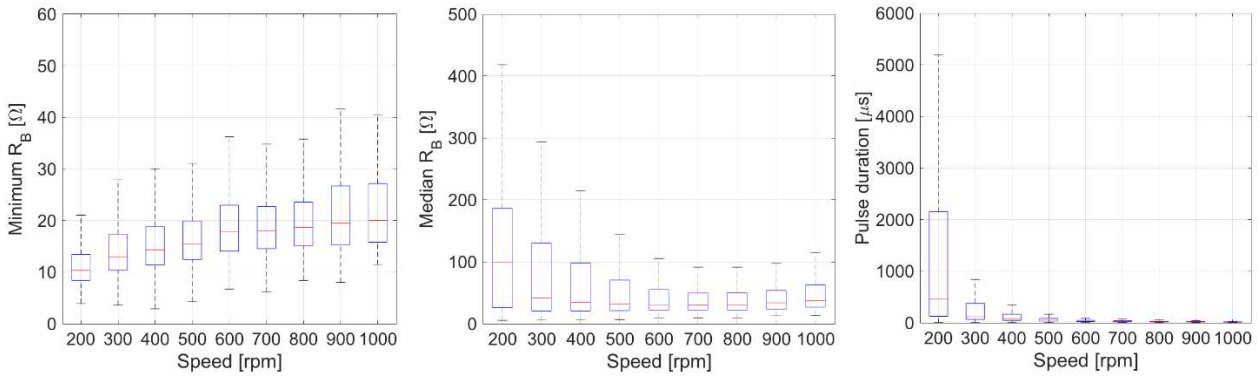

Figure 120. Box plots showing minimum (left) and median (centre) values of bearing resistance R_B at a fixed axial load of 40 N and at speeds up to 1000 rpm. Duration of breakdown pulses (right) is also displayed. No current activity was observed between 2000 and 4000 rpm.

It is reported in literature [126] that both the speed and the film thickness have considerably stronger impact on bearing resistance in conducting state as compared to the mechanical load on the bearing. The doubling of R_B is only visible in the minimum value box plots and not in median value ones. The median values of R_B are for both the load cases is fairly similar and does not show much variation.

9.2 Bearing resistance during particle-initiated breakdowns

Bearing of type 608 was lubricated with liquid lubricant Samples A, A1, A2, A3, A4 and A5 for investigating the effect of particle contamination on electrical breakdowns. The operating point of the bearing was kept constant for all the tests and speed of 2000 rpm and an axial load of 4 N was chosen to ensure hydrodynamic lubrication during operation.

The operating parameters were held constant and 5 V was applied to the bearing.

The reference tests were made using fresh lubricant of Sample A. The testing with a given lubricant sample included effects of starts and stops on the measured parameters of the electrical circuit model and a resting period of 2 minutes was maintained in between the tests, as described in the previous chapter. Up to three start-stop sequences were performed with each concentration level of the lubricating samples and the results are plotted as a function of the start-stops. Each start has a series of 5 consecutive measurements to possibly see stead state conditions during operations. For example, for Start 1, the series of 5 tests are denoted from Start 1.1 to Start 1.5 in the plots.

For these investigations, the maximum particle concentration was chosen to be 150 mg/L, which is a threshold for contamination according to recommendations provided by Elforsk [40]. Electrically degraded lubricant Sample A5 was also used in these experiments. Sample A5 was synthetically electrically aged using high voltage supply. The idea behind using electrically aged lubricant was to see if the carbonised molecules of the lubricant would cause similar phenomena to breakdowns caused due to toner contamination (lubricant Sample A2). The measurements showed that no breakdowns occurred due to electrically aged lubricant at an applied voltage of 5 V, indicating that the carbonised particles are much smaller than the lubricant film thickness breakdowns.

Bearing resistance measured for different particles at a fixed concentration level of 150 mg/L revealed that median value of bearing resistance ranges between 28 Ω to 63 Ω in case of Samples A1 and A2, while it is about 5 to 10 times higher for Samples A3 and A4, as shown in Figure 121. For Sample A1 the median value of the bearing resistance remains at while the 75th and the 25th percentile values at 54 Ω and 20 Ω. The measured R_B remains rather constant and does not change with the number of starts of the bearing and the test sequence. This can be attributed to standardised particle size of Arizona test dust.

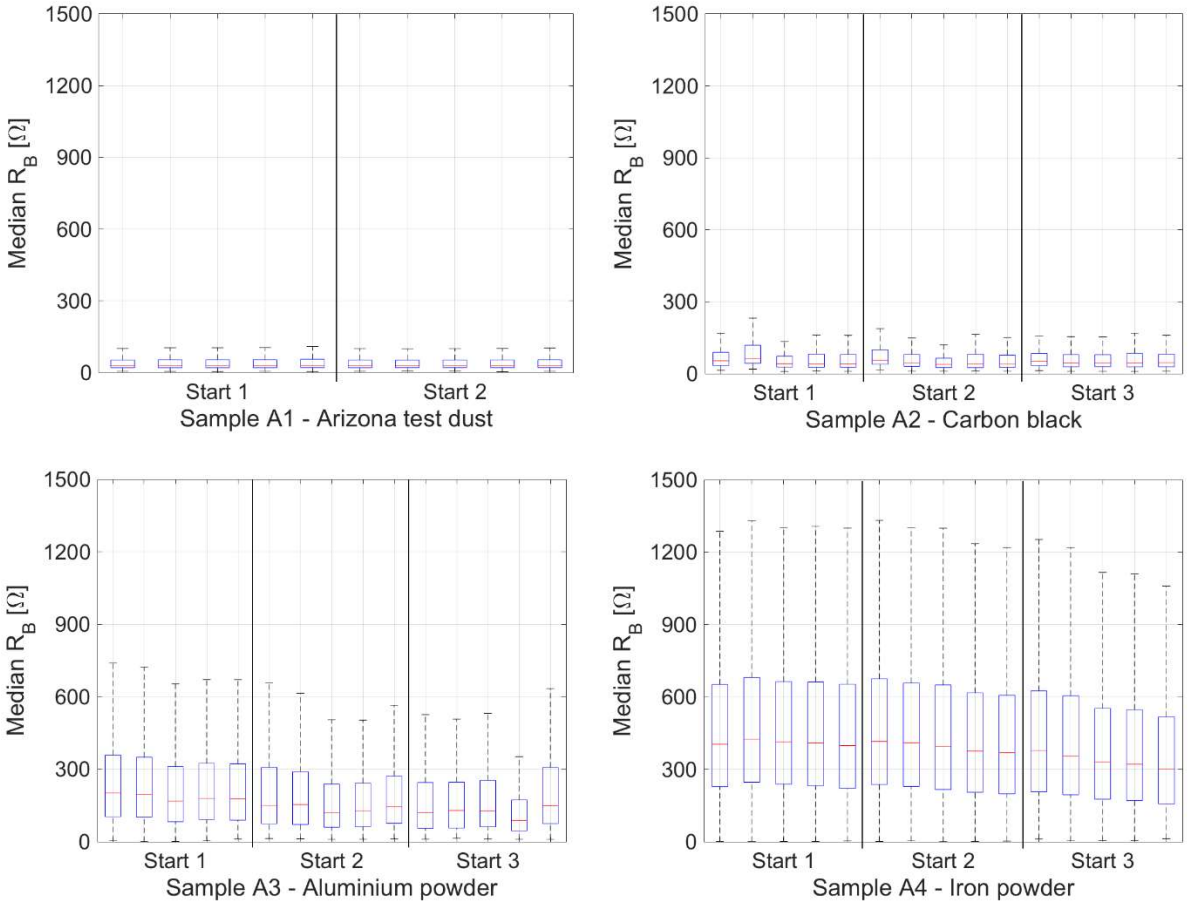

Figure 121. Median values of bearing resistance at particle concentration of 150 mg/L for different types of particles.

The contamination particles caused the breakdown events for more or less the same duration, as shown in Figure 122 and hence the 75th percentile value of the measured pulse duration during the particle-initiated breakdowns ranged up to 30 µs, while maximum values reached up to 60 µs in case of aluminium powder. The aluminium powder particles were larger than all other particles tested and hence stayed longer in the load zone until they fractured into smaller ones.

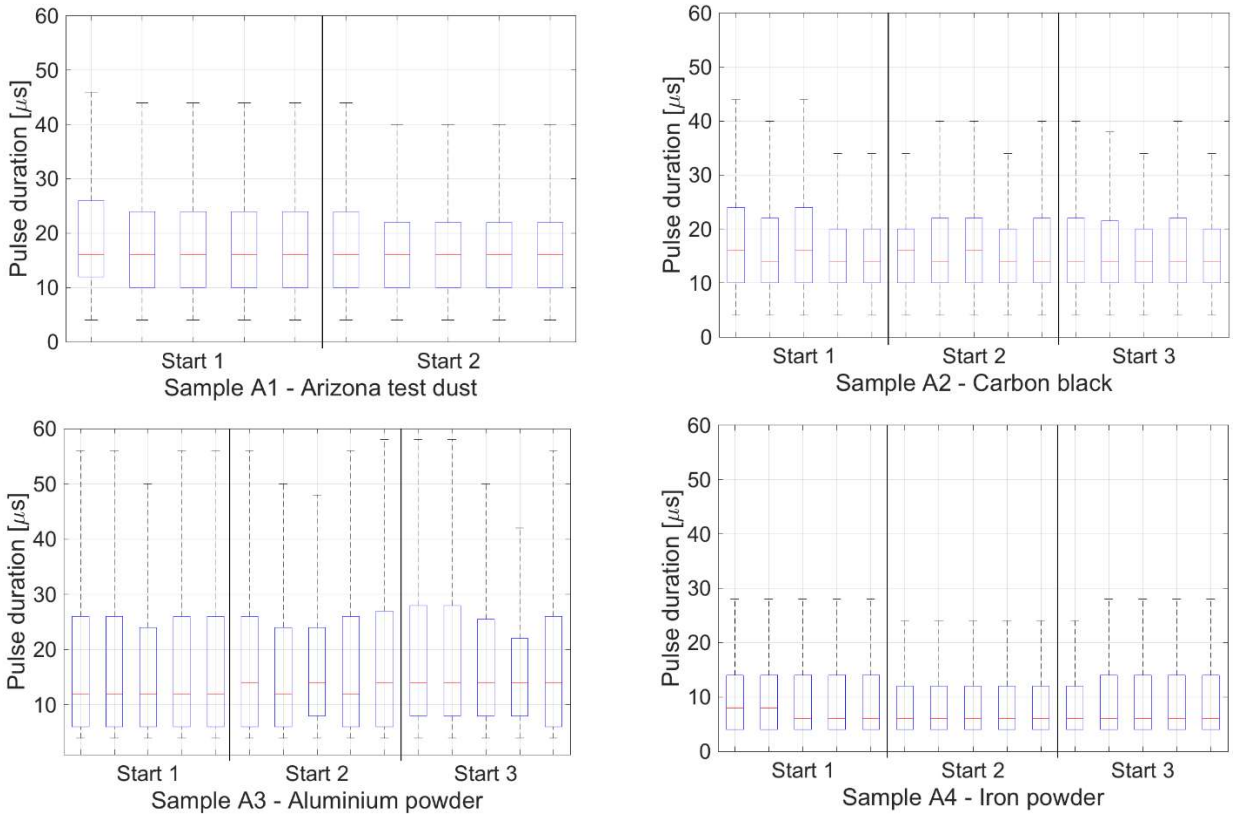

Figure 122. Median values of pulse duration during insulation breakdowns caused by different types of particles, at a fixed concentration of 150 mg/L. The median values pulse duration stays approximately in the same order of magnitude for all different types of particles, but large spread is seen with Sample A3 that could be an effect of large sized particles.

Minimum value of bearing resistance for different types of particles varies significantly. This could be due to different ranges in which external particle are found. During an event of breakdown, minimum value reached by R_B is found to have a median of 17 Ω in these tests, while the smallest value that R_B could reach less than 1 Ω and is shown in Figure 123.

9.2.1 Bearing resistance due to Arizona test dust particles

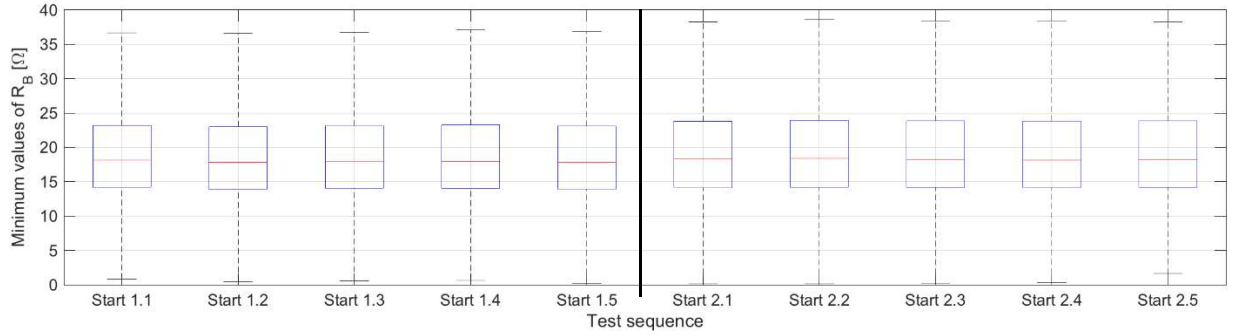

Figure 123. A plot of minimum value of R_B reached during breakdown events initiated by Arizona test dust contaminant at a concentration of 150 mg/L.

The particle-initiated breakdowns in these tests resulted in measured median value of pulse duration to be 16 µs, while values were found to be up to 46 µs, shown in Figure 124. The 75th and the 25th percentile of the presented data ranges between 26 µs and 10 µs respectively. The maximum value of the pulse duration is measured to be 682 µs in Test sequence 1.5 and is not shown in the plot below. This shows that the insulation breakdowns initiated due to Arizona test dust particles remain constant despite of the starts and stops of the bearing.

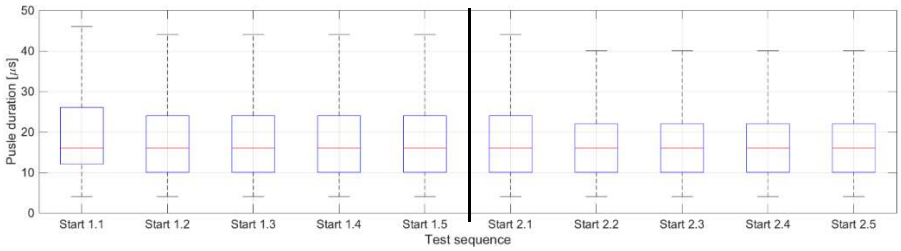

Figure 124. Pulse duration of the current pulses caused due to breakdowns initiated by Arizona test dust contaminant at concentration level of 150 mg/L in lubricant Sample A1.

Upon reducing the particle concentration to 75 mg/L, the bearing resistance is showing some variation in the median values of the recorded breakdowns. These values vary between 27 Ω and 44 Ω. The variation is also visible in the 75th and the 25th percentile values of the data and are equal to 72 Ω and 20 Ω respectively.

As particle concentration is further reduced, the resultant bearing resistance remains more or less remains on the same level. It increases slightly and the median value is up to 61 Ω in the measurements with lower particle concentration, as can be seen in Figure 125. The pulse duration of the current pulses remains similar and the 75th and the 25th percentiles are found to be up to 10 and 30 µs, shown in Figure 126.

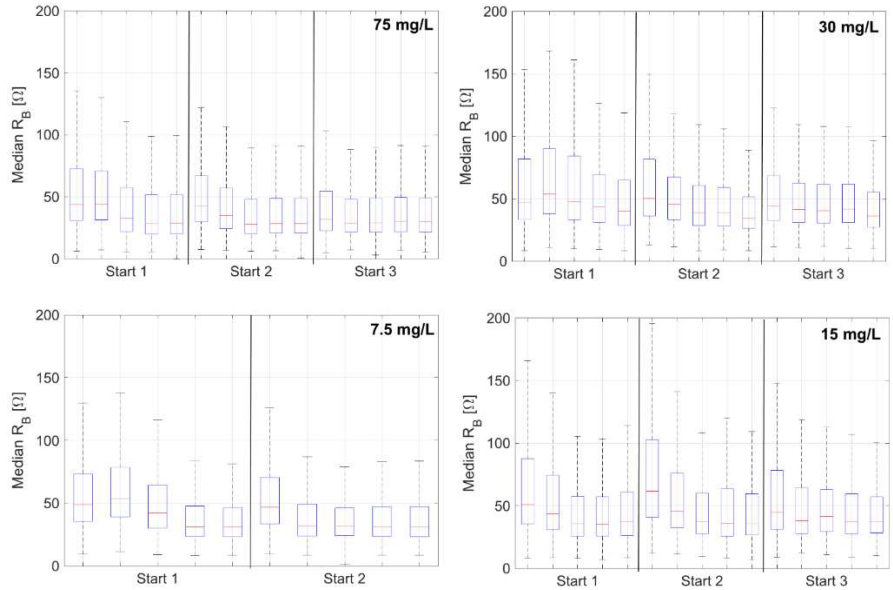

Figure 125. Median values of bearing resistance for Arizona test dust contaminated lubricant at concentration levels of 75 mg/L and below. The x-axis denotes the start stops and test sequence number.

The current pulse duration analysis revealed that the pulse duration of the conduction current pulses are independent and unaffected by the particle concentration, as it can be seen in Figure 126.

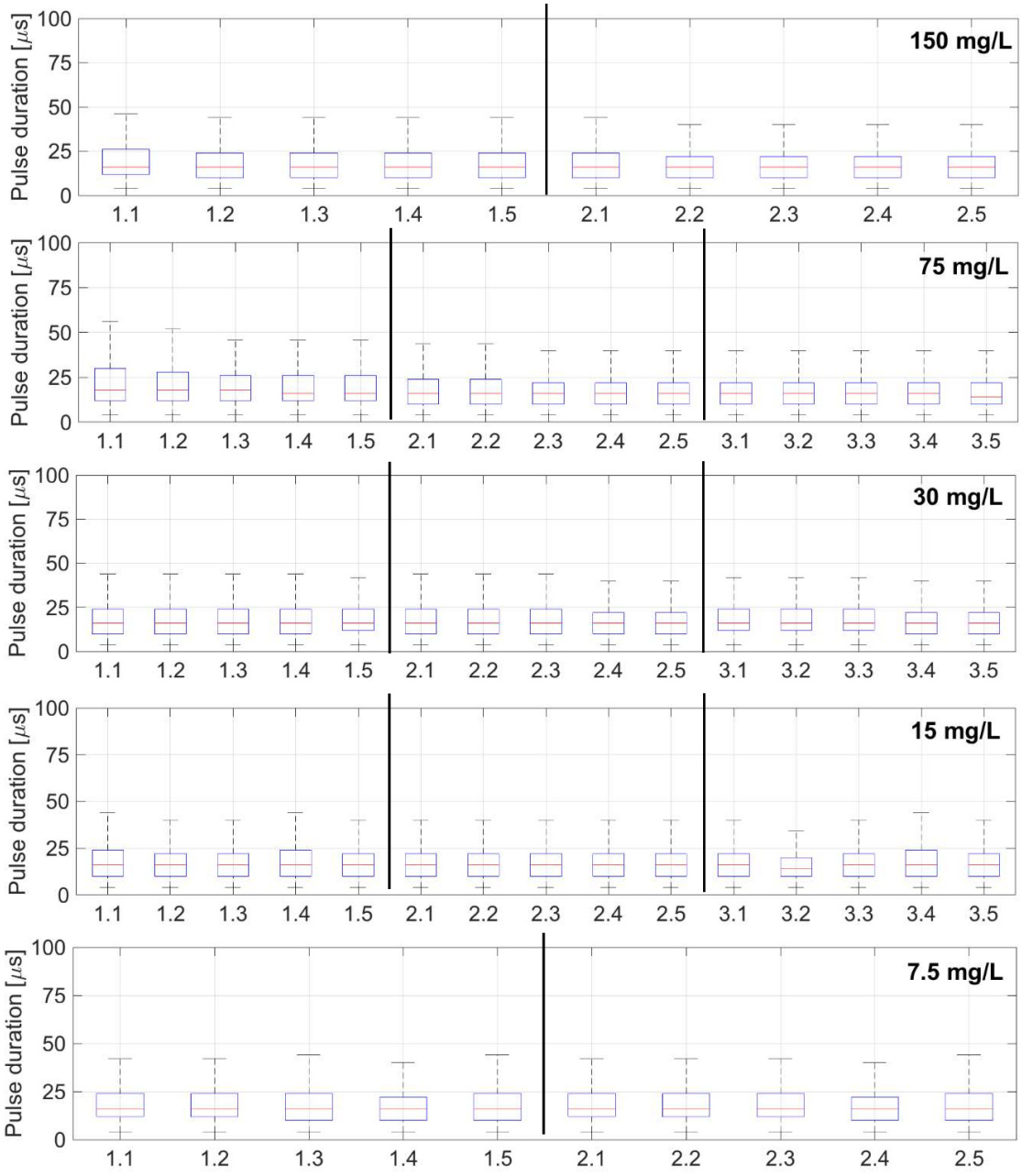

Figure 126. Box plots of pulse duration evaluated from breakdowns under tests with Arizona test dust contaminated lubricant.

9.2.2 Bearing resistance due to toner particles

The breakdown of the bearing due to the contamination of lubricant with the toner particles was also studied at different concentration levels. As seen in Figure 127, the median value of bearing resistance increases slightly as the particle concentration decreased to 75 mg/L and 30 mg/L. The

plausible reasons for this temporary increase in bearing resistance could be due to entering of agglomerated particles into the loaded zone, increasing the resistivity of the conducting bridges.

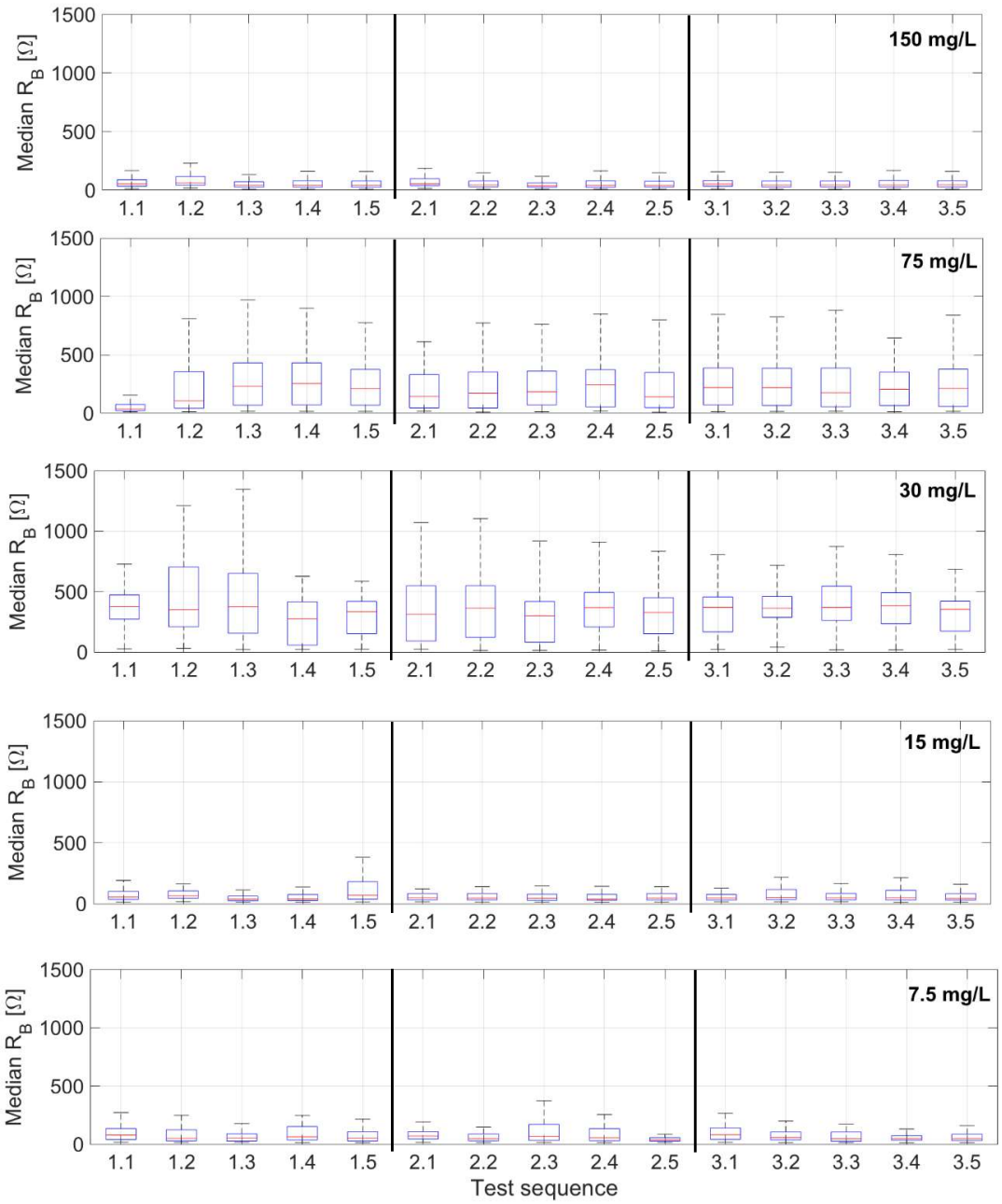

Figure 127. Median values of bearing resistance during breakdowns initiated by toner particles at different concentrations.

The current pulse duration on the other hand does not show much deviation. The current pulses between the 75th and 25th percentile of the data shown in Figure 128, range between 10 to 30 µs, while maximum value is up to approx. 50 µs.

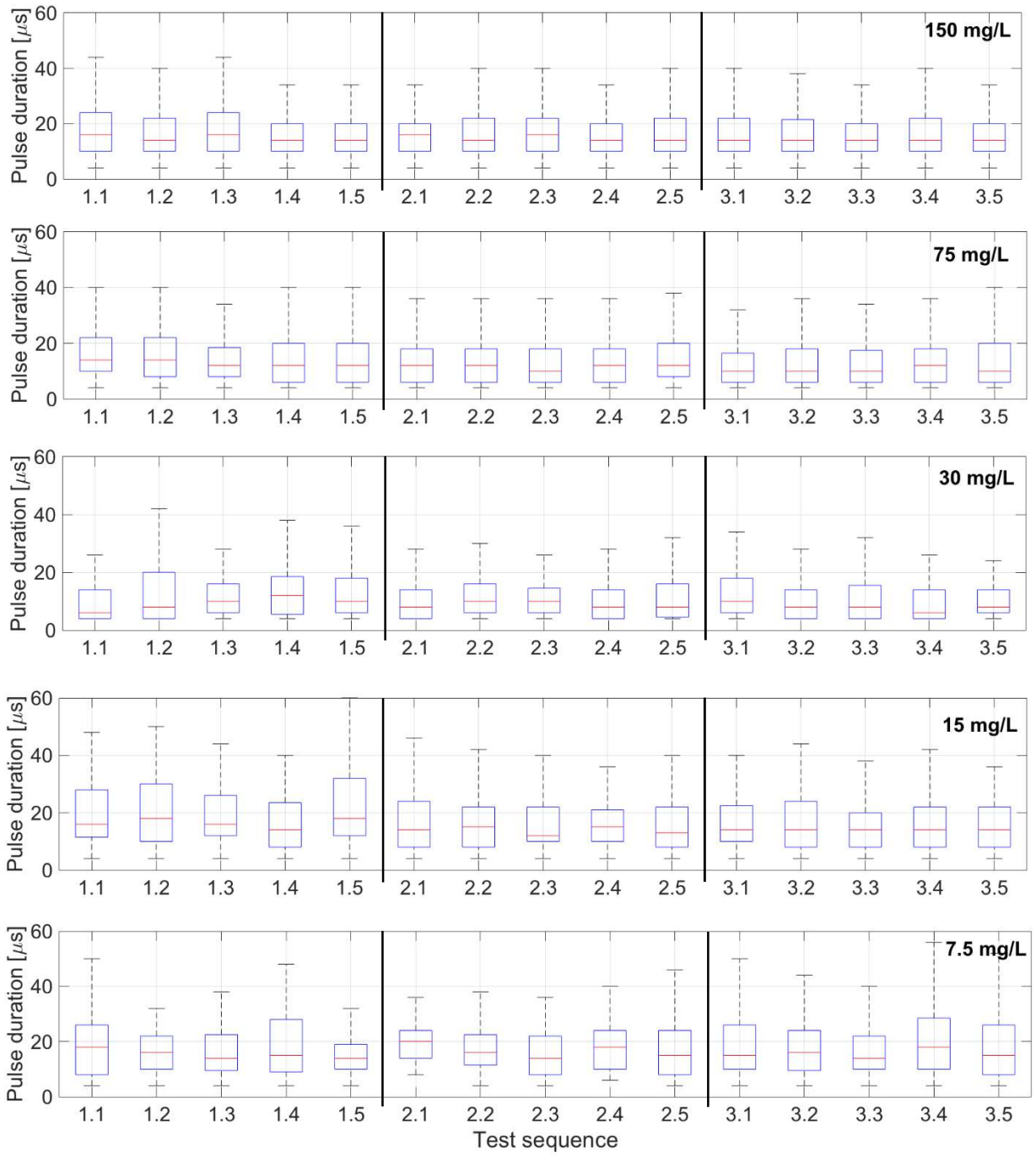

Figure 128. Pulse duration due to toner-initiated breakdowns.

10 Surface morphology of a failed bearing

Analyses and quantification of damage found on the bearing surfaces were performed by means of optical interferometry. The analysed bearing (grease lubricated bearing of type SKF 6324) was obtained from Connected Wind Services A/S (previously Triventus AB), earlier used as drive end deep groove ball bearing of the electrical generator of Vestas V52 wind turbine (asynchronous electrical generator is 850 kW and the DC link voltage is 690 V). The bearing consists of 8 balls and the bore diameter of the inner raceway of 120 mm. The average surface area of the ball is estimated to be 5358.6 mm^2, while the average diameter is 41.3 mm. Each ball was scanned at 6 different positions, as shown in Figure 129.

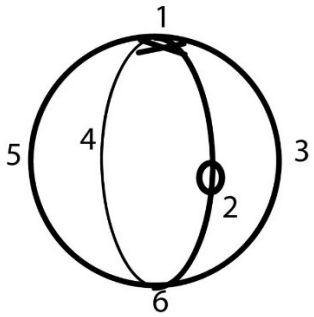

Figure 129. Measuring points on bearing balls, each of them scanned at 6 points.

The bearing failed pre-maturely and it is assumed that the damage was caused by both mechanical and electrical factors during the operation. Severe signs of damage were found on the raceways (in form of corrugation pattern, left side in Figure 130) and on the balls in the form of micro-craters (right side in Figure 130). Relatively larger cavities (marked in circles in Figure 130) could also observed by naked eye within these damages on raceways and balls, possibly due to presence of debris or electrical erosion caused by extensive discharges of high energy.

The analyses of the surface were carried out using optical interferometry using a WYKO optical profiler to study the damaged surfaces, including analyses of area roughness S_a, along with estimation of the damage extent.

The observations revealed existence on numerous small craters on the balls. These were uniformly distributed and gave a mat finish to the surface, also confirmed by other investigations [71, 72] using synthetic test bench.

Area roughness of bearing surfaces can be quantified using light interferometer by measuring the surface height from 1 nm to several millimetres. In the Vertical Scanning Interferometry (VSI) mode, the light reflected from a reference mirror can be combined with light reflected from bearing surface, which helps in determining the surface profile the bearing and allow to characterise surface roughness, namely arithmetic mean height (S_a) and the root mean square height (S_q) value.

Figure 130. Electrical fluting damage on bearing surfaces on the outer raceway (left-top), inner raceway (left-bottom) and micro-craters (electrical pitting) on the ball (right), giving it a satin, frosty or a matte like finish.

Surface roughness, S_a is the average of the absolute value of profile heights (z) over area (A = xy) evaluated mathematically as given in equation (37),

$$S_{\mathrm{a}} = \frac{1}{A}\iint_A |z(x,y)|\,\mathrm{dxdy}. \tag{37}$$

The RMS surface height (S_q) is defined by equation (38) as,

$$S_{\mathrm{q}} = \sqrt{\left(\frac{1}{A}\iint_A (z(x,y))^2\,\mathrm{dxdy}\right)}. \tag{38}$$

As an example, the mean value of surface roughness parameter (S_a) over 6 measurement points on Ball 1 is found to be 1.43 µm, while the average number of craters was found to be approximately 2.7 x 10^5 per ball. The craters appeared to be of round shape, eclipse shape, triangular shape and many other irregular shapes as shown in Figure 131. On each of the measured spots, the used optical magnification was 2.5 times (scan area was 1.9 mm by 2.5 mm) and the numbers of craters were in the range of 200 - 350. The total number of craters was in the order of 10^5 per ball and is more than 50 craters per mm^2. The volume of the craters in each measurement was evaluated (area fraction of craters was around 13 % or 700 μm^2) and the average volume was found to be around 1200 μm^3, which corresponds to average crater depth variation between 5 to 20 µm. The craters seem to be larger in some areas and more small craters can be found in some other areas, as shown in Figure 131, but were more or less uniformly distributed throughout the ball.

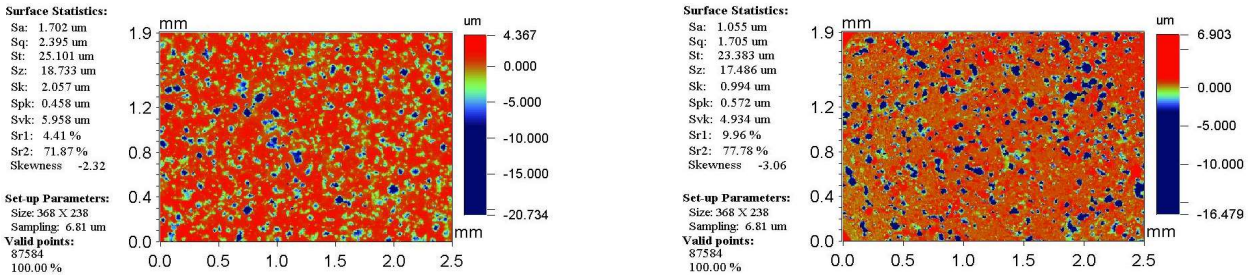

Figure 131. Surface morphology on Ball 1 shows approximately 180 craters (left) in one part of the ball, while on the other area approximately 320 craters. Size of scanned area is 1.9 mm by 2.5 mm.

The surface roughness varied very little from ball to ball, with a mean value of 1.47 µm and a standard deviation of 0.25 µm, shown in Figure 132. The error bars indicate standard deviation of 6 measurement points.

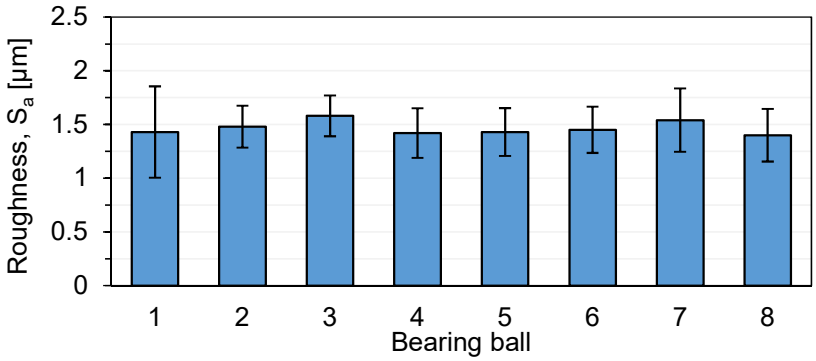

Figure 132. Surface roughness of bearing balls. The error bars indicate standard deviation of six measurement on each ball.

The estimated number of craters per square millimetre has an average value of about 53 and is shown in Figure 133. It can be seen that the number of craters does not significantly vary, indicating that the damage on all the balls is more or less evenly distributed.

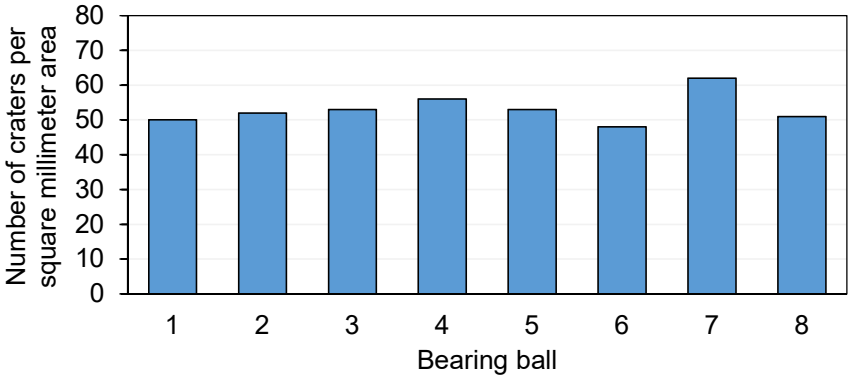

Figure 133. Estimated number of craters per square millimetre area on each bearing ball.

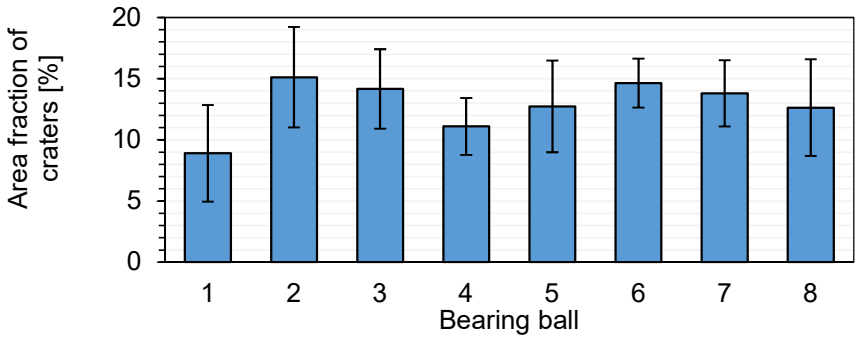

Figure 134. Area fraction of craters on each ball bearing. The error bars indicate standard deviation of six measurement points on each ball.

The estimated total number of craters is found to range between 0.26 million craters (Ball 6) and 0.33 million crater (Ball 7) and has an average value of approximately 0.28 million craters per ball. The estimated number of craters per ball is shown in Figure 135.

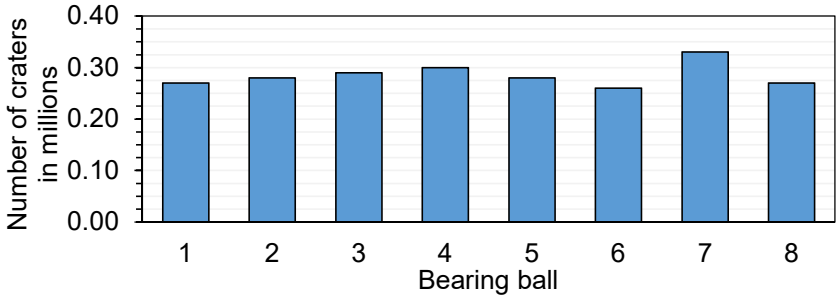

Figure 135. The estimated number of craters on each bearing ball.

While most of the balls have crater volume of ~10^3 µm^3, exceptionally large crater is found on ball 5. Morphological image of a scanned surface area of a ball 5 reveals the extent of damage and is shown in Figure 136. This crater has a volume of around 10^6 µm^3 and diameter larger than 800 µm. The diameter is larger than size of normal wear debris by one order of magnitude and could have resulted from an intensive current discharge activity. If we assume this scenario, energy of 6.70 mJ would need to be required to create a crater of these dimensions. This value of energy needed to melt the bearing steel corresponds to a peak current amplitude of 8.18 A, assuming that the breakdown event lasts for 10 µs (discharge type of bearing currents) and offers discharge resistance of 10 Ω in the conducting state using the equation (39) as,

$$E = V \times \rho \times (c(T_1 - T_2) + h) \tag{39}$$

where,

V is damaged volume of the crater in m^3,

ρ is density of steel = 7800 kg/m^3,

c is Specific heat constant of steel = 460 J/(kgK),

T_1 is melting point of steel = 1625 K,

T_2 is room temperature = 293 K, and

h is heat of fusion for steel = 2.47105 J/kg.

Nevertheless, the duration for discharge bearing currents is normally in sub-microsecond range. If we assume that the discharge lasts for 1 µs, a current with peak amplitude of approx. 25.9 A is needed to create a crater of this dimension. Similarly, a 0.5 µs event will require a peak current amplitude of 36.6 A.

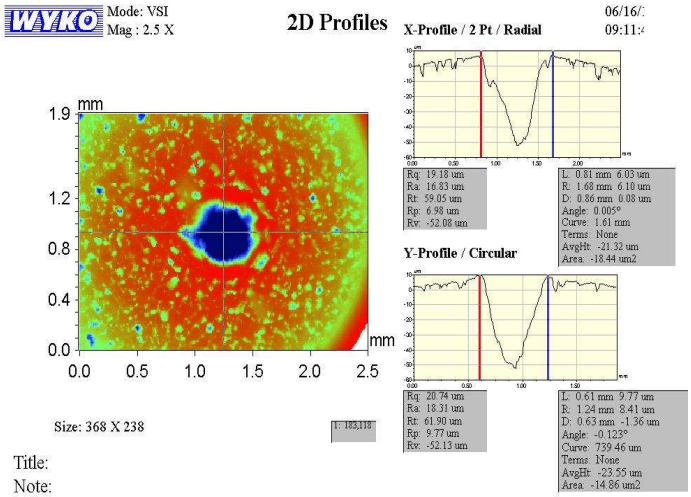

Figure 136. A large crater of diameter larger than 800 µm, found on ball 5 of the bearing, which might have resulted from electrical discharge.

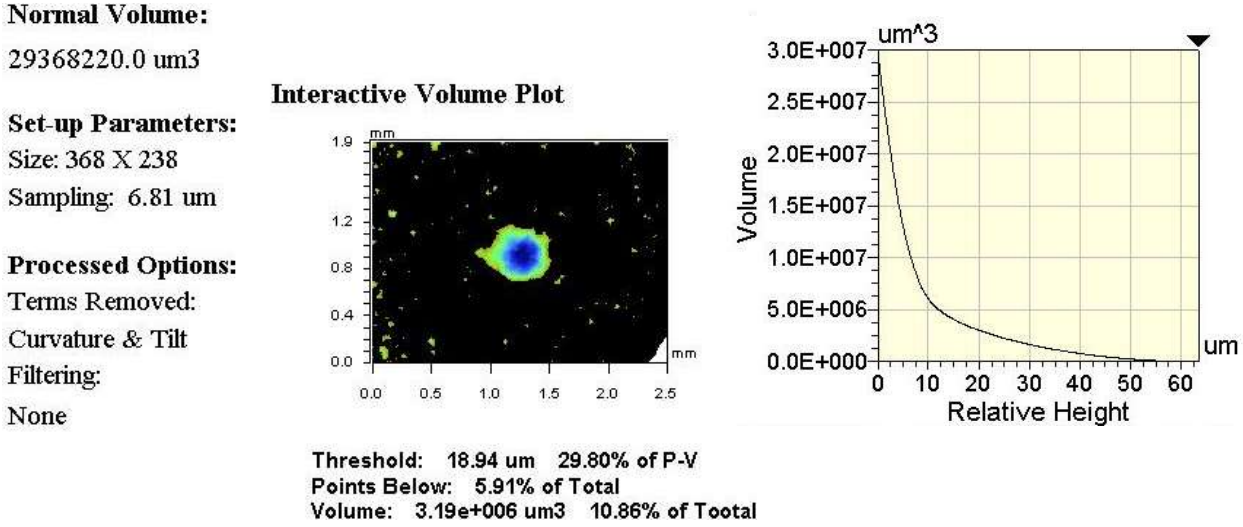

Figure 137. Crater volume evaluation using WYKO RST plus software (Ball 5)

The estimated total crater volume per ball is found to be much larger on Ball 5, due to the existence of crater shown in Figure 136 and Figure 137. The estimated crater volume on balls of the bearing is shown in Figure 138. Average value of the estimated volume of craters is found to be ~0.285 mm^3.

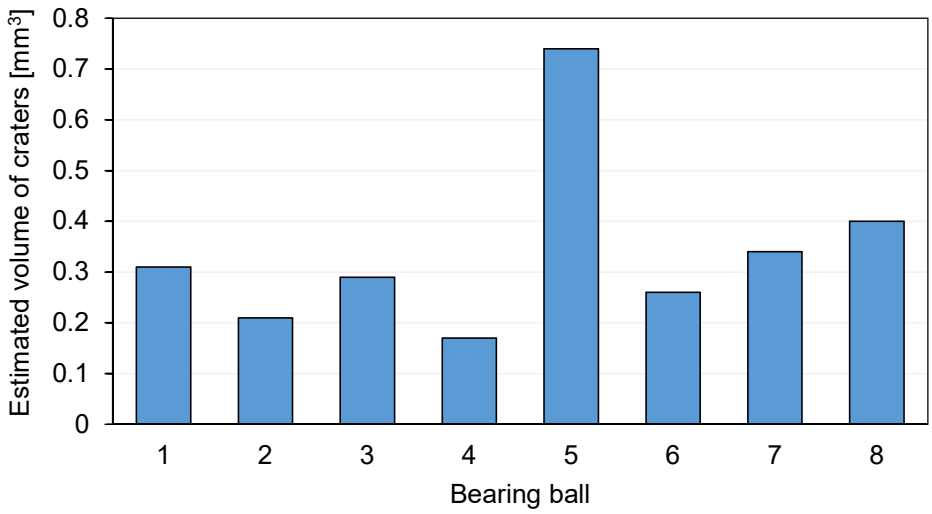

Figure 138. Total crater volume of ball bearing balls. It can be seen that the crater volume if relatively high for Ball 5 indicating a larger extent of damage.

The estimate average crater volume on individual bearing ball is ~1200 μm^3 and is volume is indicated in Figure 139. The amount of energy required to melt an average sized crater on the steel ball bearing is 8.04 μJ.

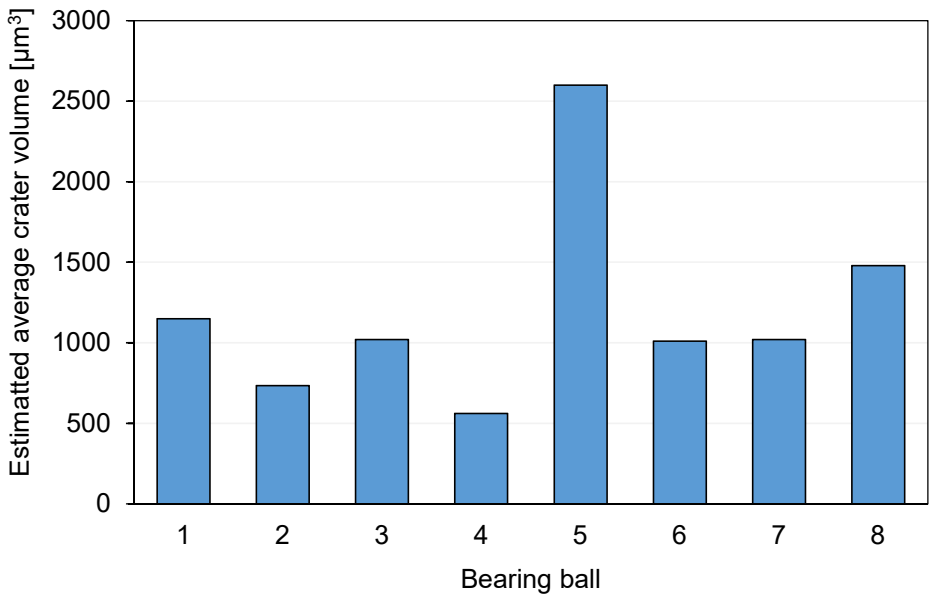

Figure 139. Estimated average crater volume of the damaged balls in the bearing.

The area fraction of craters per ball has an average value of 13 %. The ball to ball area fraction of craters is shown in Figure 140.

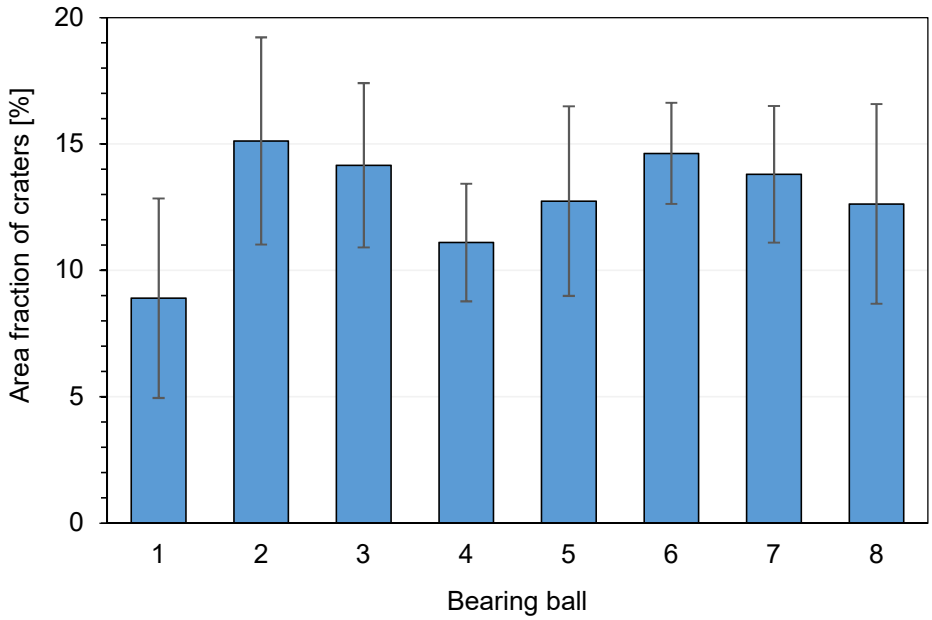

Figure 140. Area fraction of craters on each ball.

The surface morphology of the damages on individual balls within the bearing is summarised in Table X.

Table X. The summarized results of WYKO measurements on bearing balls

	Ball 1	Ball 2	Ball 3	Ball 4	Ball 5	Ball 6	Ball 7	Ball 8	Average
Roughness, S_a (µm)	1.43	1.48	1.58	1.42	1.43	1.45	1.54	1.40	1.47
No. of craters per ball	$2.7x10^5$	$2.8x10^5$	$2.9x10^5$	$3.0x10^5$	$2.8x10^5$	$2.6x10^5$	$3.3x10^5$	$2.7x10^5$	$2.85x10^5$
No. of craters per mm^2	50	52	53	56	53	48	62	51	53
Volume of craters per ball, $µm^3$	$3.1x10^8$	$2.1x10^8$	$2.9x10^8$	$1.7x10^8$	$7.4x10^8$	$2.6x10^8$	$3.4x10^8$	$4.0x10^8$	$2.85x10^8$
Average crater volume ($µm^3$)	1150	734	1020	562	2600	1010	1020	1480	1200
Area fraction of the craters (%)	8.90	15.12	14.16	11.10	12.74	14.63	13.80	12.63	12.88
Estimated crater area per ball ($µm^2$)	477	810	759	595	683	784	740	677	690

11 Discussion

This chapter briefly summarizes and discusses the findings of bearing behaviour in insulating and conducting states.

Insulating state, bearing capacitance (C_B) - It has been generally found out that C_B decreases as the rotational speed of the bearing increases. Principally, the value of C_B is dependent on the bearing geometry and lubricant properties. For the miniature ball bearing of type 608, a higher speed results in a larger film thickness in the bearing. The load on the bearing is relatively lower as compared to larger bearings and thus is assumed to not result in a large increase in temperature of the lubricant. Under such conditions, an increase in rotational speed of the bearing is also associated with an increase in lubricant film thickness around the bearing balls. For the larger bearing of type 22220, a higher speed and higher load causes a sharp increase in the lubricant temperature. A step-increase in speed of the rotation results in continuous and gradual change in lubricant temperature from ~52 °C to ~60 °C. The calculated film thickness is shown to gradually decrease as the speed and temperature increases; thus, resulting in a reduced value of bearing capacitance. Thus, it can be concluded that bearing capacitance decreases with an increasing film thickness and increasing speed of the bearing, assuming that the rise in temperature is insignificant. The bearing capacitance was also found to be a function of initial conditions of the bearing and lubricant, since reducing speed from 800 rpm to 400 rpm in steps of 100 rpm has resulted in an increase in measured bearing capacitance.

The value of C_B increases with an increase in axial load on the bearing and is associated with an increase in Hertzian contact area and slight decrease in lubricant film thickness. The hypothesis was confirmed by experiments on bearing type 608, where a higher load of 40 N results in a slightly higher bearing capacitance, as shown in Chapter 6.1. The reduction in lubricant film thickness can be corroborated with calculated lubricant film thicknesses using SKF Galaxy software and can be found in Chapter 5.1.1. Thus, it can be concluded that at higher load on the bearing results in higher bearing capacitance, assuming that the rise in temperature is insignificant.

The bearing capacitance could be theoretically modelled as a parallel plate capacitor separated by a dielectric medium of relative permittivity, ε_r. The relative permittivity (ε_r) of liquid lubricant (Sample A and B) is found to be between 2 and 3, while of grease lubricants (Sample C and D) is found to be between 4 and 5 for power frequency measurements done at temperature of 50 °C, as shown in Chapter 5.2.1. The relative permittivity of the liquid lubricant samples is close to that of insulating oil used in transformers while ε_r for greases is found to be higher compared to that of oil samples, but lower than values reported in literature review.

Insulating state, bearing resistance in insulating state ($R_{B,Ins.}$) – It is a modelled as an equivalent resistance in parallel to C_B and it represents total losses in the bearing arising due to conduction processes. The total losses are said to emanate from conduction processes in oil Sample A and D, since the imaginary part of complex capacitance (C" and dielectric losses) appears to have a straight line with a slope of -1 on a logarithmic scale, as discussed in Chapter 5.2. It is thus concluded that only one mechanism is responsible for the loss mechanism in the oil, i.e., conductive losses. Since $R_{B,Ins.}$ is modelled as an equivalent parallel resistance, a lower value of $R_{B,Ins.}$ is associated with higher dielectric losses in the lubricant. Higher losses in the oil with EP additives (Sample B) compared to the oil closer to base oil (Sample A) is more likely because of use of higher electrically conductive base oil of the lubricant, given in Chapter 5.2.2. This is confirmed from conductivity

measurements, the conductivity of Sample B (114 pS/m) is approximately two orders of magnitude higher than Sample A (2.89 pS/m) reported at frequency of 0.1 Hz and temperature of 50 °C, shown in Chapter 5.2.3. Lubricant Sample A+ (oil after run-in) shows slightly higher conductivity (7.61 pS/m measured at 0.1 Hz and at 50 °C), which is most likely occurring due to exposure to humidity in air during operation for the duration of running-in. Oil with particles (Samples A1 to A5) did not seem to have an increase in conductivity, on the contrary the conductivity decreased since the particles were added in virgin oil and they settled at the bottom of the test cell. The layer of particles could form a barrier for charge transport and could result in slightly lower values of conductivity.

A higher temperature of the lubricant results in higher conductivity which was measured for all lubricants. A higher temperature (from 35 °C to 80 °C) generally results lead to a slight higher mobility of the charge carriers in insulators. But since the rise in temperature is not too significant, the increase in conductivity is also not too pronounced.

Conducting state, switching pattern analyses (switch) - The presence of an inception voltage for conduction current was found out to be between 4 and 5 V for bearing type 608, which refers to electric field stress of 14 V/µm. The extinction voltage was measured to be in between 3 and 2 V, as shown in Chapter 8.2.2. The number of conduction current pulses in the bearing increases with an increase in amplitude of applied bearing voltage. It is shown that after exposing the bearing to a large number of discharges, the insulating properties of the bearing fail to recover most likely due to irreversible changes in electro-chemical properties of the lubricant.

Bearings operating in mixed lubrication regime will have a much lower value for inception electric field of bearing current activity. This is seen in Chapter 8.2.1 where speed of 1000 to 3000 rpm in combination of DC voltage of 4 V resulted in significant number of current pulses through the bearing. On the other hand, the same bearing lubricated with Sample A in Chapter 8.3.1 operated in the same speed range upon application of 5 V results in no bearing current activity.

For a DC voltage, the ToC increase with an increase in bearing voltage. At rotational speed of 2000 rpm and load of 4 N, the critical level of electric field strength for the bearing of type 608 is found out to be ~30 V/µm, shown in Chapter 8.5.2. Thus, it could be concluded that there exists a critical region of apparent electric field strength in bearing.

At operating point where a thinner film is formed in the bearing (for example speed of 1000 rpm and load of 40 N for bearing of type 608), $E_{10\%ToC}$ is ~9 V/µm while at the operating point leading to higher lubricating film (speed of 3000 rpm and load of 4 N), $E_{10\%ToC}$ is evaluated to be ~30 V/µm. For the larger spherical bearing with cylindrical and tapered bores of type 22220, $E_{10\%ToC}$ ranges between ~1.6 V/µm and ~7.1 V/µm, discussed in Chapter 8.3.2. The distinct difference in $E_{10\%ToC}$ for ball and spherical roller bearing is likely to arise due to larger area of contact, thus leading to a higher probability of formation of current conduction path through the lubricating film. The Hertzian line-contact area of bearing type 22220 is also assumed to be larger compared to bearing type 608's point-contact area. Thus, it can be concluded that the size of the bearing need not necessarily dictate the value of $E_{10\%ToC}$ of the bearing but is more likely to be influenced by the lubricant film thickness, type and area of contact and number of rollers in the bearing. Bearing with a longer contact area (spherical bearing of type 22220) has also much higher current pulses at same voltage levels compared to miniature bearing type 608. The author thus

attributes higher current activity due to higher likelihood of formation electrical contact in bearing type 22220 compared to type 608.

At low values of applied bearing voltage, the duration of conduction current pulses is in order of up to few microseconds and the time between successive current pulses is found to be highest. But as the applied bearing voltage is increased, it can be concluded that the duration of pulses increase and time between successive current pulses reduces. It was also shown that the duration of the conduction current pulses increases drastically when the bearing is exposed to fields equal or higher than $E_{90\%ToC}$. The time in between successive current pulses reduce to a few microseconds and the bearing is found to be mostly in conducting state.

The investigations of switching pattern analyses as a function of operating point such as rotational speed and mechanical load also conclude that the number of breakdown events and the time on conduction also reduce with an increase in rotational speed and a decrease in mechanical load on the bearing. These hypotheses were also re-verified in investigations on the larger bearing of type 22220.

After large number of insulation breakdown in the bearing upon applying of a DC voltage, the electrical insulating properties of the bearing were not able to recover and this we have termed as memory effects. This is exhibited at apparent electric field strength of ~23 V/µm and ~30 V/µm, measured for lubricant Sample E and A respectively as shown in Chapter 8.5. The bearing's insulation also experiences memory effects in the recovery of bearing's insulating properties as the voltage is step-wise decreased after a period of large number of discharges in bearing.

The threshold for occurrence of memory effect for a pre-lubricated bearing of type 608 is found to be 23 V/µm at a speed of 3000 rpm and load of 4 N. The threshold for the same bearing at a higher speed is found to be 30 V/µm. Given the difference in film thickness, and differences in the two thresholds, the resulting current activity upon decrease of the applied voltage is similar. The bearing conducts more (higher ToC of 93.8 % at 35 V in Figure 116) at the same applied electric field stress (for example at 26 V/µm) after crossing the threshold of 30 V/µm than before the threshold (lower ToC of 0.01 % at 35 V applied voltage in Figure 114), presented in Chapter 8.5.2.

For alternating voltages, as the amplitude of the applied voltage is increased, a higher bearing current activity is observed in the form of reduction of inception voltage, increase in pulse duration and reduction of time between discharges, as shown in Chapter 8.2.4. At higher frequency of applied AC voltages (1 and 2 kHz), the mean inception voltage is found to be slightly lower than AC voltage with lower frequencies of 25 and 50 Hz. A higher amount of current activity is also seen in increased ToC for tests with higher frequencies. The inception electric field for bearing current activity increases beyond a certain E-field strength (4.7 V/µm) for 25 and 50 Hz, beyond which it reduces with an increase in dV/dt of applied AC voltage. Similarly, for tests with frequency of 1 and 2 kHz, the inception E-field strength increases upto 3.3 V/µm and 3.8 V/µm respectively and reduces with a further increase in dV/dt. The polatiry of the applied AC voltage is seen to have as very low influence on the parameters of the bearing current activity such as inception voltage, pulse duration and time in between discharges. Memory effects are not observed in tests with alternating voltages, possibly due to presence of zero-crossing. The window of transition from insulating state to conducting state occurs approximately during the same range of applied AC voltage for all the tests. This could be resultant of a fixed operating point of speed and load. It is also observed that the transition of bearing from insulating state to condcuting state occurs faster in case of DC voltage as compared to alternating sinusoidal voltage.

The plausible mechanisms leading to insulation breakdown have been proposed and investigated as breakdown due to *asperity contacts*, *particle-initiated breakdowns* and *electrical breakdown* of the lubricating film of the bearing. The asperity contacts dominate at lower rotational speed (below 800 rpm) and do not play a role at speeds of 2000 rpm and above corresponding to a dimensionless speed parameter of 30,000 which is calculated using equation (36) given in Chapter 8.3. At speeds of 200 and 300 rpm, the ToC doubles with the number of conducting balls in the bearing, indicating that the number of asperity contacts have doubled indicating a trend to the number of electrical contact-establishing balls.

The particle-initiated breakdowns are found to be a function of the particle type, concentration, number of start-stops of the particle. At particle concentration of 150 mg/L, the average percentage ToC in the first start is found to be highest for lubricant Sample A1 (Arizona test dust with ToC = 9.5 %) followed by Sample A4 (fine iron powder with ToC = 5.1 %), Sample A3 (aluminium particles with ToC = 0.84 %) and Sample A2 (toner particles with ToC = 0.03 %), as shown in Chapter 8.4. The ToC reduces by one order of magnitude if the particle concentration is at 30 mg/L or lower, tested for Samples A1 and A2. Thus, in dusty environments, the particle contamination limit for lubricating oil can be lowered to 30 mg/L instead of 150 mg/L as proposed by Elforsk [40]. The number of start-stops of the bearing reduce the ToC for all types of particles nearly to half, except for toner particles, which are more likely to be electrostatically charged due to friction or due to application of static voltage.

Conducting state, bearing resistance (R_B) – Due to asperity contacts, the equivalent bearing resistance (R_B) in conduction state for bearing type 608 is found out to be ~17 **Ω**, as shown in Chapter 9. Due to the nature of the asperity contacts, the resistance is found to vary up to several 100's of ohms during the event, as it can be seen in Figure 118, chapter 9.1. The investigations concluded that the bearing resistance in conduction state varies significantly at lower speeds, where large number of metal to metal contacts are expected. At slightly higher speeds, the bearing resistance in event of breakdown due to asperity contacts has a more stable value during the extent of a contact. It was also concluded that the bearing resistance if found to be consistently higher at a higher load setting, as shown in Figure 119 and Figure 120 respectively.

Due to asperity contacts, the minimum value of bearing resistance is found to increase gradually as the speed is increased from 200 to 1000 rpm. At lower speeds (up to 500 rpm), the spread of the bearing resistance is slightly more compared to its spread at higher speeds (600 rpm and higher), shown in Chapter 9.1. This is likely due to reduction in time or duration of asperity contact due to increase in speed. It can also be concluded that as the speed is increased from 200 to 1000 rpm, the insulation breakdown events caused due to asperity contacts reduce in duration. This can be observed in box plots of current pulse duration in Figure 119 and Figure 120 for load settings of 4 N and 40 N respectively. The minimum value of equivalent discharge resistance did not vary with the amplitude of the applied DC voltage. The value of R_B was found to be highest for breakdown initiated due to metallic particles and the pulse duration was unaffected by the particle concentration.

Due to particle-initiated breakdowns, the minimum value of bearing resistance is found for Sample A1 (ATD) is ranging between 14 and 24 **Ω**, while the spread of the values could range up to 40 **Ω** different tests shown in Figure 123, chapter 9.2.1. Bearing resistance measured for different particles at a fixed concentration level of 150 mg/L revealed that median value of bearing resistance ranges between 28 **Ω** to 63 **Ω** in case of Sample A1 and A2, while it is about 5 to 10 times higher

for samples A3 and A4 as shown in Figure 121. It can be concluded that the metallic particles such as aluminium and iron powder create more variation in metal to metal contact of the bearing elements, results in an easier make and break of electrical contact between the inner and outer raceways of the bearing, as it can been from current pattern displayed in Figure 109 and Figure 111 in Chapter 8.4. The non-metallic particles are softer in nature and when immersed in oil and more likely tend to lose their hardness. The conduction current pattern of Samples A1 and A2 are shown in Figure 103 and Figure 106 and show that the conduction current does not show much variation during the event of the breakdown, resulting in slightly lower value of median R_B.

Analysis of a failed bearing replaced under normal operation in a wind turbine shows that the damage caused by electrical discharge events in the bearing could lead to formation of nano and micro-craters on the ball, with some exceptions of larger craters. The distribution of such damages is found more or less uniform in different areas of the ball, but it could slightly vary from ball to ball within a bearing, as shown in Chapter 10. The electrical damages could lead to presence of ~0.3 million craters per ball, while the area fraction of the craters could amount from 9 to 15%, as shown in Figure 135 and Figure 134 respectively. It can be concluded that the electro-erosion of bearing steel could lead to premature failures and could repeatedly lead to down times ranging from 26 months to 2 months and leads to loss of power generated and reduces sustainability of wind turbine. Certain wind turbines have repeated bearing failures and fundamental level studies in the electrical breakdown and conduction in the bearings have contributed to knowledge of limiting the amount of shaft voltage in the system.

12 Conclusions

The electrical properties of a mechanical bearing have been elaborated, which includes quantifying both insulating and conducting states of the bearing. The behaviour of a running bearing is put forth as an equivalent electrical circuit model, where different components of the model are quantified using standard electrical characterisation techniques. The equipment, methods and analyses methods to investigate every component of the model have been detailed in the thesis.

The findings show that all bearings exhibit these two states and the switching in between the states is a function of the bearing operating point and electric field strength. Electric field dependent current conduction in bearing is investigated in range of 3.7 V/µm to 44.6 V/µm. A bearing under normal operation is fully conducting at electric field strength of higher than 29 V/µm. If the bearing has limited lubrication, the bearing is fully conducting between 20 to 25 V/µm. A bearing with 0,5 µm of film thickness electrically breaks down if the voltage applied across it increases beyond a threshold of approximately 15 V, which is rather low voltage level to cause a current to flow through the bearing.

Under nominal conditions, the bearing is operating under standard speeds and loads. During this operating point, bearing can be represented by a capacitance (C_B) in parallel with resistance ($R_{B,Ins.}$), that can vary with changes in speed and load of operation. C_B decreases with an increase in speed and decrease in load on the bearing. The changes in bearing capacitance as a function of speed and load on the bearing has been quantified for two bearing types of different sizes. The capacitance of the smaller bearing as a function of number of rolling elements has been formulated in Chapter 6.1.1. In running conditions, the current flowing through the capacitive branch (C_B) can be about 2.5 times higher than the current flowing in the parallel resistive branch ($R_{B,Ins.}$) for bearing type 608 and 2.6 times higher for bearing type 22220. These findings have not been reported before. This implies that while electrically modelling a running bearing in insulating state, the equivalent circuit must consist of C_B in parallel with $R_{B,Ins.}$.

The flow of ohmic current through the bearing is studied considering multiple plausible electro-physical mechanisms that can arise during normal operation. In literature, studies were performed with focus on only one of the mechanisms, i.e., field dependent current conduction. In this thesis three electro-physical mechanisms have been investigated, i.e., asperity-initiated breakdowns, particle-initiated breakdowns and voltage or field-dependent breakdowns. The asperity-initiated breakdowns generally occur when the bearing is operated below rated speed. Above this threshold speed, the asperity contacts will become very rare and negligible and result in ohmic current conduction of less than 1 % of the duration of measurement.

As seen for bearing 608, current conduction due to electrical breakdown of oil film increases as the electric field across the bearing is increased from 3.7 V/µm to 44 V/µm. A normally operated bearing with adequate lubrication is found to have an inception level for ohmic current conduction at 29 V/µm (ToC between 0.1 and 0.8 %), while the same bearing with limited lubrication is found to have a lower inception field level of 15 V/µm (ToC = 0.6 %). Bearings operating in mixed lubrication regime (limited lubrication) will have a much lower value for inception electric field of bearing current activity. This is shown in Chapter 8.2.1 where speed of 1000 to 3000 rpm of the bearing type 608 in combination with DC voltage of 4 V that resulted in significant number of current pulses through the bearing. On the other hand, the same bearing operated with another

lubricant (Sample A) operated at the same speed range upon application of 5 V DC with no bearing current activity.

For a bearing lubricated sufficiently, it instantly goes from electrically insulating to electrically conduction state. If a high enough DC voltage is applied which results in electric fields higher than 30 V/μm, the bearing is found to exhibit memory effect or hysteresis behaviour due to after passage of a large number of current conduction pulses.

The particle-initiated breakdowns were not only investigated at the proposed by Elforsk [40] acceptable contamination level of 150 mg/L, but also at other concentration levels in the range of 7.5 mg/L to 150 mg/L. As particles form bridges inside the bearing, the voltage developed across the bearing is discharged though these paths. For dust particles, this threshold is found to be too high and leads to ohmic current conduction for about 11% of the time. It is thus recommended to reduce the acceptable contamination level to 30 mg/L in environments prone to dust particles, since it yields the conduction for less than 1 % of the operation time. As regards other tested contaminants, particles that cause most current conduction are Arizona test dust (ToC = 10.7 %), followed by iron powder (ToC = 8.3 %), aluminium powder (ToC = 1.7 %) and toner particles (ToC = 0.1 %). It is hence recommended to use filters and have clean oil and regularly pump grease at appropriate intervals.

Future work

Future work in bearing modelling and prevention of bearing damages could be conducted in several areas of interest, as follows:

1) Verify range for threshold value of apparent electric field for larger and more commonly used bearing of type 6230.
2) Investigations into memory effect as a function of multiple types of lubricants to find lubricant least prone to this phenomenon.
3) Correlate different amounts of energy of discharge to damages caused on the bearing surface in a test bench by varying the energy of discharge through the bearing.
4) Use of PWM waveform to evaluate average value breakdown voltage and corresponding E-field strength using higher number of data points.
5) In case of asperity-initiated breakdowns, verify speed limits (in terms of dimensionless speed parameter) for current conduction through different types and sizes of bearings.
6) Measure the surface roughness of the bearing steel at different points in a mechanical ageing test and correlate the measured bearing capacitance as a function of ageing.
7) Based on (5), you can prepare an equivalent parallel plate capacitor model of different surface roughness within a multi-physics simulation software and estimate and model the bearing capacitance to verify and append to the experimental results.
8) Measure threshold voltage for current conduction for bearing with distinct surface roughness. If the threshold voltage of a bearing of given size and lubricant is same for all the tested surface roughness values, the breakdown of the bearing can be seen to be independent of local field enhancements in contact area.

References

1. Whittle, M., J. Trevelyan and P.J. Tavner, *Bearing currents in wind turbine generators.* Journal of Renewable and Sustainable Energy, 2013. **5**(5): p. 53128-53128.
2. Zitzelsberger, J., et al. *Bearing currents in doubly-fed induction generators*. in *European Conference on Power Electronics and Applications*. 2005.
3. Adabi Firouzjaee, J. and F. Zare, *Investigation of shaft voltage in wind turbine systems with induction generators.* IEEJ Transactions on Industry Applications, 2009. **129**(11): p. 1092-1100.
4. Garcia, A.M., D.G. Holmes and T.A. Lipo. *Reduction of bearing currents in doubly fed induction generators*. in *IEEE Industry Applications Conference*. 2006.
5. Fischer, K., F. Besnard and L. Bertling, *Reliability-centered maintenance for wind turbines based on statistical analysis and practical experience.* IEEE Transactions on Energy Conversion, 2012. **27**(1): p. 184-195.
6. Bongiorno, M. and A. Petersson, *Development of a method for evaluation of wind turbines ability to fulfil swedish grid codes*. 2009: Stockholm, Sweden. p. 94-94.
7. Naik, R., et al., *Circuit model for shaft voltage prediction in induction motors fed by PWM-based AC drives.* IEEE Transactions on Industrial Electronics, 2003. **39**(5): p. 1294-1299.
8. Muetze, A., J. Tamminen and J. Ahola, *Influence of motor operating parameters on discharge bearing current activity.* IEEE Transactions on Industry Applications, 2011. **47**(4): p. 1767-1777.
9. Bell, S., et al. *Experience with variable frequency drives and motor bearing reliability*. in *IEEE Annual Petroleum and Chemical Industry Conference*. 1998.
10. Shaotang, C., T.A. Lipo and D. Fitzgerald, *Modeling of motor bearing currents in PWM inverter drives.* IEEE Transactions on Industry Applications, 1996. **32**(6): p. 1365-1370.
11. Kerkman, R., D. Leggate and G. Skibinski. *Interaction of drive modulation and cable parameters on AC motor transients*. in *IEEE Industry Applications Conference*. 1996.
12. Abdulahovic, T., *Analysis of high-frequency electrical transients in offshore wind parks*. 2011, Chalmers tekniska högskola. p. 134-134.
13. Muetze, A. and A. Binder, *Techniques for Measurement of Parameters Related to Inverter-Induced Bearing Currents.* IEEE Transactions on Industrial Electronics, 2007. **43**(5): p. 1274-1283.
14. Binder, A. and A. Muetze, *Scaling effects of inverter-induced bearing currents in AC machines.* IEEE Transactions on Industrial Electronics, 2008. **44**(3): p. 769-776.
15. Muetze, A. and A. Binder, *Calculation of circulating bearing currents in machines of inverter-based drive systems.* IEEE Transactions on Industrial Electronics, 2007. **54**(2): p. 932-938.
16. Muetze, A. and A. Binder, *Practical rules for assessment of inverter-induced bearing currents in inverter-fed ac motors up to 500 kw.* IEEE Transactions on Industrial Electronics, 2007. **54**(3): p. 1614-1622.
17. Di Piazza, M.C., A. Ragusa and G. Vitale, *Power-Loss Evaluation in CM Active EMI Filters for Bearing Current Suppression.* IEEE Transactions on Industrial Electronics, 2011. **58**(11): p. 5142-5153.
18. Ferreira, F.J.T.E., M.V. Cistelecan and A.T. de Almeida, *Evaluation of slot-embedded partial electrostatic shield for high-frequency bearing current mitigation in inverter-fed induction motors.* IEEE Transactions on Energy Conversion, 2012. **27**(2): p. 382-390.
19. Sayed-Ahmed, A. and G. Skibinski. *Design and analysis of an integrated differential-common mode filter for on site motor bearing problems*. in *IEEE International Electric Machines & Drives Conference (IEMDC)*. 2011.

20. Besnard, F., et al. *A limited-scope reliability-centred maintenance analysis of wind turbines*. 2011.
21. Hau, E. and H.E.v. Renouard, *Wind turbines : fundamentals, technologies, application, economics : with 552 figures and 41 tables*. 2006, Berlin; Heidelberg: Springer.
22. Obdam, T.S., L. Rademakers and H. Braam, *Flight leader concept for wind farm load counting: Offshore evaluation.* Wind Engineering, 2010. **34**(1): p. 109-122.
23. McMillan, D. and G.W. Ault, *Quantification of condition monitoring benefit for offshore wind turbines.* Wind Engineering, 2007. **31**(4): p. 267-285.
24. Faulstich, S., B. Hahn and P.J. Tavner, *Wind turbine downtime and its importance for offshore deployment.* Wind Energy, 2011. **14**(3): p. 327-337.
25. Nilsson, J. and L. Bertling, *Maintenance management of wind power systems using condition monitoring systems—life cycle cost analysis for two case studies.* IEEE Transactions on Energy Conversion, 2007. **22**(1): p. 223-229.
26. Andrawus, J.A., et al., *Optimisation of wind turbine inspection intervals.* Wind Engineering, 2008. **32**(5): p. 477-490.
27. Erdman, J.M., et al., *Effect of PWM inverters on AC motor bearing currents and shaft voltages.* IEEE Transactions on Industrial Electronics, 1996. **32**(2): p. 250-259.
28. Chen, S., T.A. Lipo and D. Fitzgerald, *Source of induction motor bearing currents caused by PWM inverters.* IEEE Transactions on Energy Conversion, 1996. **11**(1): p. 25-32.
29. Chen, S. and T.A. Lipo, *Bearing current, EMI and soft switching in induction motor drives: A systematic analysis, design and evaluation*. 1995, The University of Wisconsin - Madison: Ann Arbor. p. 234-234 p.
30. Busse, D., et al., *Characteristics of shaft voltage and bearing currents.* IEEE Industry Applications Magazine, 1997. **3**(6): p. 21-32.
31. Saunders, L.A., et al. *Riding the reflected wave-IGBT drive technology demands new motor and cable considerations*. in *IEEE Annual Petroleum and Chemical Industry Conference*. 1996.
32. Takahashi, T., et al. *Motor lead length issues for IGBT PWM drives*. in *Pulp and Paper Industry Technical Conference*. 1995.
33. Persson, E., *Transient effects in application of PWM inverters to induction motors.* IEEE Transactions on Industrial Electronics, 1992. **28**(5): p. 1095-1101.
34. Ollila, J., et al. *On the bearing currents in medium power variable speed AC drives*. in *IEEE International Electric Machines and Drives Conference Record*. 1997.
35. Muetze, A. and A. Binder, *Systematic approach to bearing current evaluation in variable speed drive systems.* European Transactions on Electrical Power, 2005. **15**(3): p. 217-227.
36. Muetze, A., *Bearing currents in inverter-fed AC motors*. 2003, Darmstadt University of Technology: Darmstadt, Germany.
37. Cacciato, M., et al., *Reduction of common-mode currents in PWM inverter motor drives.* IEEE Transactions on Industrial Electronics, 1999. **35**(2): p. 469-476.
38. Magdun, O. and A. Binder, *High-frequency induction machine modeling for common mode current and bearing voltage calculation.* IEEE Transactions on Industry Applications, 2014. **50**(3): p. 1780-1790.
39. Niskanen, V., A. Muetze and J. Ahola, *Study on bearing impedance properties at several hundred kilohertz for different electric machine operating parameters.* IEEE Transactions on Industrial Electronics, 2014. **50**(5): p. 3438-3447.
40. Ukonsaari J, M.H., *Oil cleanliness in wind turbine gearboxes*. 2012.
41. SKF, *SKF Rolling bearings catalogue*, S. Group, Editor. 2013: Gothenburg, Sweden.
42. Megger, *IDAX 300/350 Broucher*. 2013-2014, Sweden: Megger Sweden AB.

43. SKF, *LGMT 2 - SKF general purpose industrial and automotive bearing grease*. 2014.
44. Hamrock, B.J., *Fundamentals of Fluid Film Lubrication*. NASA Reference publication. 1991: National aeronautics and space administration, scientific and technical information office.
45. Bonnett, A.H. *Root cause failure analysis for AC induction motors in the petroleum and chemical industry*. in *57th Annual Petroleum and Chemical Industry Conference (PCIC)*. 2010.
46. Bonnett, A.H., *Root cause AC motor failure analysis with a focus on shaft failures.* IEEE Transactions on Industry Applications, 2000. **36**(5): p. 1435-1448.
47. SKF, *Bearing damage and failure analysis*. 2014.
48. SKF, *Bearing failures and their causes*. 1994: Gothenburg.
49. Scott, R. *Basic wear modes in lubricated systems*. 2008; July:[Available from: http://www.machinerylubrication.com/Read/1375/wear-modes-lubricated.
50. Alewine, K. and W. Chen. *A review of electrical winding failures in wind turbine generators*. in *Electrical Insulation Conference (EIC)*. 2011.
51. Alewine, K., *Understanding wind turbine generator failures - modes and occurances - An update*, in *Wind Project O&M and Safety seminar*. 2014. p. 17.
52. Amirat, Y., et al., *A brief status on condition monitoring and fault diagnosis in wind energy conversion systems.* Renewable and Sustainable Energy Reviews, 2009. **13**(9): p. 2629-2636.
53. Tavner, P.J., *Review of condition monitoring of rotating electrical machines.* IET Electric Power Applications, 2008. **2**(4): p. 215-215.
54. O'Donnell, P., *Report of large motor reliability survey of industrial and commercial installations, Part I.* IEEE Transactions on Industrial Electronics, 1985. **IA-21**(4): p. 853-864.
55. O'Donnell, P., *Report of large motor reliability survey of industrial and commercial installations, Part II.* IEEE Transactions on Industrial Electronics, 1985. **IA-21**(4): p. 865-872.
56. O'Donnell, P., *Report of large motor reliability survey of industrial and commercial installations: Part 3.* IEEE Transactions on Industrial Electronics, 1987. **IA-23**(1): p. 153-158.
57. Spinato, F., et al., *Reliability of wind turbine subassemblies.* Renewable Power Generation, IET, 2009. **3**(4): p. 387-401.
58. Albrecht, P.F., et al., *Assessment of the reliability of motors in utility applications - updated.* IEEE Transactions on Energy Conversion, 1986. **EC-1**(1): p. 39-46.
59. Pinjia, Z., et al., *A survey of condition monitoring and protection methods for medium-voltage induction motors.* IEEE Transactions on Industrial Electronics, 2011. **47**(1): p. 34-46.
60. IEEE, *IEEE Recommended practice for the design of reliable industrial and commercial power systems*, in *IEEE Std 493-2007 (Revision of IEEE Std 493-1997)*. 2007. p. 1-689.
61. IEEE, *IEEE Recommended practice for the design of reliable industrial and commercial power systems (gold book)*, in *IEEE Std 493-1997*. 1998. p. 1-464.
62. Thorsen, O.V. and M. Dalva, *A survey of faults on induction motors in offshore oil industry, petrochemical industry, gas terminals and oil refineries.* IEEE Transactions on Industrial Electronics, 1995. **31**(5): p. 1186-1196.
63. Tavner, P.J. and J.P. Hasson, *Predicting the design life of high integrity rotating electrical machines.* IEEE International Conference on Electrical Machines (ICEM), 1999.
64. Boyanton, H., *Bearing damage due to electrical discharge (ED)*. 2010, Shaft Groundmg Systems Inc.: Albony, OR.

65. Bearings, B.P., *Bearing failure: Causes and cures*. Barden Precsion Bearings.
66. Schnabel, S., *Monitoring of wear in elasto- hydrodynamic lubricated contacts. Running-in and failure propagation.* 2014/2/24, Luleå tekniska universitet.
67. Dwyer-Joyce, R.S., *Predicting the abrasive wear of ball bearings by lubricant debris.* Wear, 1999. **233–235**(0): p. 692-701.
68. Dwyer-Joyce, R.S., R.S. Sayles and E. Ioannides, *An investigation into the mechanisms of closed three-body abrasive wear.* Wear, 1994. **175**(1–2): p. 133-142.
69. Gröschl, M., et al., *Surface analysis on rolling bearings after exposure to defined electric stress.* Proceedings of the Institution of Mechanical Engineers, Part J: Journal of Engineering Tribology, 2009. **223**(5): p. 787-797.
70. Jagenbrein, A., et al., *Investigation of the physical mechanisms in rolling bearings during the passage of electric current.* Tribotest, 2005. **11**(4): p. 295-306.
71. Jagenbrein, A., *Investigation of bearing failures due to electric current passage*. 2005, Technical University of Vienna: Vienna.
72. Preisinger, G., *Cause and effect of bearing currents in frequency converter drive electrical motors - investigations of electrical proprerties of rolling element bearings*. 2002, Technical University of Vienna: Steyr, Austria.
73. Tischmacher, H. and S. Gattermann. *Bearing currents in converter operation*. in *IEEE International Conference on Electrical Machines (ICEM)*. 2010.
74. Schenk, O.A., Staffan, *Stromdurchgang durch Wälzlager.* 1955. **87**.
75. ABB, *Technical guide No. 5 - Bearing currents in modern AC drive systems*. 2011, ABB Drives.
76. Busse, D., et al., *System electrical parameters and their effects on bearing currents.* IEEE Transactions on Industrial Electronics, 1997. **33**(2): p. 577-584.
77. Busse, D., et al., *Bearing currents and their relationship to PWM drives.* IEEE Transactions on Power Electronics, 1997. **12**(2): p. 243-252.
78. IEEE, *IEEE Standard test procedure for polyphase induction motors and generators*, in *IEEE Std 112-2004 (Revision of IEEE Std 112-1996)*. 2004. p. 0_1-79.
79. Busse, D.F., et al., *An evaluation of the electrostatic shielded induction motor: a solution for rotor shaft voltage buildup and bearing current.* IEEE Transactions on Industrial Electronics, 1997. **33**(6): p. 1563-1570.
80. Firouzjaee, J.A., *Redemption strategies of shaft and common mode voltages in adjustable speed drive systems*, in *Faculty of Built Environment and Engineering*. 2010, Queensland University of Technology: Queensland, Australia.
81. Zoelen, M.T.v., *Thin layer flow in rolling element bearings*. 2009, s.n.]: S.l.
82. Hausberg, V. and H.O. Seinsch, *Kapazitive Lagerspannungen und -ströme bei umrichtergespeisten Induktionsmaschinen.* Electrical Engineering, 2000. **82**(3-4): p. 153-162.
83. Macdonald, D. and W. Gray. *A practical guide to understanding bearing damage related to PWM drives*. in *Pulp and Paper Industry Technical Conference*. 1998.
84. Kriese, M., et al. *Prediction of motor bearing currents for converter operation*. in *IEEE International Conference on Electrical Machines (ICEM)*. 2010.
85. Lipo, T.A., S. Chen and D.W. Novotny, *Circulating type of motor bearing currents in inverter drives*. 1996, University of Wisconsin-Madison: Madison, Wisconsin.
86. Cacciato, M., et al. *High frequency modeling of bearing currents and shaft voltage on electrical motors*. in *Proceedings of the Eighth International Conference on Electrical Machines and Systems (ICEMS)*. 2005.
87. Busse, D.F., et al., *The effects of PWM voltage source inverters on the mechanical performance of rolling bearings.* IEEE Transactions on Industrial Electronics, 1997. **33**(2): p. 567-576.

88. Nieuwenhuizen, J., *Method and arrangement to monitor a bearing of a wind turbine*. 2014, Google Patents.
89. SKF, *INSOCOAT® Electrically insulated rolling bearings*, S.Ö. AG, Editor. 2002: Austria.
90. Muetze, A. and H.W. Oh, *Application of static charge dissipation to mitigate electric discharge bearing currents.* IEEE Transactions on Industrial Electronics, 2008. **44**(1): p. 135-143.
91. Edvall, M., et al., *Experimental study of current damages in bearings*, in *Proceedings of the Third International Conference on Advances in Processing, Testing and Application of Dielectric Materials*. 2007. p. 141-146.
92. Tischmacher, H. and S. Gattermann. *Investigations on bearing currents in converter-fed electrical motors*. in *International Conference on Electrical Machines (ICEM)*. 2012.
93. Costabile, G., et al. *Performances of dielectric greases for rolling bearings employed in high power induction motors fed by PWM inverters*. in *Conference on Electrical Insulation and Dielectric Phenomena (CEIDP)*. 2007.
94. Der Houhanessian, V., *Measurement and analysis of dielectric response in oil-paper insulation systems*. 1998.
95. Beroual, A., et al., *Behavior of streamers in liquids under step voltages in point-plane geometry.* IEEE Transactions on Electrical Insulation, 1988. **23**(6): p. 955-959.
96. Chadband, W.G. *From bubbles to breakdown, or vice-versa*. in *IEEE International conference on conduction and breakdown in dielectric liquids (ICDL)*. 1993.
97. Aka-Ngnui, T. and A. Beroual, *Bubble dynamics and transition into streamers in liquid dielectrics under a high divergent electric field.* Journal of Physics D: Applied Physics, 2001. **34**(9): p. 1408-1412.
98. Qian, J., et al., *Microbubble-based model analysis of liquid breakdown initiation by a submicrosecond pulse.* Journal of Applied Physics, 2005. **104**(11): p. 113304-113310.
99. Chadband, W.G., *A pre-breakdown phenomenon in liquid dielectrics.* British Journal of Applied Physics 1965. **16**.
100. Devins, J.C., S.J. Rzad and R.J. Schwabe, *Breakdown and prebreakdown phenomena in liquids.* Journal of Applied Physics, 1981. **52**(7): p. 4531-4545.
101. Butcher, M., et al., *Conduction and breakdown mechanismsin transformer oil.* IEEE Transactions on Plasma Science, 2006. **34**(2): p. 467-475.
102. Kuffel, E., et al., *High voltage engineering: fundamentals*. 2000, Boston: Butterworth-Heinemann.
103. Naidu, M.S. and V. Kamaraju, *High voltage engineering*. 1996, New York: McGraw-Hill.
104. Prashad, H., *Appearance of craters on track surface of rolling element bearings by spark erosion.* Tribology International, 2001. **34**(1): p. 39-47.
105. Kolbe, H., A. Muetze and K. Hameyer, *Modelling of impulse currents in mechanical rolling element bearings.* COMPEL: The International Journal for Computation and Mathematics in Electrical and Electronic Engineering, 2012. **31**(6): p. 1575-1589.
106. Tischmacher, H. and S. Gattermann. *Multiple signature analysis for the detection of bearing currents and the assessment of the resulting bearing wear*. in *International Symposium on Power Electronics, Electrical Drives, Automation and Motion (SPEEDAM)*. 2012.
107. Wittek, E., et al. *Capacitances and lubricant film thicknesses of motor bearings under different operating conditions*. 2010. IEEE.

108. Magdun, O. and A. Binder. *Calculation of roller and ball bearing capacitances and prediction of EDM currents*. in *35th Annual Conference of IEEE Industrial Electronics, IECON*. 2009.
109. Roberts, C.W.D., *Condition monitoring of wind turbines: Technology overview, seeded-fault testing and cost-benefit analysis.*, C. Palo Alto, Editor. 2006, EPRI.
110. Hameed, Z., et al., *Condition monitoring and fault detection of wind turbines and related algorithms: A review.* Renewable and Sustainable Energy Reviews, 2009. **13**(1): p. 1-39.
111. Bangalore, P., *Load and risk based maintenance management of wind turbines*. 2014, Chalmers University of Technology: Göteborg.
112. Bangalore, P. and L. Bertling. *Self evolving neural network based algorithm for fault prognosis in wind turbines : A case study*. 2011.
113. Sonerud, B., *Characterization of electrical insulation exposed to arbitrary voltage waveforms*. 2010, Chalmers University of Technology: Göteborg.
114. Duracell, *Duracell DX1500H data sheet*.
115. Smolenski, R., A. Kempski and J. Bojarski, *Statistical approach to discharge bearing currents.* COMPEL: The International Journal for Computation and Mathematics in Electrical and Electronic Engineering, 2010. **29**(3): p. 647-666.
116. Kempski, A., R. Smolenski and J. Bojarski, *Statistical model of electrostatic discharge hazard in bearings of induction motor fed by inverter.* Journal of Electrostatics, 2005. **63**(6-10): p. 475-480.
117. Tobazeon, R., J.C. Filippini and C. Marteau, *On the measurement of the conductivity of highly insulating liquids.* IEEE Transactions on Dielectrics and Electrical Insulation, 1994. **1**(6): p. 1000-1004.
118. Leslie, R.R., *Additives for Lubricants*, in *Handbook of lubrication and tribology: Theory and design, second volume*. 2012, CRC Press. p. 1-22.
119. Garton, C.G., *Dielectric loss in thin films of insulating liquids.* Journal of the Institution of Electrical Engineers Part III Communication Engineering, including the Proceedings of the Wireless Section of the Institution, 1941. **88**: p. 23-40.
120. Alexander, J.C., *Dielectric properties of polyamides: Polyhexamethylene adiparnide and polyhexarnethylene sebacarnide.* Jorunal of Research of the National Bureau of Standards-A. Physics and Chemistry, 1961. **65A**: p. 185-196.
121. Richard, H.B., *Dielectric Loss in 66 Nylon (Polyhexamethylene Adipamide).* The Journal of Chemical Physics, 1959. **30**: p. 1276-1283.
122. Tischmacher, H., I.P. Tsoumas and S. Gattermann. *Probability model for discharge activities in bearings of converter-fed electric motors*. in *IEEE International Conference on Electrical Machines (ICEM)*. 2014.
123. DeNure, D.G. and E.S. Sproles, *Dust test results on multicontact circuit board connectors.* IEEE Transactions on Components, Hybrids and Manufacturing Technology, 1991. **14**(4): p. 802-808.
124. Inc., P.T. *History of test dust*. 2016; Available from: http://www.powdertechnologyinc.com/test-dust-contaminants/test-dust-history/.
125. Adair, J.H., J.J. Mecholsky, Jr. and D.J. Mitchell, *Effects of particulate debris morphology on the rolling wear behavior of all-steel and si3n4-steel bearing element couples*. Annual cocoa beach conference and exposition. 1999, Cocoa Beach, FL (US): Oak Ridge National Lab., TN (US). Medium: P; Size: 12 pages.
126. Prashad, H., *Effect of operating parameters on the threshold voltages and impedance response of non-insulated rolling element bearings under the action of electrical currents.* Wear, 1987. **117**(2): p. 223-240.

127. Song, B., *Impact of dust on the reliability of printed circuit assemblies*, in *Mechanical Engineering*. 2013, University of Maryland: Maryland.
128. Dwyer-Joyce, R.S., *The life cycle of a debris particle*, in *Tribology and interface engineering series*, M.P.G.D. D. Dowson and A.A. Lubrecht, Editors. 2005, Elsevier. p. 681-690.
129. Hamer, J.C., R.S. Sayles and E. Ioannides, *Particle deformation and counterface damage when relatively soft particles are squashed between hard anvils.* Tribology Transactions, 1989. **32**(3): p. 281-288.
130. RICOH, *Print Cartridge Black MP C3504 (Black toner) Safety Data Sheet*. 2017, Ricoh Company,Ltd.
131. Kojima, T. and J.A. Elliott, *Incipient flow properties of two-component fine powder systems and their relationships with bulk density and particle contacts.* Powder Technology, 2012. **228**: p. 359-370.
132. Gascoin, N., P. Gillard and G. Baudry, *Characterisation of oxidised aluminium powder: Validation of a new anodic oxidation bench.* Journal of Hazardous Materials, 2009. **171**(1–3): p. 348-357

Appendix A – Results of particle counting analysis

- **Arizona test dust particle information (Sample A1) and particle counting analysis**

Arizona test dust, in which particle size distribution ranges between 5.5 and 176 μm, has bulk density of 1200 kg/m^3. The dust is majorly composed of silicone oxide (SiO_2, 68 to 76 % mass fraction) and aluminium oxide (Al_2O_3, 10 to 15 % mass fraction), Other components of the dust are listed in Table XI and dry and wet sample images are shown in Figure 141 and Figure 142 respectively.

The reported [127] conductivity of Arizona test dust, measured in an aqueous solution, is less than 106 μS/cm (measured by mixing 250 mg of test dust in deionized (DI) water of (18.2 MΩcm). It was reported that the Arizona test dust contamination of lubricant (size 0 to100 μm) can create in a rolling bearing craters of depths 0.6 to 1.0 μm and of width ~50 μm [128](the evaluation is based on a model proposed by Hamer et al in [129]). Formation of dust pellets under high pressure changes its structural properties and affects the DC conductivity for the short duration of being in the loaded zone. Particle of Arizona test dust dispersed in oil shrink in size, as shown below and smaller fractions are found to be in the range of the lubricant film thickness during operation.

Table XI. Particle size distribution and chemical composition of Arizona test dust

Size (μm)	Mass fraction % less than
5.5	13±3
11	24±3
22	37±3
44	56±3
88	84±3
176	100

Chemical	Mass fraction (%)
SiO_2	68 to 76
Al_2O_3	10 to 15
Fe_2O_3	2 to 5
Na_2O	2 to 4
CaO	2 to 5
MgO	1 to 2
TiO_2	0.5 to 1
K_2O	2 to 5

Photos of dry samples are shown below in Figure 141and results of the particle counting analysis for the dry powder and the wet sample (particulate in oil with concentration of 150 mg/L, Sample A1) are shown on the next two pages.

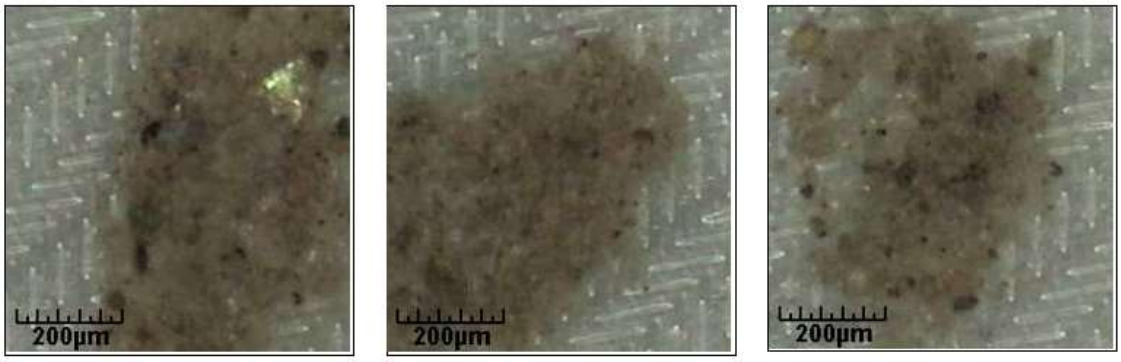

Figure 141- Dry sample images of Arizona test dust

Particle counting analysis of dry Arizona Test Dust.

Cleanliness analysis MP A27

General			
Component	*Arizona dust (dry powder)*	Customer	
Type nr.		SKF Site	*Chalmers*
Membrane nr.		Channel / Area	
Component area	*1000 cm²*	Operation	

Extraction			
Method	*Pressure Rinsing 1.5 bar*	Operator	*Petter Hagg*
Fluid type	*Solvent Class III Shellsol T*	Extraction date	
Total volume	*0 liter*	Number of components	*1*
US		Membrane type	*5.0 um Nylon Pall PCC501MEM5*

Microscopic analysis			
Resolution	*X:2.6 µm/Pxl Y:2.6 µm/Pxl*	Operator	*Jonas Peterson*
Meas. dia. membrane	*44.0 mm*	Analysing date	*22/06/2016*

Measurement results - Counts per size classes

		Number of particles per component			Number of particles referring to 1000 cm²			Max. blank level**
Particle size x(µm)	Code	All types	Metallic	Fibres*	All types	Metallic	Fibres*	All types
5 ≤ x < 15	B	*5500.0*	0.0	*0.0*	*5500.0*	0.0	*0.0*	*550*
15 ≤ x < 25	C	*1538.0*	1.0	*0.0*	*1538.0*	1.0	*0.0*	*154*
25 ≤ x < 50	D	*1121.0*	1.0	*0.0*	*1121.0*	1.0	*0.0*	*112*
50 ≤ x < 100	E	*314.0*	4.0	*0.0*	*314.0*	4.0	*0.0*	*31*
100 ≤ x < 150	F	*27.0*	1.0	*0.0*	*27.0*	1.0	*0.0*	*3*
150 ≤ x < 200	G	*4.0*	0.0	*0.0*	*4.0*	0.0	*0.0*	*0*
200 ≤ x < 400	H	*4.0*	0.0	*0.0*	*4.0*	0.0	*0.0*	*0*
400 ≤ x < 600	I	*1.0*	0.0	*1.0*	*1.0*	0.0	*1.0*	*0*
600 ≤ x < 1000	J	*0.0*	0.0	*0.0*	*0.0*	0.0	*0.0*	*0*
1000 ≤ x	K	*2.0*	0.0	*2.0*	*2.0*	0.0	*2.0*	*0*
5 ≤ x	B-K	*8511.0*	*7.0*	*3.0*	*8511.0*	*7.0*	*3.0*	*851*
15 ≤ x	C-K	*3011.0*	*7.0*	*3.0*	*3011.0*	*7.0*	*3.0*	*301*
100 ≤ x	F-K	*38.0*	*1.0*	*3.0*	*38.0*	*1.0*	*3.0*	*4*

CCC (Component Cleanliness Code)			
CCCa	*A(B13/C11/D11/E9/F5/G2/H2/I0/J00/K1)*	*CCCwoF*	*A(B13/C11/D11/E9/F5/G2/H2/I00/J00/K00)*
CCCm	*A(B00/C0/D0/E2/F0/G00/H00/I00/J00/K00)*	*CCCo*	*A(B13/C11/D11/E9/F5/G2/H2/I00/J00/K00)*
a: all types, woF: without fibers, m: metallic, o:non metallic, fibers excluded			

Largest particle				
	Length	Width		
Largest particle (fibres excluded)	*361 µm*	*171 µm*		
Largest metallic particle	*130 µm*	*104 µm*		
Largest fibre*	*1539 µm*		Total length of fibres	*3.48 mm*

Comments:

* Definition fibre: Non metallic particle with a compactness <30% or length/width > 10.

** Calculation of the maximum allowed blank level - for comparison with the actual blank level.

Particle counting analysis of Sample A1 with particle concentration of 150 mg/L.

Cleanliness of hydraulic liquid – ISO 4406

General	
Customer	*Joshi Abhishek*
SKF Site	*Chalmers University*
Channel / Area	
Machine number	

Liquid & Filtering			
Hydraulic liquid	-	Membrane no.	*Arizona dust particles*
Brand / Type		Membrane type	*1.2 um Nylon Pall PCC501MEM5*
Amount of liquid	*5*	Filtering date	

Microscopic analysis			
Resolution	*X:2.6 µm/Pxl Y:2.6 µm/Pxl*	Operator	*Jonas Peterson*
Meas. dia. membrane	*44.0*	Analysing date	*21/06/2016*

Particle size x(µm)	Number of particles per sample	Number of particles per 100 ml
	All types	All types
5 ≤ x	*8450*	*169000*
15 ≤ x	*2458*	*49160*
5 ≤ x < 15	*5992*	*119840*
15 ≤ x < 25	*1194*	*23880*
25 ≤ x < 50	*846*	*16920*
50 ≤ x < 100	*358*	*7160*
100 ≤ x < 150	*46*	*920*
150 ≤ x < 200	*7*	*140*
200 ≤ x < 400	*5*	*100*
400 ≤ x < 600	*1*	*20*
600 ≤ x < 1000	*0*	*0*
1000 ≤ x	*1*	*20*

ISO 4406 code	
	18/16

Largest particle			
	Length	Width	
	2254	*35*	

Comments:

Largest particle

2nd largest particle

3rd largest particle

Total filter

Figure 142 - Wet sample images of Arizona test dust from lubricant Sample A1.

- **Toner particle information (Sample A2) and particle counting analysis**

The chemical composition of toner is given in product safety data sheet [130]. The main ingredients is a form of polyester resin constituting up to 60 to 90 % by weight. The other components are wax, carbon black, titan oxide and silica, tabulated in Table XII.

Table XII - Ingredients of a toner and their corresponding weight %

Ingredients	Chemical formula	Contents [Weight %]
Polyester Resin	Confidential	60 – 90
Wax	Confidential	1- 20
Carbon Black	C	1 - 20
Titan Oxide	TiO_2	0.1 - 1
Silica	SiO_2	< 10

Bulk density of toner particles is reported to be between 1100 and 1300 kg/m^3 [131]. As seen in Figure 143 and Figure 144, the size of dry and wet toner particles is almost identical and is not affected by the sonication process. The particle size of toner particles is about one order of magnitude smaller than the median particle size of Arizona test dust (up to 100 μm).

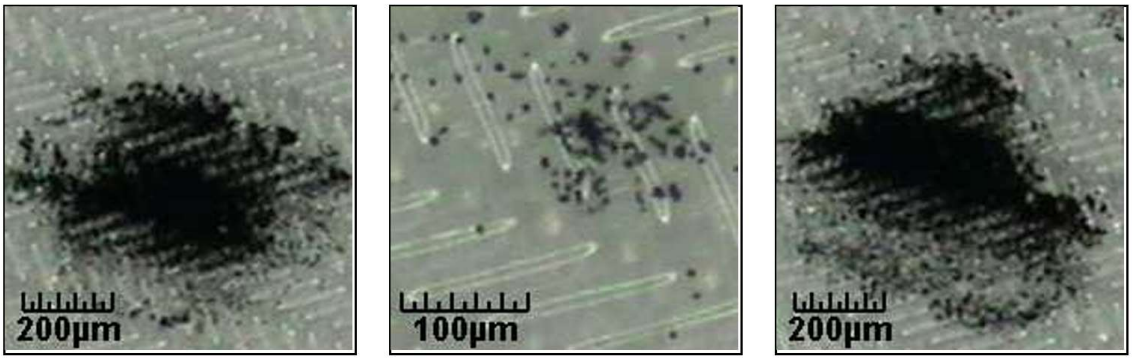

Figure 143 - Dry sample images of the toner particles.

The results of the dry and wet particle counting analysis of lubricant Sample A2 is shown on the next two pages.

Particle counting analysis of dry toner powder.

Cleanliness analysis MP A27

General			
Component	*Toner (dry powder)*	Customer	
Type nr.		SKF Site	*Chalmers*
Membrane nr.		Channel / Area	
Component area	*1000 cm²*	Operation	

Extraction			
Method	*Pressure Rinsing 1.5 bar*	Operator	*Petter Hagg*
Fluid type	*Solvent Class III Shellsol T*	Extraction date	
Total volume	*0 liter*	Number of components	*1*
US		Membrane type	*5.0 um Nylon Pall PCC501MEM5*

Microscopic analysis			
Resolution	*X:2.6 µm/Pxl Y:2.6 µm/Pxl*	Operator	*Jonas Peterson*
Meas. dia. membrane	*44.0 mm*	Analysing date	*22/06/2016*

Measurement results - Counts per size classes

		Number of particles per component			Number of particles referring to 1000 cm²			Max. blank level**
Particle size x(µm)	Code	All types	Metallic	Fibres*	All types	Metallic	Fibres*	All types
5 ≤ x < 15	B	*26563.0*	4.0	*0.0*	*26563.0*	4.0	*0.0*	*2656*
15 ≤ x < 25	C	*6012.0*	3.0	*0.0*	*6012.0*	3.0	*0.0*	*601*
25 ≤ x < 50	D	*3236.0*	1.0	*3.0*	*3236.0*	1.0	*3.0*	*324*
50 ≤ x < 100	E	*835.0*	1.0	*9.0*	*835.0*	1.0	*9.0*	*84*
100 ≤ x < 150	F	*136.0*	0.0	*10.0*	*136.0*	0.0	*10.0*	*14*
150 ≤ x < 200	G	*47.0*	0.0	*1.0*	*47.0*	0.0	*1.0*	*5*
200 ≤ x < 400	H	*77.0*	0.0	*7.0*	*77.0*	0.0	*7.0*	*8*
400 ≤ x < 600	I	*27.0*	0.0	*0.0*	*27.0*	0.0	*0.0*	*3*
600 ≤ x < 1000	J	*16.0*	0.0	*0.0*	*16.0*	0.0	*0.0*	*2*
1000 ≤ x	K	*4.0*	0.0	*0.0*	*4.0*	0.0	*0.0*	*0*
5 ≤ x	B-K	*36953.0*	*9.0*	*30.0*	*36953.0*	*9.0*	*30.0*	*3695*
15 ≤ x	C-K	*10390.0*	*5.0*	*30.0*	*10390.0*	*5.0*	*30.0*	*1039*
100 ≤ x	F-K	*307.0*	*0.0*	*18.0*	*307.0*	*0.0*	*18.0*	*31*

CCC (Component Cleanliness Code)			
CCCa	*A(B15/C13/D12/E10/F8/G6/H7/I5/J4/K2)*	*CCCwoF*	*A(B15/C13/D12/E10/F7/G6/H7/I5/J4/K2)*
CCCm	*A(B2/C2/D0/E0/F00/G00/H00/I00/J00/K00)*	*CCCo*	*A(B15/C13/D12/E10/F7/G6/H7/I5/J4/K2)*
a: all types, woF: without fibers, m: metallic, o:non metallic, fibers excluded			

Largest particle				
	Length	Width		
Largest particle (fibres excluded)	*1268 µm*	*1069 µm*		
Largest metallic particle	*58 µm*	*47 µm*		
Largest fibre*	*345 µm*		Total length of fibres	*4.00 mm*

Comments:

* Definition fibre: Non metallic particle with a compactness <30% or length/width > 10.

** Calculation of the maximum allowed blank level - for comparison with the actual blank level.

Particle counting analysis of Sample A2 with particle concentration of 150 mg/L.

Cleanliness of hydraulic liquid – ISO 4406

General	
Customer	*Joshi Abhishek*
SKF Site	*Chalmers University*
Channel / Area	
Machine number	

Liquid & Filtering			
Hydraulic liquid	-	Membrane no.	*Toner*
Brand / Type		Membrane type	*1.2 um Nylon Pall PCC501MEM5*
Amount of liquid	*5*	Filtering date	

Microscopic analysis			
Resolution	*X:2.6 µm/Pxl Y:2.6 µm/Pxl*	Operator	*Jonas Peterson*
Meas. dia. membrane	*44.0*	Analysing date	*21/06/2016*

Particle size x(µm)	Number of particles per sample	Number of particles per 100 ml
	All types	All types
5 ≤ x	*977870*	*19557400*
15 ≤ x	*286264*	*5725280*
5 ≤ x < 15	*691606*	*13832120*
15 ≤ x < 25	*179189*	*3583780*
25 ≤ x < 50	*87868*	*1757360*
50 ≤ x < 100	*16931*	*338620*
100 ≤ x < 150	*1624*	*32480*
150 ≤ x < 200	*356*	*7120*
200 ≤ x < 400	*262*	*5240*
400 ≤ x < 600	*25*	*500*
600 ≤ x < 1000	*8*	*160*
1000 ≤ x	*1*	*20*

ISO 4406 code	
	-/23

Largest particle			
	Length	Width	
	1376	*34*	

Comments:

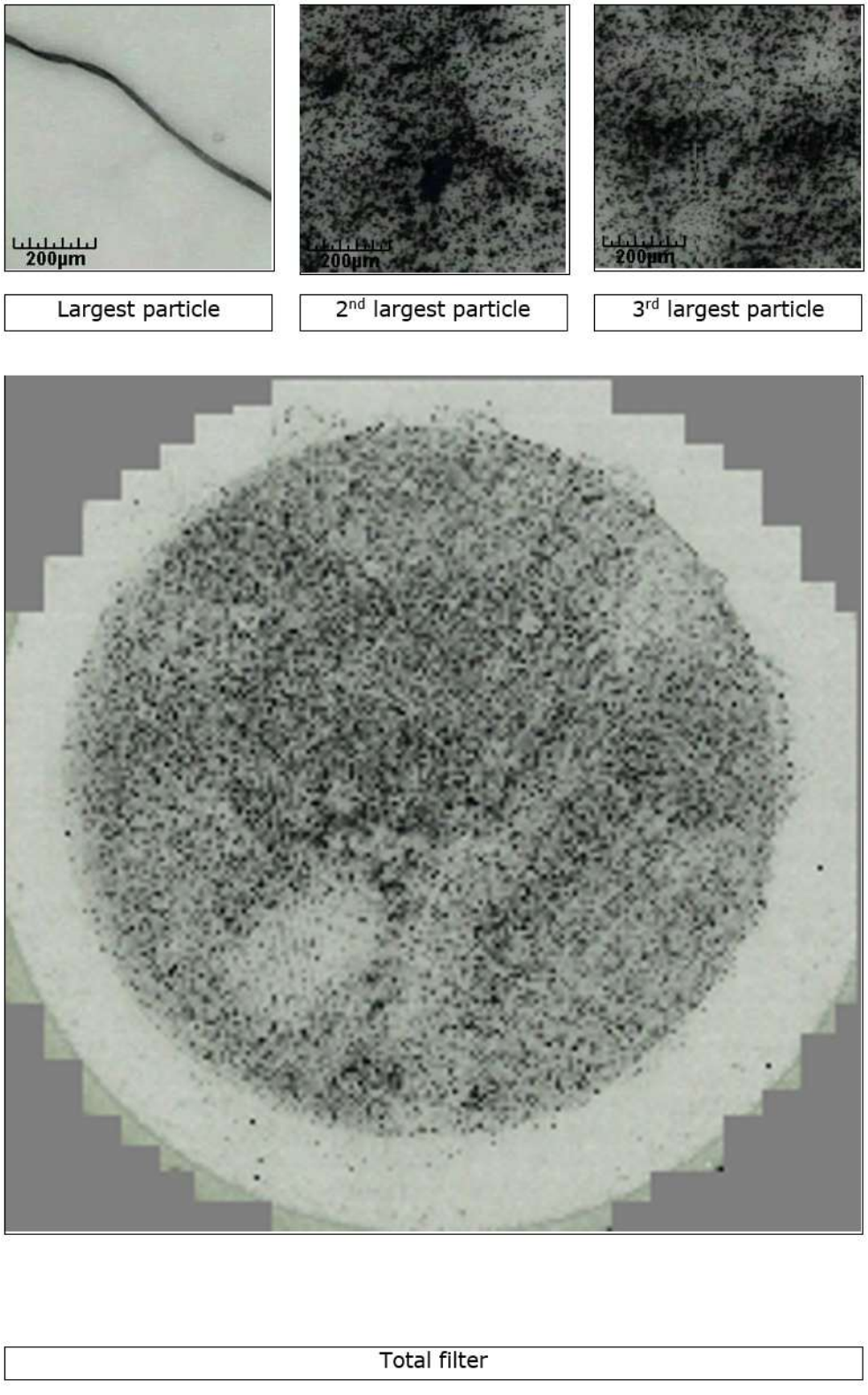

Figure 144 - Wet sample images of toner particles from lubricant Sample A2.

- **Aluminium powder information (Sample A3) and particle counting analysis**

  Aluminium powder has a density of 2.7 g/cm^3, reported at 20 °C. The average size of the aluminium particle size distribution is shown below. The aluminium particles are electrically conducting, but could also develop a layer of oxide, of up to 0.6 μm [132]. Dry aluminium particles are shown in Figure 145, while the images of aluminium powder from the lubricant Sample A3 is shown in Figure 146.

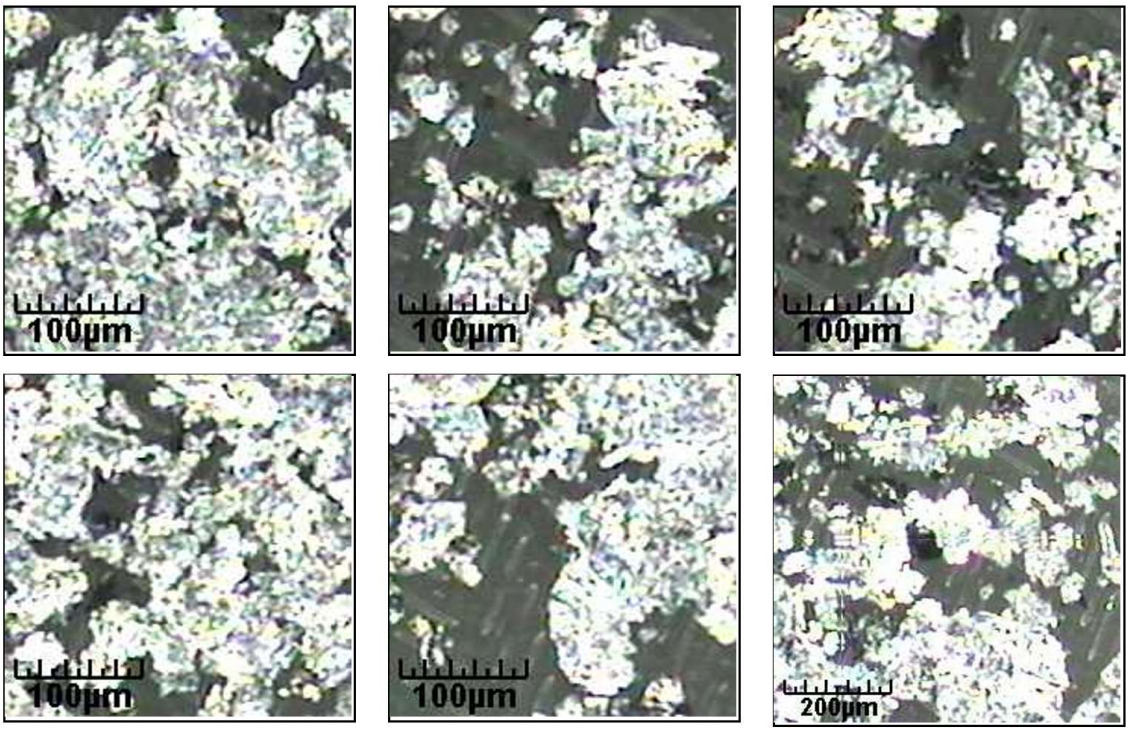

Figure 145 - Dry sample images of aluminium powder.

The results of the dry and wet particle counting analysis of lubricant Sample A3 is shown on the next two pages.

Particle counting analysis of dry aluminium powder.

Cleanliness analysis MP A27

General			
Component	*Aluminium (dry powder)*	Customer	
Type nr.		SKF Site	*Chalmers*
Membrane nr.		Channel / Area	
Component area	*1000 cm²*	Operation	

Extraction			
Method	*Pressure Rinsing 1.5 bar*	Operator	*Petter Hagg*
Fluid type	*Solvent Class III Shellsol T*	Extraction date	
Total volume	*0 liter*	Number of components	*1*
US		Membrane type	*5.0 um Nylon Pall PCC501MEM5*

Microscopic analysis			
Resolution	*X:2.6 µm/Pxl Y:2.6 µm/Pxl*	Operator	*Jonas Peterson*
Meas. dia. membrane	*44.0 mm*	Analysing date	*22/06/2016*

Measurement results - Counts per size classes

		Number of particles per component			Number of particles referring to 1000 cm²			Max. blank level**
Particle size x(µm)	Code	All types	Metallic	Fibres*	All types	Metallic	Fibres*	All types
5 ≤ x < 15	B	*2618.0*	1290.0	*0.0*	*2618.0*	1290.0	*0.0*	*262*
15 ≤ x < 25	C	*2049.0*	1549.0	*0.0*	*2049.0*	1549.0	*0.0*	*205*
25 ≤ x < 50	D	*2629.0*	2172.0	*3.0*	*2629.0*	2172.0	*3.0*	*263*
50 ≤ x < 100	E	*1926.0*	1766.0	*2.0*	*1926.0*	1766.0	*2.0*	*193*
100 ≤ x < 150	F	*887.0*	874.0	*1.0*	*887.0*	874.0	*1.0*	*89*
150 ≤ x < 200	G	*500.0*	497.0	*2.0*	*500.0*	497.0	*2.0*	*50*
200 ≤ x < 400	H	*555.0*	554.0	*1.0*	*555.0*	554.0	*1.0*	*56*
400 ≤ x < 600	I	*107.0*	106.0	*1.0*	*107.0*	106.0	*1.0*	*11*
600 ≤ x < 1000	J	*48.0*	44.0	*4.0*	*48.0*	44.0	*4.0*	*5*
1000 ≤ x	K	*14.0*	14.0	*0.0*	*14.0*	14.0	*0.0*	*1*
5 ≤ x	B-K	*11333.0*	*8866.0*	*14.0*	*11333.0*	*8866.0*	*14.0*	*1133*
15 ≤ x	C-K	*8715.0*	*7576.0*	*14.0*	*8715.0*	*7576.0*	*14.0*	*872*
100 ≤ x	F-K	*2111.0*	*2089.0*	*9.0*	*2111.0*	*2089.0*	*9.0*	*211*

CCC (Component Cleanliness Code)			
CCCa	*A(B12/C12/D12/E11/F10/G9/H10/I7/J6/K4)*	*CCCwoF*	*A(B12/C12/D12/E11/F10/G9/H10/I7/J6/K4)*
CCCm	*A(B11/C11/D12/E11/F10/G9/H10/I7/J6/K4)*	*CCCo*	*A(B11/C9/D9/E8/F4/G0/H00/I00/J00/K00)*
a: all types, woF: without fibers, m: metallic, o:non metallic, fibers excluded			

Largest particle				
	Length	Width		
Largest particle (fibres excluded)	*2657 µm*	*1355 µm*		
Largest metallic particle	*2657 µm*	*1355 µm*		
Largest fibre*	*908 µm*		Total length of fibres	*4.59 mm*

Comments:

* Definition fibre: Non metallic particle with a compactness <30% or length/width > 10.

** Calculation of the maximum allowed blank level - for comparison with the actual blank level.

Particle counting analysis of Sample A3 with particle concentration of 150 mg/L.

Cleanliness of hydraulic liquid – ISO 4406

General	
Customer	*Joshi Abhishek*
SKF Site	*Chalmers University*
Channel / Area	
Machine number	

Liquid & Filtering			
Hydraulic liquid	-	Membrane no.	*Aluminium*
Brand / Type		Membrane type	*1.2 um Nylon Pall PCC501MEM5*
Amount of liquid	*10*	Filtering date	

Microscopic analysis			
Resolution	*X:2.6 µm/Pxl Y:2.6 µm/Pxl*	Operator	*Jonas Peterson*
Meas. dia. membrane	*44.0*	Analysing date	*21/06/2016*

Particle size x(µm)	Number of particles per sample	Number of particles per 100 ml
	All types	All types
5 ≤ x	*192956*	*1929560*
15 ≤ x	*109890*	*1098900*
5 ≤ x < 15	*83066*	*830660*
15 ≤ x < 25	*41572*	*415720*
25 ≤ x < 50	*36683*	*366830*
50 ≤ x < 100	*19627*	*196270*
100 ≤ x < 150	*5882*	*58820*
150 ≤ x < 200	*2516*	*25160*
200 ≤ x < 400	*2852*	*28520*
400 ≤ x < 600	*523*	*5230*
600 ≤ x < 1000	*211*	*2110*
1000 ≤ x	*24*	*240*

ISO 4406 code	
	21/21

Largest particle			
	Length	Width	
	1804	*471*	

Comments:

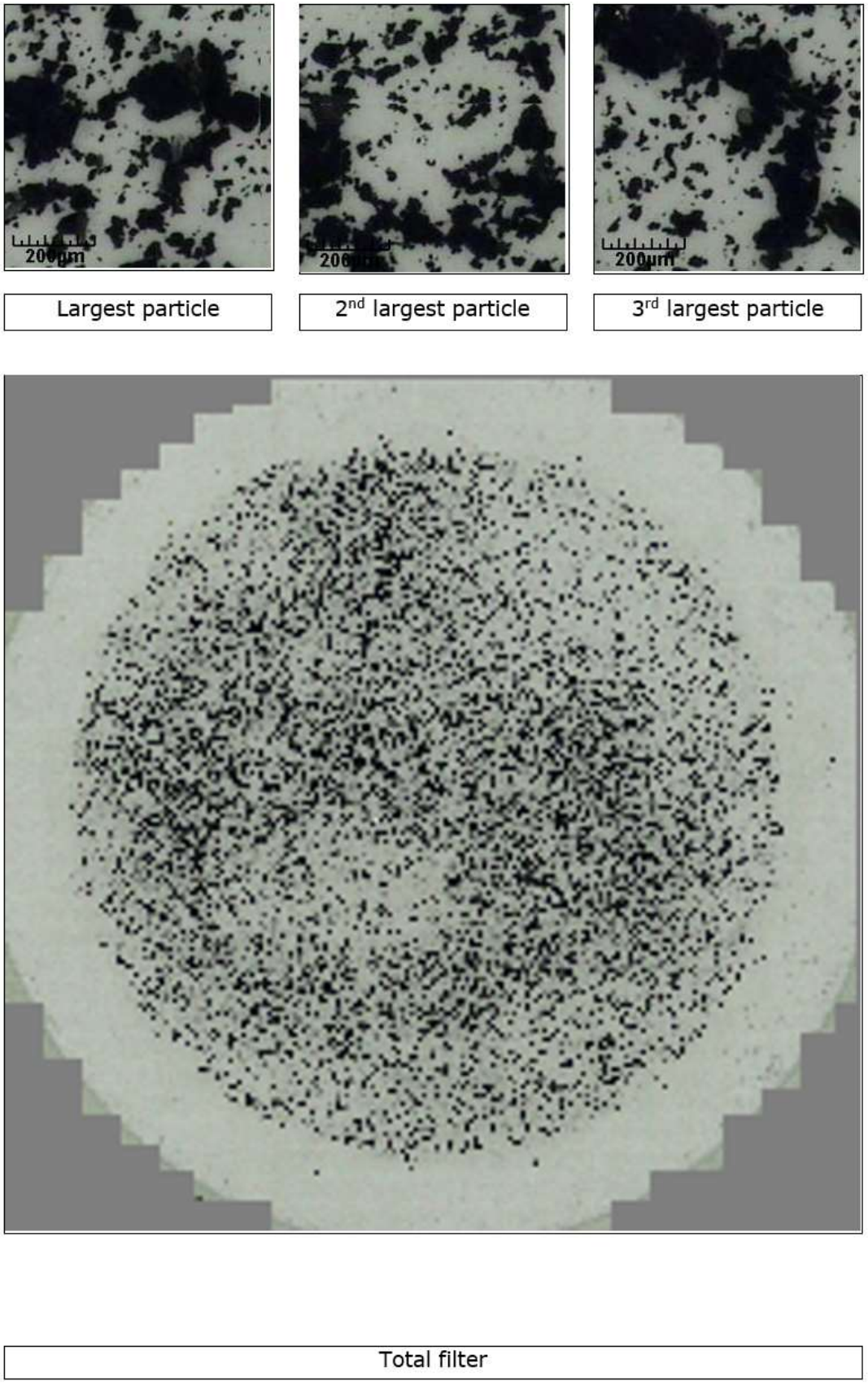

Figure 146- Wet sample images of the aluminium powder from lubricant Sample A3.

- **Iron powder information (Sample A4) and particle counting analysis**

Iron powder particles are metallic and hence are of electrically conducting nature.

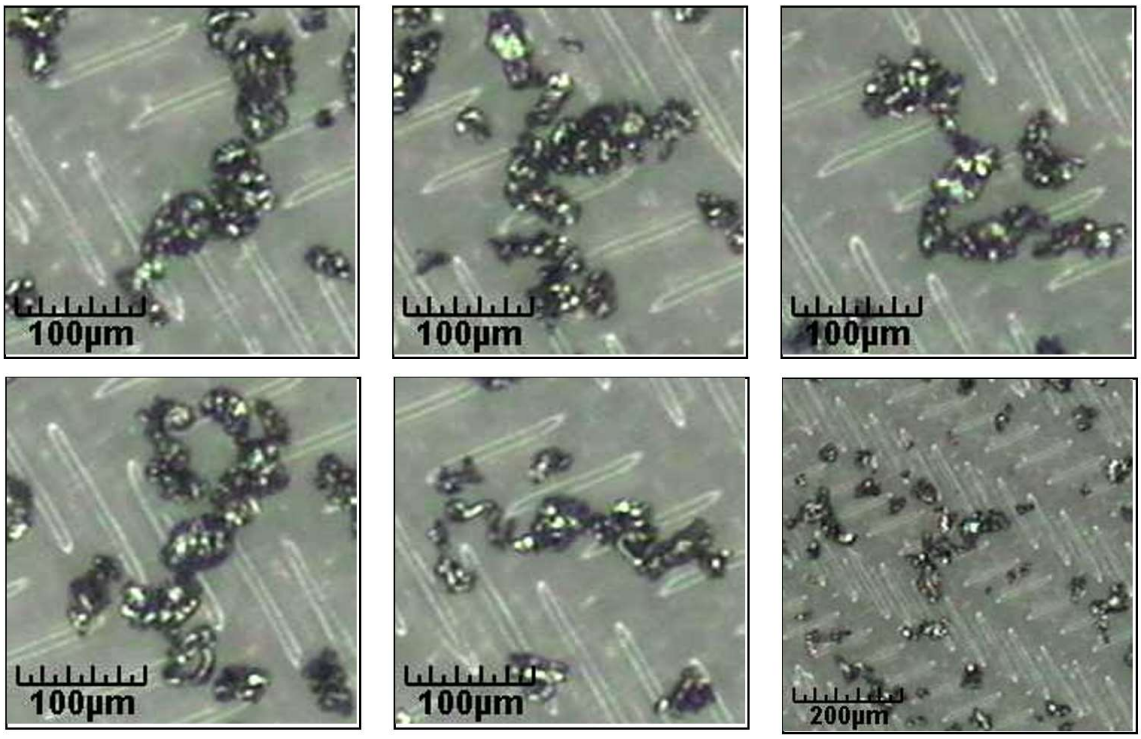

Figure 147 - Dry sample images of iron powder.

The results of the dry and wet particle counting analysis of lubricant Sample A4 is shown on the next two pages.

Particle counting analysis of dry iron powder.

Cleanliness analysis MP A27

General			
Component	*Fe (dry powder)*	Customer	
Type nr.		SKF Site	*Chalmers*
Membrane nr.		Channel / Area	
Component area	*1000 cm²*	Operation	

Extraction			
Method	*Pressure Rinsing 1.5 bar*	Operator	*Petter Hagg*
Fluid type	*Solvent Class III Shellsol T*	Extraction date	
Total volume	*0 liter*	Number of components	*1*
US		Membrane type	*5.0 um Nylon Pall PCC501MEM5*

Microscopic analysis			
Resolution	*X:2.6 µm/Pxl Y:2.6 µm/Pxl*	Operator	*Jonas Peterson*
Meas. dia. membrane	*44.0 mm*	Analysing date	*22/06/2016*

Measurement results - Counts per size classes

		Number of particles per component			Number of particles referring to 1000 cm²			Max. blank level**
Particle size x(µm)	Code	All types	Metallic	Fibres*	All types	Metallic	Fibres*	All types
5 ≤ x < 15	B	*2362.0*	15.0	*0.0*	*2362.0*	15.0	*0.0*	*236*
15 ≤ x < 25	C	*2377.0*	267.0	*0.0*	*2377.0*	267.0	*0.0*	*238*
25 ≤ x < 50	D	*8174.0*	3074.0	*0.0*	*8174.0*	3074.0	*0.0*	*817*
50 ≤ x < 100	E	*6965.0*	4781.0	*0.0*	*6965.0*	4781.0	*0.0*	*697*
100 ≤ x < 150	F	*649.0*	574.0	*0.0*	*649.0*	574.0	*0.0*	*65*
150 ≤ x < 200	G	*76.0*	74.0	*1.0*	*76.0*	74.0	*1.0*	*8*
200 ≤ x < 400	H	*12.0*	11.0	*0.0*	*12.0*	11.0	*0.0*	*1*
400 ≤ x < 600	I	*0.0*	0.0	*0.0*	*0.0*	0.0	*0.0*	*0*
600 ≤ x < 1000	J	*0.0*	0.0	*0.0*	*0.0*	0.0	*0.0*	*0*
1000 ≤ x	K	*0.0*	0.0	*0.0*	*0.0*	0.0	*0.0*	*0*
5 ≤ x	B-K	*20615.0*	*8796.0*	*1.0*	*20615.0*	*8796.0*	*1.0*	*2062*
15 ≤ x	C-K	*18253.0*	*8781.0*	*1.0*	*18253.0*	*8781.0*	*1.0*	*1825*
100 ≤ x	F-K	*737.0*	*659.0*	*1.0*	*737.0*	*659.0*	*1.0*	*74*

CCC (Component Cleanliness Code)			
CCCa	*A(B12/C12/D14/E13/F10/G7/H4/I00/J00/K00)*	*CCCwoF*	*A(B12/C12/D14/E13/F10/G7/H4/I00/J00/K00)*
CCCm	*A(B4/C9/D12/E13/F10/G7/H4/I00/J00/K00)*	*CCCo*	*A(B12/C12/D13/E12/F7/G0/H0/I00/J00/K00)*
a: all types, woF: without fibers, m: metallic, o:non metallic, fibers excluded			

Largest particle				
	Length	Width		
Largest particle (fibres excluded)	*264 µm*	*73 µm*		
Largest metallic particle	*264 µm*	*73 µm*		
Largest fibre*	*171 µm*		Total length of fibres	*0.17 mm*

Comments:

* Definition fibre: Non metallic particle with a compactness <30% or length/width > 10.

Particle counting analysis of Sample A4 with particle concentration of 150 mg/L.

Cleanliness of hydraulic liquid – ISO 4406

General	
Customer	*Joshi Abhishek*
SKF Site	*Chalmers University*
Channel / Area	
Machine number	

Liquid & Filtering			
Hydraulic liquid	-	Membrane no.	*Fe 150 mg/L*
Brand / Type		Membrane type	*1.2 um Nylon Pall PCC501MEM5*
Amount of liquid	*5*	Filtering date	

Microscopic analysis			
Resolution	*X:2.6 µm/Pxl Y:2.6 µm/Pxl*	Operator	*Jonas Peterson*
Meas. dia. membrane	*44.0*	Analysing date	*21/06/2016*

Particle size x(µm)	Number of particles per sample	Number of particles per 100 ml
	All types	All types
5 ≤ x	*7266*	*145320*
15 ≤ x	*4443*	*88860*
5 ≤ x < 15	*2823*	*56460*
15 ≤ x < 25	*566*	*11320*
25 ≤ x < 50	*1892*	*37840*
50 ≤ x < 100	*1874*	*37480*
100 ≤ x < 150	*97*	*1940*
150 ≤ x < 200	*11*	*220*
200 ≤ x < 400	*1*	*20*
400 ≤ x < 600	*0*	*0*
600 ≤ x < 1000	*2*	*40*
1000 ≤ x	*0*	*0*

ISO 4406 code	
	18/17

Largest particle			
	Length	Width	
	791	*47*	

Comments:

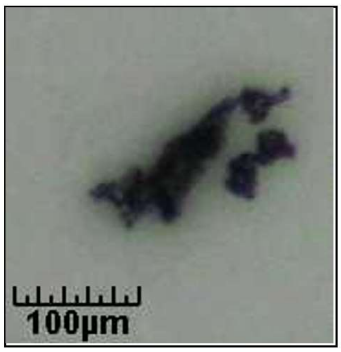

Largest particle

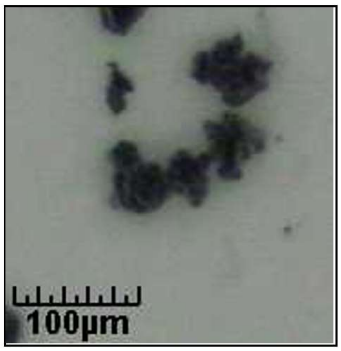

2nd largest particle

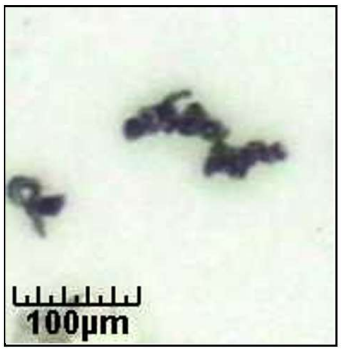

3rd largest particle

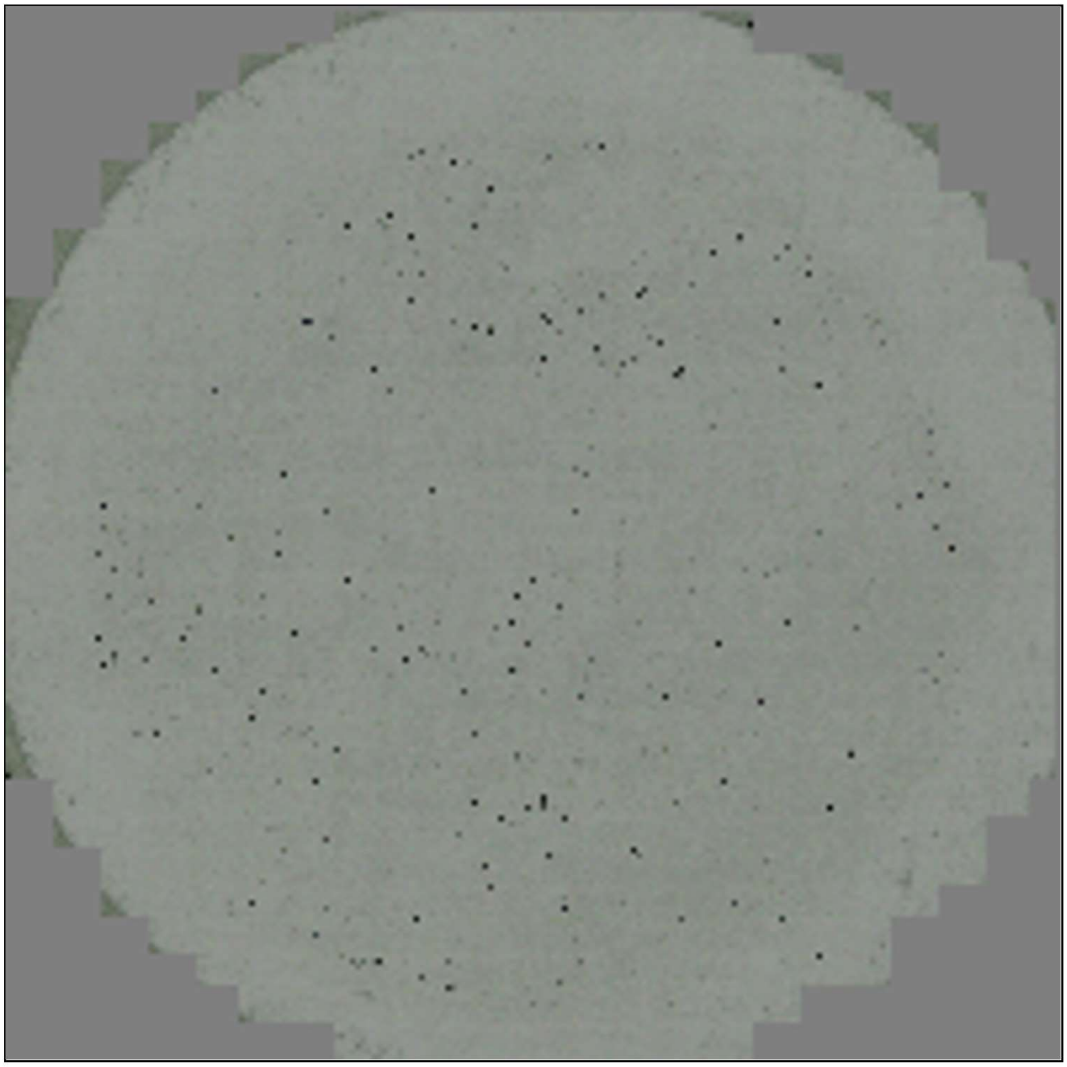

Total filter

Figure 148. Wet sample images of the iron powder from lubricant Sample A4.